Linear amplification in nonequilibrium turbulent boundary layers

Thesis by
Salvador Rey Gomez De La Cruz

In Partial Fulfillment of the Requirements for the
Degree of
Doctor of Philosophy in Aeronautics

CALIFORNIA INSTITUTE OF TECHNOLOGY
Pasadena, California

2024
Defended September 14, 2023

Salvador Rey Gomez De La Cruz
ORCID: 0000-0002-7568-721X

ACKNOWLEDGEMENTS

Before leaving Hayward, CA, I held the misconstrued belief that science and engineering were done in isolation. Thankfully, Berkeley and Caltech taught me that these disciplines are, in fact, collaborative. I'd like to take this space to thank my family, friends, mentors, and colleagues who have supported me throughout my graduate school journey. Words cannot express my gratitude towards all of your contributions, patience, and love.

First, I want to thank my advisor, Beverley McKeon, for all her guidance, encouragement, and support throughout my time at Caltech. As your student, thank you for all your patience and invaluable advice whenever I've been stuck, the freedom to explore research ideas, teaching me how to be detail-oriented, and always reminding me of the 'big picture.' As your mentee, thank you for letting me partake in professional development opportunities and introducing me to the fluids community. The welcoming and inclusive environment that you've built within, and outside of, the group has allowed me, and others, to thrive. You've been an inspirational role model for me as a researcher, academic, and person.

Next, I would like to thank the rest of my committee, Dan Meiron, Tony Leonard, and Mario Di Renzo. Dan, you were the first person to welcome me to Caltech when I applied, and ever since, you've been a welcoming and instructive figure during my time at Caltech. Tony, I am really grateful you started joining our group meetings. I've learned a lot from your insights, comments, and questions during group meetings. Thank you for sharing your expertise and always being available to talk. Mario, thank you for sharing your data and expertise in hypersonics, along with your patience throughout the 2022 summer program. Speaking of which, I am grateful to the funding and support from the U.S. Office of Naval Research through grants N00014-17-1-2307 and N00014-17-1-3022, which supported much of this research, the Center for Turbulence Research (CTR) Summer Program for supporting my research in hypersonics, and the Research University Alliance program for funding my visit to Harvard and providing professional development opportunities.

I want to thank all the faculty and staff who have made my time in this department enjoyable. To the faculty, thank you for your high expectations, instructive questions, and humility. These qualities have helped me think deeper about my work and inspired me to push my work to the highest quality. To the administrative staff,

thank you so much for all the help with any troubles I've faced and for always making this department an enjoyable place to work. A special thanks goes to Liza Bradulina, Christine Ramirez, and Jamie Meighen-Sei who have always gone above and beyond with their help. I also want to thank Glenda, and the rest of the facilities staff on campus, for ensuring that our surroundings are welcoming and well-kept.

A big reason why I enjoyed my time at Caltech was because I was fortunate enough to be surrounded by all the wonderful people in the McKeon group. Inside the office, I've learned a lot about turbulence and math from all the talented graduate students and postdocs. During lunch, I've had amazing conversations that have helped expand my world view. I am particularly indebted to Ryan McMullen, Ben Barthel, Simon Toedtli, David Huynh, Jane Bae, Greg Stroot, Anagha Madhusudanan, Yuting Huang, and Arslan Ahmed for all the time they graciously provided to answer my (many) questions. I am really grateful to have had the honor of being surrounded by so many talented individuals.

I want to also thank my collaborators, Ben Barthel, Chris Williams, and Peter Schmid. It's been an honor working with you; I've learned a lot from each of you.

During my PhD, I have had several hosts outside of the Institute who have graciously welcomed me. I'd like to thank Petros Koumoutsakos for hosting me during my visit to Harvard. Thank you to CTR for hosting me during the summer of 2022. A special thank you to Chris Williams and Kevin Griffin who helped me feel extremely welcome during my time at Stanford. Finally, words cannot express my gratitude towards my mother-in-law, Julia Ruiz, who selflessly opened her doors to me and allowed me to stay with her during the two ~~weeks~~ years of the pandemic. Much of the work in this thesis was done at her home. *Muchas gracias, Julia.*

I also want to thank the many friends who have supported me. First, my friends from HES at Berkeley have shown me nothing but support throughout this journey. I am grateful especially to David Barba, Francisco Ojeda, Giovanni Pacheco, Jesus Navarro, Johnny Hernandez, and Juan Fuentes for their humor and encouragement. To my friends from Club Latino, Yazmin Gonzalez, Victor Garcia, Karen Orta, Eric Ocegueda, and Noel Esparza-Duran: thank you for building a community on campus that I can call home. A special thank you goes to Vatsa Gandhi, Andrew Akerson, and Josh Lassman for the memories I'll cherish while studying for quals. I want to also thank Ben Barthel, Greg Stroot, Jacque Tawney, and Tanner Harms for the friendships we've developed as part of the McKeon group. Finally, my deepest thanks goes to my friend and mentor Douglas Varela, who taught me how to learn

and teach. Thank you for all your advice and all you've done for our community.

To my family, thank you, I love you all. A special thank you to my brother Eduardo, for always being a call away whenever I feel homesick. I want to thank Juan Diaz, whom I consider a brother, and his family for always being there for me since we met on the first day of kindergarten. I want to thank my dad, Salvador, for teaching me valuable life lessons and instilling in me a powerful work ethic. *Gracias papá, te amo*. To my mom, Arcelia, thank you for your love and instilling in me a love for reading and learning. *Gracias mamá, te amo y te extraño*. To my stepmom Jovita, thank you for bringing joy to my dad and supporting my family. *Gracias Jovita, te amo*. And to my baby brothers, Noe Gael and Elias, you two have brought so much energy and happiness to my family. You all inspire me to do my best.

Finally, I want to thank my wife, Heather Ruiz, who has been a constant source of happiness, comfort, love, and support during all the strenuous times during undergrad and graduate school. Whenever I am feeling down, you lift me up. You've encouraged me every step of the way, and for that I am grateful. Thank you, Heather, for bringing out the best in me and believing in me. I love you.

Psalms 27:1

ABSTRACT

Resolvent analysis is applied to nonequilibrium incompressible adverse pressure gradient (APG) turbulent boundary layers (TBL) and hypersonic boundary layers with high temperature real gas effects, including chemical nonequilibrium. Resolvent analysis is an equation-based, scale-dependent decomposition of the Navier Stokes equations, linearized about a known mean flow field. The decomposition identifies the optimal response and forcing modes, ranked by their linear amplification. To treat the nonequilibrium APG TBL, a biglobal resolvent analysis approach is used to account for the streamwise and wall-normal inhomogeneities in the streamwise developing flow. For the hypersonic boundary layer in chemical nonequilibrium, the resolvent analysis is constructed using a parallel flow assumption, incorporating N_2, O_2, NO, N, and O as a mixture of chemically reacting gases.

Biglobal resolvent analysis is first applied to the zero pressure gradient (ZPG) TBL. Scaling relationships are determined for the spanwise wavenumber and temporal frequency that admit self-similar resolvent modes in the inner layer, mesolayer, and outer layer regions of the ZPG TBL. The APG effects on the inner scaling of the biglobal modes are shown to diminish as their self-similarity improves with increased Reynolds number. An increase in APG strength is shown to increase the linear amplification of the large-scale biglobal modes in the outer region, similar to the energization of large scale modes observed in simulation. The linear amplification of these modes grows linearly with the APG history, measured as the streamwise averaged APG strength, and relates to a novel pressure-based velocity scale.

Resolvent analysis is then used to identify the length scales most affected by the high-temperature gas effects in hypersonic TBLs. It is shown that the high-temperature gas effects primarily affect modes localized near the peak mean temperature. Due to the chemical nonequilibrium effects, the modes can be linearly amplified through changes in chemical concentration, which have non-negligible effects on the higher order modes. Correlations in the components of the small-scale resolvent modes agree qualitatively with similar correlations in simulation data.

Finally, efficient strategies for resolvent analysis are presented. These include an algorithm to autonomously sample the large amplification regions using a Bayesian Optimization-like approach and a projection-based method to approximate resolvent analysis through a reduced eigenvalue problem, derived from calculus of variations.

PUBLISHED CONTENT AND CONTRIBUTIONS

Gomez, Salvador R. and Beverley J. McKeon (2023). "Linear amplification of large scale structures in adverse pressure gradient turbulent boundary layers through resolvent analysis". In: *Progress in Turbulence. X: Proceedings. of the iTi Conference in Turbulence*. Submitted. Springer, pp. 167–172.
S. R. G. developed the biglobal resolvent code applied to the APG TBL, ran the parametric sweeps, and was the primary author.

Barthel, Benedikt, Salvador R Gomez, and Beverley J McKeon (2022a). "Variational formulation of resolvent analysis". In: *Physical Review Fluids* 7.1, p. 013905. DOI: https://doi.org/10.1103/PhysRevFluids.7.013905.
S. R. G. developed the code used for the biglobal resolvent analysis of the ZPG TBL in Section 5, assisted with the computations and analytics in Section 6, and assisted with writing as second author.

Barthel, Benedikt, Salvador R. Gomez, and Beverley J. McKeon (2022b). "The role of an optimal modeling basis in variational resolvent analysis". In: *Turbulence and Shear Flow Phenomena*. Vol. 12. URL: http://www.tsfp-conference.org/proceedings/2022/205.pdf.
S. R. G. developed the example for the optimal basis, ran the code for the ZPG TBL biglobal resolvent modes, and assisted with writing as second author. He also developed code for the biglobal resolvent modes.

Gomez, Salvador R., Christopher T. Williams, et al. (2022). "Adaptive resolvent analysis with application to high enthalpy flows". In: *Proceedings of the CTR Summer Program*, pp. 87–96. URL: https://web.stanford.edu/group/ctr/ctrsp22/ii04_Gomez.pdf.
S. R. G. provided the theoretical and computational developments required for the hypersonic resolvent analysis that incorporates real gas effects, developed and applied the adaptive resolvent analysis, and was the primary author.

TABLE OF CONTENTS

LIST OF ILLUSTRATIONS

Number *Page*

LIST OF TABLES

Chapter 1

INTRODUCTION

Transportation connects people and commerce across the globe, encompassing cargo ships moving across the oceans, commercial airplanes soaring through the skies, and pipelines pumping products across regions. It is estimated that these industries account for 25% of the world's energy use (Jiménez, 2013). Part of this energy is used to overcome the drag from a fluid flowing past solid surfaces or walls. The flow near these surfaces in industrial applications is typically turbulent—i.e., categorized by chaotic, vortical, and multiscale motions that promote mixing. These turbulent motions require energy, which is supplied by the surface moving relative to the fluid. For example, 50% of the fuel used in a commercial flight is used to overcome the turbulence near the vehicle's surface (Marušić, Mathis, and Hutchins, 2010b). Despite their technological relevance, wall-bounded turbulent flows lack a comprehensive underlying theory and remain computationally and experimentally difficult to study.

Mathematically, the presence of a solid surface imposes a boundary condition on wall-bounded flows. For incompressible flows, this is manifested as the "no-slip" boundary condition which states that the relative velocity between the fluid and the wall is zero at the wall. In the wall-normal direction, this is a constraint that imposes no fluid flow through the surface. In the transverse directions, the no-slip condition is a purely viscous effect. For free-surface flows, like the flow over a vehicle surface, the no-slip condition creates a boundary layer—the thin wall-normal region of the flow where the flow adjusts from zero velocity at the wall to the freestream conditions. For an airplane wing, the boundary layer can be a few centimeters tall. This wall-normal anisotropy in the streamwise velocity creates a velocity gradient within the boundary layer, causing the shear stress at the wall and vorticity within the boundary layer.

Boundary layers evolve in the streamwise direction as the effect of the wall accumulates downstream of the leading edge. For a flat plate with a constant freestream velocity, this results in streamwise growth of the boundary layer. Although the flow may begin laminar downstream of the leading edge, it eventually transitions naturally to a turbulent state. The region of transition is typically described by the

Reynolds number, the nondimensional group defined colloquially as the ratio of inertial effects to viscous effects. Here, $Re_x = U_\infty x/\nu$, where U_∞ is the freestream velocity, x is the distance downstream of the leading edge, and ν is the kinematic viscosity, which acts to dampen disturbances. As Re_x becomes large ($Re_x \gtrsim 6 \times 10^5$), the disturbances become too energetic to be quickly dissipated by viscosity. This allows for streamwise growth of said disturbances, which breakdown in the transitional region. As these disturbances interact with one another, the flow eventually becomes fully turbulent. Predicting where and how this occurs is still a matter of debate and of important engineering interest because the turbulent boundary layer (TBL) experiences larger shear stresses and heat fluxes than its laminar counterpart. These effects can have detrimental effects on the vehicle's performance.

The turbulent boundary layer and laminar boundary layer (LBL) differ in many ways. The LBL admits a single wall-normal length scale, the boundary layer thickness, $\delta(x)$. On the other hand, the TBL is multiscale. In the vicinity of the wall, the flow is categorized by the effect of the wall and is thus scaled with a viscous length scale, ℓ_ν. Further from the wall, the majority of the TBL is categorized by the outer length scale, δ. The ratio of these two length scales defines the friction Reynolds number, $Re_\tau = \delta/\ell_\nu$, which is the only parameter in the zero pressure gradient (ZPG) TBL. For turbulent flow, Re_τ is at smallest 180 and can be as large as $10^4 - 10^6$ for industrially relevant flows (Smits and Marušić, 2013). The viscous region extends $O(100\ell_\nu)$ from the wall, encompassing less than a percent of δ for flows of engineering interest. Despite its size, a large portion of the turbulent activity occurs within this near wall region (Pope, 2000). This separation of scales is one of the hallmarks of wall bounded turbulence, and one of the challenges, as resolving the near wall activity requires sensitive experimental equipment or a large number of grid points in a simulation. Despite these challenges, the mean flow field and, consequently, the skin friction of the ZPG TBL can be modeled due to well-established asymptotic theories and similarity laws.

Despite the advances in the ZPG TBL, flows that depart from these canonical configurations have received less attention and are increasingly difficult to predict. Real vehicles have curvature, which create streamwise deceleration or acceleration of the freestream velocity. To isolate the effects of a streamwise deceleration of the freestream velocity, many researchers consider the flat plate with an adverse pressure gradient (APG). The APG is commonly seen in the flow around airfoils or within diffusers. If the APG becomes too strong, it can lead to separation which

creates adverse effects on vehicles. Here, the focus is on mild-moderate APG such that the flow remains attached. Under these conditions, the APG primarily affects the outer region of the TBL, strengthening the turbulent fluctuations, thickening the boundary layer, and increasing the outer region velocity, $\overline{U}/u_\tau$, relative to a ZPG TBL at the same Re_τ, where $\overline{U}$ is the mean velocity and u_τ is the friction velocity.

Since the APG affects the turbulent flow, a measure of the APG strength must also parameterize the TBL. Here, the parameter chosen to represent the APG strength is the Clauser parameter,

$$\beta = \frac{\delta^*}{\tau_W}\frac{dp}{dx}, \tag{1.1}$$

where δ^* is the displacement thickness, τ_W is the shear stress at the wall, and $\frac{dp}{dx}$ is the pressure gradient. β represents the ratio of the pressure gradient acting on the boundary layer to the shear stress at the wall. The APG TBL can not be solely categorized by the local values of β and Re_τ since its streamwise development is affected by the accumulated upstream β (Bobke et al., 2017), similar to how the ZPG TBL grows as it is increasingly retarded by the wall. Following the definition in Clauser (1954), the APG TBL will be considered to be in equilibrium if β is constant. Here, nonequilibrium effects in the APG TBL will be considered as history effects from a streamwise varying β.

For now, the discussion has focused on incompressible flows which assume that U_∞ is significantly smaller than the speed of sound in the freestream, a_∞. The Mach number, $Ma = U_\infty/a_\infty$, is a nondimensional quantity commonly used in compressible flows. A TBL with $Ma > 1$ is considered supersonic, and the air can be modeled as a calorically perfect ideal gas. These flows experience large temperatures as the kinetic energy from the freestream flow is converted into heat as the flow comes to rest at the wall. This causes the largest temperatures within the boundary layer, which increase with Ma. When the $Ma > 5$, the flow can be categorized as a hypersonic TBL. These hypersonic flows have temperatures where high-temperature real gas effects become important. For example, vibrational excitation of the gas begins at 800 K, O_2 dissociates at 2000 K, and N_2 dissociates at 4000 K (Anderson Jr., 2006). In hypersonic flows, the calorically perfect ideal gas assumption no longer holds.

For a hypersonic vehicle, the TBL needs to be accurately modeled because it experiences $O(10)$ times larger heat fluxes than the LBL (Van Driest, 1956). Poor modeling of these heat loads can cause detrimental effects to the vehicle and its

payload. For hypersonic TBLs with large Ma, the O_2 and N_2 dissociate, requiring the air to be modeled as a mixture of N_2, O_2, NO, N, and O, and other species if, for example, ionization or ablation are considered. These reactions occur as the individual molecules collide with one another, meaning that the reactions occur in a finite amount of time, t_r. The modeling of the chemical reactions depends on the advection time of the flow, t_f, relative to t_r. This is measured by the Damköhler number, $Da = t_f/t_r$. At the two extremes are the chemically frozen assumption ($Da = 0$) and the chemical equilibrium assumption ($Da \to \infty$). In between these two extremes, the flow is assumed to be in chemical nonequilibrium, meaning that the changes in concentration and heat release due to the reactions need to be accounted for. This requires the explicit handling of nonlinear functions that describe the thermophysical properties in the flow as well as a state vector that includes the concentrations of the species elements. These extra terms make the equations computationally stiff.

Despite the complexities in the TBL, the flow tends to organize itself in coherent structures that sustain the flow. From the turbulent data, their signature can be seen in the premultiplied energy spectra, which reveal distinct peaks corresponding to a small-scale near-wall cycle and large-scale outer layer motions at sufficiently high Re_τ. Understanding the processes that sustain and amplify these distinct length scales can lead to a better understanding of the laminar-turbulent transition, length and time scales to target in flow control, and improved reduced order models.

This chapter will provide a brief overview of the topics seen in the rest of the thesis. First, Section 1.1 provides an overview of turbulent statistics and coherent motions present for channels, pipes, and ZPG flat plates. Section 1.2 discusses how an APG changes the structure of the TBL, including nonequilibrium effects. Supersonic and hypersonic TBLs are briefly explained in Section 1.3, with special attention given to the high temperature gas effects. Section 1.4 discusses linear methods applied to shear-driven flows, with an emphasis on the resolvent analysis approach. Section 1.5 provides a preliminary discussion on Bayesian Optimization, which is often used for parameter optimization in fluid systems. Finally, Section 1.6 provides a brief outline for the rest of the thesis.

1.1 Canonical Wall Bounded Turbulence

The earliest insights on canonical wall-bounded turbulence originate from self-similar scalings for the mean streamwise velocity, $\overline{U}$, derived from empirical ob-

servations or asymptotics from the governing equations. The flow near the wall is governed by a balance between the viscous stresses, $\rho\nu\, \partial\overline{U}\Big/\partial y$, and the wall shear stress, τ_W, while all other stresses are negligible, due to either the no-slip condition or because they scale as $O\left(Re_\tau^{-1}\right)$. This balance introduces a friction velocity, $u_\tau = \sqrt{\tau_W/\rho}$, and a viscous length scale, $\ell_\nu = \nu/u_\tau$ such that $\partial\overline{U}^+\Big/\partial y^+ = 1$ at the wall. Variables nondimensionalized with these coordinates are denoted with + superscripts. Upon nondimensionalization with u_τ and ℓ_ν, the Reynolds averaged Navier Stokes (RANS) equations integrated in y for a turbulent channel, pipe, or a two-dimensional TBL under the typical boundary layer approximations (Pope, 2000) become

$$\frac{\partial\overline{U}^+}{\partial y^+} - 1 + T^+ = \frac{1}{Re_\tau}\int_0^{y^+} C^+ d\tilde{y}^+, \tag{1.2}$$

where $T = -\overline{uv}$ denotes the Reynolds shear stress and $C = \rho^{-1}\, \partial p/\partial x$ for a channel and pipe or $C = \partial\overline{U}\Big/\partial x\, \overline{U} + \partial\overline{U}\Big/\partial y\, \overline{V}$ for a TBL (Wei, Fife, et al., 2005). C denotes the terms that drive the flow, which for the internal flows is the pressure gradient and in a TBL is the advection. In the region where $y^+ \ll Re_\tau$, the integral can be neglected making Equation 1.2 Re_τ-independent. This forms the 'law of the wall,'

$$\overline{U}(y^+) = f_W(y^+), \tag{1.3}$$

which holds in the near wall region (von Kármán, 1939; Coles, 1956).

Further from the wall, the flow becomes Re_τ dependent in the viscous-scaled units as the integral is no longer negligible. ℓ_ν can not be used to scale the velocity gradients in this outer region since the viscous stresses are negligible (Wei, Fife, et al., 2005). The turbulence's wall-normal extent in the outer region is constrained by a length scale, δ, which is either the channel half-height, pipe radius, or a measure of the boundary layer thickness. There is ambiguity in the correct choice of δ for a ZPG TBL. One choice is the boundary layer thickness, δ_{99}. The length scale proposed by Clauser (1954), Δ, has seen success, though Nagib, Chauhan, and Monkewitz (2007) demonstrate that Δ/δ_{99} approaches a constant for previously unavailable large Re_τ ZPG TBL data. Due to this, δ_{99} is chosen as the δ for the ZPG TBL. Experimentally, it has been observed that outside of the inner region,

$$\overline{U}_\infty^+ - \overline{U}^+ = g\left(\frac{y}{\delta}\right), \tag{1.4}$$

where $\overline{U}_\infty$ denotes the freestream velocity in a TBL or the centerline velocity in an internal flow (Coles, 1956; von Kármán, 1934). Equation 1.4 is known as the 'law

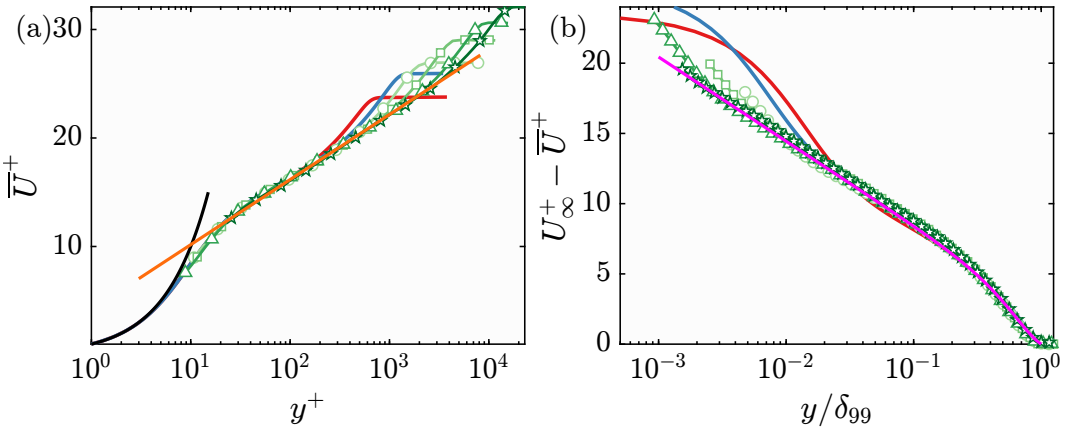

Figure 1.1: Plots of experimental and DNS $\overline{U}$. (a) $\overline{U}^+(y^+)$ with y^+ plotted in black and $1/k\log(y^+) + A$ in orange. (b) $U_\infty^+ - \overline{U}^+(y/\delta_{99})$ with Coles (1956)'s law of the wake fitted to the highest Re_τ data plotted in magenta. The blue and red lines are from the ZPG TBL DNS of Schlatter and Örlü (2010) with Re_τ = 670 and 1270, respectively. The green lines are from the ZPG TBL experiment of Baidya et al. (2017) with Re_τ = 2500 (circles), 5000 (squares), 10^4 (triangles), and 1.8×10^4 (stars). Here, κ = .384 and A = 4.173 (Nagib, Chauhan, and Monkewitz, 2007).

of the wake' and suggests that the velocity defect is Re_τ independent, although g may be a function of the geometry.

Equations 1.3 and 1.4 hold in two separate regions of the flow. As a result, it must be the case that these two expressions have to overlap in some intermediate region. Millikan (1938) showed that in order for this to be the case, then $\overline{U}$ must be logarithmic such that

$$\overline{U}^+ = \frac{1}{\kappa}\log\left(y^+\right) + A, \tag{1.5}$$

where κ is the Kármán 'constant' and A is an additive 'constant' that can account for flow roughness (Marušić, Monty, et al., 2013). Although the parameters in Equation 1.5 may be denoted as constants, there is increasing evidence that they may be flow dependent (Smits, McKeon, and Marušić, 2011).

ZPG TBL mean flow field data from the direct numerical simulation (DNS) of Schlatter and Örlü (2010) and the high Re_τ experiments of Baidya et al. (2017) are plotted in viscous units in Figure 1.1(a) and in wake-deficit form in Figure 1.1(b). The linear relationship in the viscous sublayer, log law, and Coles (1956)'s law of the wake are included as well. These plots illustrate the Re_τ independence of $\overline{U}^+$ in the near wall region and in the outer regions of the flow, when scaled in the appropriate units. For the smallest Re_τ data, deviations from Equation 1.3 and 1.4 are observed both closer to and farther from the wall compared to the larger Re_τ

data. In addition, the logarithmic region becomes wider in viscous units as Re_τ increases, which increases the inner and outer scale separation.

The region $y^+ \in [0, 5]$ where $\overline{U}^+ \approx y^+$ is the viscous sublayer. Between that region and the log layer is the buffer layer, $y^+ \in [5, 30]$. The log layer holds for $y^+ \in \left[y_s^+, .15Re_\tau\right]$, while the outer layer is $y^+ \geq .15Re_\tau$. Different authors have denoted the start of the log layer with values of $y_s^+ = 30$, 200, and $2.6\sqrt{Re_\tau}$, to name a few (Wei, Fife, et al., 2005; Marušić, Monty, et al., 2013). While these layers describe different qualities of $\overline{U}$, they do not necessarily describe the dynamics within these flows. Wei, Fife, et al. (2005) considered the balance of terms in the RANS equation, which describes the balance of stress gradients in the mean momentum equation, rather than the balance of stresses in Equation 1.2. From this balance, they mathematically determined four distinct layers with Re_τ-dependent thicknesses where two or three of the stress gradients, $\nu\, \partial^2\overline{U}\Big/\partial y^2$, $\partial T/\partial y$, and C, balance. The mesolayer, the sole layer where the three terms balance, is categorized by a mixed length scale $\ell_m = \sqrt{\ell_\nu \delta}$, in agreement with Afzal (1984).

The self-similar relationships have inspired many models to predict the behavior of $\overline{U}$ at higher Re_τ. For example, Monkewitz, Chauhan, and Nagib (2007) used matched asymptotics to create a self-consistent composite profile, fitted to high Re_τ data, for $\overline{U}$ that only requires an Re_τ as an input. These ideas have also been used to build computationally efficient strategies to approximate high Re_τ ZPG TBL DNSs, without the need for a laminar-turbulent transition region. The strategy described in Lund, Wu, and Squires (1998) generates inflow data from a rescaling and recycling of the outflow data. The work of Ruan (2021) demonstrates that through a rescaling of the governing equations using the momentum thickness, θ, the NSE can be treated as streamwise homogeneous, provided that $(\delta_{99}/\theta)\ \partial\theta/\partial x \ll 1$ and some terms are neglected. Although these methods allow for great reductions in computational cost, caution must be used in interpreting the results as the inlet conditions can affect the statistics of the flow (Schlatter and Örlü, 2010). Due to this, researchers have opted to use tripping-based methods to trigger the laminar-turbulent transition and better compare with experiment (Eitel-Amor, Örlü, and Schlatter, 2014).

Owing to the scale separation in the wall-bounded turbulent flows, turbulent structures with different characteristic length scales are also energetic in different regions of the flow. These are denoted coherent structures, and are typically streak-like, with streamwise lengths, λ_x, larger than their spanwise lengths, λ_z. The wavenumbers associated with these length scales are $k_x = 2\pi/\lambda_x$ and $k_z = 2\pi/\lambda_z$. Through

experiment and simulation, the premultiplied streamwise kinetic energy spectra, $k_x E_{uu}(y, k_x)$, premultiplied spanwise kinetic energy spectra, $k_z E_{uu}(y, k_z)$, and spectral energy density, $k_x k_z E_{uu}(y, k_x, k_z)$ reveal ample evidence of a near-wall peak at $y^+ = 15$, $\lambda_x^+ = 1000$, and $\lambda_z^+ = 100$ for ZPG TBLs (Harun et al., 2013; Marušić, Mathis, and Hutchins, 2010a; Baidya et al., 2017; Smits, McKeon, and Marušić, 2011; Eitel-Amor, Örlü, and Schlatter, 2014) and channels (Hoyas and Jiménez, 2006; M. Lee and Moser, 2015). Further from the wall, the cited studies also observe a secondary peak in the spectra with $\lambda_z \sim \delta$ and $\lambda_x \sim 6\delta$ that becomes energetic for $Re_\tau > 4000$. The wall-normal location of these peaks are observed to scale as $y^+ \sim 3.9\sqrt{Re_\tau}$ for a ZPG TBL (Marušić, Mathis, and Hutchins, 2010a).

The second-order statistics do not exhibit the same self-similar scaling as $\overline{U}$. Evidence for this can be seen in the mesolayer theory which argues that near the peak $|\overline{uv}|$, $\partial^2 \overline{uv}^+ \Big/ \partial y^{+2}$ scales as $Re_\tau^{-3/2}$ (Wei, Fife, et al., 2005; Afzal, 1984). Furthermore, the near-wall behavior of $\overline{uu}^+$, $\overline{uv}^+$, $\overline{vv}^+$, and $\overline{ww}^+$ is Re_τ-dependent (M. Lee and Moser, 2015; Baidya et al., 2017). In particular, the inner peak of $\overline{uu}^+$ increases with Re_τ while in the outer region, $\overline{uu}^+$ also increases with Re_τ, with evidence of a secondary outer peak developing for $Re_\tau > 10^4$ (Hoyas, Oberlack, et al., 2021; Marušić, Mathis, and Hutchins, 2010a). This secondary peak is tied to the increased energization of large scale structures with increased Re_τ while the inner peak's Re_τ dependence is from the increased interactions between the large scale motions and small scale motions (Marušić, Mathis, and Hutchins, 2010b). The interactions of the turbulent structures, whose size depends on the distance from the wall, have inspired phenomenological models that explain the observed behavior in the second-order statistics (Marušić and Kunkel, 2003; Marušić and Perry, 1995). In order to understand the behavior of the large scale structures and fully characterize the log layer, the future of wall-bounded turbulence aims at achieving larger Re_τ with well-resolved near-wall regions.

1.2 Adverse Pressure Gradient Turbulent Boundary Layers

Unlike the canonical turbulent flows, the APG TBL can model effects from deceleration due to curvature seen on realistic vehicle surfaces. The discussion here will focus TBLs over flat plates with mild to moderate APG to isolate the effect of the pressure gradient on the turbulence while avoiding flow separation. The APG strength will be measured with the Clauser parameter from Equation 1.1. Although there are many options to measure the APG strength, β is chosen because $\overline{uu}^+$

demonstrates considerably less variation with Re_τ if β is matched as opposed to holding other measures constant (Monty, Harun, and Marušić, 2011). Following Clauser (1954), the APG TBL will be considered to be in equilibrium if β is constant. Other researchers define the equilibrium TBL with a stronger definition, requiring self-similarity in the wake deficit (Aubertine and Eaton, 2005), though a constant β is a 'necessary condition' (Monty, Harun, and Marušić, 2011). This work will consider many APG TBLs ranging from equilibrium to nonequilibrium conditions.

Before delving into how the APG TBL affects the structure, it is instructive to consider the RANS equations, integrated in the wall-normal direction,

$$\int_0^{y^+} \left(\frac{\partial \overline{U}^+}{\partial x^+} \overline{U}^+ + \frac{\partial \overline{U}^+}{\partial y^+} \overline{V}^+ \right) d\widetilde{y}^+ + y^+ \frac{\mathrm{d}\overline{p}^+}{\mathrm{d}x^+} + T^+ = \frac{\partial \overline{U}^+}{\partial y^+} - 1. \tag{1.6}$$

One difference between the RANS for an APG TBL and the canonical wall bounded turbulent flows is the presence of both the advective terms and the pressure gradient. Since the pressure gradient can be approximated to be constant across the TBL (Pope, 2000), $\partial \overline{p}^+ / \partial x^+ = -U_\infty^+ \, \partial \overline{U}_\infty^+ \Big/ \partial x^+$ as opposed to $\partial \overline{p}^+ / \partial x^+ = Re_\tau^{-1}$ in a channel or pipe. For the data of Marušić and Perry (1995), the mild APG TBLs ($\beta < 1$) have $Re_\tau^{-1} \left(\partial \overline{p}^+ / \partial x^+ \right) \sim O(5)$ and moderate APG TBLs ($\beta \simeq 3$) have $Re_\tau^{-1} \left(\partial \overline{p}^+ / \partial x^+ \right) \sim O(20)$. $\partial \overline{p}^+ / \partial x^+$ introduces freestream information into the TBL, which can be several times larger than its effect in the canonical flow. If the APG is strong, these effects can disrupt the near-wall scaling (Kitsios, Sekimoto, et al., 2017). Since $y^+ \, \partial \overline{p}^+ / \partial x^+$ enters Equation 1.6, it also suggests that the APG effects are more severe in the wake. Lastly, it is worth emphasizing that the APG introduces streamwise deceleration into the turbulent boundary layer, which in turn creates significant nonparallel effects.

Compared to the ZPG TBL, APGs change the turbulent statistics by increasing the wake deficit (Monty, Harun, and Marušić, 2011; Aubertine and Eaton, 2005), amplifying the secondary statistics in the outer region (Harun et al., 2013; Marušić and Perry, 1995), and dropping the velocity in the log layer below the canonical log-law (Deshpande et al., 2023; Monty, Harun, and Marušić, 2011). The strengthened secondary statistics in the outer region are tied to the energization of large scale structures in the outer region of an APG TBL (Harun et al., 2013; Sanmiguel Vila et al., 2020). The energization is so significant that even low Re_τ ($Re_\tau < 700$) mild/moderate APG TBLs exhibit a secondary large scale peak in $k_z E_{uu}(y, k_z)$ (Bobke et al., 2017; J. H. Lee, 2017). This energization leads to a sec-

ondary outer peak emerging in $\overline{uu}$, present even in large Re_τ APG TBLs (Sanmiguel Vila et al., 2020), that can surpass even the inner peak.

Just like the ZPG TBL can be sensitive to its upstream conditions (Schlatter and Örlü, 2010), so too is the APG TBL. This is denoted as a history effect, where differences in upstream $\beta(x)$ can lead to differences in the turbulent statistics (Bobke et al., 2017). Due to this, the APG TBL can be parameterized by its Re_τ, β, and history, here considered as the upstream variation in $\beta(x)$. Several studies have isolated the effects of Re_τ and β by focusing on APG TBLs with constant $\beta(x)$ (Kitsios, Atkinson, et al., 2016; Kitsios, Sekimoto, et al., 2017; J. H. Lee, 2017; Pozuelo et al., 2022; Monty, Harun, and Marušić, 2011). These studies identify a monotonic strengthening of the wake and amplification of $\overline{uu}^+$ in the outer region with increasing β. The growth in $\overline{uu}^+$ is coupled to an increased energization of the large scale structures in the outer region with β. Similarly, as β increases, $\overline{U}^+$ continues to drop below the canonical log-law (J. H. Lee, 2017; Monty, Harun, and Marušić, 2011). Due to the influence of the large scale motions, $\overline{uu}^+$ is dependent on both β and Re_τ in the near-wall region (Sanmiguel Vila et al., 2020; Pozuelo et al., 2022; Aubertine and Eaton, 2005). The effects of history on APG TBL were studied in Bobke et al. (2017). The history can be measured as $\overline{\beta}$, the streamwise average of β over some distance upstream (Vinuesa et al., 2017). It was shown that if both β, $\overline{\beta}$, and Re_τ are matched, then the turbulent statistics are the same. For flows with matched Re_τ and β, flows with larger $\overline{\beta}$ have stronger outer fluctuations. Furthermore, $\overline{uu}^+$ is more sensitive to changes in $\overline{\beta}$ than $\overline{U}^+$.

Although there are quite a few differences in the APG TBL, there are still some similarities with canonical flows, especially in the near wall region for a mild-moderate APG. For example, inner scaling holds for $\overline{U}^+$ within the viscous subregion (Bobke et al., 2017) and up to the start of the log layer in larger Re_τ APG TBL (Pozuelo et al., 2022; Harun et al., 2013). Furthermore, the APG TBLs exhibit a near-wall cycle with $\lambda_z^+ \approx 100$ and $\lambda_x^+ = 1000$, located around $y^+ = 15$ (Pozuelo et al., 2022; Harun et al., 2013).

There has been a considerable amount of work focused on the scaling of the APG TBL statistics and here, a few novel scalings will be discussed. The work of Romero et al. (2022) and Sekimoto et al. (2019) identified a hybrid velocity scale that can account for the APG effects on the secondary statistics. This hybrid velocity scale is defined as $u_h^2 = u_\tau^2 + y/\rho\frac{\partial \overline{p}}{\partial x}$, which indicates that close to the wall, the velocity scale is dominated by the shear while further from the wall is defined by the pressure

gradient. It has its basis in the mean momentum balance (Romero et al., 2022), and was shown to remove the APG-related energized secondary peaks in the turbulent fluctuations. Another scaling is that of Wei and Knopp (2023) which defines a novel defect-velocity scaling for $\overline{U}$, $\overline{V}$, and $\overline{uv}$, based on the wall-normal location of the maximum of $\overline{uv}$, as a departure from the classical law of the wake. It as been shown to collapse the outer region of the APG TBL in a myriad of Re_τ, β, and $\overline{\beta}$, and is based on an analogy with a planar mixing layer (Gungor et al., 2016). This scaling illustrates structural differences in the APG TBL now present in the canonical flows.

1.3 High Enthalpy Turbulent Boundary Layers

The incompressible TBL studies so far assumed that $U_\infty \ll a_\infty$ so that compressibility effects are negligible. In the case where the $Ma > 1$, these compressible effects take shape, requiring modeling of the air's thermodynamics and thermophysical properties. Following Spina, Smits, and Robinson (1994), the energy equation can be nondimensionalized by using the freestream U_∞, a_∞, dynamic viscosity, μ_∞, thermal conductivity, k_∞, specific heat capacity at constant pressure, $c_{p,\infty}$, and a length scale L, as

$$\rho c_p \frac{DT}{Dt} = (\gamma - 1)Ma^2 \frac{Dp}{Dt} + \frac{1}{Re\,\mathrm{Pr}} \boldsymbol{\nabla} \cdot k \nabla T - \frac{(\gamma - 1)Ma^2}{Re} \Phi, \tag{1.7}$$

where T is the temperature, γ is the ratio of specific heats, $Pr = c_{p,\infty}\mu_\infty / k_\infty$ is the Prandtl number, and $\Phi = \rho\nu\left(\partial u_j / \partial x_i + \partial u_i / \partial x_j - 2/3(\boldsymbol{\nabla} \cdot \mathbf{u})\delta_{i,j}\right) \partial u_i / \partial x_j$ is the dissipation, which is a positive-definite function. As Ma increases, the positive-definite temperature source from the dissipation term increases, which raises the temperature in the shear-dominated boundary layer. Physically speaking, this is the temperature due to viscous heating and is a result of the kinetic energy in the freestream being converted to heat as the velocity satisfies the no-slip condition. As a result, the thermophysical properties experience large variations within the boundary layer where the T is largest. Although this behavior is present in the LBL, the associated heat transfer to the wall is much larger in the TBL because of the sharp gradients near the wall (Van Driest, 1956).

These property variations have inspired many theories to compare the statistics of a supersonic TBL to those of an incompressible TBL. Starting with the Morkovin hypothesis, it is argued that if the fluctuating Ma_L, where Ma_L is the Mach number defined with the local streamwise velocity and speed of sound within the TBL, is small (less than 0.3), then the dynamics of the compressible TBL follow those

of the incompressible TBL so long as the thermophysical property variations are accounted for (Morkovin, 1962; Spina, Smits, and Robinson, 1994). While many transformations have been proposed and tested in the past to map the compressible TBL's $\overline{U}$ to the incompressible counter part in the inner region, the stress-based transformation of Griffin, Fu, and Moin (2021) has shown promise at accounting for a wide variety of conditions (Cogo et al., 2022; Pirozzoli and Bernardini, 2011). Furthermore, the premultiplied energy spectra for supersonic TBLs identify a near-wall small scale peak while the turbulent fluctuations demonstrate a strengthening of the outer region turbulent fluctuations with Re_τ, similar to the incompressible TBL (Cogo et al., 2022; Passiatore et al., 2022).

In compressible flow, the assumption of a calorically perfect gas (CPG) is frequently used for supersonic flow. However, as the thermodynamic heating increases with Ma, the temperatures can become so large that the CPG assumption breaks and modeling of the high-temperature real gas effects is required. These flows are considered hypersonic and are often characterized with $Ma > 5$ (Anderson Jr., 2006). When the temperatures exceed 600 K, vibrational excitation in the air begins, which causes the specific heat capacities to become temperature dependent, requiring the air to be treated as a chemically imperfect gas (CIG). For a high-enthalpy $Ma = 5$ flow over a compression ramp with $T_\infty = 500$ K, it was shown that using the CPG assumption lead to a 10% reduction in the wall-pressure fluctuations and skin-friction coefficient as well as a 20% difference in heat transfer coefficient (Di Renzo et al., 2022).

Chemical effects become relevant at even larger temperatures. The dissociation of O_2 begins at 2000 K, creating O in solution. When the temperatures exceed 4000 K, the dissociation of N_2 begins, which creates N in solution. NO is also present while O_2 and N_2 dissociate. How the chemistry is modeled depends on the Damköhler number, $Da = t_f/t_r$, the ratio of a relevant convection time, t_f, to a characteristic chemical reaction time, t_r. When $Da \to \infty$, the flow is considered to be in chemical equilibrium as the chemical reactions occur instantly. Flows in chemical equilibrium can be treated as a single-species CIG with the specific heats, and other thermophysical properties, updated based on the thermodynamic state (Edwards, 1992). At the other extreme is the chemically frozen flow where the convection occurs much faster than the chemical reactions with $Da = 0$. In this case, the individual species do not interact with one-another, though their chemical concentrations can still change via diffusion. These flows require individual species continuity equations to handle the diffusion, though they do not require the chemical

production or destruction rates. In between is the chemical nonequilibrium case, where the chemical concentrations can change via chemical reactions and species diffusion. The modeling of the chemical production or destruction rates can be computationally taxing as these are highly nonlinear functions of the thermodynamic state (Edwards, 1992).

Despite the computational challenges associated with modeling hypersonic TBLs, DNS remains a valuable tool to learn about these flows since they can provide temporal and spatial data of all the flow variables. However, the thermophysical properties need to be modeled, many of which can not be derived solely on first principles. For the CIG, the McBride (2002) polynomials, computed from a fit to experimental data, are commonly used. For the chemical reaction, the (Park, 1990) model is also often used, although new models are being designed with improved experimental and simulation data (Candler, 2019). For an example of how the thermophysical properties are modeled, see Di Renzo, Fu, and Urzay (2020). To highlight the different approaches used for the chemistry model, one can consider the DNSs of Di Renzo and Urzay (2021) and Passiatore et al. (2022) where the former uses a single-temperature model and the latter uses a two-temperature model. Differences in the chemistry model can have profound effects on the laminar-turbulent transition (Franko, MacCormack, and Lele, 2010).

1.4 Linear Analysis in Shear Flows

The developments in Section 1.1 and 1.2 relied on the RANS equations for the mean flow field. If the RANS equations are subtracted from the original dynamical system, then the fluctuations, $\mathbf{q}$, can be written as

$$\left(\frac{\partial}{\partial t} + \mathcal{L}(\overline{\mathbf{q}})\right)\mathbf{q} = \mathcal{N}(\mathbf{q}), \tag{1.8}$$

where $\overline{\mathbf{q}}$ is the known mean state, and $\mathcal{L}$ and $\mathcal{N}$ are the linear terms and nonlinear terms in the equations, respectively. Here, it is assumed that a nondimensionalization has been chosen such that $\overline{\mathbf{q}} \sim O(1)$. In the case of an incompressible laminar flow, $\mathbf{q} \sim O(\epsilon)$ where $\epsilon \ll 1$ so that $\mathcal{N}(\mathbf{q}) \sim O(\epsilon^2)$. Thus for an incompressible laminar flow, the nonlinearities can be neglected as they are $O(\epsilon)$ compared to the linear terms. For a turbulent flow, this is not the case as the nonlinearities drive the flow and appear as Reynolds stresses. Furthermore, for a chemically-reacting laminar flow, the Hessian could have large terms due to exponential-variation in the

thermophysical properties (Park, 1990) that can create non-negligible higher-order terms for realistic disturbances.

Focusing on a laminar flow, the linearized form of Equation 1.8 are often used to identify characteristics of the flow that lead to the growth of perturbations, and eventually the onset to turbulence. Historically, the first strategy is to identify parameters that lead to the fastest unbounded exponential growth in the linear initial value problem. Generally, the idea is to treat $\mathbf{q}$ as a Fourier mode in time, and any homogeneous spatial directions, $\mathbf{x}_h$, as

$$\mathbf{q}(\mathbf{x}, t) = \widehat{\mathbf{q}}(\mathbf{x}_n) e^{i(-\lambda t + \mathbf{k}\cdot\mathbf{x}_h)}, \tag{1.9}$$

where $\mathbf{x}_n$ are coordinates for the anisotropic directions, $\mathbf{k}$ is a known wavenumber vector in the same subspace as $\mathbf{x}_h$, and $\lambda \in \mathbb{C}$ is the unknown temporal growth term. As an example, for a channel, $\mathbf{x}_h = [x, 0, z]^T$ and $\mathbf{x}_n = [0, y, 0]^T$. This produces an eigenvalue problem

$$\left(-i\lambda_j \mathcal{I} + \widehat{\mathcal{L}}\right)\widehat{\mathbf{q}}_j = \mathbf{0}, \tag{1.10}$$

where $\mathcal{I}$ is the identity operator and $\widehat{\mathcal{L}}$ is the Fourier transformed $\mathcal{L}$ and $\widehat{\mathbf{q}}_j$ and λ_j are the eigenmodes and eigenvalues. If $\mathrm{Im}\{\lambda_j\} > 0$, the flow is considered unstable and stable if $\mathrm{Im}\{\lambda_j\} < 0$. This eigenvalue problem has been applied to shear flows (Schmid and Henningson, 2002), compressible and incompressible LBLs under the parallel flow assumption (Mack, 1984; Malik, 1990), and spatially developing flows (Theofilis, 2011; Chomaz, 2005).

In shear flows, it is often the case that transition occurs even though $\mathrm{Im}\{\lambda_j\} < 0$ because of nonorthogonality in the eigenmodes that creates non-negligible transient growth (Trefethen et al., 1993). A linear operator, $\mathcal{A}$, is non-normal if it does not commute with its adjoint, $\mathcal{A}^\dagger$, i.e., $\mathcal{A}\mathcal{A}^\dagger \neq \mathcal{A}^\dagger\mathcal{A}$. For these operators, $\mathcal{A}$ does not admit an orthogonal set of eigenvectors, and as a result, experiences transient growth. The eigenvalues are not a good indicator for the temporal behavior of a non-normal system since they do not solely predict the transient growth (Trefethen, 1999). For a shear flow, the linearized Navier Stokes (LNS) operator, $\widehat{\mathcal{L}}$, is non-normal because the component-wise non-normality from $\partial\overline{U}\big/\partial y$, convective non-normality from a spatially developing $\overline{U}(x)$, and the Orr-mechanism, among others (Symon et al., 2018; Cossu and Chomaz, 1997; Jovanović and Bamieh, 2005).

Because of the non-normality in $\widehat{\mathcal{L}}$, many researchers have looked for the largest transient growth in the linearized Navier Stokes equations (LNSE). Since these non-normal measures of growth require an inner product to define the adjoint operator, a

suitable inner product must be chosen (Chandler et al., 2012). For the incompressible flows, the kinetic energy norm is chosen while for compressible flows, the Chu norm is chosen since it removes the compressive work (Chu, 1965). Armed with the Chu norm, researchers have considered transient growth in compressible flows (Hanifi, Schmid, and Henningson, 1996; Franko, MacCormack, and Lele, 2010).

Although linear stability theory has provided a lot of insight into fluid dynamics, it neglects an essential feature in both transition and turbulence—namely the nonlinear terms. By treating $\mathcal{N}(\mathbf{q})$ as an uncorrelated forcing $\mathbf{f}$ such that

$$\mathbf{f}(\mathbf{x}, t) = \widehat{\mathbf{f}}(\mathbf{x}_n) e^{i(-\omega t + \mathbf{k}\cdot\mathbf{x}_h)}, \tag{1.11}$$

along with Equation 1.9 with $\lambda = \omega \in \mathbb{R}$, then Equation 1.9 can be written as

$$\widehat{\mathbf{q}} = \left(-i\omega\mathcal{I} + \widehat{\mathcal{L}}\right)^{-1} \widehat{\mathbf{f}}. \tag{1.12}$$

The operator $\left(-i\omega\mathcal{I} + \widehat{\mathcal{L}}\right)^{-1}$ is known as the resolvent of $\widehat{\mathcal{L}}$ and is tied to its psuedospectrum, which characterizes the behavior of a non-normal operator (Trefethen, 1999). Physically, the resolvent acts as a transfer function between a harmonic forcing input and its harmonic response. This has been applied to systems where $\overline{\mathbf{q}}$ is a laminar base flow where perturbations are excited by the forcing (Jovanović and Bamieh, 2005; Ran et al., 2019; Bagheri et al., 2009; Sipp and Marquet, 2013). In McKeon and Sharma (2010), this approach was applied to a fully turbulent pipe flow with $\overline{\mathbf{q}}$ as the mean flow field. In resolvent analysis, the goal is to find the unit-norm forcing inputs that leads to the largest amplification in the response. If the norm is chosen as an induced norm, then this can be found through a Schmidt decomposition, or singular value decomposition (SVD) for a discretized system, which identifies the gains, σ_j, optimal forcing modes, $\boldsymbol{\phi}_j$, and optimal response modes, $\boldsymbol{\psi}_j$ of the resolvent, where $\sigma_j \geq \sigma_{j+1} \geq 0$. These modes represent two orthonormal bases. In general, $\boldsymbol{\psi}_j$ and $\boldsymbol{\phi}_j$ reflect something related to the non-normality of $\widehat{\mathcal{L}}$, such as large transverse components in $\boldsymbol{\phi}_j$ and an associated large streamwise response in $\boldsymbol{\psi}_j$ due to the component wise non-normality or a large upstream amplitude in $\boldsymbol{\phi}_j$ leading to a large downstream amplitude in $\boldsymbol{\psi}_j$ due to the convective non-normality (Jovanović and Bamieh, 2005; Symon et al., 2018). Norms other than an induced norm can be used to characterize the resolvent amplification, though they can not take advantage of the SVD (Skene et al., 2022).

For certain $\mathbf{k}$ and ω, the resolvent operator can be low-rank ($\sigma_1 \gg \sigma_2$). For these cases, $\boldsymbol{\psi}_1$ can represent flow structures found through data driven decompositions (Towne, Schmidt, and Colonius, 2018; Schmidt et al., 2018; Gómez et al.,

2014; Abreu, Tanarro, et al., 2021). Moarref, Sharma, et al. (2013) showed that for a channel, the ω, k_x, and k_z associated with the near-wall cycle were low-rank. Abreu, Cavalieri, et al. (2020) demonstrated that the resolvent modes associated with the lift-up mechanism, a component-wise non-normality with $\partial\overline{U}\Big/\partial y$, were low-rank and compared well with the data-driven modes. Due to the orthogonality in the resolvent modes, they are often used as a basis to reconstruct flow structure (Rosenberg, 2018; Moarref, Jovanović, et al., 2014). Through consideration of the triadic interactions in the nonlinear terms in the incompressible NSE, the resolvent modes can even recover behavior representative of the amplitude modulation from large scales on small scales (Sharma and McKeon, 2013). It has also been used as a tool to investigate acoustic disturbances in compressible systems (Bae, Dawson, and McKeon, 2020; Madhusudanan and McKeon, 2022; Jeun, Nichols, and Jovanović, 2016).

Solving the eigenvalue problem in Equation 1.10, computing the inverse for the resolvent operator, and the SVD are $O\left(n^3\right)$ operations for the discretized system, where n is the product of the number of grid points and state variables. To solve the eigenvalue problem numerically, many algorithms exist, like the Arnoldi iteration (Saad, 2011). To reduce the computational cost, many have used sparse differentiation schemes, like finite differences, to reduce memory requirements and take advantage of sparse solvers (Schenk and Gärtner, 2004; Malik, 1990; Lele, 1992; Mattsson and Nordström, 2004). To reduce the spatial domain size and number of grid points required for acoustic disturbances, absorbing layers are commonly used (Appelö and Colonius, 2009). Due to the linear amplification of the resolvent operator onto $\boldsymbol{\psi}_1$, resolvent analysis can be estimated with matrix sketching techniques (Ribeiro, Yeh, and Taira, 2020). To avoid the inversion of the resolvent operator for flows with weak spatial development, the resolvent can be approximated by spatial marching techniques instead of inversion (Sasaki et al., 2022; Kamal et al., 2020; Davis, Uzun, and Alvi, 2019). The action of the resolvent operator can also be approximated through a transient and steady state response of the linearized system, forced harmonically, which can replace matrix operations with time-integration (Martini et al., 2021). In theory, the resolvent analysis can also be done by considering only the LNS operator, without the need for inversion, though it is in practice, a computationally ill-posed problem since it requires looking for the smallest singular values of the LNS operator. This can be circumvented through a projection onto an optimal basis or analytically through asymptotic methods (Barthel, Gomez, and McKeon, 2022b; Barthel, Gomez, and McKeon, 2022a; Dawson and McKeon, 2019).

1.5 Bayesian Optimization

Often times, the required calculations or experiments are too expensive to feasibly explore the entire parameter space. For these problems, one may be interested in finding the parameter input that leads to the optimization of the system of interest. For example, finding the best chord to length ratio in a wing that creates the optimal lift in an airplane can be an expensive and iterative search where all the ratios can not be feasibly tested. For these problems, the samples of the parameter space may be sparse or the system may be too complicated to define analytically, so the calculation of gradients may even be unfeasible and the system is effectively treated as a black box. For these problems, one approach at optimization is Bayesian Optimization (Williams and Rasmussen, 2006; Huhn and Magri, 2022). These approaches compute a surrogate model from the measured samples with an associated uncertainty in the surrogate model. This surrogate model can be calculated using Gaussian Process Regression (Williams and Rasmussen, 2006; Eriksson et al., 2018). Using the surrogate model and the uncertainty, the next point is determined by using an acquisition function that balances exploration and exploitation. Exploration looks for regions with large uncertainty while exploitation looks for regions where the surrogate model is predicted to be large. As new samples are found, the surrogate model improves, which improves the prediction from the Bayesian Optimization. This approach was applied in resolvent analysis of a hypersonic TBL in Gómez et al. (2014) with an augmented acquisition function that was used to sample the large amplification regions. Compared to a fixed-grid parameter search, the proposed scheme is able to increase the resolution of the large amplification regions in the spectral space.

1.6 Thesis Overview

This thesis focuses on the resolvent amplification of incompressible nonequilibrium APG TBL and hypersonic TBL with nonequilibrium chemistry. In order to deal with the nonequilibrium APG effects, the resolvent operator must account for both the streamwise and wall-normal anisotropy in the APG TBL. For the hypersonic TBL, the resolvent analysis needs to account for all the species of the gases in the mixture. These ultimately increase the computational cost of the resolvent analysis, so methods are discussed that can efficiently approximate the resolvent modes and autonomously sample the large amplification regions.

Chapter 2 will focus on the derivation of the resolvent analysis, and then tailor the

discussion to the incompressible NSE, where the biglobal resolvent operator will be described and validated. Chapter 3 will extend scaling relationships from the ZPG TBL to the biglobal resolvent modes, extending the work of Moarref, Sharma, et al. (2013) outside of the parallel flow assumption. Chapter 4 will consider resolvent modes computed from nonequilibrium APG TBLs. The effect of the APG on the canonical scaling on the biglobal modes will be discussed, while the effects of β and $\overline{\beta}$ on the resolvent amplification on the resolvent amplification are discussed. High-temperature real gas effects in hypersonic TBLs are included in the resolvent modes to predict the length scales most affected by the high temperature effects in Chapter 5. Finally, Chapter 6 considers an autonomous sampling technique applied to resolvent amplification using Bayesian Optimization and an inverse-free resolvent approach, specifically looking at the role of an appropriate modeling basis. This thesis concludes in Chapter 7, with key findings summarized and future work proposed.

Chapter 2

BIGLOBAL RESOLVENT ANALYSIS

2.1 Introduction

The high-dimensionality, nonlinearity, and multi-scale behavior in wall-bounded turbulent flows warrants simplified scale-dependent analyses that can capture relevant physics in the flow. In wall bounded flows, the presence of the surface creates anisotropy due to the no-slip boundary condition. This anisotropy leads to shear in wall bounded flows creating the non-normal behavior in the linearized Navier Stokes operator as explained in Section 1.4. In the turbulent regime, the shear contributes directly to the production of turbulent kinetic energy and the separation of scales in the wall-normal direction (Pope, 2000). In addition to the linear mechanisms, turbulence is also fed by nonlinear interactions which serve to distribute energy across different scales of the flow. The resolvent analysis framework of McKeon and Sharma (2010) creates a scale-dependent decomposition of the linear transfer function between the nonlinear terms and the turbulent fluctuations that respects the non-normality in the equations. This analysis identifies two optimal orthonormal bases for the linear dynamics where the bases elements are ranked by their corresponding linear amplification. The eigenvectors of non-normal operators are non-orthogonal, which limits their use as a basis (Trefethen, 1999). The resolvent analysis framework produces an orthogonal basis for the optimal forcing inputs and a complimentary orthogonal basis for the linear responses. The forcing inputs and response outputs take advantage of linear amplification mechanisms, including non-normal amplification mechanisms, that reflect mechanisms in wall-bounded turbulence (Symon et al., 2018; McKeon and Sharma, 2010).

In this chapter, the resolvent analysis framework is defined for a general dynamical system. It is then specialized to the case of incompressible wall bounded flows. The local approach, that uses the parallel flow assumption, is defined and contrasted with the biglobal approach, which uses the nonparallel flow assumption. The latter is useful for the study of streamwise developing flows. Finally, the resolvent analysis will be validated with published results.

2.2 Resolvent Analysis

Consider the state $\mathbf{Q}(\mathbf{x},t) = \left[Q_1(\mathbf{x},t),\ldots,Q_{n_s}(\mathbf{x},t)\right] \in \mathbb{R}^{n_s}$ of a statistically stationary dynamical system evolving under a sufficiently smooth nonlinear differential operator $\mathcal{F} : \mathbb{R}^{n_s} \rightarrow \mathbb{R}^{n_s}$ with boundary conditions embedded on the surface domain such that

$$\partial_t \mathbf{Q} + \mathcal{F}(\mathbf{Q}) = \mathbf{0}; \mathbf{Q}(\mathbf{x}, t=0) = \mathbf{Q}_0(\mathbf{x}). \tag{2.1}$$

Here $\mathbf{x}$ denotes spatial coordinates, t denotes time, n_s denotes the number of state variables, Q_i, and $\mathbf{Q}_0$ denotes the initial condition. The state can be written as $\mathbf{Q} = \overline{\mathbf{Q}} + \mathbf{q}$, where $\overline{\mathbf{Q}} = \overline{\mathbf{Q}}(\mathbf{x}_n)$ denotes the known mean state, averaged over time and homogeneous spatial coordinates, $\mathbf{x}_h$, and $\mathbf{x}_n$ denotes the inhomogenous spatial coordinates. For example, for a TBL, $\mathbf{x}_h = [0,0,z]$ while $\mathbf{x}_n = [x,y,0]$. Equation 2.1 can be rewritten as

$$\partial_t \mathbf{q} + \mathcal{L}\mathbf{q} = -(\mathcal{F}(\mathbf{Q}) - \mathcal{L}\mathbf{q}) \doteq \mathbf{n}, \tag{2.2}$$

where the linear operator $\mathcal{L}$ denotes the Jacobian of $\mathcal{F}$ evaluated at $\overline{\mathbf{Q}}$ and $\mathbf{n} \in \mathbb{R}^{n_s}$ denotes the nonlinear terms in the governing equations. Alternatively, $\mathbf{n}$ can be interpreted as all the terms other than the linear term in a Taylor expansion of $\mathcal{F}$ evaluated at $\overline{\mathbf{Q}}$. In general, this decomposition can use any $\overline{\mathbf{Q}} = \overline{\mathbf{Q}}(\mathbf{x}_n)$ and is not restricted to be a realizable state of the system. However, unless otherwise specified, $\overline{\mathbf{Q}}$ will denote the mean state. The domain of the inhomogenous spatial coordinates, Ω_n, is assumed to be closed with boundary conditions on $\partial\Omega_n$.

Due to the stationarity in time and homogeneity in $\mathbf{x}_h$, $\mathbf{q}$ and $\mathbf{n}$ will be expanded in a modal manner with modes, $\widehat{\mathbf{q}}$ and $\widehat{\mathbf{n}}$, respectively, such that

$$[\mathbf{q},\mathbf{n}](\mathbf{x},t) = \left[\widehat{\mathbf{q}},\widehat{\mathbf{n}}\right](\mathbf{x}_n) e^{-i\omega t + \mathbf{k}\cdot\mathbf{x}_h}, \tag{2.3}$$

where $\omega \in \mathbb{R}$ and $\mathbf{k} \in \mathbb{R}^{\dim(\mathbf{x}_h)}$ denote the temporal frequency and spatial wavenumbers in $\mathbf{x}_h$. Physically, these modes can be interpreted as structures in the dynamical system with specified temporal and spatial length scales, $2\pi/\omega$ and $2\pi/k_i$, respectively. The Fourier Transform allows Equation 2.2 to be rewritten as

$$\left(-i\omega\mathcal{I} + \widehat{\mathcal{L}}\right)\widehat{\mathbf{q}} = \widehat{\mathbf{n}}, \tag{2.4}$$

where $\widehat{\mathcal{L}}$ is the Fourier Transform of $\mathcal{L}$ and $\mathcal{I}$ is the identity operator. To ensure that $\left(-i\omega\mathcal{I} + \widehat{\mathcal{L}}\right)$ is invertible, $-i\omega$ is chosen to not be an eigenvalue of $\widehat{\mathcal{L}}$ (Trefethen, 1999). Although $\mathbf{n}$ is correlated to $\mathbf{q}$, $\mathbf{n}$ will hereinafter be assumed to be the

uncorrelated forcing input, $\mathbf{f}$, unless otherwise stated. Hence, $\widehat{\mathbf{f}}$ is independent of $\mathbf{q}$. The response $\widehat{\mathbf{q}}$ is then governed by

$$\widehat{\mathbf{q}} = \left(-i\omega\mathcal{I} + \widehat{\mathcal{L}}\right)^{-1}\widehat{\mathbf{f}} = \mathcal{R}\widehat{\mathbf{f}}, \tag{2.5}$$

where $\mathcal{R}$ is the resolvent operator. Note that $\mathcal{R}$ is parameterized by $\overline{\mathbf{Q}}$, $\mathbf{k}$, and ω.

In engineering applications, forcing inputs, $\widehat{\mathbf{f}}$, and response outputs, $\widehat{\mathbf{q}}$, of Equation 2.5 are not available over Ω_n due to either limitations in actuation, the span of $\widehat{\mathbf{n}}$, or measurement constraints for sensing. Alternatively, one may be interested in the linear amplification of a linear combination of the state variables or in a subset of Ω_n. Equation 2.5 can be augmented to consider the linear operators $\mathcal{B}$ and C that linearly augment $\widehat{\mathbf{f}}$ and $\widehat{\mathbf{q}}$, respectively, as

$$\begin{aligned}\widehat{\mathbf{q}} &= \mathcal{R}\mathcal{B}\widehat{\mathbf{f}}\\ \widehat{\mathbf{y}} &= C\widehat{\mathbf{q}} = C\mathcal{R}\mathcal{B}\widehat{\mathbf{f}} = \mathcal{H}\widehat{\mathbf{f}}.\end{aligned} \tag{2.6}$$

Here, $\widehat{\mathbf{y}}$ denotes the observables of the state $\widehat{\mathbf{q}}$ due to the linear operator C and $\mathcal{H}$ denotes the transfer function between $\widehat{\mathbf{f}}$ and $\widehat{\mathbf{y}}$. The resolvent analysis framework will be applied to $\mathcal{H}$ to generalize the approach to multiple systems. Results for $\mathcal{R}$ are recovered by setting $\mathcal{B}$ and C to identity operators.

To study linear amplification, relevant norms need to be defined. In this study, the choice of norm will be limited to inner product norms to allow for the use of linear algebra techniques, though other norms can be studied (Skene et al., 2022). The relevant inner products will be defined as

$$\langle \mathbf{a}, \mathbf{b}\rangle_r = \langle \mathbf{a}, \mathcal{W}_r\mathbf{b}\rangle\,, \tag{2.7}$$

$$\langle \mathbf{a}, \mathbf{b}\rangle_f = \left\langle \mathbf{a}, \mathcal{W}_f\mathbf{b}\right\rangle, \tag{2.8}$$

where $\mathcal{W}_r$ and $\mathcal{W}_f$ are positive-definite operators and

$$\langle \mathbf{a}, \mathbf{b}\rangle = \int_{\Omega_n} \mathbf{a}^*\mathbf{b}d\mathbf{x}_n. \tag{2.9}$$

Here the asterisks denote the conjugate transpose and $\mathbf{a}^*\mathbf{b} = a_i^* b_i$. These inner products induce the norms $\|\mathbf{a}\|_r = \sqrt{\langle \mathbf{a}, \mathbf{a}\rangle_r}$ and $\|\mathbf{a}\|_f = \sqrt{\langle \mathbf{a}, \mathbf{a}\rangle_f}$. With these norms, the linear amplification of $\mathcal{H}$ is defined as

$$\sigma^2 = \frac{\left\|\widehat{\mathbf{y}}\right\|_r}{\left\|\widehat{\mathbf{f}}\right\|_f} = \frac{\left\|\mathcal{H}\widehat{\mathbf{f}}\right\|_r}{\left\|\widehat{\mathbf{f}}\right\|_f} = \frac{\left\langle \mathcal{H}\widehat{\mathbf{f}}, \mathcal{H}\widehat{\mathbf{f}}\right\rangle_r}{\left\langle \widehat{\mathbf{f}}, \widehat{\mathbf{f}}\right\rangle_f} = \frac{\left\langle \mathcal{H}\widehat{\mathbf{f}}, \mathcal{W}_r\mathcal{H}\widehat{\mathbf{f}}\right\rangle}{\left\langle \widehat{\mathbf{f}}, \widehat{\mathbf{f}}\right\rangle_f} = \frac{\left\langle \widehat{\mathbf{f}}, \mathcal{H}^\dagger\mathcal{W}_r\mathcal{H}\widehat{\mathbf{f}}\right\rangle}{\left\langle \widehat{\mathbf{f}}, \mathcal{W}_f\widehat{\mathbf{f}}\right\rangle}, \tag{2.10}$$

where † on an operator denotes the adjoint of the operator with respect to the inner product in Equation 2.9. For $\mathcal{H}$, $\mathcal{H}^\dagger = \mathcal{B}^\dagger\mathcal{R}^\dagger\mathcal{C}^\dagger$. The largest amplification, subject to unit norm forcing, $\left\|\widehat{\mathbf{f}}\right\|_f = 1$, is found by considering stationary points of the cost function

$$\begin{aligned}\mathcal{J}(\mathbf{a}) &= \|\mathcal{H}\mathbf{a}\|_r - \lambda^2\Big(\|\mathbf{a}\|_f - 1\Big) \\ &= \left\langle \mathbf{a}, \mathcal{H}^\dagger\mathcal{W}_r\mathcal{H}\mathbf{a}\right\rangle - \lambda^2\big(\left\langle \mathbf{a}, \mathcal{W}_f\mathbf{a}\right\rangle - 1\big),\end{aligned} \tag{2.11}$$

where λ denotes the Lagrange multiplier. The optimal forcing input, $\boldsymbol{\phi}$, is found as the stationary point of $\mathcal{J}$ such that

$$\frac{\mathrm{d}\mathcal{J}(\boldsymbol{\phi} + \epsilon\mathbf{h})}{\mathrm{d}\epsilon} = 2\Re\left\{\left\langle \mathbf{h}, \mathcal{H}^\dagger\mathcal{W}_r\mathcal{H}\boldsymbol{\phi}\right\rangle - \lambda^2\left\langle \mathbf{h}, \mathcal{W}_f\boldsymbol{\phi}\right\rangle\right\} = 0, \tag{2.12}$$

for any $\mathbf{h}$ in the same vector space as $\boldsymbol{\phi}$. By replacing $\mathbf{h}$ with $\boldsymbol{\phi}$ in Equation 2.13 and comparing with Equation 2.10, it is clear that the Lagrange multiplier, λ^2, is equal to the optimal linear amplification, σ^2. Since Equation 2.12 holds for any $\mathbf{h}$, it must be the case that $\boldsymbol{\phi}$ satisfies the generalized eigenvalue problem,

$$\mathcal{H}^\dagger\mathcal{W}_r\mathcal{H}\boldsymbol{\phi} = \sigma^2\mathcal{W}_f\boldsymbol{\phi}. \tag{2.13}$$

Because $\mathcal{H}^\dagger\mathcal{W}_r\mathcal{H}$ and $\mathcal{W}_f$ are both Hermitian operators, the eigenvalues and eigenvectors of Equation 2.13 are non-negative and orthonormal with respect to the inner product in Equation 2.8, respectively. The eigenvalues, σ_i^2, and eigenvectors, $\boldsymbol{\phi}_i$, are sorted such that $\sigma_1^2 \geq \sigma_2^2 \geq \sigma_3^2 \geq \cdots \geq 0$. Taking the inner product of the eigenvector $\boldsymbol{\phi}_j$ and Equation 2.13 for the eigen-pair $\left(\sigma_i^2, \boldsymbol{\phi}_i\right)$ and using orthonormality, one can show

$$\begin{aligned}\sigma_i^2\left\langle \boldsymbol{\phi}_j, \mathcal{W}_f\boldsymbol{\phi}_i\right\rangle &= \left\langle \boldsymbol{\phi}_j, \mathcal{H}^\dagger\mathcal{W}_r\mathcal{H}\boldsymbol{\phi}_i\right\rangle \\ \sigma_i^2\delta_{ij} &= \left\langle \mathcal{H}\boldsymbol{\phi}_j, \mathcal{W}_r\mathcal{H}\boldsymbol{\phi}_i\right\rangle = \left\langle \mathcal{H}\boldsymbol{\phi}_j, \mathcal{H}\boldsymbol{\phi}_i\right\rangle_r.\end{aligned} \tag{2.14}$$

Hence $\mathcal{H}\boldsymbol{\phi}_i$ defines orthonormal vectors $\boldsymbol{\psi}_i$, with respect to the inner product in Equation 2.7, as

$$\mathcal{H}\boldsymbol{\phi}_i = \sigma_i\boldsymbol{\psi}_i. \tag{2.15}$$

The set of orthonormal vectors $\boldsymbol{\psi}_i$ and $\boldsymbol{\phi}_i$ are identified as the left and right singular vectors of $\mathcal{H}$ and are termed the response and forcing modes, respectively. The singular values of $\mathcal{H}$ are then σ_i, which are the linear amplification of the system. $\boldsymbol{\psi}_i$, $\boldsymbol{\phi}_i$, and σ_i with $i = 1$ are termed the optimal modes and amplification, while $i > 1$ are termed sub-optimal modes and amplifications.

The response modes can be found independent of $\boldsymbol{\phi}_i$ by multiplying both sides of Equation 2.15 by $\mathcal{H}\mathcal{W}_f^{-1}\mathcal{H}^\dagger\mathcal{W}_r$ and using Equation 2.13 and solving the eigenvalue problem

$$\mathcal{H}\mathcal{W}_f^{-1}\mathcal{H}^\dagger\mathcal{W}_r\boldsymbol{\psi}_i = \sigma_i^2\boldsymbol{\psi}_i. \tag{2.16}$$

Similarly, by multiplying both sides of Equation 2.15 by $\mathcal{W}_f^{-1}\mathcal{H}^\dagger\mathcal{W}_r$, it is shown that $\boldsymbol{\phi}_i$ and $\boldsymbol{\psi}_i$ are related through

$$\mathcal{W}_f^{-1}\mathcal{H}^\dagger\mathcal{W}_r\boldsymbol{\psi}_i = \sigma_i\boldsymbol{\phi}_i. \tag{2.17}$$

$\mathcal{W}_f^{-1}\mathcal{H}^\dagger\mathcal{W}_r$ is the adjoint of $\mathcal{H}$ with respect to the inner products in Equation 2.7 and 2.8 such that $\langle\mathbf{a},\mathcal{H}\mathbf{b}\rangle_r = \left\langle\mathcal{W}_f^{-1}\mathcal{H}^\dagger\mathcal{W}_r\mathbf{a},\mathbf{b}\right\rangle_f$.

The resolvent operator can be rewritten using the Schmidt decomposition as

$$\mathcal{H} = \sum_j \sigma_j\boldsymbol{\psi}_j\boldsymbol{\phi}_j^*. \tag{2.18}$$

Hence $\mathcal{H}$ can be rewritten as the sum of rank-1 operators, $\boldsymbol{\psi}_i\boldsymbol{\phi}_i^*$, ranked in descending order by their coefficients σ_i. This decomposition depends on the choice of inner product for $\widehat{\mathbf{f}}$ and $\widehat{\mathbf{q}}$ and is parameterized by ω, $\mathbf{k}$, and $\overline{\mathbf{Q}}$. This can be contrasted with the eigendecomposition of a linear operator $\mathcal{N}$ as $\mathcal{N} = \sum_j \lambda_j\mathbf{p}_j\mathbf{q}_j^*$, where λ_j, $\mathbf{p}_j$, and $\mathbf{q}_j$ denote its eigenvalues, eigenvectors, and adjoint eigenvectors. $\boldsymbol{\psi}_i$ and $\boldsymbol{\phi}_i$ each form separate orthonormal bases while $\mathbf{p}_i$ and $\mathbf{q}_i$ do not form orthogonal sets of eigenvectors, in general. Note that for $\lambda_i \neq \lambda_j$, $\mathbf{p}_i$ is orthogonal to $\mathbf{q}_j$. For the special case where $\mathcal{N}$ is a normal operator, its eigendecomposition is $\mathcal{N} = \sum_j \lambda_j\mathbf{p}_j\mathbf{p}_j^*$. In this case, $\mathbf{p}_j$ forms an orthogonal basis. The Schmidt decomposition can be thought of as an extension of the eigendecomposition for normal operators to non-normal operators since the non-normal operator can be decomposed using two separate orthonormal bases.

In the case where C and $\mathcal{B}$ are invertible, Equation 2.6 can be written as

$$\mathcal{B}^{-1}\left(-i\omega\mathcal{I} + \widehat{\mathcal{L}}\right)C^{-1}\widehat{y} = \mathcal{A}\widehat{y} = \widehat{f}. \tag{2.19}$$

In this case, $\mathcal{A}$ is the inverse of $\mathcal{H}$. $\mathcal{A}$ can be interpreted as a transfer function from $\widehat{y}$ to $\widehat{f}$. The gain, g between $\widehat{f}$ to $\widehat{y}$, is defined as

$$g^2 = \frac{\left\|\widehat{\mathbf{f}}\right\|_f}{\left\|\widehat{\mathbf{y}}\right\|_r} = \frac{\left\|\mathcal{A}\widehat{\mathbf{y}}\right\|_f}{\left\|\widehat{\mathbf{y}}\right\|_r} = \frac{\left\langle\widehat{\mathbf{y}},\mathcal{A}^\dagger\mathcal{W}_f\mathcal{A}\widehat{\mathbf{y}}\right\rangle}{\left\langle\widehat{\mathbf{y}},\mathcal{W}_r\widehat{\mathbf{y}}\right\rangle}. \tag{2.20}$$

Before, the search was performed for the largest gain of $\mathcal{H}$. Now, because the problem uses its inverse, the search is for the smallest gain of $\mathcal{A}$. To find the minimum value of g subject to $\left\|\widehat{\mathbf{y}}\right\|_r = 1$, one must minimize the cost functional

$$\begin{aligned}\mathcal{J}_m(\mathbf{a}) &= \|\mathcal{A}\mathbf{a}\|_f - \lambda^2\|\mathbf{a}\|_r \\ &= \left\langle \mathbf{a}, \mathcal{A}^\dagger \mathcal{W}_f \mathcal{A}\mathbf{a} \right\rangle - \lambda^2 \left\langle \mathbf{a}, \mathcal{W}_r \mathbf{a} \right\rangle .\end{aligned} \tag{2.21}$$

Repeating the steps from before to find the stationary points of the cost functional, $\mathcal{J}_m$ gives the following eigenvalue problem

$$\mathcal{A}^\dagger \mathcal{W}_f \mathcal{A}\boldsymbol{\psi}_i = \lambda_i^2 \mathcal{W}_r \boldsymbol{\psi}_i. \tag{2.22}$$

By inverting the left hand side of Equation 2.22 and comparing with Equation 2.16, it is clear that $\lambda^2 = \sigma_i^{-2}$ and the eigenvectors are the response modes. Equation 2.22 provides an alternate way to compute resolvent analysis without inverting $(-i\omega + \mathcal{L})^{-1}$ and provides an interpretation of the resolvent modes as the minima of a constrained minimization problem (Barthel, Gomez, and McKeon, 2022b). This formulation will be used for analytic arguments in future sections. A similar expression for Equation 2.22 can also be derived for the forcing modes, though it is omitted here.

Going from Linear Operators to Matrices

So far the discussion has been limited to operators acting on continuous fields. The discussion will now be tailored to discrete spaces that are encountered in computational settings.

The inhomogenous spatial coordinates will be discretized into n points, $\mathbf{x}_i \in \Omega_n$ and the state vector will be treated as a column vector $\widehat{\mathbf{q}} = \left[\widehat{q}_1^1, \ldots, \widehat{q}_1^n, \ldots, \widehat{q}_{n_s}^1, \ldots, \widehat{q}_{n_s}^n\right]^T \in \mathbb{C}^{n_s n}$, where $\widehat{q}_j^i = \widehat{q}_j(\mathbf{x}_i)$. The identity operator, $\mathcal{I}$ is replaced with the identity matrix, $\mathbf{I} \in \mathbb{R}^{n_s n \times n_s n}$. Likewise, the linear operators, $\widehat{\mathcal{L}}$,$\mathcal{C}$,$\mathcal{B}$,$\mathcal{W}_r$, and $\mathcal{W}_f$ are discretized into the $\mathbb{C}^{n_s n \times n_s n}$ matrices, $\mathbf{L}$,$\mathbf{C}$,$\mathbf{B}$,$\mathbf{W}_r$, and $\mathbf{W}_f$ based on the choice of differentiation scheme. Boundary conditions are of the form

$$\mathbf{p}^T \widehat{\mathbf{q}} = 0, \tag{2.23}$$

where $\mathbf{p}$ denotes the coefficients of the boundary condition. For example, a Dirichlet boundary condition at $\mathbf{x}_i$ would result in the entries of $\mathbf{p}$ being all 0, except for the ith component which is set to 1. The rows of $(-i\omega\mathbf{I} - \mathcal{L})$ corresponding to boundary conditions are replaced by row vectors that enforce the said boundary conditions

and a matrix $\mathbf{I}_c$ is constructed that is equal to the identity matrix, except that the rows where the boundary conditions are applied are set to 0. The resolvent matrix is then defined as $\mathbf{R} = (-i\omega\mathbf{I} - \mathcal{L})^{-1}\mathbf{I}_c$ and $\mathbf{H} = \mathbf{CRB}$. Note that in practice, $\mathbf{R}$ is not explicitly calculated due to its computational cost and dense nature.

The integration in the inner product in Equation 2.9 is done numerically through quadrature. This is accomplished by the positive-definite matrix $\mathbf{W}_I$ such that

$$\langle \mathbf{a}, \mathbf{b} \rangle = \int_{\Omega_n} \mathbf{a}^* \mathbf{b} d\mathbf{x}_n \approx \mathbf{a}^* \mathbf{W}_I \mathbf{b}. \tag{2.24}$$

Since each state variable is discretized onto the same grid, $\mathbf{W}_I$ is a block-diagonal matrix with n_s positive-definite matrices $\mathbf{W} \in \mathbb{R}^{n \times n}$ that enforce $\int_{\Omega_n} a^{i*} b^i d\mathbf{x}_n \approx \mathbf{a}^{i*} \mathbf{W} \mathbf{b}^i$. The equality is not exact because of the numerical approximations. Although in general $\mathbf{W}_I$ does not need to be block-diagonal, this choice is made here because the kinetic energy-like norms used and choice of primitive variables for the state vectors do not require off-diagonal blocks. The inner products in Equation 2.7 and 2.8 are then discretized as

$$\langle \mathbf{a}, \mathbf{b} \rangle_r = \mathbf{a}^* \mathbf{W}_I \mathbf{W}_r \mathbf{b}, \tag{2.25}$$

$$\langle \mathbf{a}, \mathbf{b} \rangle_f = \mathbf{a}^* \mathbf{W}_I \mathbf{W}_f \mathbf{b}. \tag{2.26}$$

The adjoint operators in Equation 2.13 depend on the choice of inner product and fall under two approaches. The first approach computes the adjoint based on the continuous inner product in Equation 2.9 and then discretizes the resulting continuous operator. The second approach computes the adjoint by considering Equation 2.24 such that

$$\mathbf{A}^\dagger = \mathbf{W}_I^{-1} \mathbf{A}^* \mathbf{W}_I, \tag{2.27}$$

where $\mathbf{A}^*$ denotes the complex conjugate of the matrix(Jeun, Nichols, and Jovanović, 2016; Chandler et al., 2012). The first approach is generally more stable (Chandler et al., 2012), although it requires analytic expressions for the adjoints and involves two separate inversions for $\mathbf{R}$ and $\mathbf{R}^\dagger$. The second approach can be prone to errors near the boundaries since the boundary conditions on $(-i\omega\mathbf{I} + \mathbf{L})$ and $\mathbf{I}_c$ can result in inappropriate boundary conditions for the adjoint problem. In this work, the results with incompressible flow will use the first approach while the results with compressible flow will use the second approach. In the first approach, $\mathbf{R}^\dagger = (i\omega\mathbf{I} + \mathbf{L}^\dagger)^{-1}\mathbf{I}_c^\dagger$, where $\mathbf{L}^\dagger$ is the discretized continuous adjoint of $\widehat{\mathcal{L}}$ with the appropriate boundary conditions applied. In the second approach $\mathbf{R}^\dagger = \mathbf{W}_I^{-1}\mathbf{R}^*\mathbf{W}_I$.

Finally, the discretized form of the eigenvalue problem in Equation 2.13 is,

$$\mathbf{H}^{\dagger}\mathbf{W}_r\mathbf{H}\phi_i = \sigma_i^2\mathbf{W}_f\phi_i. \tag{2.28}$$

This is solved by using the Arnoldi iteration (Saad, 2011). Note that the Arnoldi algorithm requires repeated calculations of $\mathbf{R}\mathbf{b}_i$, or equivalently, multiple solutions of $(-i\omega\mathbf{I}+\mathbf{L})\mathbf{a} = \mathbf{I}_c\mathbf{b}_i$, and similar calculations for the adjoint. To avoid storing and computing the inverse, an LU decomposition is computed once with the Intel® oneAPI Math Kernel Library PARDISO (Schenk and Gärtner, 2004), which takes advantage of the sparse form of $(-i\omega\mathbf{I}+\mathbf{L})$ and parallelized subroutines. This allows the linear system to be computed efficiently using the factors, with the overall cost of the process being the cost of one LU decomposition (Jeun, Nichols, and Jovanović, 2016; Sipp and Marquet, 2013; Schmidt et al., 2018). Despite the efficiency of using the LU factors, the LU matrices themselves can be dense and cause the calculations to be limited by computer memory. For the local analysis, the LU decomposition and Gaussian elimination are handled by the built in MATLAB® functions, `lu` and `mldivide`. See Appendix A for the Arnoldi algorithm used to compute the singular value decomposition.

2.3 Application to Incompressible Flows

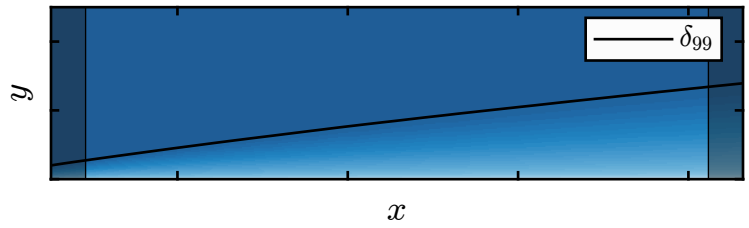

Figure 2.1: Schematic of the domain, Ω_n, with the spanwise direction pointing out of the page. The shaded rectangular regions denote the sponge regions.

For the rest of this chapter, and Chapters 3 and 4, the discussion will be tailored to the discussion of statistically stationary, two dimensional, incompressible, flat plate, wall bounded, boundary layer flows. The spatial coordinates $\mathbf{x} = [x, y, z]$ denote the streamwise, wall-normal, and spanwise coordinates, respectively, as shown in the schematic in Figure 2.1. The state $\mathbf{Q} = [\mathbf{U}, P]$ corresponds to the velocity and pressure, respectively, where $\mathbf{U} = [U, V, W]$ denotes the streamwise, wall-normal, and spanwise velocities. Note that the pressure is normalized by the density. The velocities and spatial coordinates are nondimensionalized by a reference velocity,

U_r, and reference length scale, L_r, which are used to nondimensionalize time with, L_r/U_r, and the pressure with, U_r^2. This introduces the Reynolds number, $Re = U_r L_r/\nu$, where ν is the kinematic viscosity, as a parameter for the governing equations. The state $\mathbf{Q}$ satisfies the incompressible Navier Stokes equations (NSE),

$$\partial_t \mathbf{U} + (\boldsymbol{\nabla}\mathbf{U})\mathbf{U} + \boldsymbol{\nabla} P - \frac{1}{Re}\nabla^2 \mathbf{U} = \mathbf{0}, \tag{2.29}$$

$$\boldsymbol{\nabla} \cdot \mathbf{U} = 0. \tag{2.30}$$

The convective term is written as $(\boldsymbol{\nabla}\mathbf{U})\mathbf{U}$ so it can be interpreted as the velocity gradient tensor acting on the velocity. This appears neatly in the Reynolds decomposition as the mean velocity gradient tensor acts on the fluctuations in the same way that a tensor acts on a vector. In indicial notation, this is still $\left(\partial_{x_j} U_i\right) U_j$. The boundary conditions are $\mathbf{U} = \mathbf{0}$ at $y = 0$ due to the no slip boundary condition and $\mathbf{U} \to \mathbf{U}_\infty(x)$ as $y \to \infty$ for some freestream velocity that depends on a prescribed freestream pressure gradient, $d_x P_\infty = -U_\infty d_x U_\infty$.

Following the Reynolds decomposition described in Section 2.2, where $\overline{\mathbf{Q}}$ is the incompressible mean flow field and $\mathbf{q} = [u, v, w, p]$ is the fluctuating state such that $\overline{\mathbf{q}} = \mathbf{0}$, the NSE can be rewritten as

$$\begin{aligned} \partial_t \mathbf{u} + (\boldsymbol{\nabla}\mathbf{u})\overline{\mathbf{U}} + \left(\boldsymbol{\nabla}\overline{\mathbf{U}}\right)\mathbf{u} + \boldsymbol{\nabla} p - \frac{1}{Re}\nabla^2 \mathbf{u} &= -\left(\boldsymbol{\nabla}\overline{\mathbf{U}}\right)\overline{\mathbf{U}} - \boldsymbol{\nabla}\overline{P} \\ &\quad - \frac{1}{Re}\nabla^2 \overline{\mathbf{U}} - (\boldsymbol{\nabla}\mathbf{u})\mathbf{u} = \mathbf{n}, \end{aligned} \tag{2.31}$$

$$\boldsymbol{\nabla} \cdot \mathbf{u} = 0. \tag{2.32}$$

Just as in Equation 2.2, $\mathbf{n}$ denotes all the nonlinear terms including the mean flow terms and the Reynolds stresses, $(\boldsymbol{\nabla}\mathbf{u})\mathbf{u}$. The Fourier Transform can be applied again in the temporal direction and homogeneous directions, which depend on the assumption of a local analysis (1D) or biglobal analysis (2D), as in Equation 2.3. If $\omega = 0$ and $\mathbf{k} = \mathbf{0}$, the governing equation for the mean flow field can be recovered, known as the Reynolds Averaged Navier Stokes (RANS) Equation (McKeon and Sharma, 2010).

For the incompressible flow, Equation 2.4 becomes

$$\begin{aligned} -i\omega\widehat{\mathbf{u}} + \left(\widehat{\boldsymbol{\nabla}}\widehat{\mathbf{u}}\right)\overline{\mathbf{U}} + \left(\boldsymbol{\nabla}\overline{\mathbf{U}}\right)\widehat{\mathbf{u}} + \widehat{\boldsymbol{\nabla}}\widehat{p} - \frac{1}{Re}\widehat{\boldsymbol{\nabla}}^2\widehat{\mathbf{u}} &= -\widehat{(\boldsymbol{\nabla}\mathbf{u})\mathbf{u}}, \\ \widehat{\boldsymbol{\nabla}} \cdot \widehat{\mathbf{u}} &= 0, \end{aligned} \tag{2.33}$$

where $\widehat{\boldsymbol{\nabla}}$ accounts for the wavenumbers in $\mathbf{x}_h$. The left hand side of Equation 2.33 can be identified as the left hand side of Equation 2.4. The terms in Equation 2.33

from left to right denote the temporal variation, the mean advection, the mean shear, the pressure gradient, viscous dissipation, and the quadratic, nonlinear forcing. The latter gives rise to triadic interactions, meaning that the only wavenumber-frequency pair interactions that can affect $\omega, \mathbf{k}$ are those such that $\omega_1 + \omega_2 = \omega$ and $\mathbf{k}_1 + \mathbf{k}_2 = \mathbf{k}$. unless otherwise stated, $-\widehat{(\boldsymbol{\nabla}\mathbf{u})\mathbf{u}}$ will be treated as an uncorrelated forcing input, $\widehat{\mathbf{f}}$.

Because of the continuity constraint, the identity operator, $\mathcal{I} = \mathrm{diag}\,(1, 1, 1, 0)$. The inner products are defined such that $\mathcal{W}_r = \mathcal{W}_f = \mathcal{I}$ so that the inner product in Equation 2.7 is proportional to the kinetic energy of the fluctuation, integrated over the domain. Since these are not positive definite operators, their inverses are undefined. Instead, the inverse will be defined as, $\mathcal{W}_r^{-1} = \mathcal{W}_f^{-1} = \mathcal{I}$.

With the adjoint variables denoted as $\tilde{\mathbf{q}} = [\tilde{\mathbf{u}}, \tilde{p}]^T$ and $\tilde{\mathbf{f}}$, the adjoint equations are

$$\begin{aligned} i\omega\tilde{\mathbf{u}} - \left(\widehat{\boldsymbol{\nabla}}\tilde{\mathbf{u}}\right)\overline{\mathbf{U}} + \left(\boldsymbol{\nabla}\overline{\mathbf{U}}\right)^T\tilde{\mathbf{u}} - \widehat{\boldsymbol{\nabla}}\tilde{p} - \frac{1}{Re}\widehat{\boldsymbol{\nabla}}^2\tilde{\mathbf{u}} &= \tilde{\mathbf{f}}, \\ -\widehat{\boldsymbol{\nabla}}\cdot\tilde{\mathbf{u}} &= 0. \end{aligned} \tag{2.34}$$

The values of $\tilde{\mathbf{q}}$ and $\widehat{\mathbf{q}}$ are assumed to be $\mathbf{0}$ on $\partial\Omega_n$ to avoid boundary terms from the integration by parts. Details on the derivation of the adjoint equations can found in Appendix B.

The adjoint problem has a continuity constraint on $\tilde{\mathbf{q}}$, meaning that for any $\tilde{\mathbf{q}} = \mathcal{R}^\dagger\mathbf{b} = 0$ with $\mathbf{b} \in \mathbb{C}^4$, $\widehat{\boldsymbol{\nabla}}\cdot\tilde{\mathbf{q}} = 0$. This means that $\widehat{\boldsymbol{\nabla}}\cdot\boldsymbol{\phi}_i = 0$ from Equation 2.17, which is restated for the incompressible case as

$$\mathcal{I}\mathcal{R}^\dagger\mathcal{I}\psi_i = \sigma_i\boldsymbol{\phi}_i. \tag{2.35}$$

Thus, the optimal forcing modes are purely solenoidal, despite the fact that in general, $\widehat{\boldsymbol{\nabla}}\cdot\left(\widehat{(\boldsymbol{\nabla}\mathbf{u})\mathbf{u}}\right) \neq 0$. This agrees with Rosenberg (2018) who found that the forcing entering the resolvent operator can only be solenoidal by deriving the Orr-Sommerfeld-Squire equations in the presence of an external forcing. The incompressibility constraint for $\boldsymbol{\phi}_i$, or equivalently, the adjoint velocity $\tilde{\mathbf{u}}$, comes directly from the incompressibility constraint of $\widehat{\mathbf{u}}$ and that $\widehat{p}$ enforces that constraint.

In what follows, the discussion will be applied to the local resolvent analysis which uses the parallel flow assumption, and then contrasted with the biglobal resolvent analysis.

Local (1D) Resolvent Analysis

In the local approach, the analysis makes use of the parallel flow assumption. This assumes that $\mathbf{x}_h = [x, z]$ and thus $\mathbf{k} = [k_x, k_z]$, where k_x and k_z define the streamwise

and spanwise wavenumbers, respectively. Due to the parallel flow assumption, the mean flow field, $\overline{\mathbf{U}} = \overline{U}(y)\mathbf{e}_x$. For pipes and channels, this approximation is exact due to the homogeneity in x but is a simplification for the boundary layers of interest. The velocity and length scale are chosen as $U_r = U_\infty$, the freestream velocity, and $L_r = \delta_{99}$, the boundary layer thickness. Finally, the Fourier modes $\widehat{\mathbf{q}} = \widehat{\mathbf{q}}(y)$ and $\widehat{\mathbf{f}} = \widehat{\mathbf{f}}(y)$ represent three-dimensional disturbances. Equation 2.33 and 2.34 become

$$\begin{aligned} \left(-i\omega + ik_x\overline{U}\right)\widehat{\mathbf{u}} + \partial_y\overline{U}\widehat{v}\mathbf{e}_x + \widehat{\boldsymbol{\nabla}}\widehat{p} - \frac{1}{Re}\widehat{\boldsymbol{\nabla}}^2\widehat{\mathbf{u}} &= -\widehat{\mathbf{f}}, \\ \widehat{\boldsymbol{\nabla}}\cdot\widehat{\mathbf{u}} &= 0, \end{aligned} \tag{2.36}$$

and

$$\begin{aligned} \left(i\omega - ik_x\overline{U}\right)\tilde{\mathbf{u}} + \partial_y\overline{U}\widehat{u}\mathbf{e}_y - \widehat{\boldsymbol{\nabla}}\tilde{p} - \frac{1}{Re}\widehat{\boldsymbol{\nabla}}^2\tilde{\mathbf{u}} &= -\tilde{\mathbf{f}}, \\ -\widehat{\boldsymbol{\nabla}}\cdot\tilde{\mathbf{u}} &= 0, \end{aligned} \tag{2.37}$$

respectively, where $\widehat{\boldsymbol{\nabla}} = \left[ik_x, \partial_y, ik_z\right]$ and $\widehat{\boldsymbol{\nabla}}^2 = \partial_{yy} - k_x^2 - k_z^2$. The domain is chosen as the bounded domain, $y \in \Omega_n = [0, y_{max}]$, although it is unbounded physically. Here, $y_{\max} \geq 3$. The boundary conditions are $\widehat{\mathbf{u}}(y = 0) = \mathbf{0}$, $\partial_y\widehat{\mathbf{u}}(y = y_{max}) = \mathbf{0}$, $\tilde{\mathbf{u}}(y = 0) = \mathbf{0}$, and $\tilde{\mathbf{u}}(y = y_{max}) = \mathbf{0}$.

Numerically, the wall-normal grid is discretized using a fourth-order summation by parts (SBP) scheme (Mattsson and Nordström, 2004) using N_y grid points. Grid stretching is employed in the wall-normal direction so that half the points are below y_{min} as in Madhusudanan and McKeon (2022), Kamal et al. (2020), and Malik (1990). Here y_{min} is chosen to be closer to the wall than in their studies since they focused on capturing freestream acoustics. Although spectral collocation methods have been used in other studies (Moarref, Sharma, et al., 2013), the SBP scheme is preferred because it generates sparse operators unlike the spectral codes. The scheme also creates a matrix $\mathbf{W}_I$ that is used for the numerical integration. After discretization, the linear operators $(-i\omega\mathbf{I} + \mathbf{L})$, $\left(i\omega\mathbf{I} + \mathbf{L}^\dagger\right) \in \mathbb{C}^{4N_y \times 4N_y}$ meaning that the most expensive operation for resolvent analysis, the LU decomposition, scales with $O\left(\left(4N_y\right)^3\right)$.

In the local analysis, because both k_x and ω are specified, this in turn specifies a wavespeed $c = \omega/k_x$ that the modes convect at. If viscous terms are neglected in Equation 2.36, a singularity emerges at the critical layer location y_c such that $\omega/k_x = \overline{U}(y_c)$ that creates infinite amplification. The viscous terms regularize this inviscid singularity in Equation 2.36, yet it remains a source of amplification for

the resolvent operator (Schmid and Henningson, 2002; McKeon and Sharma, 2010) and centers the response and forcing modes around y_c. Hence, by specifying ω and k_x, the wall-normal location and wavespeed of the resolvent mode can be specified *a priori*. This amplification is related to the normal aspects of the operator, though the presence of shear makes the operator non-normal and creates amplification mechanisms such as the Orr mechanism or the lift-up mechanism (Schmid and Henningson, 2002). In the parallel flow assumption, the streamwise development and wall-normal components of the mean flow are not accounted for.

The local analysis has been successful in describing observations in turbulent channels and pipes (McKeon and Sharma, 2010; Sharma and McKeon, 2013), where the parallel flow assumption holds. This is partly due to the observation that for length and time scales relevant to near-wall turbulence, the local resolvent operator tends to be low-rank (Abreu, Cavalieri, et al., 2020; Moarref, Sharma, et al., 2013), meaning that $\sigma_1 \gg \sigma_2$. Hence the local resolvent operator is a highly directional amplifier in the direction of $\boldsymbol{\psi}_1$.

Biglobal Resolvent Analysis

Since boundary layers are inherently nonparallel due to their streamwise development, it is desirable to have an operator that can account for these nonparallel effects. U_r and L_r are chosen as $U_\infty(x_r)$ and $\delta_{99}(x_r)$ at some reference location x_r. Here, $\mathbf{x}_h = z$ and hence $\mathbf{k} = k_z$ and $\mathbf{x}_n = [x, y] \in \Omega_n = [x_0, x_0 + L_x] \times [0, y_{max}]$, where x_0 and L_x are the problem dependent origin of the domain and domain length, respectively, and $y_{max} = 5$. The mean flow field is assumed to be two-dimensional such that $\overline{\mathbf{U}} = \left[\overline{U}(x,y), \overline{V}(x,y), 0\right]$ while the Fourier modes, $\widehat{\mathbf{q}} = \widehat{\mathbf{q}}(x,y)$ and $\widehat{\mathbf{f}} = \widehat{\mathbf{f}}(x,y)$, represent three-dimensional disturbances. Equations 2.33 and 2.34 become

$$\begin{aligned}\Big(-i\omega + \overline{U}\partial_x + \overline{V}\partial_y\Big)\widehat{\mathbf{u}} + \Big(\partial_x\overline{U}\widehat{u} + \partial_y\overline{U}\widehat{v}\Big)\mathbf{e}_x + \\ \Big(\partial_x\overline{V}\widehat{u} + \partial_y\overline{V}\widehat{v}\Big)\mathbf{e}_y + \widehat{\boldsymbol{\nabla}}\widehat{p} - \frac{1}{Re}\widehat{\boldsymbol{\nabla}}^2\widehat{\mathbf{u}} + s(x)\widehat{\mathbf{u}} = -\widehat{\mathbf{f}}, \\ \widehat{\boldsymbol{\nabla}}\cdot\widehat{\mathbf{u}} = 0,\end{aligned} \tag{2.38}$$

and

$$\begin{aligned}\Big(i\omega - \overline{U}\partial_x - \overline{V}\partial_y\Big)\tilde{\mathbf{u}} + \Big(\partial_x\overline{U}\tilde{u} + \partial_x\overline{V}\tilde{v}\Big)\mathbf{e}_x + \\ \Big(\partial_y\overline{U}\tilde{u} + \partial_y\overline{V}\tilde{v}\Big)\mathbf{e}_y - \widehat{\boldsymbol{\nabla}}\tilde{p} - \frac{1}{Re}\widehat{\boldsymbol{\nabla}}^2\tilde{\mathbf{u}} + s(x)\tilde{\mathbf{u}} = -\tilde{\mathbf{f}}, \\ -\widehat{\boldsymbol{\nabla}}\cdot\tilde{\mathbf{u}} = 0,\end{aligned} \tag{2.39}$$

respectively, where $\widehat{\boldsymbol{\nabla}} = \left[\partial_x, \partial_y, ik_z\right]$, $\widehat{\boldsymbol{\nabla}}^2 = \partial_{xx} + \partial_{yy} - k_z^2$, and $s(x)$ is an added sponge to make the modes compact in x and avoid spurious reflections from the end-points. The implementation of the sponge zones is similar to Ran et al. (2019), although applied to the NSE as opposed to the Orr-Sommerfeld-Squire equations. $s(x)$ is 0 for 90% of the domain at which point it ramps up quadratically from 0 to ϵ_s at the endpoints of the domain. The explicit form of $s(x)$ is

$$s(x) = \begin{cases} \epsilon_s \dfrac{(|x - x_0 - L_x/2| - .45L_x)^2}{.0025L_x^2} & \text{if } |x - x_0 - L_x/2| \geq .45L_x \\ 0 & \text{else.} \end{cases} \tag{2.40}$$

In this work, ϵ_s depends on Re, so its value will be specified throughout. The boundary conditions in the wall-normal direction are the same as the local analysis. The streamwise boundary conditions are Dirichlet boundary conditions at the inlet and outlet of the domain for both $\widehat{\mathbf{q}}$ and $\tilde{\mathbf{q}}$ due to the action of the sponge. This ensures that there are no boundary terms from the integration by parts when defining the adjoint operators.

The wall-normal coordinates are discretized using the same scheme as in the local code. The streamwise direction is discretized with a fourth-order SBP scheme, where the grid spacing is uniform, unless otherwise specified. These schemes produce the numerical weight matrices $\mathbf{W}_I$. After discretization, the linear operators $(-i\omega\mathbf{I} + \mathbf{L})$, $\left(i\omega\mathbf{I} + \mathbf{L}^\dagger\right) \in \mathbb{C}^{4N_xN_y \times 4N_xN_y}$, meaning that now the LU decomposition scales with $O\left(\left(4N_xN_y\right)^3\right)$. The biglobal analysis is $O\left(N_x^3\right)$ times more expensive to compute than the local approach, due to the increased degrees of freedom required to discretize the streamwise direction. The inner product in Equation 2.9 is augmented to normalize by the streamwise domain length such that

$$\langle \mathbf{a}, \mathbf{b} \rangle = \frac{1}{L_x} \int_{x_0}^{x_0+L_x} \int_0^{y_{max}} \mathbf{a}^* \mathbf{b} dy dx. \tag{2.41}$$

The response and forcing modes computed with the biglobal approach have both wall-normal and streamwise variation. Their streamwise structure, wall-normal location, and convective speed are not specified *a priori*. Nonparallel components of the mean flow field are incorporated into the linear analysis, making this operator apt for studying the nonequilibrium effects in incompressible boundary layer flows, such as adverse pressure gradients, $d_x P_\infty = -U_\infty d_x U_\infty$.

One possible way of reducing the computational cost of the biglobal resolvent analysis is to use an Orr-Sommerfeld-Squire (OSS) formulation for the LNSE.

This approach is commonly used in local linear stability analysis (Schmid and Henningson, 2002) and has seen use in local resolvent analysis (Rosenberg, 2018). The OSS formulation can reduce the LNSE to a system of two equations for the wall-normal vorticity, $\widehat{\omega}_2 = ik_z\widehat{u} + \partial\widehat{w}/\partial x$, and $\widehat{v}$ by eliminating $\widehat{p}$ by using the continuity equation. Since the state is reduced to $\mathbf{q}_{OSS} = [\widehat{v}, \widehat{\omega}_2]$, the discretized degrees of freedom are now $2n$. With this approach, the resolvent analysis would scale as $O(8n^3)$ when discretized, compared to a scaling of $O(64n^3)$ when using the LNSE with primitive variables $(\widehat{u}, \widehat{v}, \widehat{w}, \widehat{p})$. Although the OSS formulation has seen success in studying the receptivity of a boundary layer (Ran et al., 2019), using the OSS formulation for biglobal resolvent analysis can be cumbersome for a number of reasons. For starters, the OSS formulation requires second (and higher) order derivatives of $\overline{\mathbf{U}}$ to create the linear operators, which may be difficult to obtain from experimental and low-fidelity simulation data. Secondly, the entries in the OSS linear operator require operations involving $\left(k_z^2\mathcal{I} - \partial_{xx}\right)^{-1}$, which is a dense operator. This can cause detrimental effects when computing the LU decompositions used in the Arnoldi algorithm since many linear solvers like the Intel® oneAPI Math Kernel Library PARDISO (Schenk and Gärtner, 2004) require sparse matrices. See Appendix C for more details. The dense nature of the OSS linear operator may circumvent any of the potential computational advantages of using a smaller system of equations in the biglobal resolvent analysis. For these reasons, the OSS formulation is not used for any of the calculations in this work, though it is used for some analytic developments in Chapter 3.

2.4 Verification of Resolvent Analysis

The resolvent analysis will be verified against the results of Sipp and Marquet (2013) and Sasaki et al. (2022). The two studies differ in that the former considers two-dimensional disturbances across a finite flat plate, including the leading edge, while the former considers three-dimensional streaky disturbances over a flat plate in a truncated domain. Although there are differences between the cited approaches and the approach described herein because of the differences in base flows and boundary conditions, it will be shown that similar flow structures and linear amplifications can be computed with the strategy presented here. This will serve as a verification of the linear operators, boundary conditions, and Arnoldi iteration. Although the study of Abreu, Tanarro, et al. (2021) uses similar boundary conditions for the biglobal analysis as the ones described herein, their publication only present contours of

different velocity components of the resolvent modes so quantitative comparisons are not possible with their results.

Verification with Spanwise Constant Modes

Beginning with Sipp and Marquet (2013), their study considers two-dimensional disturbances, $\widehat{\mathbf{q}} = [\widehat{u}(x,y), \widehat{v}(x,y), 0, \widehat{p}(x,y)]^T$, about a laminar boundary layer over a finite flat plate of length l, including the leading edge at $x = 0$. The length and velocity scale are chosen as $L_r = l$, and $U_r = U_\infty$, the freestream velocity, for a $Re = 6 \times 10^5$. Their computational domain is $x, y \in \Omega_s = [-.5, 1.25] \times [0, .02]$, which includes the region upstream of the leading edge and downstream of the trailing edge of the plate. Their base flow was computed numerically and their response modes satisfy the same boundary conditions as the base flow. Their adjoint operator is constructed using the conjugate-transpose approach. More computational details can be found in their publication.

The base flow, $\overline{\mathbf{U}}$, used in this comparison is approximated as the laminar Blasius boundary layer similarity solution for a semi-infinite flat plate, which is not valid near $x = 0$. To remedy this, the domain is chosen as $\Omega_n = [0.025, 1.25] \times [0, .0219]$ to avoid the leading edge. The boundary conditions are treated differently from the original study since the domain is truncated at the inlet, the flat plate is assumed to extend to $x = 1.25$, and the ends of the domain are treated with sponge layers. Since the comparison used here assumes that the flat plate extends past $x = 1$, the base flow adds an extra source of shear not present in Sipp and Marquet (2013) which changes the amplification within the domain. The changes in the base flow will be shown to affect the sub-optimal modes the most. Despite these differences, this comparison will illustrate that similar amplification mechanisms can be identified from the strategy described here. To model two-dimensional disturbances with the operator described in Equations 2.38, k_z is set to 0. Finally, $\mathcal{W}_r$ and $\mathcal{W}_f$ are set such that the inner products are

$$\langle \mathbf{a}, \mathbf{b} \rangle_f = \int_{.025}^{1} \int_{0}^{.0219} \mathbf{a}^* \mathcal{I}_c \mathbf{b} dy dx \tag{2.42}$$

and

$$\langle \mathbf{a}, \mathbf{b} \rangle_r = \int_{.025}^{1} \int_{0}^{.0219} \mathbf{a}^* \mathcal{I}_c \mathbf{b} dy dx. \tag{2.43}$$

The limits of integration in the streamwise direction reflect the choice of inner product used in Sipp and Marquet (2013), except their study includes the region

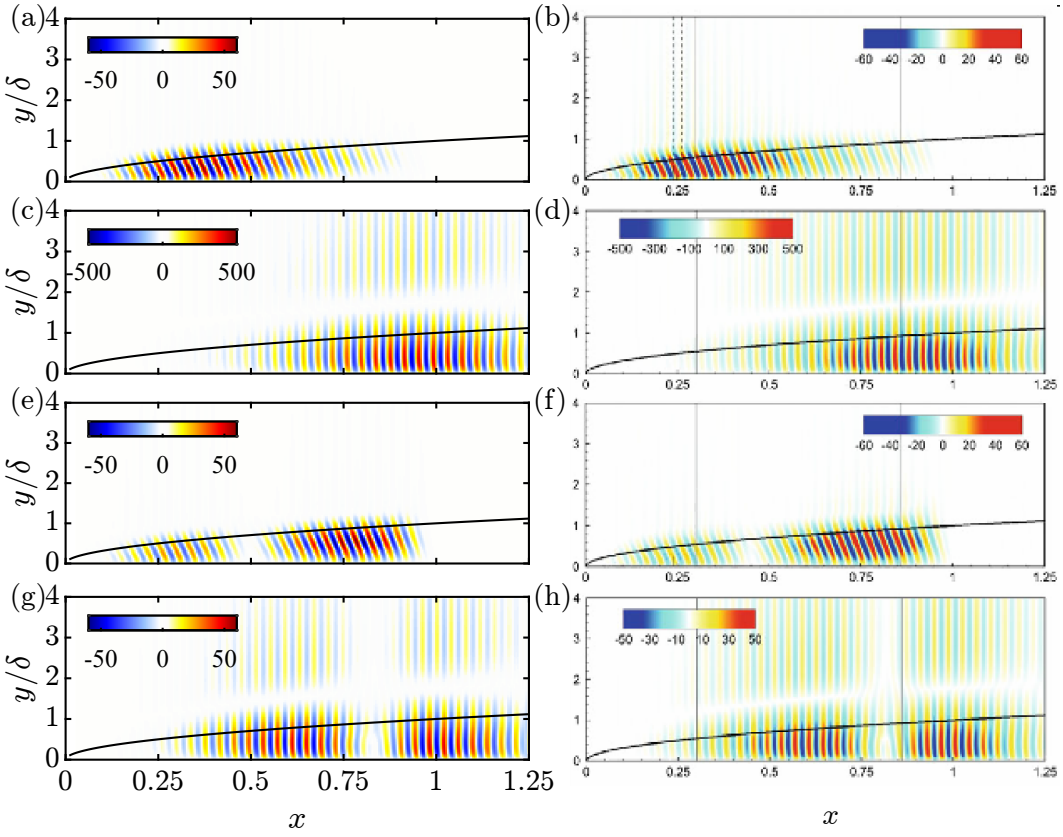

Figure 2.2: Real part of $\boldsymbol{\phi}_{u,1}$ (a,b), $\sigma_1\boldsymbol{\psi}_{u,1}$ (c,d), $\boldsymbol{\phi}_{u,2}$ (e,f), and $\sigma_2\boldsymbol{\psi}_{u,2}$ (g,h) from the strategy described in Section 2.3 (a,c,e,g) and subplots from Figure 2 of Sipp and Marquet (2013), reproduced with permission (b,d,f,h). δ denotes the displacement thickness at $x = 1$. The black curves indicate the local displacement thickness.

upstream of the leading edge in their integrals. Furthermore, the limits of integration are truncated in Equation 2.42 to reflect that the plate is only present from $x \in [0, 1]$ in Sipp and Marquet (2013). The same computational scheme described in Section 2.3 is used with equi-spaced grid points in x. The computational parameters are $N_x = 1400$, $N_y = 151$, $y_{min} = 0.0046$, and $\epsilon_s = 30$.

In Figures 2.2(a-d), the streamwise component of $\boldsymbol{\phi}_1$ and $\sigma_1\boldsymbol{\psi}_1$ are compared with the results from Sipp and Marquet (2013) at $\omega = 60$. The overall structure of the dominant resolvent modes agree well with the published results, despite the difference in the treatment of the boundary conditions. At this frequency, $\boldsymbol{\psi}_1$ is reminiscent of Tollmein-Schlichting waves, sporting the characteristic π phase jump in the wall-normal direction (Schmid and Henningson, 2002; Sipp and Marquet, 2013). The forcing is inclined against the direction of the mean flow field, indicative of the Orr amplification mechanism which amplifies upstream leaning disturbances to downstream leaning responses (Schmid and Henningson, 2002). Furthermore, the

forcing being upstream of the response is indicative of the convective non-normality present in the biglobal operator (Chomaz, 2005; Symon et al., 2018). In fact, this convective non-normality causes a difference between the approach described herein and Sipp and Marquet (2013)—the optimal forcing is able to start slightly further upstream in the latter. As mentioned earlier, the base flow in Sipp and Marquet (2013) is over a flat plate from $x \in [0, 1]$ and then flows into a freestream for $x \geq 1$ where the base flow is expected to have less shear because of the lack of a no-slip boundary condition in that region. As a result, their forcing modes are mostly supported in $x \in [0, 1]$ to take advantage of the amplification due to the mean shear. Here, the limits of integration in Equation 2.42 were chosen to only capture the regions where the mean shear is present in the original study. Because the flat plate is assumed to extend across the entire domain in the approach described here, the responses are supported on $x \in [0, 1.25]$. As a result the response modes in this study have more support downstream. Despite the differences in the base flow, the truncated domain, and sponge applied, the optimal modes identified compare well with the published results.

In Figure 2.2(e-g), the second leading modes are compared. The secondary modes, $\boldsymbol{\phi}_2$ and $\boldsymbol{\psi}_2$, also demonstrate behavior in line with the Orr-amplification mechanism exemplified in the upstream tilt of the forcing. The secondary modes demonstrate two wavepacket-like structures in the streamwise direction and, though not shown here, higher order $\boldsymbol{\psi}_j$ and $\boldsymbol{\phi}_j$ demonstrate j wavepacket-like structures. This behavior is a consequence of the finite streamwise domain coupled with the orthogonality constraints in the modes. Because of the extra shear in $x \geq 1$, the sub-optimal forcing modes have more downstream support. As a result, the two wavepacket structures are longer and further downstream for both $\psi_{u,2}$ and $\phi_{u,2}$ in this study than in the published results. Despite this difference in streamwise amplitudes, the modes once again identify similar structures with the response modes having Tollmien-Schlichting-like structure.

Now, the energy densities,

$$e_{u,i}(\omega, x) = \int_0^{y_{max}} \sigma_i^2(\omega) \left(\left| \psi_{u,i}(x, y; \omega) \right|^2 + \left| \psi_{v,i}(x, y; \omega) \right|^2 \right) dy, \tag{2.44}$$

and

$$e_{f,i}(\omega, x) = \int_0^{y_{max}} \left(\left| \phi_{u,i}(x, y; \omega) \right|^2 + \left| \phi_{v,i}(x, y; \omega) \right|^2 \right) dy, \tag{2.45}$$

are compared for the modes plotted in Figure 2.2 with the published results in Figure 2.3. The $e_{u,i}$ and $e_{f,i}$ agree quite well, despite the differences in the approaches.

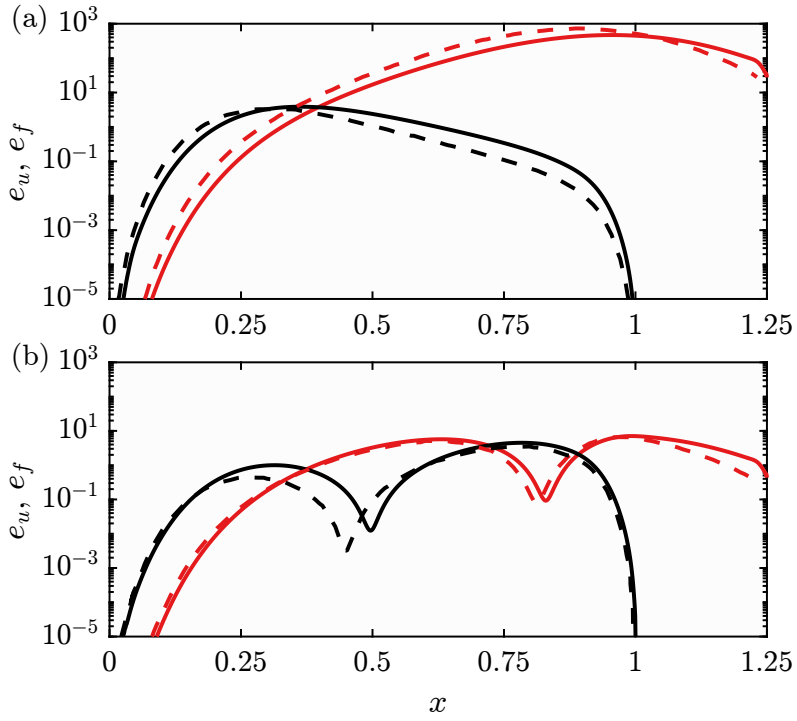

Figure 2.3: $e_{u,1}(60, x)$ (red) and $e_{f,1}(60, x)$ (black) (a) and $e_{u,2}(60, x)$ (red) and $e_{f,2}(60, x)$ (black) (b). The solid lines are computed with the approach described herein while the dashed lines are extracted from Sipp and Marquet (2013).

One difference alluded to earlier is that $\boldsymbol{\phi}_1$ and $\boldsymbol{\phi}_2$ can begin further upstream in the published results because of the large shear caused by the leading edge that is not included in the domain of the approach described herein. The published $e_{f,1}$ reaches its largest amplitude slightly upstream of the results using the approach described herein. This is also true for the local minima of $e_{f,2}$. Due to the differences in $\boldsymbol{\phi}_i$, $\boldsymbol{\psi}_i$ also has more support slightly upstream in the published results. Despite these differences, there is good agreement in the identified $e_{u,i}$ and $e_{f,i}$ for $\omega = 60$ using a different base flow and boundary conditions.

Now, contours of $e_{u,1}(\omega, x)$ and $e_{f,1}(\omega, x)$ are are plotted over $F = \omega \times 10^5/Re$ and $Re_\delta(x) = 1.72\sqrt{x/Re}$ in Figure 2.4. The comparison between the approach described herein and Sipp and Marquet (2013) is striking for e_f. Although the amplitudes of the response modes and linear amplification can not be matched exactly because of the differences with regard to the leading edge, base flow, and truncation of the domain, the structure of e_u agrees well with the published results, capturing the increased amplitude in the downstream direction for only $F < 120$ and agreement in the locations of the maximum e_u and e_f. As F increases, the forcing becomes concentrated near the upstream region in both analyses. This then

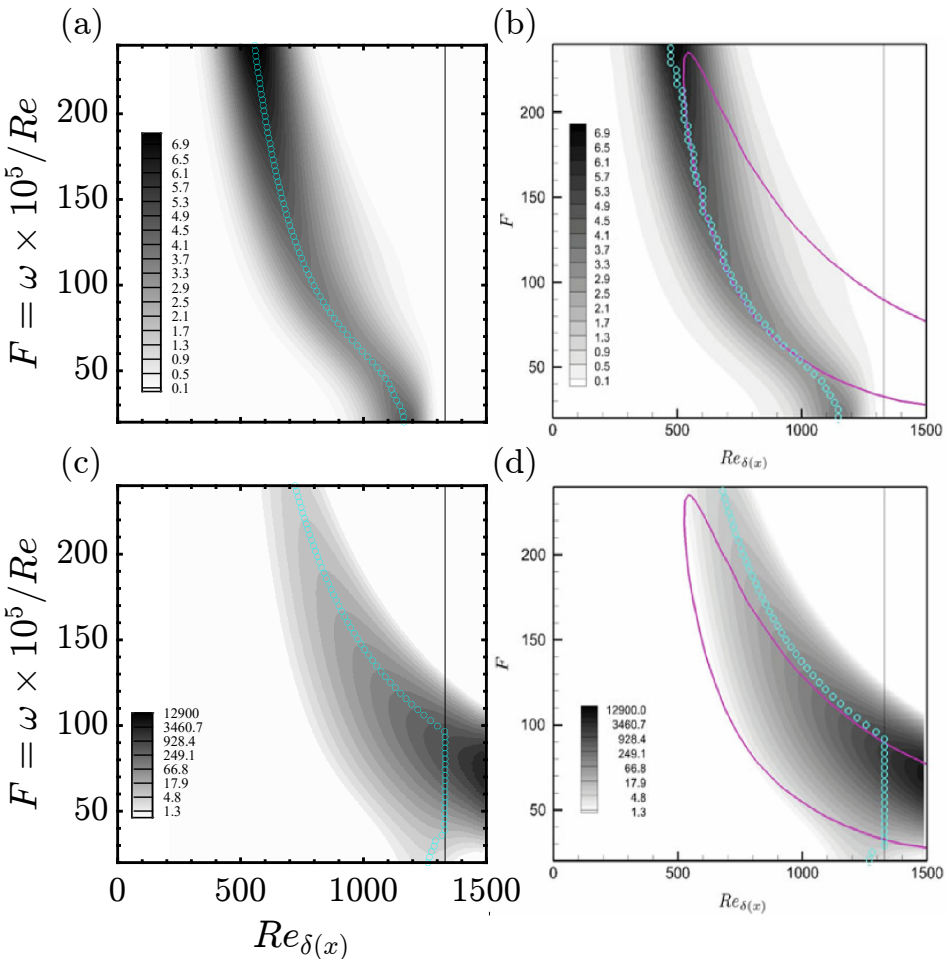

Figure 2.4: Isocontours of $e_f(F, Re_\delta(x))$ (a,b) and $e_u(F, Re_\delta(x))$ (c,d) of the strategy described in Section 2.3 (a,c) and subplots from Figure 3 of Sipp and Marquet (2013), reproduced with permission (b,d). The cyan circles denote the maximum energy density in $x \in [0, 1]$ and vertical black lines denote $x = 1$. The magenta curve in (b,d) denotes the neutral stability curve.

leads the response modes to have support further upstream with increased F. It is expected that the higher frequency modes may agree better than the modes plotted in Figure 2.2 because their energy is concentrated withing the domain, away from the inlet and outlet.

Finally, $\sigma_1(\omega)$ and $\sigma)_2(\omega)$ are plotted over F in Figure 2.5 along with the published results. The differences in σ_1 may be attributed to the differences in the base flows. The approach described herein does not incorporate the large-shear region near the leading edge. Nonetheless, the two approaches both identify a similar optimal frequency at $F \approx 90$. The σ_2 are closer in amplitude between the two approaches. This is likely because of the orthogonality constraints—since $\boldsymbol{\phi}_1$ takes advantage

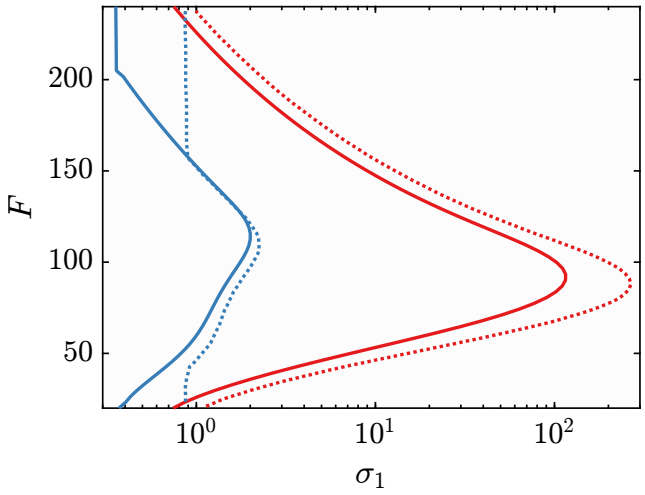

Figure 2.5: $\sigma_1(F)$ (red) and $\sigma_2(F)$ (blue) using the approach described herein (solid line) and the results of Sipp and Marquet (2013) (dotted lines).

of forcing near the leading edge, $\boldsymbol{\phi}_2$ must be supported downstream within the boundary layer where the two base flows agree. They are both also able to identify a local maxima with a larger frequency than the local maxima of σ_1. Despite the differences in the approaches, the approach described herein can identify similar amplification mechanisms, as evidenced by the forcing and response mode structure and the most amplified frequencies.

Verification of 3D streaks

To validate the results with modes that model three-dimensional disturbances, comparisons will be made with Sasaki et al. (2022) that considers modes with $k_z > 0$ and $\omega = 0$. The results are nondimensionalized by $L_r = \delta_0^*$, the displacement thickness at the inlet of the domain, and $U_r = U_\infty$ which defines their Re. Their domains extend from $x \in [x_0, x_0 + L_x]$ where x_0 and L_x depend on the Re of interest. Here $Re_x(x) = xU_\infty/\nu$ and $Re_\delta(x) = \delta^*(x)U_\infty/\nu = 1.72\sqrt{Re_x}$ with $Re = Re_\delta(x_0)$. The base flow for the comparisons is the Blasius similarity solution. The wall-normal discretization uses Chebyshev polynomials while the streamwise direction is computed using a parabolic approach which allows spatial marching in x. This neglects ∂_{xx} in the equations since $\omega = 0$ creates long streamwise streaks. Their approach was validated with a biglobal approach like the one described here. Finally the inner products that they consider are

$$\langle \mathbf{a}, \mathbf{b} \rangle_f = \int_{x_0}^{x_0+L_x} \int_0^{y_{max}} \mathbf{a}^* \mathcal{I}_c \mathbf{b} dy dx, \tag{2.46}$$

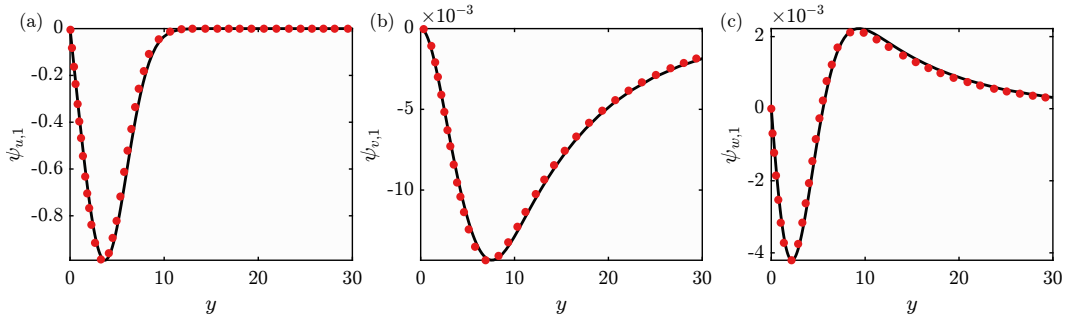

Figure 2.6: Comparison of the real parts of $\boldsymbol{\psi}_1$ for $k_z = 0.1$ at $Re_\delta(x) = 1000$. Red dots denote the results from Sasaki et al. (2022), reproduced with permission, and black lines denote results from the strategy described here.

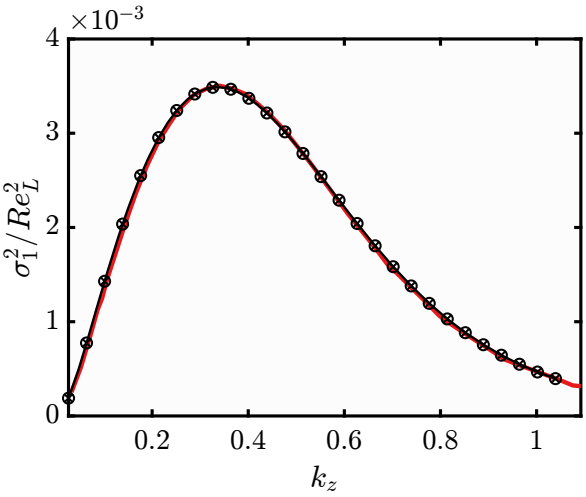

Figure 2.7: Comparison of σ_1^2, normalized by Re_L^2, between the results of Sasaki et al. (2022) in red, reproduced with permission, and the strategy described here in black. The black line, circles, and crosses denote $Re = 1000$, 2000, and 3000.

and

$$\langle \mathbf{a}, \mathbf{b} \rangle_r = \int_{x_0}^{x_0+L_x} \int_0^{\delta_{99}(x)} \mathbf{a}^* \mathcal{I}_c \mathbf{b} dy dx, \tag{2.47}$$

to discourage response modes with freestream support. To compare with their results, the verifications are done with the biglobal approach described herein with SBP finite differences in x and y, and sponge zones applied at the edges of the domain. Apart from the parabolic approach, one difference is the treatment of sponge layers at the inlet and outlet that are not employed in the parabolic approach. Unlike the comparison with Sipp and Marquet (2013), the base flow of Sasaki et al. (2022) does not include the leading edge, like the approach described herein. As a result, the only differences in the approaches are the parabolic approach used in the published results and their wall-normal discretization.

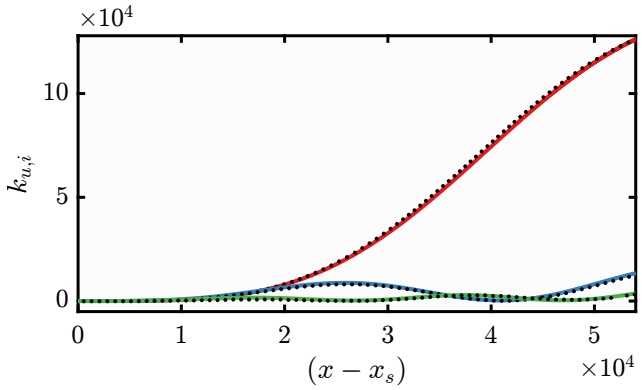

Figure 2.8: Comparison of $k_{u,i}(x)$, between the results of Sasaki et al. (2022) in black dots, reproduced with permission, and the strategy described here in colored lines for $k_z = 0.04$ and $\omega = 0$. The red, blue, and green lines denote $i = 1$, 2, and 3

The following parameters are used in the verification in Figure 2.6: $N_x = 500$, $N_y = 251$, $y_{max} = 60$, $y_{min} = 1.02$, and $\epsilon_s = 30$. The optimal response modes are compared between the approach described here and Sasaki et al. (2022)'s results for $k_z = 0.1$, $\omega = 0$, and $Re = 300$ with $Re_\delta(x_s + L_x) = 1000$. In the approach described here, the $Re_\delta(x_s + L_x) = 1080$ to account for the sponge layers. The response modes from the two strategies show excellent agreement at $Re_\delta(x) = 1000$. Note that although the modes from the published study used the parabolic approach, those modes were validated against the biglobal approach.

In Figure 2.7, the normalized σ_1 are compared between the parabolic approach described in Sasaki et al. (2022) and the approach described here over a sweep of k_z and $Re = 1000$, 2000, and 3000. The domain was chosen as $x/(x_s + L_x) \in [.1, 1]$, where x_s is determined by Re. In the approach described here, the domain is $x/(x_s + L_x) \in [.1, 1.1]$ to account for the sponge zones, which take up 10% of the domain. Here, $N_x = 500$, $N_y = 251$, $y_{max} = 180$, $y_{min} = 1.02$, $\epsilon_s = 300$. Following Sasaki et al. (2022), the σ_1 were found to be self-similar with $Re_L = Re_x(x_s + L_x)$, which is why there is only one line for their results at the different Re in Figure 2.7. The normalized σ_1 agree with the published results, even demonstrating the self-similarity with respect to Re_L. See Chapter 3, Section 3.5 for an explanation of the Re_L scaling. The differences observed in σ_1 are related to the use of sponges that are not used in the parabolic approach.

Finally, in Figure 2.8, the kinetic energy density of the responses,

$$k_{u,i}(x) = \int_0^{y_{max}} \sigma_i^2 \left(\left|\psi_{u,i}(x,y)\right|^2 + \left|\psi_{v,i}(x,y)\right|^2 + \left|\psi_{w,i}(x,y)\right|^2 \right) dy, \tag{2.48}$$

are plotted for $k_z = 0.04$ along with Sasaki et al. (2022)'s results for $i = 1$, 2, and 3. Since their streamwise domain was not reported for this comparison, the streamwise domain and Re was chosen to match the plotted $\delta_{99}(x)$. This lead to $Re = 400$ and $x \in [1, 440.5]$. The streamwise resolution was increased to get an appropriate resolution. This lead to $N_x = 1800$, $N_y = 201$, $\epsilon_s = 300$, $y_{min} = 1$, and $y_{max} = 154.8$. $k_{u,1}$ increases monotonically in x while $k_{u,2}$ and $k_{u,3}$ have 2 and 3 peaks, respectively. The peaks in the higher order $k_{u,i}$ is related to the orthonormality constraint that was also seen in Figure 2.2. Despite the differences in the strategy used to compute the resolvent modes, the agreement is encouraging. Differences in $e_{u,i}$ are likely due to differences in the domains used as well as the sponges at the inlet and outlet of the domains.

2.5 Chapter Summary

The resolvent formulation was described for a general dynamical system, including the discretization approach and Arnoldi iteration to compute the singular value decomposition. The resolvent formulation was then specified for incompressible boundary layers, where the direct and adjoint linear equations were defined for both the parallel flow assumption and the biglobal approach.

The biglobal resolvent approach was then validated against published results. The results for two dimensional disturbances illustrated that the approach described here can identify the linear amplification mechanisms despite the differences at the boundaries and in the base flow. The differences were observed to affect the sub-optimal modes more substantially than the optimal modes. Computing a sweep over ω demonstrated that the energy densities of the forcing and responses were in agreement with Sipp and Marquet (2013). The results were then validated against results for three dimensional streaky disturbances. These results illustrated quantitatively that the response modes and singular values are in agreement with the published results. The self-similarity in the amplifications were also observed, indicating that the resolvent approach described here can reproduce the physics captured in Sasaki et al. (2022). There were differences that are once again related to the use of sponges at the boundaries that are not included in the original studies. These verifications give confidence in the discretization of the linear operators, boundary conditions, and Arnoldi iteration. The biglobal resolvent approach described here will be used in Chapters 3, 4, and 6.

Chapter 3

SCALING OF BIGLOBAL RESOLVENT MODES FOR ZPG TBL

3.1 Introduction

The mean flow field of a ZPG TBL has regions of self-similarity in different wall-normal regions of the flow. Each of these regions have their associated length and velocity scales. These scalings generate the classical law of the wall and the law of the wake that are valid in the near-wall region of the flow and in the outer region, respectively (Coles, 1956). The mean flow field is traditionally characterized into four layers, the viscous layer, buffer layer, log layer, and wake layer, where viscous scaling holds in the first two, outer scaling holds in the latter, and the log layer is an overlap layer where both scalings hold. Using a mean momentum balance, the RANS equation reveals four distinct layers characterized by a balance of two or three of its terms (Wei, Fife, et al., 2005). These terms correspond to the viscous stresses, Reynolds stresses, and advection terms. In the mesolayer, where all three terms are balanced $\left(y^+ \in \left[1.6\sqrt{Re_\tau}, 2.6\sqrt{Re_\tau}\right]\right)$, a mixed length scale, $\ell_m = \sqrt{\ell_\nu \delta_{99}}$, emerges that makes the RANS equations independent of Re (Afzal, 1984). Although this length scale is based on the dynamics of the flow, it does not collapse the mean flow field, though it makes $\ell_m \partial_y \overline{U}^+ \sim O(1)$ in the mesolayer region.

Since the resolvent operator is defined with the mean flow field, it is natural to examine how self-similarity of the mean flow field extends to the resolvent amplification and resolvent modes. Moarref, Sharma, et al. (2013) finds scaling for the local resolvent modes based on the critical layer location, which anchors the modes to specific self-similar regions of $\overline{U}$. In the local analysis, the critical layer location can be predicted *a priori* by specifying a streamwise wavenumber and temporal frequency that specifies the wavespeed.

Since a streamwise wavenumber is not specified in the biglobal analysis, the wavespeed and critical layer location of the biglobal resolvent modes can not be specified either. In order to determine scaling relationships that lead to biglobal resolvent modes, the wall-normal support of said modes needs to be appropriately predicted. Here, the wall-normal support of the biglobal resolvent modes is predicted by balancing linear amplification mechanisms related to the lift-up effect, which amplifies near-wall modes, and the convection, which amplifies large scale

modes. Since the mean flow field develops in the streamwise direction, modifications are made to the biglobal resolvent operator that can account for the streamwise development of the length and velocity scales that evolve with the mean flow field.

In Section 3.2, the results of Moarref, Sharma, et al. (2013) are first discussed to illustrate how the streamwise and spanwise wavenumbers and temporal frequencies need to scale to admit self-similar local resolvent modes. In Section 3.3, it shown that the spanwise wavenumber can specify the wall-normal support of the biglobal resolvent by strengthening or weakening the linear amplification from the lift-up effect. In Section 3.4, scalings are presented for the spanwise wavenumbers and temporal frequencies that admit self-similar biglobal resolvent modes for a general self-similar mean flow field. Modifications to the biglobal resolvent operator are also presented to demonstrate how the streamwise varying velocity and length scales are incorporated. In Sections 3.5, 3.6, 3.7, and 3.8, the biglobal scaling is applied to the laminar boundary layer and the inner layer, mesolayer, and outer layer of the ZPG TBL, respectively. Finally, conclusions are presented in Section 3.9.

3.2 Generalization of Local Scaling Results

In this chapter, all the derivations are done with dimensional quantities to identify the physical scales that achieve self-similarity. All the terms in Equation 2.33 will denote dimensional quantities so that the Re is replaced by $1/\nu$. In this section, the scalings of Moarref, Sharma, et al. (2013) are summarized in a general form so that the scaling arguments can be extended to the biglobal operator in Section 3.4. The general form of the 1D scaling is applied to a novel scaling for the APG TBL in Section 4.2 (Wei and Knopp, 2023). Since the geometric scaling of Moarref, Sharma, et al. (2013) relies on specified wall-normal locations that do not have a counterpart in the biglobal operator, the geometric scaling is omitted. The parallel flow assumption of Section 2.3 is invoked. It is assumed that there exists physical scales such that

$$\eta = \frac{y - y_d}{y_s}, \qquad f(\eta) = \frac{\overline{U}(y) - U_d}{U_s}, \tag{3.1}$$

where y_d denotes an offset wall-normal distance, y_s is the velocity scale, U_d is a velocity offset, and U_s is a velocity scale. The general form of Equation 3.1 is inspired by the scaling studied in Wei and Knopp (2023) for adverse pressure gradients, though it can relate to traditional scalings in canonical flows (Coles, 1956). For example, η denotes y^+ if $y_d = 0$ and $y_s = \ell_\nu$ for the near-wall viscous

scaling or f can denote the velocity-defect as in Equation 1.4 if $U_d = U_e$ and $U_s = u_\tau$ for the outer region.

A Reynolds number is introduced as $Re_s = y_s U_s/\nu$, based on the mean velocity profile's scalings. The scaling for the streamwise wavenumber, spanwise wavenumber, and wavespeed are

$$k_x = \frac{\alpha}{x_s}, \quad k_z = \frac{\zeta}{z_s}, \quad c = u_s f_c + u_d, \tag{3.2}$$

where x_s and z_s denote streamwise and spanwise length scales, α and ζ denote nondimensionalized streamwise and spanwise wavenumbers, and f_c is the nondimensionalized wavespeed. The wavespeed is chosen such that the critical layer is fixed at η_c, in the nondimensional coordinates. The temporal frequency is then $\omega = ck_x = u_s/x_s(f_c + u_d/u_s)\alpha = u_s/x_s\tilde{\omega}$, where $\tilde{\omega}$ is the nondimensional frequency. In general, $\tilde{\omega}$ is Re dependent because of the possible Re dependence on u_d/u_s while α, ζ, and f_c are Re independent constants.

It is assumed that the optimal response modes are streak-like streamwise fluctuations where $|\widehat{u}| \gg |\widehat{v}|, |\widehat{w}| \gg |\widehat{p}|/u_s$ and $k_x \ll k_z, 1/y_s$. The pressure components can be assumed to be small compared to the velocity components and thus negligible. These response modes are assumed to be forced with wall-normal and spanwise components such that $\left|\widehat{f_v}\right|, \left|\widehat{f_w}\right| \gg \left|\widehat{f_u}\right|$, and $O\left(\left|\widehat{f_v}\right|\right) \sim O\left(\left|\widehat{f_w}\right|\right)$ (Jovanović and Bamieh, 2005).

As discussed in Section 2.3, the adjoint equation constrains the forcing modes to be solenoidal because of the incompressibility constraint on $\widehat{\mathbf{u}}$. In addition, Rosenberg (2018) had shown that the irrotational component of the forcing can be lumped into the pressure term in the LNSE. When the Orr-Sommerfeld Squire (OSS) equations are derived, the pressure terms are eliminated by using the divergence free constraint on the velocity (Schmid and Henningson, 2002). As a result, only solenoidal forcing can amplify $\widehat{\mathbf{u}}$ and increase the kinetic energy. A relationship between y_s and z_s is found by respecting the divergence-free constraint on the optimal forcing modes and neglecting the $ik_x\widehat{f_u}$ term,

$$ik_x\widehat{f_u} + \partial_y\widehat{f_v} + ik_z\widehat{f_w} = 0 \sim \frac{1}{y_s}\partial_\eta\widehat{f_v} + \frac{i\zeta}{z_s}\widehat{f_w}. \tag{3.3}$$

In order for the leading terms of the divergence-free constraint to balance, $z_s = y_s$. To determine the scaling for x_s, scaling arguments for the LNSE must be made. Neglecting the pressure component, it is required that the advective term,

$\left(-i\omega + ik_x\overline{U}\right)$, scales with the viscous term, $\nu\widehat{\nabla}^2$, to balance the singularity at the critical layer. Introducing the nondimensionalizations and neglecting the k_x^2 term in the viscous term, one finds that

$$-i\frac{u_s}{x_s}(f_c - f)\alpha \sim \frac{\nu}{y_s^2}\left(\partial_{\eta\eta} - \zeta^2\right). \tag{3.4}$$

In order for these two terms to balance, $x_s = y_s^2 u_s/\nu = y_s Re_s$. From this relationship, Re_s can be considered a ratio between x_s and y_s or a ratio between the shear, u_s/y_s, and the advection, u_s/x_s. Finally, due to the normalization constraint on the resolvent modes, $\boldsymbol{\psi}$ and $\boldsymbol{\phi}$ must scale with $y_s^{-1/2}$.

Using the identified scales, the scaling of the LNSE follows

$$\mathcal{L} \sim \frac{\nu}{y_s^2}\begin{bmatrix} a_{1,1} & Re_s f & 0 & \alpha \\ 0 & a_{1,1} & 0 & Re_s a_{2,4} \\ 0 & 0 & a_{1,1} & Re_s\zeta \\ \alpha & Re_s a_{2,4} & Re_s\zeta & 0 \end{bmatrix}, \tag{3.5}$$

where $a_{i,j}$, f, α, and ζ are independent of Re. The variables $a_{i,j}$ account for the derivatives, mean flow, and the nondimensional wavenumbers or frequencies. If $Re_s = 1$ as in the case of viscous scaling, $\mathcal{L} \sim \nu/y_s^2$ such that $\mathcal{R} \sim y_s^2/\nu$. In the case where $Re \gg 1$, the resolvent operator scales as

$$\mathcal{R} \sim \frac{y_s^2 Re_s}{\nu}\begin{bmatrix} \chi_{1,1}Re_s^{-1} & \chi_{1,2} & \chi_{1,3} & 0 \\ \chi_{2,1}Re_s^{-2} & \chi_{2,2}Re_s^{-1} & \chi_{2,3}Re_s^{-1} & 0 \\ \chi_{3,1}Re_s^{-2} & \chi_{3,2}Re_s^{-1} & \chi_{3,3}Re_s^{-1} & 0 \\ \chi_{4,1}Re_s^{-2} & \chi_{4,2}Re_s^{-2} & \chi_{4,3}Re_s^{-2} & 0 \end{bmatrix}, \tag{3.6}$$

where $\chi_{i,j}$ are coefficients that are once again independent of Re. Hence, $\|\mathcal{R}\| \sim y_s^2 Re_s/\nu$. From Equation 3.6, the optimal response components scale as $|\widehat{u}|/u_s \sim O(1)$, $|\widehat{v}|/u_s \sim O\left(Re_s^{-1}\right)$, $|\widehat{w}|/u_s \sim O\left(Re_s^{-1}\right)$, and $|\widehat{p}|/u_s^2 \sim O\left(Re_s^{-2}\right)$. Similarly, looking at the adjoint of Equation 3.6, the optimal forcing components scale as $\left|\widehat{f_u}\right|/u_s \sim O\left(Re_s^{-1}\right)$, $\left|\widehat{f_v}\right|/u_s \sim O(1)$, and $\left|\widehat{f_w}\right|/u_s \sim O(1)$. This is consistent with the initial assumptions made.

$\boldsymbol{\psi}_i$ and $\boldsymbol{\phi}_i$ are nondimensionalized as

$$\tilde{\psi}_{u,i} = \sqrt{y_s}\psi_{u,i}, \qquad \tilde{\psi}_{v,i} = \sqrt{y_s}Re_s\psi_{v,i}, \qquad \tilde{\psi}_{w,i} = \sqrt{y_s}Re_s\psi_{w,i}, \tag{3.7}$$

and

$$\tilde{\phi}_{u,i} = \sqrt{y_s}Re_s\phi_{u,i}, \qquad \tilde{\phi}_{v,i} = \sqrt{y_s}\phi_{v,i}, \qquad \tilde{\phi}_{w,i} = \sqrt{y_s}\phi_{w,i}, \tag{3.8}$$

Case	y_s	U_s	U_d	Re_s	f_c	x_s
Inner	ℓ_ν	u_τ	0	1	$f_c \lesssim 16$	ℓ_ν
Mesolayer	ℓ_m	u_τ	0	$\sqrt{Re_\tau}$	$\left\|\overline{U}^+(y_{ML}) - f_c\right\| \lesssim 1$	δ_{99}
Outer	δ_{99}	u_τ	U_e	Re_τ	$-6.5 < f_c < 0$	$\delta_{99}Re_\tau$
Blasius	δ	U_∞	0	$\sqrt{Re_x}$	$f_c \in (0, 1)$	x

Table 3.1: Length scales and wavespeed range for the different regions of self-similarity for the ZPG TBL and the laminar flow. Here $y_{ML} \approx 2\sqrt{\delta_{99}\ell_\nu}$ and $y_d = 0$ for all cases.

such that $\tilde{\boldsymbol{\psi}}_i$ and $\tilde{\boldsymbol{\phi}}_i$ are Re-independent. σ_i is also nondimensionalized to be Re-independent as

$$\widetilde{\sigma} = \sigma \frac{\nu}{y_s^2 Re_s}. \tag{3.9}$$

Note that in the case where $Re_s = 1$, the Re-independence holds so long as the response and forcing modes are supported where the mean flow field is self-similar. Otherwise, the Re-Independence can only hold if $Re_s \gg 1$, since the conditions for self-similarity require the shear driven amplification to be dominant.

The local scaling is now presented for some representative parameters. The same grid is used for all the results where $N_y = 601$ points are used to resolve the near-wall region with $y_{max} = 3\delta_{99}$ and $y_{min} = .01\delta_{99}$. Although this grid does not ensure DNS resolution since the grid spacing, Δy, scales with outer units far from the wall, the structures in the outer region are expected to be resolved since they too scale with the outer length scale. The Monkewitz composite profile is used as the mean flow field to test flow fields with large Re_τ. Although this is a modeled flow, it uses asymptotic expansions inline with the canonical scalings of mean velocity profile that are predicted to hold asymptotically for large Re and is fitted to experimental results (Monkewitz, Chauhan, and Nagib, 2007). The Re_τ are chosen as 10 equispaced values of $Re_\tau \in [2000, 10000]$, ensuring a decade of Re_τ. The scales for the inner, mesolayer, and outer scaling are categorized in Table 3.1.

The scaling is shown for some characteristic modes in Figures 3.1, 3.2, and 3.3. In these plots, the top row plots $|\psi|_1$ nondimensionalized using $\sqrt{\delta_{99}}$ while the bottom row plots the modes nondimensionalized with the scaling in Equation 3.7. In Figure 3.1, the inner scaling is demonstrated using $\alpha = 2\pi/1000$, $\zeta = 2\pi/100$, and $f_c = 10$ which models the energetic structures in the near-wall cycle. Since $Re_s = 1$, all components of $\boldsymbol{\psi}_1$ are self-similar when nondimensionalized by $\sqrt{\ell_\nu}$.

For the mesolayer scaling results plotted in Figure 3.2, $\alpha = 2\pi/6$ and $\zeta = 2\pi/45$,

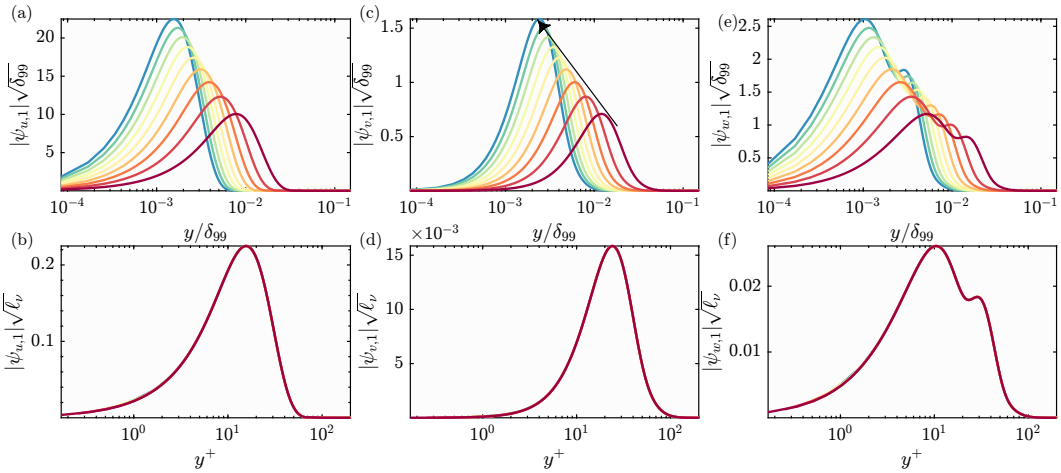

Figure 3.1: $|\psi_{u,1}|$ (a,b), $|\psi_{v,1}|$ (c,d), and $|\psi_{w,1}|$ (e,f) nondimensionalized using outer units (a,c,e) and the self-similar inner units (b,d,f). The black arrow denotes the direction of increasing Re_τ. Each colored line has Re_τ incrementing by 1000, with blue denoting $Re_\tau = 10000$ and red denoting $Re_\tau = 2000$.

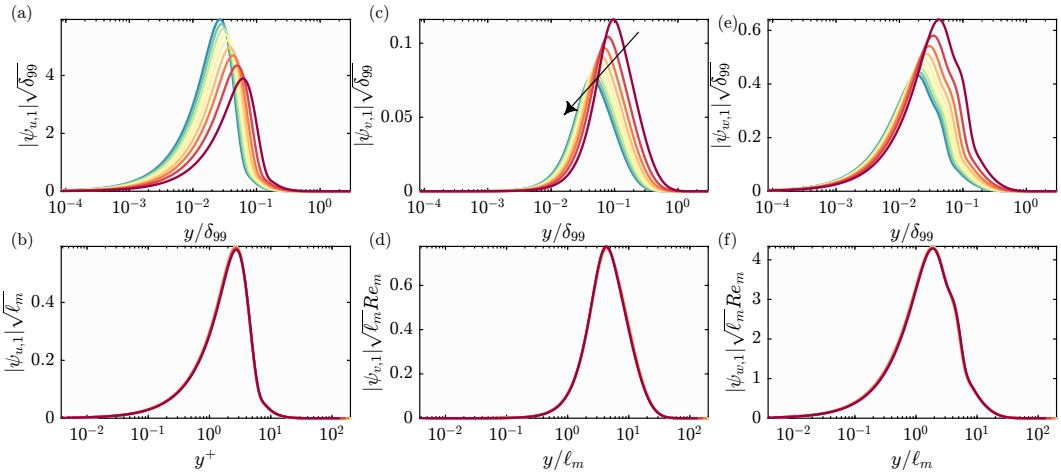

Figure 3.2: $|\psi_{u,1}|$ (a,b), $|\psi_{v,1}|$ (c,d), and $|\psi_{w,1}|$ (e,f) nondimensionalized using outer units (a,c,e) and the self-similar mesolayer units (b,d,f). The black arrow denotes the direction of increasing Re_τ. Each colored line has Re_τ incrementing by 1000, with blue denoting $Re_\tau = 10000$ and red denoting $Re_\tau = 2000$.

which makes the streamwise wavelength $O(6\delta_{99})$ and spanwise wavelength $O(\delta_{99})$. The dimensions of these modes are similar to the length scales of a VLSM, and $f_c = \overline{U}^+(2.2\ell_m)$ is chosen to center the modes near the start of the log layer (Marušić, Monty, et al., 2013). Finally, for the outer region, modes with $\alpha = 2\pi Re_{\tau,min}/6$, $\zeta = 2\pi$, and $f_c = -6$ are plotted in Figure 3.3. The prefactor of $Re_{\tau,min} = 2000$ is included to balance the Re_τ in x_s so that $\lambda_x \sim O(10\delta_{99})$. In dimensional variables, these outer scaled modes have $\lambda_x \in (6, 30)\delta_{99}$ and $\lambda_z = \delta_{99}$, which are long streaks.

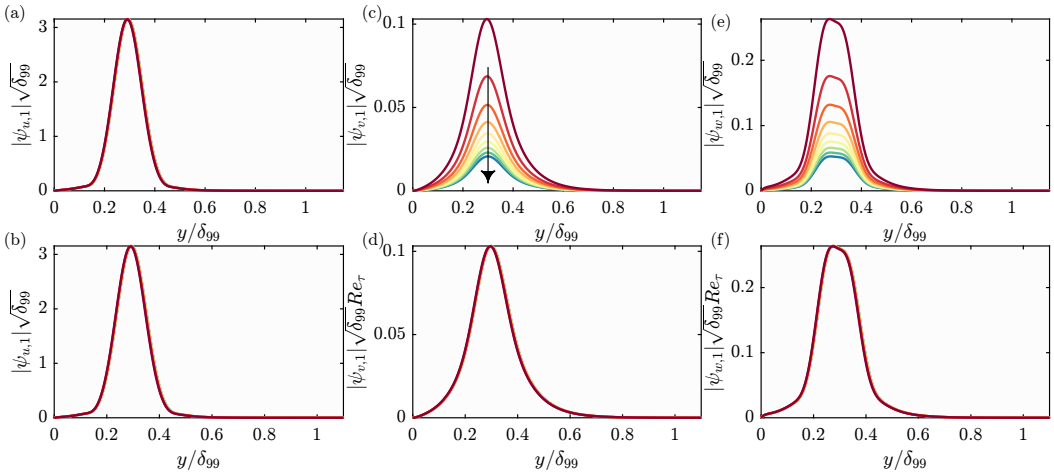

Figure 3.3: $|\psi_{u,1}|$ (a,b), $|\psi_{v,1}|$ (c,d), and $|\psi_{w,1}|$ (e,f) nondimensionalized using outer units (a,c,e) and the self-similar outer units (b,d,f). The black arrow denotes the direction of increasing Re_τ. Each colored line has Re_τ incrementing by 1000, with blue denoting $Re_\tau = 10000$ and red denoting $Re_\tau = 2000$.

Unlike the inner scaled modes, the mesolayer and outer scaled modes require an Re_s-dependent nondimensionalization for the transverse components to ensure self-similarity. The modes plotted in Figures 3.1, 3.2, and 3.3 all exhibit Re-independence when plotted using the nondimensionalization described in Equation 3.7 since these modes have specified critical layers in the appropriate self-similar regions of $\overline{U}$.

3.3 Predicting the Wall-Normal Support of the Biglobal Resolvent Modes

Before discussing the self-similarity in the biglobal modes, it must be discussed how the wall-normal support of the biglobal modes can be predicted. As illustrated in Section 2.3, the wall-normal location of the local resolvent modes are specified *a priori* by taking advantage of the singularity at the critical layer. Since k_x is not a parameter in the biglobal resolvent operator, the critical layer location can not be specified. The wall-normal support of the biglobal resolvent modes can only depend on ω and k_z for a given $\overline{\mathbf{U}}$ and fixed domain. Here, it will be shown that k_z determines the wall-normal support of the modes while ω influences the streamwise length scale of the modes.

For these arguments, the thin boundary layer assumptions will be made such that $\overline{U} \sim O(U_\infty)$, x derivatives and y derivatives of the mean flow scale as $\partial_x \sim O\left(L^{-1}\right)$, $\partial_y \sim O\left(\delta^{-1}\right)$, respectively, and gradients of $\widehat{\mathbf{q}}$ scale as $O\left(y_s^{-1}\right)$. Due to mass conservation, $\overline{V} \sim O\left(U_\infty \delta L^{-1}\right)$. It is assumed that $\delta/L = \epsilon \ll 1$ and $y_s/\delta \lesssim 1$. By reducing Equation 2.38 to the biglobal Orr-Sommerfeld-Squire (OSS) form as in

Ran et al. (2019) and neglecting terms of $O(\epsilon)$, one finds that

$$\begin{bmatrix} \mathcal{L}_{OS} + s(x) & 0 \\ ik_z\overline{U}_y & \mathcal{L}_{SQ} + s(x) \end{bmatrix} \begin{bmatrix} \widehat{v} \\ \widehat{\omega}_2 \end{bmatrix} = \begin{bmatrix} \widehat{f}_v \\ \widehat{f}_2 \end{bmatrix}, \tag{3.10}$$

where $\widehat{\omega}_2 = ik_z\widehat{u} - \partial_x\widehat{w}$, $\widehat{f}_2 = ik_z\widehat{f}_u - \partial_x\widehat{f}_w$, $\mathcal{L}_{OS} = \widehat{\nabla}^{-2}\mathcal{L}_{SQ}\widehat{\nabla}^2 - \nabla^{-2}\overline{U}_{yy}\partial_x$, and $\mathcal{L}_{SQ} = \left(-i\omega + \overline{U}\partial_x - \nu\widehat{\nabla}^2\right)$. See Appendix C for an explicit description of the full OSS formulation, or Ran et al. (2019) for the OSS formulation using the thin boundary layer assumptions.. Note that Equation 3.10 assumes that $\boldsymbol{\nabla}\cdot\widehat{\mathbf{f}} = 0$ as this discussion is tailored to finding optimal forcing modes. This reduced form of the OSS equations is equivalent to assuming a parallel mean flow, $\overline{\mathbf{U}} = \overline{U}(y)\mathbf{e}_x$.

Although Equation 3.10 ignores the nonparallel terms of $O(\epsilon)$ in the ZPG TBL, it captures the essential features of the full flow such as the advection, viscous dissipation, and mean shear without imposing a streamwise wavenumber on the response and forcing modes. The wall-normal boundary conditions are $\widehat{v} = 0, \partial_y\widehat{v} = 0, \widehat{\eta} = 0$ at $y = 0, y_{max}$. The inflow and outflow are treated with the sponges, though their effect is omitted for the arguments made in this section. Since $\widehat{v}$ is decoupled from $\widehat{\omega}_2$, Equation 3.10 can be solved explicitly as

$$\widehat{v} = \mathcal{L}_{OS}^{-1}\widehat{f}_v, \tag{3.11}$$

$$\widehat{\omega}_2 = \mathcal{L}_{SQ}^{-1}\widehat{f}_2 - ik_z\mathcal{L}_{SQ}^{-1}\overline{U}_y\mathcal{L}_{OS}^{-1}\widehat{f}_v. \tag{3.12}$$

It is assumed that $\overline{U}$ is monotonically increasing and $\partial_y\overline{U}$ is monotonically decreasing in y. By inspecting the mean flow fields for ZPG TBLs, one can neglect $\partial_{yy}\overline{U}$ since $O\left(y_s\partial_{yy}\overline{U}\right) \ll O\left(U_\infty y_s^{-1}\right)$ so that $\mathcal{L}_{OS} \approx \nabla^{-2}\mathcal{L}_{SQ}\nabla^2$, for $[\widehat{v}, \widehat{\omega}_2]$ supported sufficiently far from the wall. Attention will focus on the amplification of $\widehat{\omega}_2$ in Equation 3.12 due to the amplified streamwise response. Using the norm in Equation 2.9, maximizing

$$\widehat{\omega}_2 \approx \mathcal{L}_{SQ}^{-1}\widehat{f}_2 - ik_z\mathcal{L}_{SQ}^{-1}\overline{U}_y\nabla^{-2}\mathcal{L}_{SQ}^{-1}\nabla^2\widehat{f}_v \tag{3.13}$$

will model the amplification due to the full LNSE. The first term is amplified when the advection terms balance the viscous terms. In the second term, the mean shear acts as a weighting function that biases the optimal structures to be closer to the wall where $\overline{U}_y$ is large. This bias is related to the non-normality in the LNSE as the lift-up mechanism which amplifies wall-normal disturbances into streamwise components. This effect increases with k_z. If k_z is sufficiently small, the lift-up effect can be neglected and the amplification is due to the first term.

To get a sense of what structures $\mathcal{L}_{SQ}^{-1}$ amplifies, consider

$$\mathcal{L}_{SQ} q = f. \tag{3.14}$$

Finding the unit norm f that maximizes $\|q\|$ is equivalent to finding the unit norm q that minimizes $\|f\|$ (Barthel, Gomez, and McKeon, 2022b). To get a sense for what streamwise length scales minimize $\|f\|$, it will be assumed that $q(x,y) = \widehat{q}(y)\exp(ik_x x)$ and $f(x,y) = \widehat{f}(y)\exp(ik_x x)$, where $\widehat{q}$ and $\widehat{f}$ have a characteristic wall-normal length scale of y_s. It is also assumed that $\overline{U}(y) = \overline{U}(y_c) + \partial_y\overline{U}(y_c)(y-y_c) + \mathcal{O}\Big(\partial_{yy}\overline{U}(y_c)(y-y_c)^2\Big)$, where $\overline{U}(y_c) = \omega/k_x$. Neglecting second order terms, one finds that

$$\mathcal{L}_{SQ}\widehat{q} \approx \left[ik_x\partial_y\overline{U}(y_c)(y-y_c) - \nu\Big(\partial_{yy} - k_x^2 - k_z^2\Big)\right]\widehat{q} \tag{3.15}$$

$$\sim \left[k_x\partial_y\overline{U}(y_c)y_s - \nu/y_s^2\right]\widehat{q}. \tag{3.16}$$

The dependence of k_z^2 and k_x^2 in the viscous terms were ignored since they act as additive constants (Dawson and McKeon, 2019). For the two terms on the right to be of the same order,

$$y_s \sim \left(\frac{\nu\overline{U}(y_c)}{\omega\partial_y\overline{U}(y_c)}\right)^{1/3}, \tag{3.17}$$

where the critical layer approximation, $k_x = \omega/\overline{U}(y_c)$, was used. Since $\mathcal{L}_{SQ} \sim \nu/y_s^2$,

$$\mathcal{L}_{SQ}^{-1} \sim \frac{y_s^2}{\nu} = \frac{\overline{U}(y_c)^{2/3}}{\nu^{1/3}\omega^{2/3}\Big(\partial_y\overline{U}(y_c)\Big)^{2/3}}. \tag{3.18}$$

From Equation 3.18, the amplification of $\mathcal{L}_{SQ}^{-1}$ and y_s increases with y_c. This in turn means that $\mathcal{L}_{SQ}^{-1}$ amplifies modes with smaller k_x. Finally, increased ω increases k_x.

Although the biglobal operator does not support modes of the form $q = \widehat{q}(y)e^{ik_x x}$ because of the boundary conditions and the convective non-normality, similar arguments still hold. The biglobal $\mathcal{L}_{SQ}^{-1}$ amplifies large scale structures in the outer region. Increasing ω decreases the streamwise length-scales of the identified modes, regardless of the wall-normal location of the modes. Increasing k_z increases the role of the amplification due to the mean shear and moves the modes closer to the wall, competing directly with $\mathcal{L}_{SQ}^{-1}$. These large k_z modes have smaller wall-normal extent and are close to the wall to get amplified by the lift-up effect. These modes are expected to have smaller streamwise length-scales. For smaller k_z, the effect of the mean shear is negligible so the resolvent modes will be large scale structures in the outer region of the flow.

Superscript	k_z^+	ω^+
a	$2\pi/120$	$2\pi/294$
b	$2\pi/1200$	$2\pi/294$
c	$2\pi/1200$	$2\pi/98$

Table 3.2: k_z^+ and ω^+ of the modes with the labeled superscripts. Note that the viscous units are defined at the inlet of the computational domains.

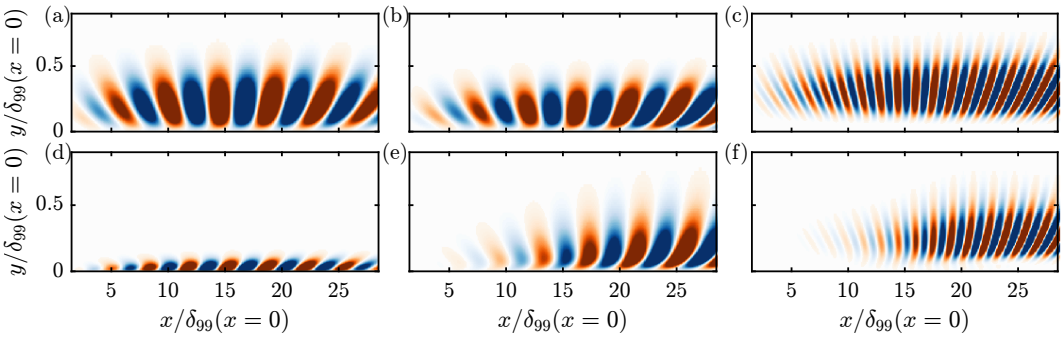

Figure 3.4: Comparison the real parts of ψ^a_{SQ} (a), ψ^b_{SQ} (b), ψ^c_{SQ} (c), $\psi^a_{\omega,1}$ (d), $\psi^b_{\omega,1}$ (e), and $\psi^c_{\omega,1}$ (f).

Note that if $k_z = 0$, the full LNSE amplifies Tollmien-Schlichting-like modes that extend across the entire boundary layer with support in the freestream (Schmid and Henningson, 2002; Sipp and Marquet, 2013). These $k_z = 0$ modes are not captured with the analysis presented here since they are not localized around a critical layer.

To demonstrate how k_z and ω affect the mode structure of the optimal responses, the leading response mode of the full LNSE, ψ_1, is compared with the leading response mode of $\mathcal{L}_{SQ}$, ψ_{SQ}. Specifically, the comparison is made using

$$\psi_{\omega,1} = ik_z\psi_{u,1} - \partial_x\psi_{w,1}, \tag{3.19}$$

the wall-normal vorticity component of ψ_1, sinceψ_{SQ} is the response mode of the first term in Equation 3.12 while $\psi_{\omega,1}$ is governed by Equation 3.12, if the nonparallel terms are ignored. These modes are computed with $Re_\tau = 1200$ and $\Omega_n = [0, 30\delta_{99}(x=0)] \times [0, 3\delta_{99}(x=0)]$.

In Figure 3.4, three representative ψ_{SQ} and $\psi_{\omega,1}$ are plotted with their k_z, ω, and superscript labels defined in Table 3.2. Superscripts a, b, and c denote a small-scale near-wall mode, a large-scale outer-region mode, and a large-scale outer-region mode with smaller streamwise length-scale. In Figures 3.4(a,d), $\psi^a_{\omega,1}$ is closer to the wall, with a smaller streamwise length scale and wall-normal extent than ψ^a_{SQ}. This is related to the increased weight of the mean shear because of the

increased k_z^+. Only considering $\mathcal{L}_{SQ}^{-1}$ will not account for the small-scale modes in the near-wall region as these require shear-driven amplification. For the larger-scale modes in Figures 3.4(b,e), $\psi_{\omega,1}^b$ and ψ_{SQ}^b have similar wall-normal extent, streamwise length-scale, and are both in the outer region of the flow. Since k_z^+ is an order of magnitude smaller, the amplification is mostly due to $\mathcal{L}_{SQ}^{-1}$, which amplifies disturbances in the outer region. For the case with the larger ω^+ in Figures 3.4(c,f), the streamwise length-scale of $\psi_{\omega,1}^c$ and ψ_{SQ}^c is significantly smaller than those from $\psi_{\omega,1}^b$ and ψ_{SQ}^b in Figures 3.4(b,e). This is related to the fact that the modes convect with $\overline{U}$, thus the length scale is proportional to $\omega/\overline{U}$. Despite the similar structure between the response modes of $\mathcal{L}_{SQ}$ and LNSE for the small k_z^+ modes, there are several differences that are not captured in the former. Namely, $\mathcal{L}_{SQ}$ ignores the component wise amplification of wall-normal disturbances to streamwise responses, the generation of Tollmien-Schlichting-like modes from $\mathcal{L}_{OS}$, and nonparallel terms present in the LNSE are all ignored in this analysis.

To summarize this section, unlike the local resolvent modes, the wall-normal position of the biglobal resolvent modes can not be specified *a priori* through a specified wavespeed. The wall-normal position and support of the biglobal resolvent modes will be influenced by k_z where increased k_z generally makes the modes smaller and closer to the wall given the same ω. If k_z is fixed, the streamwise length-scales of the resolvent modes will increase with ω. Note that the wall-normal position of the modes also influences the streamwise length-scale by setting the convective velocity of the modes. As k_z, tends to 0, the modes will resemble Tollmien-Schlichting waves, which extend across the entire boundary layer (Sipp and Marquet, 2013).

3.4 Generalization of Biglobal Scaling Results

To derive the scaling results for the biglobal operator, the nonparallel terms of $\overline{\mathbf{U}}$ are ignored, since the interest is on high *Re* ZPG TBL. As such, it is assumed that $\overline{\mathbf{U}} = U(y)\mathbf{e}_x$. Note that in the actual computations, the full nonparallel mean flow field is used. In the scaling results of (Moarref, Sharma, et al., 2013), the wall-normal location of the modes was set by setting a wavespeed, c, and the scaling of ω was set by the choice of c and the determined k_x scaling. Here, the wall-normal location is set by determining an appropriate k_z that sets the location of the mode in the wall-normal direction. Furthermore, the streamwise structure of the biglobal modes can not be set by directly specifying k_x. Instead, arguments are made for the scaling of ω, which combined with the choice of k_z, can influence the streamwise

structure. Additionally, since the biglobal modes depend on a choice of domain length, L_x, scaling arguments are also presented for L_x. It is assumed that the scaling in Equation 3.1 holds, except that y_s, y_d, U_d, and U_s are slowly varying functions in x such that $d_x y_s, d_x y_d \ll 1$ and $d_x U_s, d_x U_d \ll U_s/y_s$. The scaling of the spanwise wavenumber and temporal frequency are

$$k_z = \frac{\zeta}{y_s}, \qquad \tilde{\omega} = \frac{\omega}{t_s}, \tag{3.20}$$

where t_s denotes a yet to be determined time scale. Finally, the resolvent modes have a streamwise length scale x_s such that $\partial_x \widehat{\mathbf{q}} \sim x_s^{-1}\widehat{\mathbf{q}}$, where $x_s > 2\pi/k_z$ to allow for an elongated structure in the optimal modes. To ensure that enough streamwise wavelengths fit inside the computational domain, the domain length scales proportional to x_s.

To relate t_s to x_s, it is assumed that $t_s^{-1} \sim U_c x_s^{-1}$, where U_c is a convective velocity. In general, $U_c \gtrsim U_s$ as it accounts for any potential defect velocities. Note that $a \gtrsim b$ denotes $O(a) \geq O(b)$. Following similar arguments to Section 3.2, for the advective terms to balance the viscous terms, x_s must scale as

$$x_s \sim \frac{y_s^2 U_c}{\nu} = y_s Re_s \mu, \tag{3.21}$$

where $\mu = U_c/U_s$. This sets $t_s = y_s^2/\nu$, which is ultimately independent of U_c or U_s. The LNSE then scales as

$$\mathcal{L} \sim \frac{\nu}{y_s^2}\begin{bmatrix} O(1) & O(Re_s) & 0 & O(1) \\ 0 & O(1) & 0 & O(Re_s\mu) \\ 0 & 0 & O(1) & O(Re_s\mu) \\ O(1) & O(Re_s\mu) & O(Re_s\mu) & 0 \end{bmatrix}. \tag{3.22}$$

Recall that the nonparallel terms were neglected in this analysis since the length-scale of the streamwise development is larger than the length-scales of the disturbances. The resolvent operator scales as

$$\mathcal{R} \sim \frac{y_s^2 Re_s}{\nu}\begin{bmatrix} O\left(Re_s^{-1}\right) & O(1) & O(1) & 0 \\ O\left(Re_s^{-2}\right) & O\left(Re_s^{-1}\right) & O\left(Re_s^{-1}\right) & 0 \\ O\left(Re_s^{-2}\right) & O\left(Re_s^{-1}\right) & O\left(Re_s^{-1}\right) & 0 \\ O\left(Re_s^{-2}\right) & O\left(Re_s^{-2}\right) & O\left(Re_s^{-2}\right) & 0 \end{bmatrix}, \tag{3.23}$$

where the μ dependence reduces to a constant factor if $\mu = 1$ or $\mu \gg 1$.

The scaling of the biglobal $\mathcal{R}$ in Equation 3.23 is the same as the local scaling, which is expected since the nonparallel terms were neglected in this analysis. Because the

inner product used in Equation 2.41 normalizes with the domain length, the scaling of the response modes, forcing modes, and singular values is the same as in Equations 3.7, 3.8, and 3.9, respectively. However, the modes are able to vary in x unlike the local modes. It is important to note that when $Re_s \neq 1$, the Re_s scaling identified in Equations 3.7, 3.8, and 3.9 requires that $Re_s \gg 1$. The modes that are self-similar are amplified by the mean shear.

The scaling of the response modes requires that $k_z = \zeta/y_s$ and $\omega = \tilde{\omega}\nu/y_s^2$, where ζ and $\tilde{\omega}$ are constants. Because the mean flow field evolves over x, y_s must be a streamwise varying quantity that varies in the streamwise direction, hence both k_z and ω are streamwise varying quantities to account for the evolution of the mean flow field. Equation 2.38 is rederived, except with the assumption that

$$\begin{bmatrix}\mathbf{q}\\ \mathbf{f}\end{bmatrix}(\mathbf{x},t) = \begin{bmatrix}\widehat{\mathbf{q}}\\ \widehat{\mathbf{f}}\end{bmatrix}(x,y)e^{i(-\tilde{\omega}(x)+k_z(x))}. \tag{3.24}$$

The LNSE are now

$$\begin{aligned}-i\omega(x)\widehat{\mathbf{u}} + \left(\boldsymbol{\nabla}\overline{\mathbf{U}}\right)\widehat{\mathbf{u}} + \left(\widehat{\boldsymbol{\nabla}}\widehat{\mathbf{u}}\right)\overline{\mathbf{U}} + \widehat{\boldsymbol{\nabla}}\widehat{p} - \nu\widehat{\nabla}^2\widehat{\mathbf{u}} - i\nu\partial_{xx}[-\omega(x)t + k_z(x)z]\widehat{\mathbf{u}} + \\ i\partial_x[-\omega(x)t + k_z(x)z]\left[\overline{U}\widehat{\mathbf{u}} + \widehat{p}\mathbf{e}_x - 2\nu\partial_x\widehat{\mathbf{u}}\right] + s(x)\widehat{u} = \widehat{\mathbf{f}}\\ \widehat{\boldsymbol{\nabla}}\cdot\widehat{\mathbf{u}} + \partial_x[-\omega(x)t + k_z(x)z]\widehat{u} = 0,\end{aligned} \tag{3.25}$$

where $\widehat{\boldsymbol{\nabla}} = \left(\partial_x, \partial_y, ik_z(x)\right)$ and $\widehat{\nabla}^2 = \partial_{xx} + \partial_{yy} - k_z(x)^2$. Equation 3.25 has a similar form as Equation 2.38, except with streamwise varying k_z and ω and additional terms related to streamwise derivatives of k_z and ω. The additional terms can be neglected since $\partial_x(-\omega(x) + k_z(x)) \sim \partial_x y_s \ll 1$ for a high Re TBL. The governing equations are now

$$\begin{aligned}-i\omega(x)\widehat{\mathbf{u}} + \left(\boldsymbol{\nabla}\overline{\mathbf{U}}\right)\widehat{\mathbf{u}} + \left(\widehat{\boldsymbol{\nabla}}\widehat{\mathbf{u}}\right)\overline{\mathbf{U}} + \widehat{\boldsymbol{\nabla}}\widehat{p} - \nu\widehat{\nabla}^2\widehat{\mathbf{u}} + s(x)\widehat{u} = \widehat{\mathbf{f}}\\ \widehat{\boldsymbol{\nabla}}\cdot\widehat{\mathbf{u}} = 0,\end{aligned} \tag{3.26}$$

which are of the same form as Equation 2.38, except that k_z and ω vary in x to respect the self-similarity in the mean flow field. Results will now be tailored to the laminar scaling and the inner scaling, mesolayer, and outer scaling of the ZPG TBL.

3.5 Self-similar Laminar Scaling of the Biglobal Resolvent Operator

The scaling of the resolvent modes is presented for the Blasius similarity solution. This flow is completely characterized by a single wall-normal length scale, y_s =

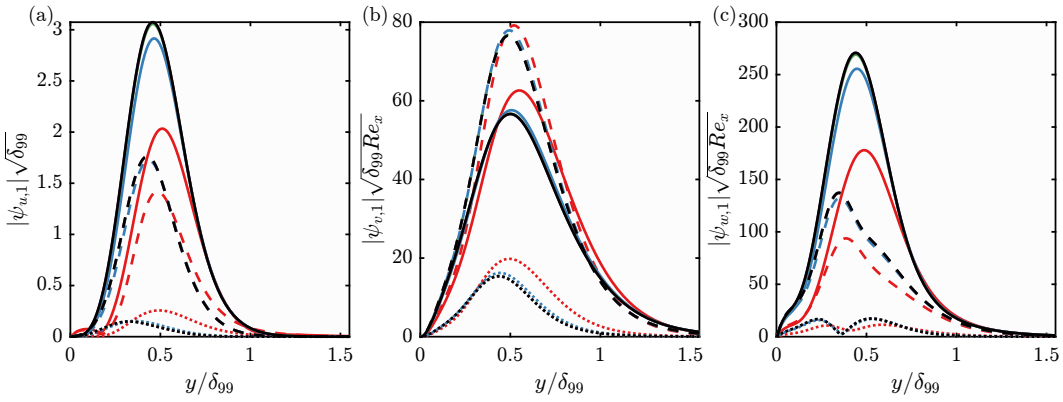

Figure 3.5: Amplitudes of $\psi_{u,1}(x,y)$ (a), $\psi_{v,1}(x,y)$ (b), and $\psi_{w,1}(x,y)$ (c) in the self-similar laminar scaling for $L = .08\delta_{99}Re_L$, $\zeta = 2\pi$ and $\tilde{\omega} = 60$. The dotted, dashed, and solid lines denote $x = 1.1L, 1.25L, 1.4L$. The red, blue, greeen, purple, and black lines denote $Re_L = 10^4, 10^5, 10^6, 10^7$, and 10^8.

$\delta = x/\sqrt{Re_x}$, where x denotes the distance from the leading edge and $Re_x = xU_\infty/\nu$. Note that δ_{99} and δ^* are proportional to δ, so rescaling with either of these length scales would be equivalent, up to a constant factor. The velocity scale is $U_s = U_\infty$, thus $Re_s = \delta U_\infty/\nu = \sqrt{Re_x}$ here. y_d and U_d are both zero for this flow. The scales $x_s = x$ and $t_s = x/U_\infty$ both scale with the distance from the leading edge. This is consistent with the scaling arguments of the spatial coordinates in the Blasius similarity solution. Re_s can be interpreted as a ratio between the time it takes a particle to travel from the leading edge to the point x, t_s, to the characteristic time, y_s/U_s. For the Blasius scaling, the scaling is Re_x dependent and self-similarity is only expected for $Re_x \gg 1$, as described in the previous Section.

The prediction that $\tilde{\sigma}_i = \sigma_i U_\infty/(\delta_{99}Re_L)$ is in agreement with the self-similarity discussed in Sasaki et al. (2022). However, their results focused on modes with $\omega = 0$ whereas here, the scaling is shown to apply for $\omega > 0$. Here, the analysis that identifies the σ_i scaling also identifies scaling for $\boldsymbol{\psi}_i$ and $\boldsymbol{\phi}_i$ while also demonstrating that the scaling requires $Re_L \gg 1$ for the scaling to hold.

To test the scaling, both $\zeta = k_z/\delta$ and $\tilde{\omega} = \omega\delta/U_\infty$ are held constant across the domain. The streamwise domain ranges from $x \in [1, 1.5]L$, where L is the distance from the leading edge to the inlet of the domain and is used to define $Re_L = LU_\infty/\nu$. The Re_L of interest are $Re_L = 10^4, 10^5, 10^6, 10^7$, and 10^8. For these calculations, $N_x = 500$, $N_y = 151$, $y_{max} = 3\delta_{99}$, $y_{min} = .35\delta_{99}$, and $\epsilon_s = 300$.

In Figure 3.5, the amplitudes of $\psi_{u,1}$ $\psi_{v,1}$, and $\psi_{w,1}$ at different streamwise locations are plotted for $\zeta = 2\pi$ and $\tilde{\omega} = 60$ nondimensionalized with the self-similar vari-

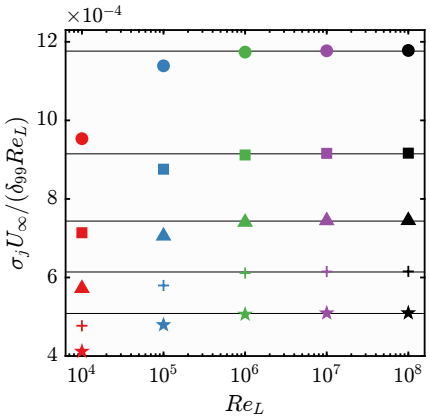

Figure 3.6: The first five σ_j with the self-similar laminar scaling for $L = .08\delta_{99}Re_L$, $\zeta = 2\pi$ and $\tilde{\omega} = 60$. Red, blue, greeen, purple, and black denote $Re_L = 10^4$, 10^5, 10^6, 10^7, 10^8 while the circle, square, triangle, cross, and star denote $j = 1, 2, 3, 4,$ and 5. The horizontal black lines are consant values at σ_j.

ables described in this section. The temporal frequency is large and similar to the frequency studied in Sipp and Marquet (2013). As Re_L increases, the self-similarity improves, as noted by the $Re_L = 10^5$ modes (blue) approaching the $Re_L = 10^8$ modes (black). Furthermore, the $Re_L \geq 10^6$ modes all collapse on top of one another. The Re dependence on the self-similar collapse is seen most clearly in Figure 3.6 where σ_1 is plotted in self-similar variables. σ_1 asymptote to the black horizontal lines as Re_L increases. The $Re_L \leq 10^5$ modes do not exhibit the self-similarity because the scaling requires that $\sqrt{Re_L} \gg 1$ for the Re based scaling to hold. This Re_L dependence is reflected in the local resolvent operator and is not related to the presence of nonparallel terms. Rather, the Re dependence occurs because of the difference in x_s and y_s scaling. Since $Re_L \gg 1$ for the self-similarity to hold, this illustrates that the self-similarity requires amplification due to the shear rather than the convection.

3.6 Inner Scaling of the Biglobal Resolvent Operator

Now the scaling is applied to the ZPG TBL that is characterized by multiscale physics. For the inner region close to the wall, it is assumed that the law of the wall scaling holds for $y \lesssim .15\delta_{99}$. As was discussed in Section 1.1, the mean flow field is self-similar under viscous inner units, $u_s = u_\tau$, $u_s = 0$, $y_s = \ell_\nu = \nu/u_\tau$, and $y_d = 0$ and variables scaled with these coordinates are denoted with + superscripts. The convective velocity scale, $u_c = u_\tau$, because the modes are expected to reside in the near-wall region. Due to the rescaling, $k_z^+ = \zeta = k_z\ell_\nu$ and $\omega^+ = \tilde{\omega} = \omega\nu/u_\tau^2$. Because friction units are used, $Re_s = 1$. This ensures that there is no Reynolds

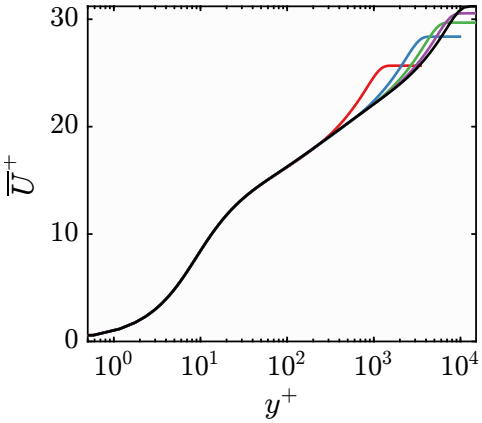

Figure 3.7: Inner scaled mean flow fields with $Re_\tau = 1200$, 3400, 5600, 7800, and 10000 plotted in red, blue, green, purple, and black lines, respectively.

number dependence in the scaling of the response modes, forcing modes, or singular values, provided they are supported in the inner region of the flow. If the modes have support in the outer region of the flow, then the characteristic length and velocity scales of the mean flow field differ. The streamwise domain length is fixed at a constant L_x^+, where the viscous units used for the domain length are defined at the inlet of the domain. In order for the inner scaling to hold, $k_z^+ \lesssim O\left(Re_\tau^{-1}\right)$. If k_z^+ is too small, then the modes will have support in the outer region due to the amplification from $\mathcal{L}_{SQ}^{-1}$ as seen in Figure 3.4.

The inner scaling is first done for scales representative of the near-wall cycle with $k_z^+ = 2\pi/100$ and $\omega^+ = 2\pi/100$ with $L_x^+ = 10000$. This choice of ω^+ is chosen to represent near-wall streaks ($k_x^+ = 2\pi/1000$) convecting in the buffer layer ($u_c^+ = 10$), which were represented in Figure 3.1. The Re_τ at the inlet of the domain spans (1200, 10000) so that a decade in Re_τ is studied. The $N_x = 600$, $N_y = 301$, $\epsilon_s = 30$, $y_{max}^+ = 3Re_\tau$, and $y_{min}^+ = 200$ to resolve the near-wall region, where the modes are expected to reside. The mean flow fields are computed using the Monkewitz composite profile (Monkewitz, Chauhan, and Nagib, 2007). The inlet $\overline{U}^+$ is plotted in Figure 3.7 for reference. The inner scaling in $\overline{U}$ holds up to $y^+ \sim 300$. Modes that extend past $y^+ \sim 300$ are not expected to be self-similar using inner scaling for this Re_τ range.

In Figure 3.8, $\left|\psi_{u,1}(x,y)\right|$ is plotted in outer and inner scaled coordinates at $x = .2L_x$, $.5L_x$, $.8L_x$ for all the Re_τ and $\overline{U}^+$ is plotted for reference. The resolvent modes illustrate that the streamwise evolution of these modes is self-similar across the different Re_τ. In Figure 3.9(a), $\sigma_j U_\infty/\delta_{99}$ are shown to grow linearly with ν/u_τ^2,

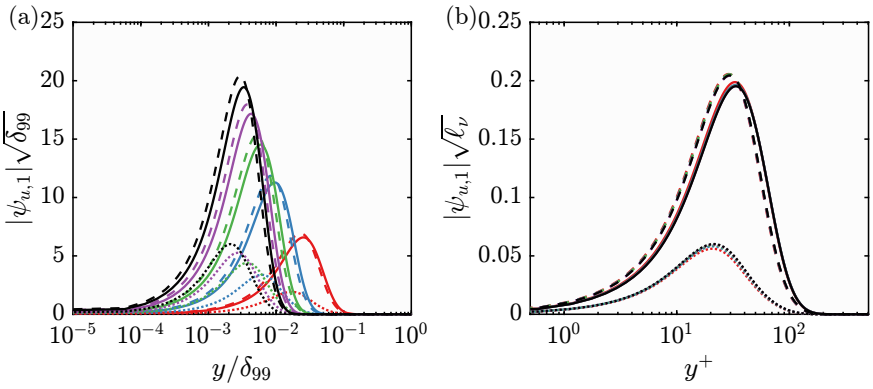

Figure 3.8: $|\psi_{u,1}|$ in outer (a) and inner (b) units for $L_x^+ = 10000$, $k_z^+ = 2\pi/100$ and $\omega^+ = 2\pi/100$. Red, blue, green, purple, and black denote $Re_\tau = 1200$, 3400, 5600, 7800, and 10000, respectively. The dotted, dashed, and solid lines denote $x = .2L_x$, $.5L_x$, $.8L_x$.

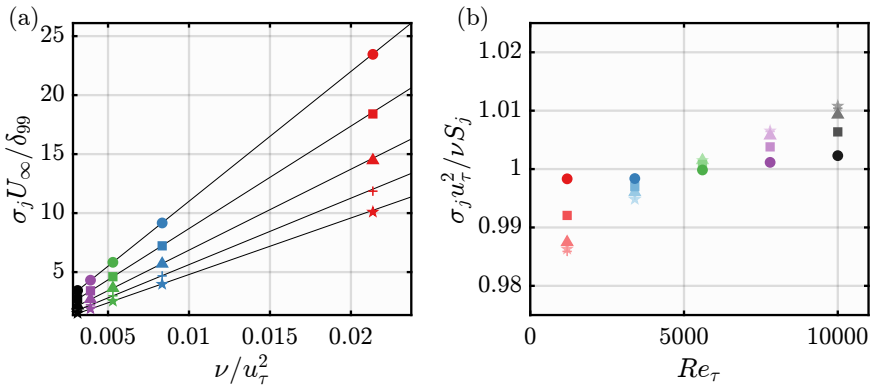

Figure 3.9: σ_j in outer units with the black lines denoting $S_j\nu/u_\tau^2$ (a) and σ_j in inner units, normalized by S_j (b) for $L_x^+ = 10000$, $k_z^+ = 2\pi/100$ and $\omega^+ = 2\pi/100$. The circle, square, triangle, cross, and star denote $j = 1, 2, 3, 4$, and 5, respectively. The colors are the same as in Figure 3.8.

with slopes, S_j, that are constants independent of Re_τ. In Figure 3.9(b), $\sigma_j u_\tau^2/\nu$ is plotted and normalized by S_j, showing that $\sigma_1 u_\tau^2/\nu$ is independent of Re_τ. As j increases, $\sigma_j u_\tau^2/\nu$ shows a slight Re_τ dependence. The higher order response modes and their velocity components are plotted in Figure 3.10. Similar to σ_j, ψ_j shows self-similarity even for the higher order modes. The forcing modes also demonstrate self-similarity, though they are not plotted for brevity.

Finally, the inner scaling is shown to hold for a sweep over ω^+ and k_z^+. ω^+ uses 24 logarithmically spaced points between 4π and $2\pi/140000$ and k_z^+ uses 22 logarithmically spaced points between $2\pi/10$ and $2\pi/9000$. These sweeps are computed using $L_x^+ = 10000$, $N_x = 500$, $y_{min}^+ = 125$, and $y_{max} = 3Re_\tau$. The Re_τ are 800,

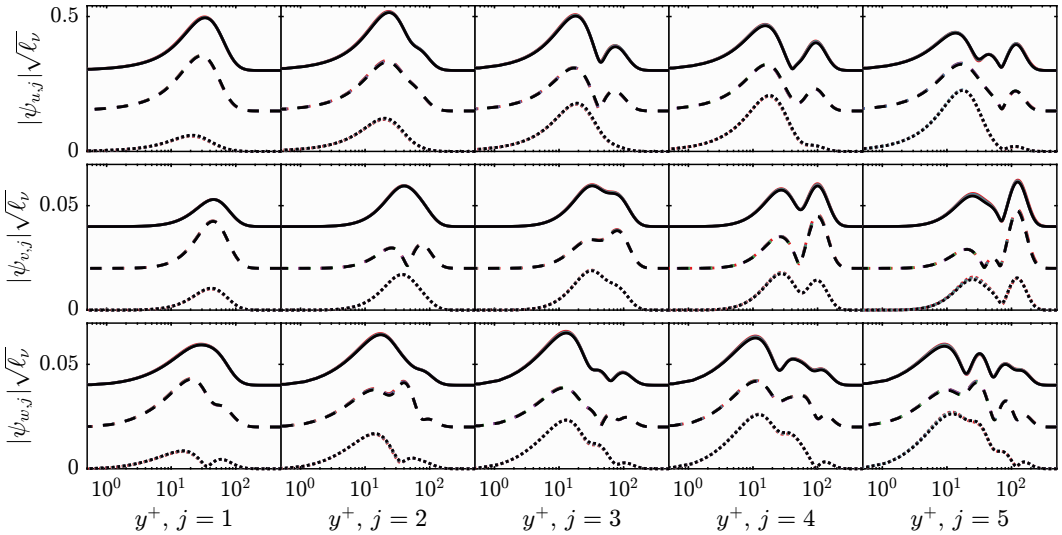

Figure 3.10: Rows from top to bottom are the magnitude of the streamwise, wall-normal, and spanwise components of the jth response mode in inner units and vertically offset to distinguish different streamwise locations. Left to right is increasing j. The colors and line types are the same as in Figure 3.8. The modes are computed using $L_x^+ = 10000$, $k_z^+ = 2\pi/100$ and $\omega^+ = 2\pi/100$.

2500, and 6000 requiring $N_y = 201, 251, 301$ and $\epsilon_s = 30, 30, 60$, respectively. The premultiplied response, E_{uu}^+, is defined as

$$E_{uu}^+(x, y, k_z^+) = k_z^+ \int_{\omega_{min}^+}^{\omega_{max}^+} \left|\sigma_1^+(k_z^+, \omega^+)\psi_{u,1}^+(x, y; k_z^+, \omega^+)\right|^2 d\omega^+, \tag{3.27}$$

where ω_{min} and ω_{max} are the limits of ω in the sweep. The unweighted streamwise kinetic energy of the response, K_{uu}^+, is

$$K_{uu}^+(x, y) = \int_{k_{z,min}^+}^{k_{z,max}^+} E_{uu}^+(x, y, k_z^+) d\left(\ln k_z^+\right). \tag{3.28}$$

E_{uu}^+ and K_{uu}^+ are the premultiplied streamwise kinetic energy spectra and streamwise turbulent intensity for fluctuations, $\widehat{\mathbf{q}} = \sigma_1 \boldsymbol{\psi}_1$. In actual turbulent flows, $\widehat{\mathbf{q}} = \sum_i \xi_i \sigma_i \boldsymbol{\psi}_i$, where the weights, ξ_i, come from projection onto data or satisfying the full NSE and set the units of velocity. Here, E_{uu}^+ and K_{uu}^+ are both computed with only knowledge of the linear operator.

In Figure 3.11(a), $E_{uu}^+(.7L_x, y^+, k_z^+)$ is plotted for the different Re_τ. E_{uu}^+ is self-similar due to the self-similarity of the resolvent operator. The largest values of E_{uu} are at $y^+ = 33$, $\lambda_z^+ = 116$, similar to where the near-wall cycle is expected, albeit further from the wall. This indicates that the near-wall cycle is preferentially amplified through the biglobal LNSE without a specification of a streamwise wavenumber.

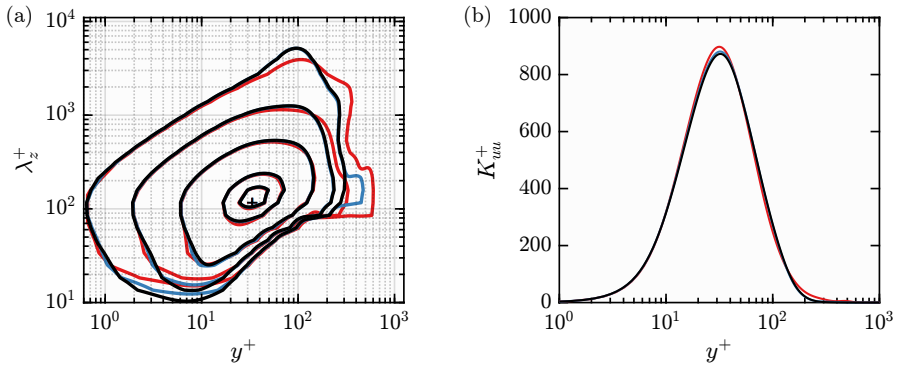

Figure 3.11: Contours of E_{uu}^+ (a) and K_{uu}^+ (b) for $Re_\tau = 800$ (red), $Re_\tau = 2500$ (blue), and $Re_\tau = 6000$ (black). The contour levels are at 0.62, 6.17, 61.66, 369.96, 554.94 and the crosses denote the maxima of $\widehat{E}_{uu}^+(x, y, k_z)$.

Although large scales in the outer region are expected to emerge with increased Re_τ, the amplified large scales are not observed here. This is because the domain, $L^+ = 10000$ corresponds to $L_x = 12.5\delta_{99}$, $4\delta_{99}$, $1.6\delta_{99}$ for $Re_\tau = 800$, 2500, 6000, which are too small to support the large scale structures. The amplification of the large scale structures increases with increasing domain length. Other linear analyses have also noted that large streamwise domains are required for the amplification of large scale structures and emergence of the secondary large scale peaks (Davis, Uzun, and Alvi, 2019). The effect of the domain length is shown in Appendix D.1 where smaller L_x^+ is shown to suppress E_{uu}^+ for $y^+ > 200$. For $y^+ > 200$, the E_{uu}^+ of $Re_\tau = 800$ does not collapse with the larger Re_τ sweeps, likely due to the lack of scale separation in $\overline{\mathbf{U}}$ for the smaller Re_τ.

In Figure 3.11(b), $K_{uu}^+(.7L_x, y^+)$ is plotted. The curves at the different Re_τ all collapse on top of one another, although the $Re_\tau = 800$ curve shows small deviations from the larger Re_τ curves do to the lack of collapse in E_{uu}^+ caused by the lack of scale separation. The $Re_\tau = 800$ curve shows a slight increase in $y^+ > 100$ since the larger domain (in outer units) can support large scale structures which are more energetic in the outer region of the flow. Since the constant L_x^+ domain filters the large scales, K_{uu}^+ can be approximated as a contribution from only the small scales. Many investigations have noted a lack of collapse in inner units for the inner peak in $\overline{uu}$ due to the footprint of large scale structures (Marušić, Mathis, and Hutchins, 2010a; Hoyas and Jiménez, 2006; M. Lee and Moser, 2015). The collapse of K_{uu}^+ is a consequence of the unsupported large scale structures that add outer scaled linear dynamics to the near-wall region and the lack of nonlinear information in χ_i. This is analogous to the results of Marušić, Mathis, and Hutchins (2010a) who showed

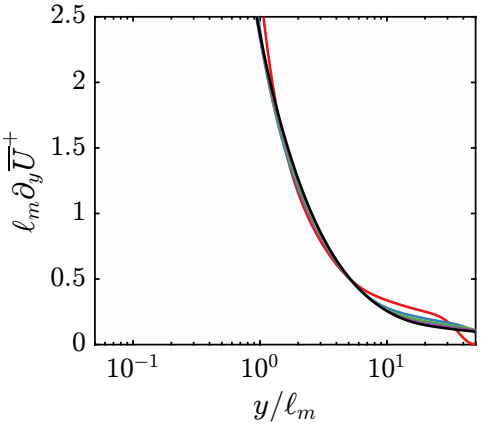

Figure 3.12: Mesolayer scaled $\overline{U}_y$ with $Re_\tau = 1200$, 3400, 5600, 7800, and 10000 plotted in red, blue, green, purple, and black lines, respectively.

that the inner peak of $\overline{uu}^+$ collapses if the large scale structures are filtered out.

3.7 Mesolayer Scaling of the Biglobal Resolvent Operator

The mesolayer region is characterized by a mixed length scale, $y_s = \ell_m = \sqrt{\ell_\nu \delta_{99}}$, with $y_d = 0$ and the same inner velocity scales as in Section 3.4. The Reynolds number, $Re_s = Re_m = \ell_m u_\tau / \nu$, which makes the streamwise length scale, $x_s = Re_m \ell_m = \delta_{99}$. Just like the local counterparts, the scaling of the biglobal modes will scale with Re_m as in Equations 3.7 and 3.8. Following Equation 3.9, the singular values scale with $\ell_m \delta_{99}/\nu$. In order for the scaling to hold, the domain length L_x/δ_{99}, $\tilde{\omega} = \omega \ell_m \delta_{99}/\nu$, and $\zeta = k_z \ell_m$ are held constant. While $\tilde{\omega}$ and ζ are allowed to vary with x due to streamwise development of ℓ_m and δ_{99}, the domain length is set with δ_{99} from the inlet of the domain.

The mean flow fields are once again computed using the Monkewitz composite profile using $Re_\tau = 1200$, 3400, 5600, 7800, and 10000 (Monkewitz, Chauhan, and Nagib, 2007). $\overline{U}_y$ is plotted in Figure 3.12 using the mesolayer scaling. Since this scaling is found using the mean momentum balance, the scaling ensures that $\overline{U}_y \ell_m / u_\tau \sim O(1)$ in a region $y/\ell_m \sim O(1)$ (Wei, Fife, et al., 2005; Afzal, 1984). Note that this scaling does not collapse $\overline{U}$. In the region where $y/\ell_m \ll 1$ or $y/\ell_m \gtrsim O(10)$, the mesolayer scaling does not hold for the mean shear. As a result, any mode with support in those regions is not expected to be self-similar with the mesolayer scaling.

The mesolayer scaled modes are computed with $N_y = 251$, $N_x = 600$, $L_x = 40\delta_{99}$, $y_{min} = 2.6\ell_m$, and $\epsilon_s = 30$. Only the domain length and the wall-normal grid spacing

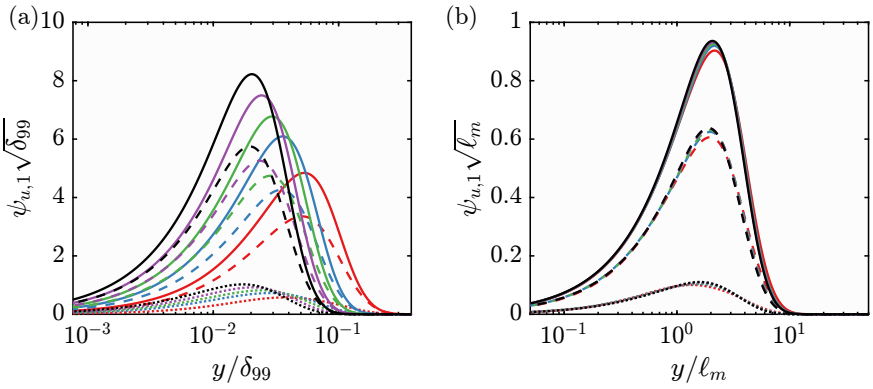

Figure 3.13: $|\psi_{u,1}|$ in outer (a) and mesolayer (b) units for $L_x = 40\delta_{99}$, $\zeta = 2\pi/7$, and $\tilde{\omega} = 25$. Red, blue, green, purple, and black denote $Re_\tau = 1200$, 2700, 3950, 5700, and 8000, respectively. The dotted, dashed, and solid lines denote $x = .2L_x$, $.5L_x$, $.8L_x$.

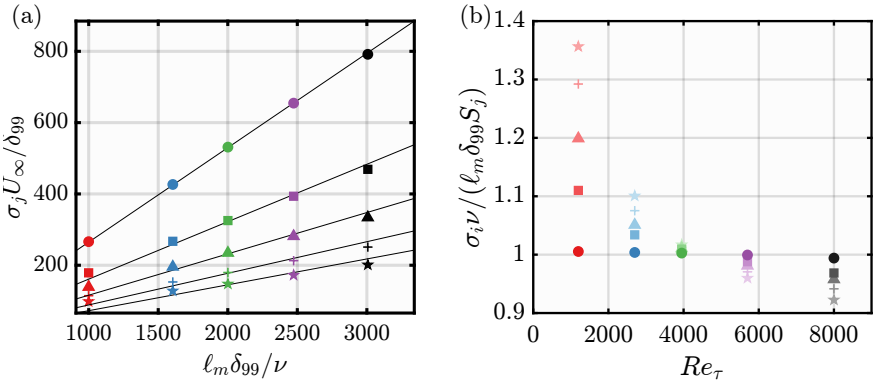

Figure 3.14: σ_j in outer units with the black lines denoting $S_j\ell_m\delta_{99}/\nu$ (a) and σ_j in mesolayer units, normalized by S_j (b) using $L_x = 40\delta_{99}$, $\zeta = 2\pi/7$, and $\tilde{\omega} = 25$. The circle, square, triangle, cross, and star denote $j = 1, 2, 3, 4$, and 5, respectively. Colors are the same as in Figure 3.13.

are Re_τ dependent, with y_{min} chosen to increase the resolution in the mesolayer. The modes are characterized by $\zeta = 2\pi/7$ and $\tilde{\omega} = 25$. For comparison, the λ_z^+ ranges from 240 to 620. In Figure 3.13, the streamwise components of the optimal response modes are computed in both outer and mesolayer scaled coordinates. Here, ψ_u peaks at $y/\ell_m \approx 2$, which is within the region of self-similarity where $\overline{U}_y$ has self-similar collapse in Figure 3.12. Unlike the local scaling, the self-similarity shows some Re_τ dependence due to the modes having support near the wall. The local modes are localized at the critical layer whereas the biglobal modes can spread out more in the wall-normal direction.

In Figure 3.14(a), $\sigma_1 U_\infty/\delta_{99}$ is shown to grow linearly with $\ell_m\delta_{99}/\nu$ with slope S_1.

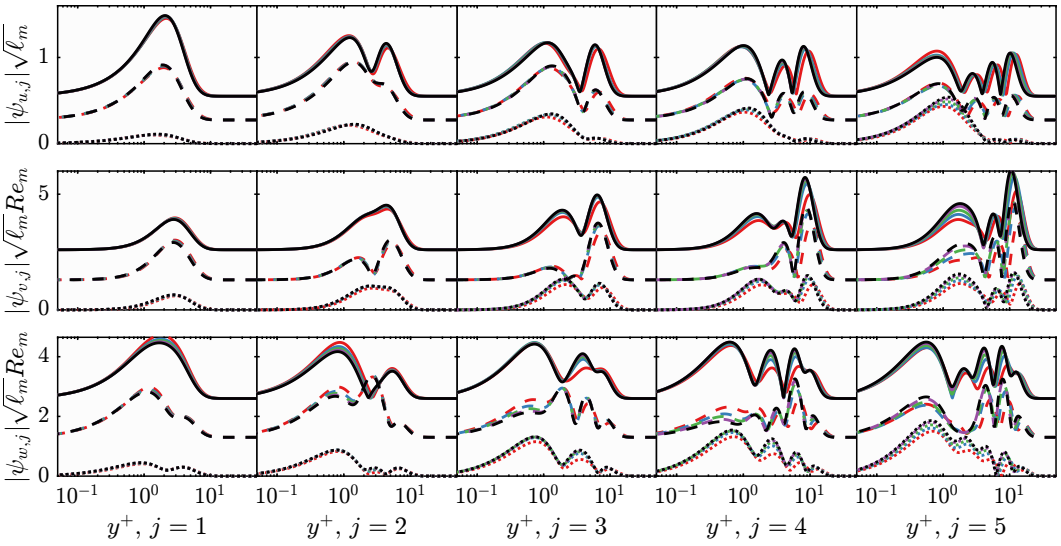

Figure 3.15: Rows from top to bottom are the magnitude of the streamwise, wall-normal, and spanwise components of the jth response mode in mesolayer units and vertically offset to distinguish different streamwise locations. Left to right is increasing j. The colors and linetypes are the same as in Figure 3.13. The modes are all computed using $L_x = 40\delta_{99}$, $\zeta = 2\pi/7$, and $\tilde{\omega} = 25$.

The higher order modes grow with $\ell_m\delta_{99}/\nu$, though their growth is not linear as Figure 3.14(b) illustrates an Re_τ dependence in the higher order gains. In Figure 3.15, the magnitude of the velocity components of $\boldsymbol{\psi}_j$ are plotted for the different Re_τ. Although these modes exhibit some degree of self-similarity, it is evident that only $\boldsymbol{\psi}_1$ is localized at $y/\ell_m \sim 1$. The higher order modes, due to orthogonality, have increased support in the near-wall region or further from the wall, where the mesolayer scaling does not hold. This causes the Re_τ dependence in $\sigma_j\nu/(\ell_m\delta_{99})$ for $j > 1$.

3.8 Outer Scaling of the Biglobal Resolvent Operator

In the outer scaling of the mean flow field, the velocity deficit $f = \overline{U}^+(y/\delta_{99}) - U_\infty^+$ is self-similar. The velocity scales are $u_s = u_\tau$, and $u_d = U_\infty$ with the length scales $y_s = \delta_{99}$ and $y_d = 0$. This sets $Re_s = Re_\tau$ and $x_s = Re_\tau\delta_{99}$. In the local scaling, the wavespeed was set such that $c^+ = U_\infty^+ + f_c$, where f_c is a constant, to ensure that all the modes are localized at a specific y/δ_{99}. In the biglobal case, the wavespeed of the modes can not be set *a priori*, so some assumptions must be made for u_c. It is assumed that the mode has most of its support in the outer region so that the mean flow field is $\overline{U} \approx u_\tau f + U_\infty$. For large Re, $U_\infty/u_\tau \approx 2.5\log(Re_\theta) + 4.1$ (Nagib, Chauhan, and Monkewitz, 2007). For the Re of interest, U_∞/u_τ is at least twice

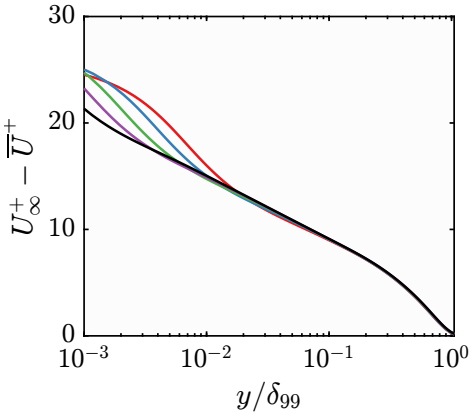

Figure 3.16: Velocity deficit in outer units with Re_τ = 1200, 2000, 3500, 6000, and 11000 plotted in red, blue, greeen, purple, and black lines, respectively.

as large as f in the outer region, so $\overline{U} \sim U_\infty$, where the approximation improves logarithmically with Re. This sets the convective velocity to scale with U_∞, which is different from u_s.

The mean flow fields are computed using the Monkewitz composite profile with Re_τ = 1200, 2000, 3500, 6000, and 11000 (Monkewitz, Chauhan, and Nagib, 2007). In Figure 3.16, the mean flow profiles at the inlet are plotted as velocity deficits. They illustrate self-similarity in the outer region of the flow. For $y/\delta_{99} \leq .01$, $\overline{U}$ is no longer self-similar as the inner region is approached. Modes that have support in this region of the flow will not be self-similar using the outer scaling since the near-wall region will influence the modes.

To achieve self-similarity, the parameters scale as $\zeta = k_z/\delta_{99}$ and $\tilde{\omega} = \omega\delta_{99}^2/\nu$. In this study, the parameters are set so that $N_x = 500$, $N_y = 301$, $y_{min} = .1\delta_{99}$, $y_{max} = 3\delta_{99}$, and $\epsilon_s = 30$. The domain length is held constant as $L_x = 15x_s/x_{s,min}$, where x_s is evaluated at the inlet of the domain and $x_{s,min}$ is x_s at $Re_\tau = 1200$. The response and forcing modes scale as in Equations 3.7 and 3.8, respectively, and the singular values scale with $\delta_{99}^2 Re_\tau/\nu$.

In Figure 3.17, the magnitude of the streamwise component of the outer region modes is plotted for $\zeta = \pi$ and $\tilde{\omega} = 16$. For comparison, the response modes are also plotted in inner scaled coordinates. Due to the scaling, this $\tilde{\omega}$ corresponds to long streamwise streaks since $\omega\delta_{99}/U_\infty \sim O(10^{-4})$. These modes illustrate self-similarity for $Re_\tau \geq 2000$, due to the increased scale separation between the inner region and outer region at larger Re_τ.

In Figure 3.18(a), σ_j are plotted against $S_j\delta_{99}^2 Re_\tau/\nu$, indicating linear growth with

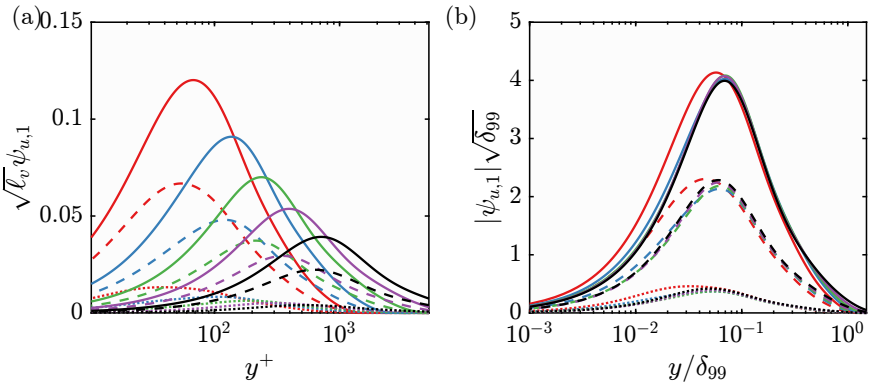

Figure 3.17: $|\psi|_{u,1}$ in inner (b) and outer (c) units computed using $L_x = 15x_s/x_{s,min}$, $\zeta = \pi$ and $\tilde{\omega} = 16$. Red, blue, greeen, purple, and black lines denote $Re_\tau = 1200$, 2000, 3500, 6000, and 11000, respectively. The dotted, dashed, and solid lines denote $x = .2L_x$, $.5L_x$, $.8L_x$.

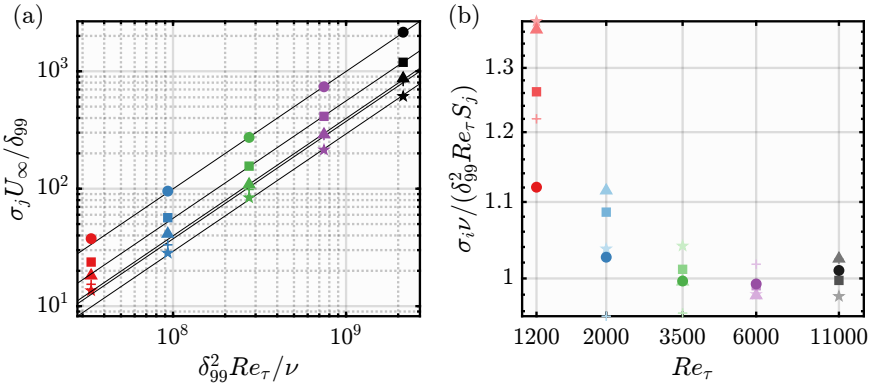

Figure 3.18: σ_j in outer units with the black lines denoting $S_j\delta_{99}^2 Re_\tau/\nu$ (a) and σ_j in outer units, normalized by S_j (b) computed using $L_x = 15x_s/x_{s,min}$, $\zeta = \pi$ and $\tilde{\omega} = 16$. The circle, square, triangle, cross, and star denote $j = 1$, 2, 3, 4, and 5, respectively. Colors are the same as in Figure 3.17.

respect to this scale for $j = 1$. Plotting the normalized singular values in Figure 3.18(b), indicates that the higher order modes have a non-negligible degree of Re_τ dependence. This Re_τ dependence is similar to what was observed in Section 3.7 except that here, the higher order modes have support in the near-wall region, where the outer scaling does not hold. For σ_1, only the larger Re_τ have self-similarity.

Despite the self-similarity in the mean velocity deficit, the outer scaled biglobal modes did not collapse as neatly as the local modes because of the Re dependence of U_∞^+ and that the modes are attached near the wall, where near-wall scaling holds. It is predicted that self-similarity will hold for larger Re_τ mean flow fields since the near-wall inner-scaled region shrinks in outer units. This reduces the influence of

the near-wall region on modes in the outer region, provided that the mode is not attached. Such large Re_τ mean flow fields require increased resolution to resolve the near-wall region, which can be prohibitively expensive for the biglobal analyses considered here.

3.9 Chapter Summary and Future Work

The self-similarity explored in Moarref, Sharma, et al. (2013) was extended to the biglobal resolvent operator. The self-similarity relies on ensuring that the modes are centered in specific wall-normal regions of the flow. These wall-normal locations are influenced by the spanwise wavenumber, which balances the mean shear and $\mathcal{L}_{SQ}^{-1}$. The former amplifies modes near the wall, while the latter amplifies modes in the outer region of the flow. The self-similarity was explored for the Blasius similarity solution, which is characterized by a single wall-normal length scale, and the ZPG TBL, which is multiscale. The Blasius similarity solution demonstrated that streamwise varying k_z and ω that account for the growth in the length and velocity scales can account for the nonparallel growth in the boundary layer. The difference in x_s and y_s makes even the Blasius case multiscale. For the Blasius case, the collapse improved when Re_s increased because of the dominance of the shear driven amplification over the convective terms. For the ZPG TBL case, the collapse improved when Re_s increased due to an increased separation of wall-normal scales.

For the ZPG TBL scaling, the inner, mesolayer, and outer scaling were investigated. The inner and mesolayer scaling hold near the wall, where k_z were chosen to be sufficiently large to ensure that the modes were amplified primarily by the lift-up effect. In the outer region, k_z needed to be sufficiently small so that the amplification was mostly due to $\mathcal{L}_{SQ}^{-1}$ in the outer region of the flow. The scaling of these modes improved as Re_τ increased which created scale separation between the inner and outer region, ensuring that the modes were localized in separate regions of self-similarity. For the mesolayer and outer scaling, the higher order modes had poor collapse because they had support in regions outside of the regions of self-similarity. For the outer scaling, because of the Re_τ dependence on the streamwise length scales, the self-similar modes are expected to be streak-like.

Unlike the scaling of Moarref, Sharma, et al. (2013), the scaling presented in this chapter did not specify a wall-normal location through an imposed wavespeed nor a streamwise wavelength. The modes identified here were found to be self-similar by only specifying appropriately scaled k_z and ω with the streamwise structure and

wall-normal location of the modes determined based on the optimal linear amplification. In Section 3.6, the biglobal resolvent analysis was shown to create the largest amplification for modes with $\lambda_z^+ \approx 100$ near the wall, similar to the identified spectra in the near-wall cycle (Hoyas and Jiménez, 2006). In the local analyses, the same λ_z^+ characteristic of the near-wall cycle were shown to produce low-rank resolvent operators, though these analyses specify a λ_x for the modes (Moarref, Sharma, et al., 2013). The biglobal analyses identifies these λ_z^+ as linearly amplified motions, without restricting their streamwise structure through an imposed λ_x. This suggests that disturbances are filtered through the linear amplification by preferentially amplifying the characteristic length scales in the near-wall cycle via the lift-up effect. The results of Abreu, Cavalieri, et al. (2020) showed that streak-like response modes amplified by the lift-up effect agree with modes from a spectral proper orthogonal decomposition of $Re_\tau = 180$ and 550 turbulent channels (Abreu, Cavalieri, et al., 2020). The agreement between data and linear analyses for those low Re_τ flows is likely because the inner region forms a large portion of the flow, lacking scale separation between the large and small scales. Thus, the low Re_τ flows are dominated by the linear amplification via the lift-up effect.

Respecting the self-similarity of the mean flow field for large scale shear-driven modes in Sections 3.7 and 3.8 leads to modes with length scales typically not observed in turbulent flows. This suggests that turbulent structures in the outer region are most influenced by the nonlinear effects, rather than the linear lift-up effects since these identified self-similar length scales are not energetic.. Further, these mesolayer and outer scaled modes have increased resolvent amplification with increased Re, suggesting an increased importance of the large scale modes with larger Re.

Another challenge of extending the results from this study to turbulent spectra is the choice of boundary conditions. If the domains are used to approximate real turbulent flows, the inflow and outflow boundary conditions should support nonlinear boundary conditions that can account for turbulent fluctuations entering and leaving the domain. The boundary conditions affect the structure of the resolvent modes. For instance, Gómez et al. (2014) considered a biglobal resolvent operator for a pipe flow using periodic boundary conditions. Their results found that under periodic boundary conditions, the biglobal resolvent modes are the local, 1D, resolvent modes with streamwise wavenumbers being harmonics of $2\pi/L$, where L is the domain length, exhibiting no spatial variation in the amplitude. Other boundary conditions

have been investigated for ZPG TBL DNS which employ the ZPG TBL scaling laws, such as the recycling and recycling method of Lund, Wu, and Squires (1998) or the approximations made in Ruan (2021) to treat the ZPG TBL as streamwise homogeneous flow under an appropriate outer scaling with the nonparallel growth term serving as a source term. Incorporating such scaling assumptions into the biglobal resolvent operator between the inflow and outflow may lead to more realistic turbulent structures entering and leaving the domain compared to the sponges. However, imposing predetermined scaling through boundary conditions is likely to impose said scaling on the resolvent modes. Further, there is the choice of which scaling to apply to the resolvent modes as the different k_z and ω regimes push the modes to different regions of the flow where different scalings hold. If the goal is to approximate the turbulent fluctuations, the scaling of the turbulent fluctuations must be agreed upon since the turbulent fluctuations do not scale with the mean flow field's scaling (Marušić, Mathis, and Hutchins, 2010a; Hoyas and Jiménez, 2006; M. Lee and Moser, 2015). Lastly, these sort of scalings were not considered since the ZPG TBL scaling they are derived with will not apply to the APG TBL in Chapter 4. Future work will need to consider more realistic inflow and outflow boundary conditions to improve comparisons with experiment and simulation. The scalings explained in this chapter can thus only be applied to the resolvent modes when the boundary conditions are compact.

The self-similarity studied here can be used to scale resolvent decompositions from low Re_τ to high Re_τ, which require large resolutions to resolve the near-wall region. These increased resolutions can quickly become prohibitive if all scales of the flow need to be resolved since the calculations scale with $O(N^3)$. Even though the scalings did not collapse the identified modes as well as in the local analysis, these scaled modes can be used as preconditioners for large Re_τ linear systems. Consider the LNSE for a large Re_τ flow, $\mathcal{A}_L$, and a small Re_τ flow, $\mathcal{A}_S$, with their associated resolvent decompositions, $(\boldsymbol{\psi}_{L,i}, \boldsymbol{\phi}_{L,i}, \sigma_{L,i})$ and $(\boldsymbol{\psi}_{S,i}, \boldsymbol{\phi}_{S,i}, \sigma_{S,i})$, respectively. The response, $\widehat{\mathbf{q}}$, and forcing, $\widehat{\mathbf{f}}$, in Equation 2.4 for the large Re_τ case can be projected onto the rescaled response modes, $\tilde{\boldsymbol{\psi}}_{S,i}$, and forcing modes, $\tilde{\boldsymbol{\phi}}_{S,i}$, as

$$\left\langle \tilde{\boldsymbol{\phi}}_{S,i}, \mathcal{A}_L \tilde{\boldsymbol{\psi}}_{S,j} \right\rangle_f \left\langle \tilde{\boldsymbol{\psi}}_{S,j}, \widehat{q} \right\rangle_r = \left\langle \tilde{\boldsymbol{\phi}}_{S,i}, \mathcal{R}\widehat{f} \right\rangle_f . \tag{3.29}$$

This is a projection of $\mathcal{A}_L$ onto the rescaled resolvent basis of $\mathcal{A}_S$. The basis can be truncated to only retain the first r elements so that this produces a linear system, with the $r \times r$ matrix $\tilde{A}_{LS} = \left\langle \tilde{\boldsymbol{\phi}}_{S,i}, \mathcal{A}_L \tilde{\boldsymbol{\psi}}_{S,j} \right\rangle_f$. Taking the inverse of this matrix and its subsequent singular value decomposition gives the bi-orthonormal modes

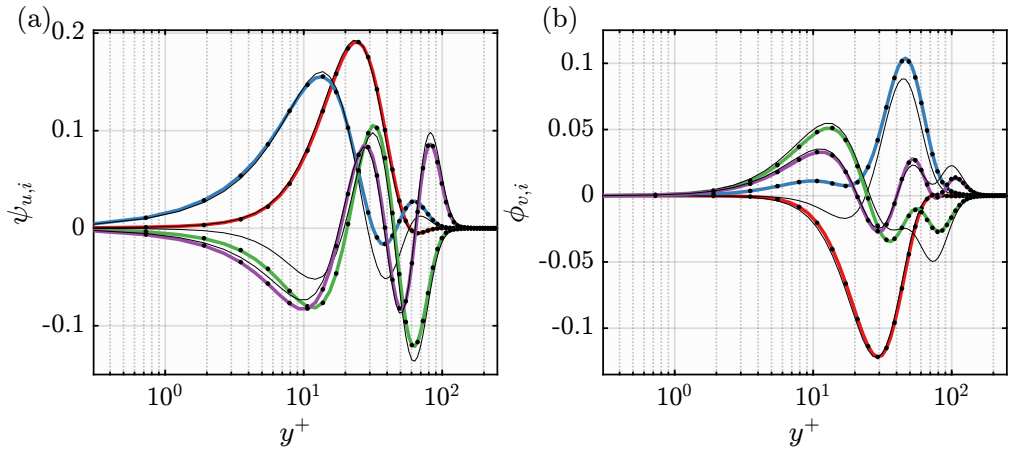

Figure 3.19: Real part of $\boldsymbol{\psi}_{L,u,i}$ (colored lines), $\tilde{\boldsymbol{\psi}}_{L,u,i}$ (dots), and $\tilde{\psi}_{S,u,i}$ (thin black lines) (a) and real part of $\boldsymbol{\phi}_{L,v,i}$ (colored lines), $\tilde{\boldsymbol{\phi}}_{L,v,i}$ (dots), and $\tilde{\phi}_{S,v,i}$ (thin black lines). Red, blue, green, and purple denote $i = 1$, 2, 3, and 4. The modes are computed using $k_z^+ = 2\pi/100$, $k_x^+ = 2\pi/1000$, and $c^+ = 12.5$.

$\mathbf{q}_i$ and $\mathbf{f}_i$, for $i = 1, \ldots, r$ and the singular values, λ_i. Note that the jth entries of $\mathbf{q}_i$ and $\mathbf{f}_i$ denote coefficients for the basis vectors, $\tilde{\boldsymbol{\psi}}_{S,j}$ and $\tilde{\boldsymbol{\phi}}_{S,j}$. This provides the approximations for $\boldsymbol{\psi}_{L,i}$ and $\boldsymbol{\phi}_{L,i}$ as

$$\tilde{\boldsymbol{\psi}}_{L,i} = q_{i,j}\tilde{\boldsymbol{\psi}}_{S,j}, \tag{3.30}$$

and

$$\tilde{\boldsymbol{\phi}}_{L,i} = q_{i,j}\tilde{\boldsymbol{\phi}}_{S,j}, \tag{3.31}$$

respectively. The overall cost of this approximation is the cost of computing the resolvent analysis for the smaller Re_τ flow, which can be computed with a significantly smaller grid resolution.

The usefulness of these approximations can be shown with an example using channel flows under the parallel flow assumption. These correspond to $Re_\tau = 550$ (M. Lee and Moser, 2015) and $Re_\tau = 10000$ (Hoyas, Oberlack, et al., 2021). The former uses 192 points and the latter uses 1051 points for $y \in [0, h]$, where h is the channel half height. Using the same DNS grids for a local resolvent analysis using only half the channel for a local analysis, $Re_{\tau,L}$ takes 40 seconds to compute while $Re_{\tau,S}$ takes 0.32 seconds to compute on a personal laptop (Lenovo ThinkPad T490s). Using the approximation described here, $\boldsymbol{\psi}_{L,i}$ and $\boldsymbol{\phi}_{L,i}$ can be approximated with error less than .1% in .38 seconds for $r = 15$. The majority of the time is spent computing the modes from $Re_{\tau,S}$. Comparing with only the rescaling, the error between the true $\boldsymbol{\psi}_{L,1}$ and $\tilde{\boldsymbol{\psi}}_{S,1}$ is about 1%. The order of magnitude improvement between $\tilde{\boldsymbol{\psi}}_{S,1}$

and the approximation is that $\boldsymbol{\psi}_{L,1}$ can be approximated with multiple modes. In Figure 3.19, the approximations are compared to the true modes for $k_z^+ = 2\pi/100$, $k_x^+ = 2\pi/1000$, and $c^+ = 12.5$. The approximations described in Equations 3.30 and 3.31 are better able to approximate the higher order modes than using the simple rescaling. These approximations can help with real time sensing of flows, especially when large resolutions are required to reconstruct DNS results by decreasing the time required to create the resolvent basis. Although only shown for the local analysis, these results can be extended to the biglobal case as well. One challenge of this approach is that for the self-similarity to hold, the resolvent modes must be supported in a region where $\overline{U}$ is self-similar. As Re_τ increases, this becomes less of an issue due to the increased scale separation. Furthermore, the use of multiple resolvent modes in Equations 3.30 and 3.31 help improve the predictions since they do not rely solely on the scaling of an individual mode.

The scalings identified here only deal with the LNSE and do not account for any nonlinear interactions in the flow. In the full nonlinear problem, the triadic interactions create a forcing that is constructed from a variety of scales. For example, the inner region is influenced by the large scale structures, which becomes more prevalent at larger Re_τ. The ideas presented in this chapter show how a basis of optimal resolvent modes will scale as the Re_τ varies. In order to scale the full nonlinear statistics to higher Re_τ, the scaling of the coefficients of the resolvent modes must be identified as well. In order for the turbulent spectra to be self-similar with the identified spectra, the lift-up effect must be a dominant mechanism. Near the wall, where the shear is dominant, the length and velocity scales are all dominated by viscosity and lead to the agreement between the biglobal resolvent results and turbulent spectra. To account for the large scales, and their increased influence near the wall, the nonlinear coefficients need to be accounted for.

Chapter 4

NONEQUILIBRIUM EFFECTS IN TURBULENT BOUNDARY LAYER FLOWS

4.1 Introduction

This chapter will focus on mild APG TBLs, where the flow remains attached. For these attached flows, the presence of the APG changes the mean flow field by increasing the wake component and shifting the log layer down from the canonical turbulent flow (Monty, Harun, and Marušić, 2011). Close to the wall, the APG TBL mean velocity profile still resembles the canonical ZPG TBL when β is small. The streamwise kinetic energy, $\overline{uu}$, reveals the presence of a secondary peak in the outer region of the flow that increases in amplitude with increasing β (Monty, Harun, and Marušić, 2011). For sufficiently large β, this secondary peak can be as large as the near-wall peak (Bobke et al., 2017). The premultiplied streamwise kinetic energy spectra for these APG flows identify the near-wall cycle along with a secondary outer peak, demonstrating energized large scale structures (Harun et al., 2013). These large scale structures are also more energetic with increased β. This secondary peak is reminiscent of high Re_τ flows, where the large scale structures are also energized. In the APG TBL flow, the amplified large scales are found even in low Re_τ ($Re_\tau < 1000$) flows (J. H. Lee, 2017; Bobke et al., 2017).

As mentioned in Section 1.1, the APG TBL is characterized by Re_τ, β, and its streamwise history, $\beta(x)$. Even when β and Re_τ are matched locally, differences in the upstream $\beta(x)$ change the statistics of the flow. Typically, the flow with the larger upstream $\beta(x)$ displays more energetic turbulent fluctuations in the outer region of the flow (Bobke et al., 2017). Thus analyses must include the streamwise variation of the flow to capture these effects.

By separating the RANS equations from Equation 2.31, the following system is found for the fluctuations, $[\mathbf{u}, p]$, and the mean, $\left[\overline{\mathbf{U}}, \overline{P}\right]$,

$$\left(\boldsymbol{\nabla}\overline{\mathbf{U}}\right)\overline{\mathbf{U}} + \boldsymbol{\nabla}\overline{P} - \frac{1}{Re}\nabla^2\overline{\mathbf{U}} = -\overline{(\boldsymbol{\nabla}\mathbf{u})\mathbf{u}}, \tag{4.1}$$

$$\partial_t\mathbf{u} + (\boldsymbol{\nabla}\mathbf{u})\overline{\mathbf{U}} + \left(\boldsymbol{\nabla}\overline{\mathbf{U}}\right)\mathbf{u} + \boldsymbol{\nabla}p - \frac{1}{Re}\nabla^2\mathbf{u} = -(\boldsymbol{\nabla}\mathbf{u})\mathbf{u} + \overline{(\boldsymbol{\nabla}\mathbf{u})\mathbf{u}}, \tag{4.2}$$

along with the divergence free constraint on $\mathbf{u}$ and $\overline{\mathbf{U}}$. From Equation 4.2, $\boldsymbol{\nabla}\overline{P}$ does not directly couple with $\mathbf{u}$. Rather, $\boldsymbol{\nabla}\overline{P}$ changes $\overline{\mathbf{U}}$ and $\overline{(\boldsymbol{\nabla}\mathbf{u})\mathbf{u}}$. The change in $\overline{\mathbf{U}}$ creates differences in the linear amplification of $\mathbf{u}$ while the change in $\overline{(\boldsymbol{\nabla}\mathbf{u})\mathbf{u}}$ affects the distribution of the energetic scales. This chapter will deal with the linear amplification of $\mathbf{u}$. Following McKeon and Sharma (2010), any effects of the nonlinearities will act as forcing to the LNSE. For a given frequency and wavenumber, $\sigma_1\boldsymbol{\psi}_1$ of $\mathcal{R}$ will be interpreted as the directions amplified by nonlinear forcing in the LNSE. Although the resolvent modes are found under the assumption of decorrelated, white-noise forcing, $\sigma_j\boldsymbol{\psi}_j$ has been shown to identify similar flow structures in the full nonlinear data when $\mathcal{R}$ is low-rank (Moarref, Sharma, et al., 2013; Abreu, Cavalieri, et al., 2020; Towne, Schmidt, and Colonius, 2018). When $\widehat{(\boldsymbol{\nabla}\mathbf{u})\mathbf{u}}$ has any projection onto $\boldsymbol{\phi}_1$, then responses resembling $\boldsymbol{\psi}_1$ will be preferentially amplified by the linear dynamics and are present in the full nonlinear data.

The first part of this chapter will focus on how changes in $\overline{U}$ change the local resolvent modes. In particular, a new scaling will be shown for the local resolvent modes in APG TBL using the scaling of Wei and Knopp (2023). To incorporate the nonparallel effects of the APG TBL flow, the rest of the chapter will focus on the linear amplification using the biglobal operator. First, the inner scaling of the resolvent modes will be investigated for near-wall small-scale structures. Following this, the large scale structures will be investigated to demonstrate their increased amplification with increased β. The effect of history will also be investigated for these flows as well.

4.2 Outer Scaling of Adverse Pressure Gradient Turbulent Boundary Layer Local Resolvent Modes

The presence of an APG changes the statistics of the flow through the amplification of large scale structures in the outer region. This amplification is caused by the presence of the streamwise PG, dP_∞/dx, in the RANS equations, which changes $\overline{U}$ and the Reynolds stresses. Due to the increased activity in the outer region of the flow, the peak of $\overline{uv}$ moves to the outer region of the flow. The changes in the dynamics of the flow have inspired many self-similar scalings for the statistics of the flow. Here, attention will be placed on the outer scaling of Wei and Knopp (2023), which has been shown to collapse $\overline{U}$, $\overline{V}$, and $\overline{uv}$ over a wide range of β and Re_τ for APG TBL. These scalings for y, $\overline{U}$, $\overline{V}$, and $\overline{uv}$ are found by identifying scales

that make all the terms in the RANS equation between 0 and 1 through the scaling patch analysis. The scalings depend on δ_{99} and y_m, the wall-normal location of the maximum of $|\overline{uv}|$ and the values of $\overline{U}$, $\overline{V}$, and $\overline{uv}$ at these wall-normal locations. In this chapter, length and velocity scales and variables with superscripts d denote dimensional quantities. The scaling for y and $\overline{U}$ is

$$\eta = \frac{y^d - y_m}{\delta_{99} - y_m}, f = \frac{U_e - \overline{U}^d}{U_e - U_m}, \tag{4.3}$$

where U_e and U_m denote $\overline{U}^d$, evaluated at δ_{99} and y_m, respectively. This also introduces the length scale, $y_s = \delta_{99} - y_m$, and velocity scale, $U_s = U_e - U_m$. This scaling will be denoted as the WK outer scaling to distinguish it from the outer scaling in Section 3.8. See Wei and Knopp (2023) for details along with scaling for $\overline{V}$ and $\overline{uv}$.

This scaling relies on the streamwise dependent scales, y_m, y_s, U_e, and U_s and holds in a specific wall-normal outer region of the flow, $\eta \in (0, 1)$. Due to the highly localized nature of the scaling, it is natural to explore how this scaling extends to the local resolvent modes. Following the generalization of Moarref, Sharma, et al. (2013)'s scaling results in Section 3.2 and the WK outer scaling, the scales $x_s = y_s Re_s$, $z_s = y_s$, and $u_d = U_e$ in Equation 3.2 so that

$$k_x^d = \frac{\alpha}{y_s Re_s}, k_z^d = \frac{\zeta}{y_s}, c^d = U_s f_c + U_e. \tag{4.4}$$

Here, $Re_s = y_s U_s/\nu$. For the scaling to hold, $f_c \in (0, 1)$. Since $Re_s \gg 1$, the scalings identified in Equations 3.7, 3.8, and 3.9 are expected to hold asymptotically.

In Table 4.1, the mean flow profiles from experiments and simulations are tabulated along with their Re_τ, β, and computed Re_s. Note that the δ_{99} and U_e were calculated following the method described in Wei and Knopp (2023). Although these flow fields all have different upstream β histories, the use of the local y_m accounts for any accumulated β effects in the turbulent statistics. Wei and Knopp (2023) notes that for the flows where an equilibrium condition is reached, the distance $\delta_{99} - y_m$ approaches a constant. The Re_τ reported in Table 4.1 denote the reported values, where available. Otherwise Re_τ is defined with the δ_{99} described in this section. Where β is not reported, it is computed using

$$\delta^* = \int_0^{\delta_{99}} \left(1 - \frac{U^d}{U_e}\right) dy^d, \tag{4.5}$$

Dataset	Re_τ	β	Re_s	Color	Reference
b1n1D	800	0.6	4887	—	Bobke et al., 2017
b2n1D	800	1.3	4600	—	Bobke et al., 2017
m18n1D	800	4.0	4612	—	Bobke et al., 2017
m16n1D	800	2.2	4391	—	Bobke et al., 2017
m13n1D	800	1.0	3643	—	Bobke et al., 2017
P141D	1800	1.2	10020	—	Pozuelo et al., 2022
k1	933	0.9	4580	—	Kitsios, Atkinson, et al., 2016
k39	767	45.58	14510	—	Kitsios, Sekimoto, et al., 2017
MP10	1280	4.48	12650	···	Marušić and Perry, 1995
MP30	3503	3.96	30710	···	Marušić and Perry, 1995
S0	1800	0	19770	—	Eitel-Amor, Örlü, and Schlatter (2014)

Table 4.1: Dataset descriptions of the mean flow profiles used in the local analysis in Section 4.2, with their legend color. Since the WK outer scaling only requires local quantities, only the local parameters are presented. More information on the datasets can be found in the accompanying references.

and

$$\frac{dP^d}{dx^d} = -\rho U_e \frac{dU_e}{dx^d}. \tag{4.6}$$

In this section, the values of Re_τ and β are used to parameterize the flows and are not factors in the scaling. The data from simulations are 1D profiles extracted at the x location corresponding to the specified Re_τ.

In Figure 4.1, the $\overline{U}$ are plotted in inner scaled variables and the WK outer scaling for the APG TBL profiles and ZPG TBL profile. From the inner scaled coordinates, it is clear that the mean profiles all have different wakes and log layer regions, while near the wall, $\overline{U}^+$ is self-similar for all the profiles except k39. Plotting $\overline{U}$ and $\overline{U}_y$ in WK outer scaled variables demonstrates collapse of the mean APG TBL flow profiles in $\eta \in [0, 1]$. The dashed line in Figures 4.1(b,c) denote

$$f_{SL}(\eta) = 1 - \text{erf}\left[1.3\eta + .21(1.3\eta)^4\right], \tag{4.7}$$

which has a functional form similar to planar mixing layers (Wei and Knopp, 2023), which have been noted to share similarities with APG TBLs (Gungor et al., 2016). The lack of collapse of the ZPG TBL mean flow profile demonstrates differences in the dynamics of the APG TBL absent in the ZPG TBL. In particular, this scaling relies on the location of the maximum Reynolds shear stress which moves away from the wall in an APG TBL, unlike the ZPG TBL whose peak is in the inner region. Close to the wall ($\eta < 0$), the self-similarity does not hold because the flow is characterized by inner scaled variables in that region. In the freestream

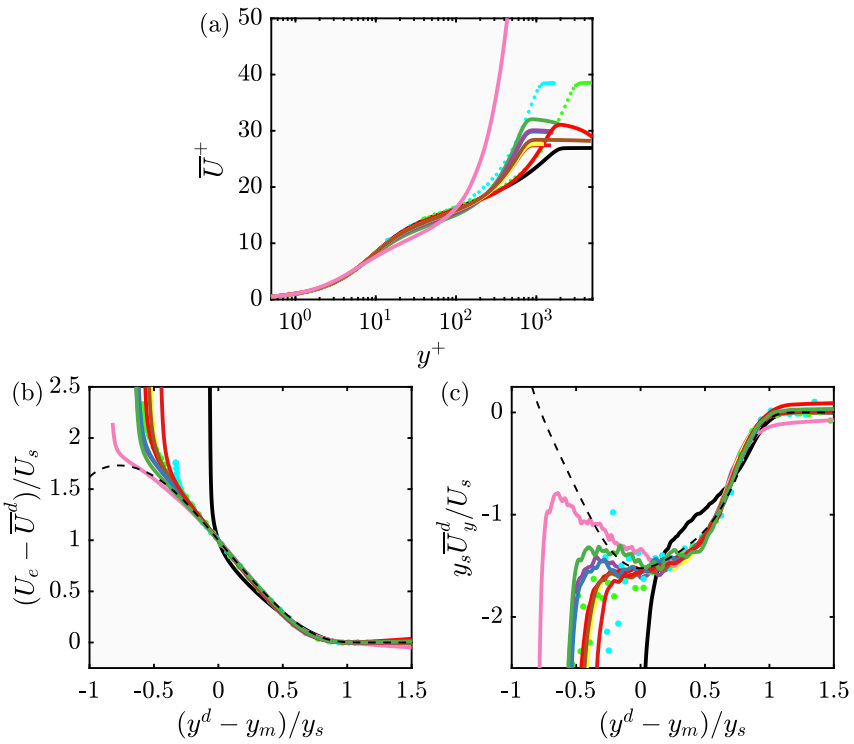

Figure 4.1: $\overline{U}$ in inner scaled coordinates (a) and WK outer scaling (b). $\overline{U}_y$ in WK outer scaled coordinates (c). The black dashed lines denote f_{SL} (a) and f'_{SL} (b). The line colors and styles are denoted in Table 4.1.

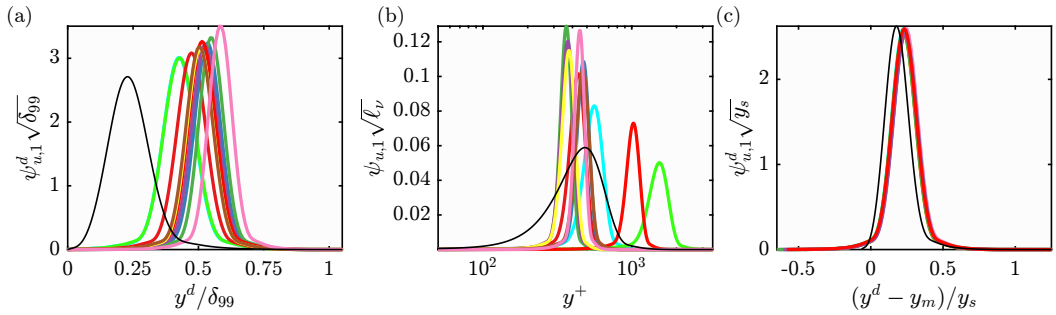

Figure 4.2: Amplitude of the local $\psi_{u,1}$ in (a) outer units, (b) inner units, (c) WK outer units for $\alpha = 2\pi Re_{s,ref}/10$, $\zeta = 2\pi$, $c = 1$. The line colors and styles are denoted in Table 4.1.

($\eta > 1$), there is a lack of collapse for the simulated profiles due to the freestream boundary conditions which have been observed to generate a nonzero $\overline{U}_y$ in the freestream (Pozuelo et al., 2022).

In Figure 4.2, $|\psi|_{u,1}$ is plotted for $\alpha = 2\pi Re_{s,ref}/10$, $\zeta = 2\pi$, $c = 1$ in outer units, inner units, and WK outer units. Here $Re_{s,ref} = 10020$ so that the λ_x are a few δ_{99} long. In outer units, $\lambda^d_z/\delta_{99} \in (.55, .75)$, $\lambda^d_x/\delta_{99} \in (2.5, 23)$, and $c^d/U_e \in (.7, .85)$.

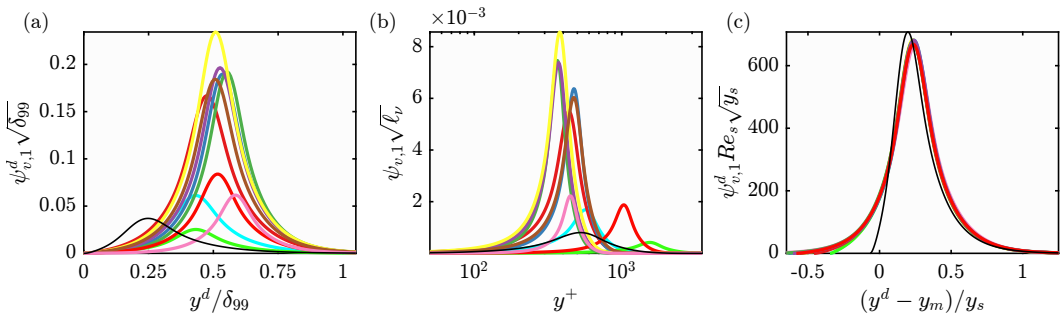

Figure 4.3: Amplitude of the Local $\psi_{v,1}$ in (a) outer units, (b) inner units, (c) WK outer units for $\alpha = 2\pi Re_{s,ref}/10$, $\zeta = 2\pi$, $c = 1$. The line colors and styles are denoted in Table 4.1.

The range in λ_x^d is due to the required Re_s dependence for self-similarity of the resolvent modes. The scaling in outer and inner units illustrate the range in the wall-normal direction where these modes have support. Using the WK outer scaling, the modes all collapse when using the APG TBL mean profiles. In Figure 4.3, $|\psi|_{v,1}$ is plotted for the same parameters. Using the WK outer scaling, the wall-normal component collapses in the region $\eta \in [0, 1]$. For the parameters chosen, the collapse of the wall-normal component fails near the wall because of the lack of collapse of the mean profile in that region. It is possible to choose ζ to make the modes more compact in the wall-normal direction such that the modes have less support near the wall. The lack of collapse for the ZPG TBL resolvent modes is due to the lack of collapse of the ZPG TBL mean profile in the WK outer scaled coordinates. The WK outer scaling depends on y_m, which is in the near-wall region for the ZPG TBL. As a result, the ZPG TBL mode resembles an attached mode, with significant support in the near-wall region. The APG TBL modes are detached because y_m is in the outer region of the flow.

In Figure 4.4, σ_1 are plotted in outer units and WK outer units for the same parameters. Using the outer units, σ_1 spans several orders of magnitude for the different velocity profiles used. Using the WK outer scaling, the σ_1 all fall around 1.14×10^{-5}, with some scatter, for the APG TBL profiles. For the ZPG TBL, σ_1 falls below the scatter of the APG TBL σ_1. The scatter in σ_1 for the APG TBL is due to the lack of collapse of $\overline{U}$ for $\eta < 0$ which affects $\psi_{v,1}$, as shown in Figure 4.3.

In this section, the scaling results of Moarref, Sharma, et al. (2013) were extended to the scaling identified by Wei and Knopp (2023) for APG TBL. The WK outer scaling of $\overline{U}$ depends on local parameters of the mean statistics and holds in the region $\eta \in (0, 1)$. For the resolvent modes to scale in WK outer scaled variables,

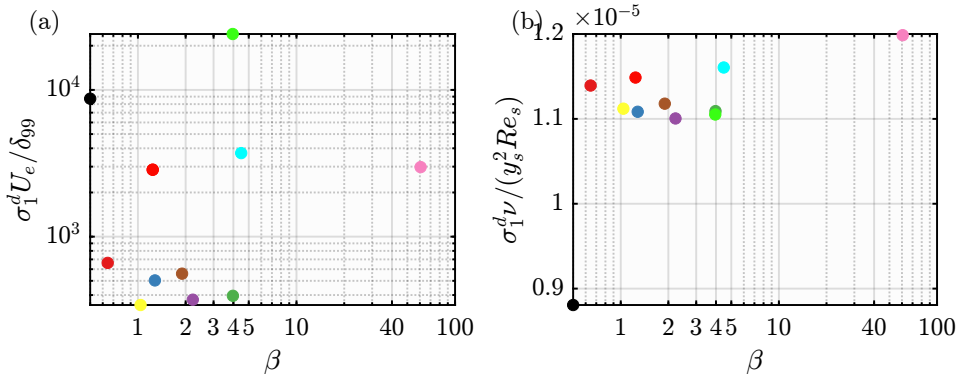

Figure 4.4: σ_1 in (a) outer units, (b) WK outer units for $\alpha = 2\pi Re_{s,ref}/10$, $\beta = 2\pi$, $c = 1$. Note that the x axis is in log scale, and σ_1 for the S0 dataset is plotted at $\beta = .5$ for visibility.

f_c must be chosen to ensure that the critical layer, η_c is in $[0, 1]$. Extending this resolvent scaling to biglobal resolvent modes requires the modes to have scale separation between the inner and outer regions of the flow to minimize the influence of the near-wall region. This is because the WK scaling requires modes highly localized in the outer region of the flow. Due to the lack of scale separation in the other LES datasets available, localization in only the outer region is not possible. To the best of the author's knowledge, the only flat plate APG TBL dataset with enough scale separation to ensure a minimal near-wall region in outer scaled coordinates is that of Pozuelo et al. (2022). Although experimental datasets are available at similar or larger Re_τ, the biglobal operator requires a mean velocity field over a large streamwise domain to support the large scale structures. The WK outer scaling is not attempted for the biglobal modes.

4.3 Inner Scaling of Adverse Pressure Gradient Turbulent Boundary Layer Biglobal Resolvent Modes

In TBL with mild APG, the near-wall region is largely unchanged, save for the change in the log layer. In the viscous sub-region, the effect of the PG is negligible. Owing to small change in the near-wall region due to the PG, it is now investigated how the PG changes the linear amplification in inner scaled modes. The inner scaling described in Section 3.6 is applied to various APG TBL LES and a ZPG TBL LES described in Table 4.2. These simulations all have different β. The data of Pozuelo et al. (2022) and Eitel-Amor, Örlü, and Schlatter (2014) will be useful to compare the differences in the inner scaling of resolvent modes with high Re_τ mean flow fields with different β. Note that in this section, $x \in [x_0 - L_x/2, x_0 + L_x/2]$,

Domain	Re_τ	Re_τ range	$\overline{\beta}$	β range	$L_x/\delta_{99}(x_0)$	Color
b1nI	650	(540, 750)	0.92	(.99, .85)	13.85	—
b2nI	650	(500, 780)	1.99	(2.12, 1.57)	13.85	—
m18nI	650	(460, 890)	3.26	(4.52, 0)	13.85	—
P14I1	650	(560, 740)	1.49	(1.26, 1.62)	13.85	—
P14I2	1200	(1090, 1310)	1.47	(1.52, 1.42)	7.5	—
P14I3	1800	(1690, 1900)	1.24	(1.27, 1.18)	5	—
S0I1	650	(590, 700)	0	(0, 0)	13.85	—
S0I2	1200	(1150, 1250)	0	(0, 0)	7.5	—
S0I3	1800	(1750, 1850)	0	(0, 0)	5	—

Table 4.2: Names of the mean flow fields in the subdomains with flow parameters and labels. Here, Re_τ range and β range denote the values of Re_τ and β at the inlet and outlet of the subdomains.

where $Re_\tau(x_0)$ denotes the Re_τ of interest. Here, $L_x^+ = 9000$ is used for all the domains. In all the domains here, $N_x = 400$, $y^+_{max} = 3Re_\tau(x_0)$, $y^+_{min} = 150$, and $\epsilon_s = 60$. Here, $N_y = 201$, 251, and 301 for the $Re_\tau = 650$, 1200, and 1800 datasets.

In Figure 4.5, u_τ is plotted against x for each domain, normalized by δ_{99}, to describe how the friction velocity and length scales vary across the domain. The APG datasets have more streamwise variation in the friction scales than the ZPG TBL. To account for this streamwise variation in the inner scaling, the Equation 3.26 will be used. In Section 3.6, the streamwise development of u_τ was small because of the large Re_τ and ZPG TBL datasets used. Because the Re_τ is significantly smaller and the APG TBL creates more streamwise variation, this effect will become more appreciable.

Figure 4.6 compares the Re_τ dependence on the inner scaling of biglobal resolvent modes with two different β by comparing modes computed using the ZPG TBL data of Eitel-Amor, Örlü, and Schlatter (2014) and the APG TBL data of Pozuelo et al. (2022). $\overline{U}^+$ at the center of the domain are compared to demonstrate the change in the inner region of the flow. There is a small change in the log region at this small β, with this change becoming smaller with increasing Re_τ. In Figure 4.6(b), $|\psi_{u,1}|$ is plotted in inner units with $k_z^+ = 2\pi/100$ and $\omega^+ = 2\pi/100$ at three different streamwise locations per domain. Due to the lack of scale separation at $Re_\tau = 650$, the ZPG TBL modes do not collapse as well as in Section 3.6 which used larger Re_τ mean flow fields. The smaller Re_τ APG TBL modes also do not collapse well onto the higher Re_τ ZPG TBL modes. The collapse of the resolvent modes improves when Re_τ increases for both the APG TBL and ZPG TBL modes.

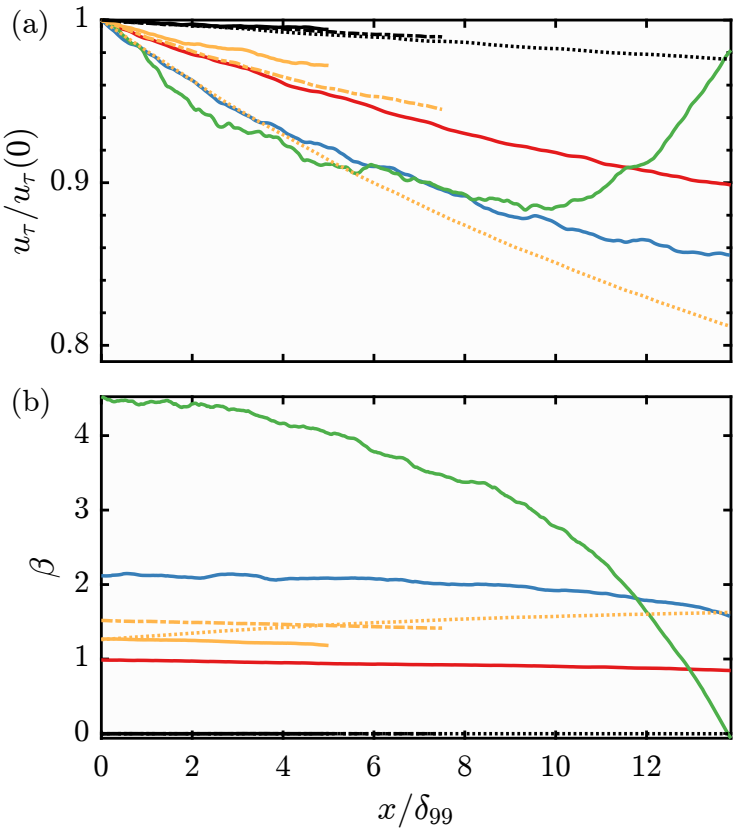

Figure 4.5: $u_\tau/u_{\tau,0}$ (a) and β (b) for the different mean flow fields used in Section 4.3. The colors are labeled in Table 4.2. For the orange and black curves, the dashed, dashed-dot, and solid lines denote the Re_τ = 650, 1200, and 1800 datasets.

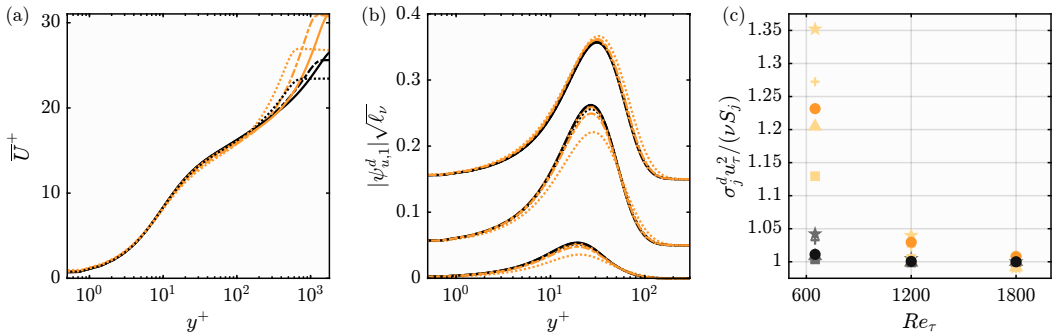

Figure 4.6: $\overline{U}^+$ at the center of the domains (a). Magnitude of $\psi_{u,1}$ in inner units at x = .2, .5, .8, vertically offset for clarity (b). The dotted, dashed-dot, and solid lines denote the Re_τ = 650, 1200, and 1800 domains. σ_j in inner units normalized by S_j, the inner scaled σ_j for the ZPG dataset at Re_τ = 1800 (c). The circle, square, triangle, cross, and star denote j = 1, 2, 3, 4, and 5. j = 1 is plotted in darker colors to aid in visibility.

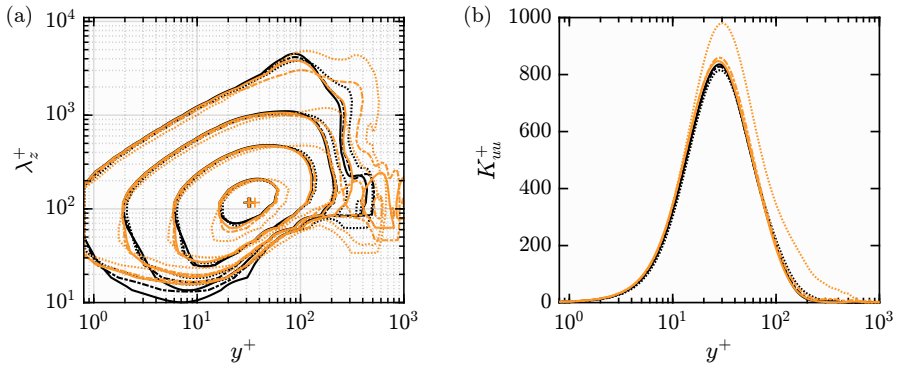

Figure 4.7: $\widehat{E}_{uu}^+(x, y, k_z)$ (a) and $K_{uu}^+(x, y)$ (b) at $x = .7L_x$. The dotted, dashed-dot, and solid lines denote the $Re_\tau = 650$, 1200, and 1800 domains. The contour lines are at 0.62, 6.17, 61.66, 369.96 and the crosses denote the maxima of $\widehat{E}_{uu}^+(x, y, k_z)$.

This is consistent with the observation that as Re_τ increases, the differences in $\overline{U}$ in the log region diminish (Pozuelo et al., 2022) and that APG effects diminish with increasing Re_τ (Deshpande et al., 2023). In Figure 4.6(c), σ_j is plotted in inner units, and normalized by S_j, the inner scaled σ_j for the ZPG dataset at $Re_\tau = 1800$. As Re_τ increases, the ZPG $\sigma_j^d u_\tau^2/\nu$ approach S_j, indicating improved collapse as scale separation increases. This is true for the APG as well, even though there is more significant Re_τ dependence on $\sigma_j^d u_\tau^2/\nu$ than the ZPG.

Just as in Section 3.6, a parameter sweep over k_z^+ and ω^+ is performed to compare E_{uu}^+ from Equation 3.27 in Figure 4.7(a). $E_{uu}^+(.7L_x, y, k_z)$ demonstrates good collapse for $y^+ \leq 100$, with the collapse improving with increasing Re_τ. The near-wall peak is found at $y^+ = 31$, $\lambda_z^+ = 116$. It is expected that for $y^+ > 100$, the inner scaling will not hold because of the departure of the inner scaling in $\overline{U}^+$ under the APG. The smallest scales, $\lambda_z^+ \leq 30$, demonstrate poor collapse for both the ZPG and APG modes because these modes do not span the entire domain and are either localized upstream or downstream of $x = .7L_x$. In Figure 4.7(b), K_{uu}^+ from Equation 3.28 is plotted at $x = .7L_x$. K_{uu}^+ demonstrates the self-similarity for the larger Re_τ in the near-wall region, despite the presence of the APG. The smaller Re_τ modes are affected by the outer region due to the lack of scale separation. Hence, modes computed with smaller Re_τ are affected more by PG effects. Note that because the domains are fixed with $L_x^+ = 9000$, the large scale structures are not supported in this domain so the amplification is only due to modes in the near-wall region. See Appendix D.1 for a discussion on how scales are suppressed with a decrease in L_x^+.

In Figure 4.8, the inner scaling of biglobal resolvent modes with $k_z^+ = 2\pi/100$, $\omega^+ = 2\pi/100$, and $Re_\tau = 650$ are compared for different β. As β increases, the PG

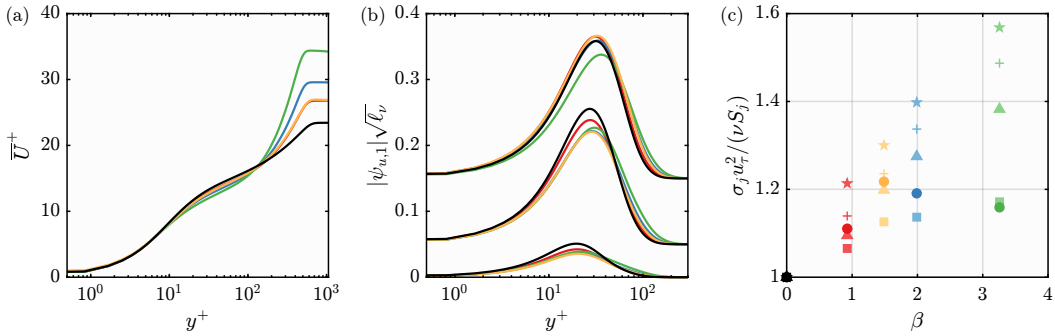

Figure 4.8: $\overline{U}^+$ at the center of the domains (a). Magnitude of $\psi_{u,1}$ in inner units at $x = .2, .5, .8$, vertically offset for clarity (b). σ_j in inner units normalized by S_j, the inner scaled σ_j for the ZPG dataset (c). The circle, square, triangle, cross, and star denote $j = 1, 2, 3, 4$, and 5. $j = 1$ is plotted in darker colors to aid in visibility.

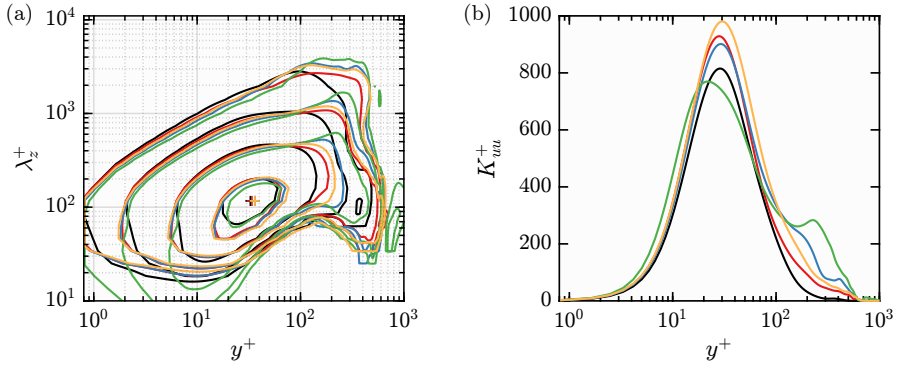

Figure 4.9: $\widehat{E}_{uu}^+(x, y, k_z)$ (a) and $K_{uu}(x, y)$ (b) at $x = .7L_x$. The contour lines are at 0.62, 6.17, 61.66, and 369.96 and the crosses denote the maxima of $\widehat{E}_{uu}^+(x, y, k_z)$.

affects the self-similarity of $\overline{U}^+$ for $y^+ \gtrsim 20$. This affects the self-similarity of $\psi_{u,1}$ as both the peaks and locations vary in Figure 4.9(b). In Figure 4.9(c), σ_j is plotted in inner variables and are normalized by S_j, denoting the inner scaled ZPG σ_j. $\sigma_j^d u_\tau^2/\nu$ demonstrates non-negligible β dependence. This β dependence increases for the higher order j since they have support further from the wall where the APG effects are stronger (not shown). Due to the limited Re_τ, the scale separation of these modes is limited which affects the quality of the inner scaling.

The k_z, ω sweep of Section 3.6 is repeated for the different β at $Re_\tau = 650$ and E_{uu}^+ is plotted in Figure 4.9(a). Although the contours once again map out the near-wall cycle, β affects the scaling of the contours due to the lack of scale separation. The local maxima of the near-wall peak is at $y^+ \approx 33$ and $\lambda_z^+ = 116$. As β increases, E_{uu}^+ increases for larger y^+, indicative of the amplification of outer-scaled structures with increased PG (J. H. Lee, 2017; Sanmiguel Vila et al., 2020). For $\lambda_z^+ \geq 1000$, E_{uu}^+

increases with β, although the contours denote .1% of the maximum E^+_{uu}. Because the large scale structures are not supported in this domain, the large scales are negligible so that E^+_{uu} can be approximated as only the small scales. K^+_{uu} is plotted in Figure 4.9(b) which illustrates the lack of collapse of the near-wall region due to the influence of the PG on the near-wall region. Further from the wall, the K^+_{uu} increases with β, although not monotonically.

The lack of collapse of the small scales was investigated in Sanmiguel Vila et al. (2020)'s experiments where $\overline{uu}$ was computed by only considering small scale fluctuations and noted a lack of collapse in the inner scaled peak as well as increased amplification of the small scales in the outer region of the flow. One key difference between their study and the study done here is that this study is absent of any nonlinear interactions and uses only a rank-1 model for $\overline{uu}$. The nonlinearity, through triadic interactions, can influence the small scales via large scale interactions, present further from the wall. These interactions can excite higher order modes, decreasing the validity of the rank-1 model. Another difference was that their study was performed at $Re_\tau \approx 4300$ which had more scale separation, although a similar range in β. The results shown here suggest that differences in the fluctuations of the small scales in the near-wall region are due to changes in the mean flow field.

4.4 Pressure Gradient Effect on the Amplification of Large Scale Structures

The previous section focused on the amplification of small scale structures near the wall. In this section, the amplification of the large scale structures will now be investigated. Since the goal will be to resolve modes representative of both the near-wall cycle and the outer region, no predetermined scaling will be investigated. The calculations will be performed using the equations described in Equations 2.38 and 2.39, without allowing for streamwise development of ω or k_z. To support the large scale modes, the streamwise domain will be kept as large as possible. First, individual modes are compared using a ZPG and APG TBL mean flow field to generalize the effect of the change in the mean flow field on the modes. Then, the effect of the PG will be compared for all the scales using a sweep over k_z and ω and mean flows with different β.

The mean flow fields are LES from Bobke et al. (2017)'s APG TBLs and Eitel-Amor, Örlü, and Schlatter (2014)'s ZPG TBL. In this section, all length scales and velocity scales are taken with respect to their values at the center of the domain, x_c, where the Re_τ is denoted for each simulation in Table 4.3. Variables without

Domain	Re_τ	Re_τ range	$\overline{\beta}$	β range	max β	$L_x/\delta_{99}(x_0)$	Color
b1n	537	(240, 784)	0.95	(.38, .85)	1.12	43.4	—
b2n	537	(189, 900)	1.62	(.08, −.47)	2.19	43.4	—
m18n	505	(193, 968)	2.81	(.14, −1.30)	4.53	36.5	—
S0I	537	(373, 684)	0	(0, 0)	0	43.4	—

Table 4.3: Names of the mean flow fields in the subdomains with flow parameters and labels. Here, Re_τ range and β range denote the values of Re_τ and β at the inlet and outlet of the subdomains. Max β is the largest β achieved within the domain.

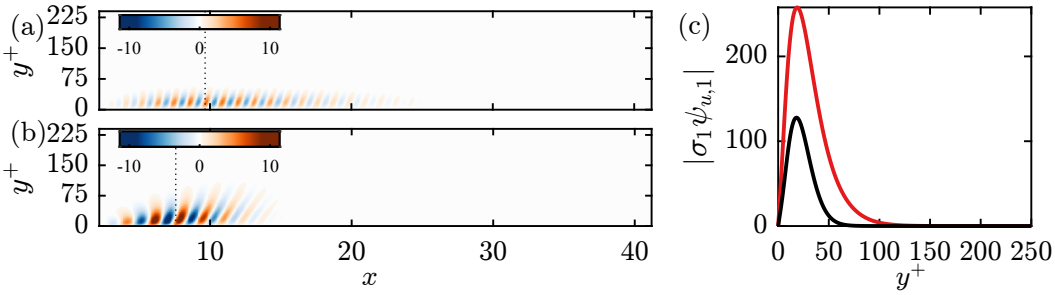

Figure 4.10: $\sigma_1\psi_{u,1}$ using S0I (a) and b2n (b) for $\lambda_z^+ = 50$, $\lambda_t^+ = 50$. The dashed vertical lines denote the streamwise location of the largest amplitude, x_a. Line plots of $\left|\sigma_1\psi_{u,1}(x_a, y)\right|$ (c) for b2n (red) and s0 (black).

superscripts are normalized with respect to $\delta_{99}(x_c)$ and $U_\infty(x_c)$ and variables with + superscripts will be normalized with $\ell_\nu(x_c)$ and $u_\tau(x_c)$. Again, any variables with d superscripts denote dimensional variables. The calculations will use $\epsilon_s = 30$, $N_y = 251$, $y_{max} = 5$, and $y_{min} = .24Re_\tau/537$. $L_x = 43.4$ corresponds to the entire domain length of the full b2n dataset, normalized by $\delta_{99}(x_c)$. This domain length and reference Re_τ were fixed for b1n and S0, which both have larger computational domains in the full dataset than b2n when normalized by $\delta_{99}(x_c)$. The entire domain of m18n is used, which corresponds to $L_x = 36.5$. The y_{min} is slightly closer to the wall in m18n due to the larger Re_τ at the outlet of its domain. $N_x = 900$ for all the datasets, except m18n which uses $N_x = 750$, so that $\Delta x \approx .048$ for all the calculations.

Effect on Individual Modes

First, the effect of the pressure gradient is illustrated for representative small scales, $\lambda_z^+ = 50$ and $\lambda_t^+ = 50$. $\left|\sigma_1\psi_{u,1}\right|$ is plotted for these small scales in Figure 4.10. As explained in Section 3.3, the small scale modes are amplified by the mean shear, and tend to cluster near the areas of largest shear. In the datasets examined here, the APG TBL has significant streamwise evolution for the shear stress compared to the

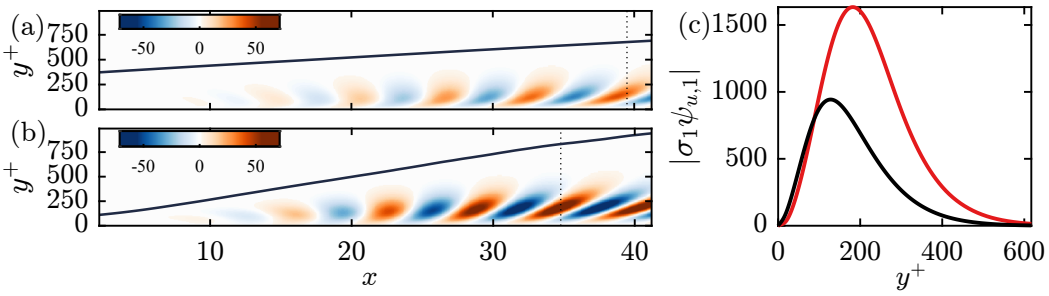

Figure 4.11: $\sigma_1\psi_{u,1}$ using S0I (a) and b2n (b) for $\lambda_z^+ = 537$, $\lambda_t^+ = 200$. The dashed vertical lines denote the streamwise location of the largest amplitude, x_a. The navy blue lines denote the boundary layer thickness. Line plots of $\left|\sigma_1\psi_{u,1}(x_a, y)\right|$ (c) for b2n (red) and s0 (black).

ZPG TBL. For example, $\overline{U}_y(0,0)/\overline{U}_y(L_x,0)$ is 84% for S0 and 17% for b2n. While both modes for S0 and b2n are located in the upstream half of the domain due to the increased non-normal amplification due to the shear, the mode for b2n is mostly congregated in the upstream quarter of the domain. In turn, $\sigma_1\psi_{u,1}$ is negligible at x_c. Most of the shear in the TBL is in the near-wall region that decreases in wall-normal extent with $Re_\tau(x)$. As a result, $\left|\sigma_1\psi_{u,1}\right|$ has more wall-normal extent for b2n than S0 because the local Re_τ is smaller in the former than the latter. The amplification changes as well since $\sigma_1 = 18.99$ (347.08 in friction units) for b2n and $\sigma_1 = 10.96$ (256.80 in friction units) for S0. The changes in the modes can be seen in the line plots in Figure 4.10(c) where $\left|\sigma_1\psi_{u,1}\right|$ is plotted at the streamwise location of its local maxima. If they were plotted with the local friction units, the peak for b2n would be further from the wall. The effects of the streamwise varying shear stress was accounted for in the previous section by introducing a streamwise varying k_z and ω that accounts for the change in the inner scale but is not pursued in this section.

The effect of the PG is now explored for representative large scales, $\lambda_z^+ = 537$, $\lambda_t^+ = 200$, by plotting $\sigma_1\psi_{u,1}$ in Figure 4.11. Here, the modes span the entire streamwise domain, reaching their largest amplitude near the outlet of the domain. These modes are amplified by the convective non-normality, where the forcing is concentrated in the upstream region, as well as the Orr tilting mechanism. Visually, the modes are similar except that b2n extends further from the wall. The amplification is larger for the large scale modes as $\sigma_1 = 561$ (10254 in friction units) for b2n and $\sigma_1 = 280$ (6570 in friction units) for S0. Comparing the line plots, it is evident that the large scale mode for b2n peaks further from the wall with significant support in the outer region of the flow compared to the S0 mode. This is true even if the local friction

units are accounted for. Lastly, the large scale mode has a slightly longer streamwise length scales for b2n than S0.

By comparing the effect on the representative small scales and large scales, two effects stand out. The first is that the streamwise variation in the mean shear changes where the small scale modes will be located. This ultimately changes their amplification and wall-normal extent when the change in the streamwise scales are not accounted for. The second effect is that the large scale structures are amplified under the presence of the APG TBL and are pushed further into the outer region of the flow.

Effect on All Scales

To investigate the effect of the APG on all the scales of the flow, a parameter sweep will be studied. To mitigate the effect of the streamwise variation in $\overline{U}_y$, the response modes will be weighted only in a region near x_c. The inner products are chosen such that

$$\langle \mathbf{a}, \mathbf{b} \rangle_f = \int_0^{L_x} \int_0^{y_{max}} \mathbf{a}^* \mathcal{I}_c \mathbf{b} dy dx, \tag{4.8}$$

and

$$\langle \mathbf{a}, \mathbf{b} \rangle_r = \int_{x_c-2}^{x_c+2} \int_0^{y_{max}} \mathbf{a}^* \mathcal{I}_c \mathbf{b} dy dx. \tag{4.9}$$

The forcing is weighted across the entire domain while the response is only weighted in the region $x \in \Omega_r = (-2 + x_c, x_c + 2)$. Since Ω_r is constant, this will help mitigate effects related to the difference in domain size in m18n. This inner product forces the small scale modes to be centered within Ω_r, where the Re_τ are similar in all four of the mean flow fields examined here. Since the forcing is weighted across the entire domain, the large scale structures are supported upstream and downstream of Ω_r and still have access to the convective non-normality. This was not the case in Section 4.3 where the domain size was limited and the large scales were not supported. The effects of increasing Ω_r are demonstrated in Appendix D.2. Note that apart from the differences in the inner product, the resolvent modes are computed using the same boundary conditions and numerical scheme described in chapter 2.

The effect of this inner product on the leading resolvent modes of b2n is visualized in Figure 4.12 for representative small scales ($\lambda_z^+ = 50$, $\lambda_t^+ = 50$). These modes are compared with modes computed using the inner product in Equation 4.8 for the response modes. When $\langle \cdot, \cdot \rangle_r$ is not constrained, the small scale modes are localized upstream, and takes advantage of the increased amplification due to the larger wall

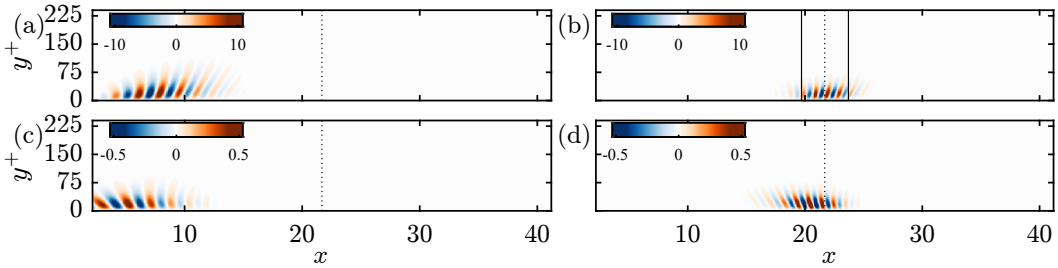

Figure 4.12: Real parts of $\sigma_1\psi_{u,1}$ (a,b) and $\phi_{v,1}$ (c,d) for $k_z^+ = 2\pi/50$, $\omega^+ = 2\pi/50$ with (a,c) computed using $\langle\cdot,\cdot\rangle_r = \langle\cdot,\cdot\rangle_f$ and (b,d) using $\langle\cdot,\cdot\rangle_r$ from Equation 4.9. The dashed vertical line denotes x_c and the solid vertical lines in (b) denote Ω_r.

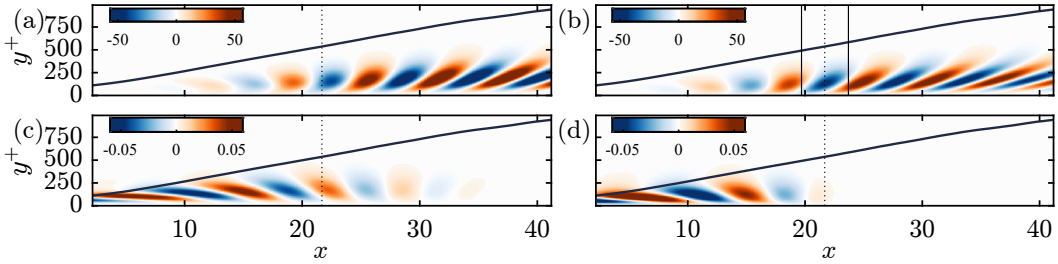

Figure 4.13: Real parts of $\sigma_1\psi_{u,1}$ (a,b) and $\phi_{v,1}$ (c,d) for $k_z^+ = 2\pi/Re_\tau(x_c)$, $\omega^+ = 2\pi/200$ with (a,c) computed using $\langle\cdot,\cdot\rangle_r = \langle\cdot,\cdot\rangle_f$ and (b,d) using $\langle\cdot,\cdot\rangle_r$ from Equation 4.9. The dashed vertical line denotes x_c and the solid vertical lines in (b) denote Ω_r. The navy blue lines denote the boundary layer thickness.

shear stress in that region. When Equation 4.9 is used as the inner product for the response modes, the modes are now constrained within the region of interest, Ω_r. These modes are closer to the wall than the latter because they take advantage of the amplification due to shear in the near-wall region which shrinks in the wall-normal direction as Re_τ increases downstream.

In Figure 4.13, leading resolvent modes with representative large scales ($\lambda_z^+ = Re_\tau(x_c)$, $\lambda_t^+ = 200$) are compared using the two inner products. The large scale modes both have support outside of Ω_r and are in the outer region. These modes display a strong convective non-normality with the forcing upstream of the response. The effect of using the inner product in Equation 4.9 for the resolvent modes is to constrain the forcing to have no support downstream of Ω_r since amplification of the response downstream of Ω_r will not increase σ_1. As a result, the response has a smaller amplitude near the outlet of the domain compared to the response mode computed without the constraint on the inner product. Although Ω_r is smaller than the domains used in Section 4.3, the large scales are supported because $\langle\cdot,\cdot\rangle_f$ allows for amplification from the convective non-normality.

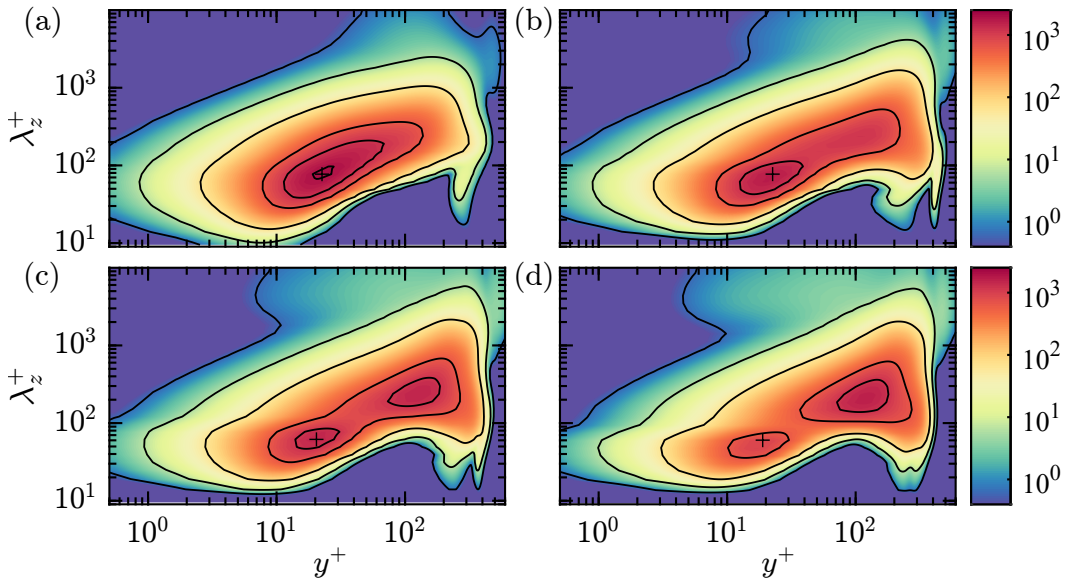

Figure 4.14: Contour maps of $E_{uu}^+(x, y, k_z)$ for S0 (a), b1n (b), b2n (c), and m18n (d) at $x = x_c$. The black contour lines denote $E_{uu}^+ = .62, 6.17, 61.66, 616.62, 1950$. The black crosses denote the near-wall peaks.

A sweep is computed using 31 logarithmically spaced k_z^+ between $2\pi/9.5$ and $2\pi/11000$ and 33 logarithmically spaced ω^+ between $2\pi/1.25$ and $2\pi/20000$. This sweep encompasses both the small and large scales.

In Figure 4.14, $E_{uu}^+(x_c, y^+, k_z^+)$ is plotted for the four mean flow fields in Table 4.2. For S0, the peak in the amplification is concentrated in the near-wall region, with the local maxima near $y^+ \approx 20$ and $\lambda_z^+ \approx 77$. Although E_{uu}^+ is larger in the outer region for large scales than the sweep for S0I1 in Figure 4.7, there is no semblance of an outer scaled peak, as is expected for this Re_τ. The results using b1n, b2n, and m18n also have a near-wall peak occurring at $y^+ \approx 20$ and $\lambda_z^+ \approx 77$ for b1n and $\lambda_z^+ \approx 60$ for b2n and m18n. The spectral location of the near-wall peaks in these sweeps are lower than the peaks seen in Figures 3.11, 4.7, and 4.8.

Using the APG TBL mean flow fields, the sweeps reveal the presence of a secondary peak with larger scale structures further from the wall that increase in amplitude with $\overline{\beta}$. A similar secondary peak has been observed in the premultiplied energy spectra in simulation, where the peak is amplified with increasing pressure gradient strength (J. H. Lee, 2017; Bobke et al., 2017; Pozuelo et al., 2022). Here, the secondary peak is at $y^+ \approx 150$ and $\lambda_z^+ \approx 150$. The premultiplied energy spectra of J. H. Lee (2017) at $Re_\tau \approx 360$ find the secondary peak at $y^+ \approx 100 - 150$ and $\lambda_z^+ \approx 340$ while Bobke et al. (2017) finds the secondary peak at $y^+ \approx 200$ and

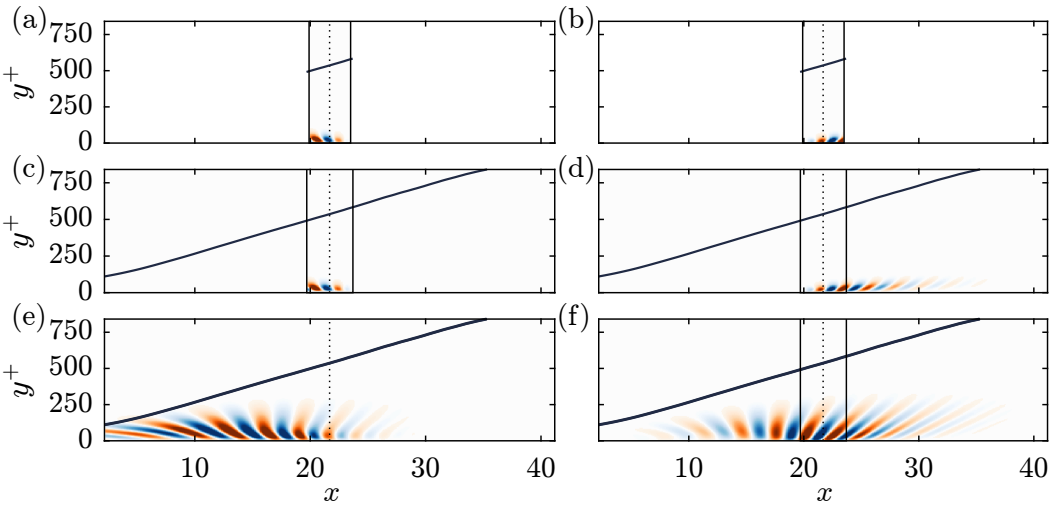

Figure 4.15: Real components of $\phi_{v,1}$ (a,c,e) and $\psi_{u,1}$ (b,d,f) for $\lambda_z^+ = 50$ and $\lambda_t^+ = 50$ using b2n. (a,b) are computed with domain length of $L_x = 4$. Using the entire domain, (c,d) are computed using the inner product in Equation 4.9 for both the forcing and response and (e,f) are computed using the inner products in Equations 4.8 and 4.9. The navy blue line denotes the boundary layer thickness and the vertical lines denote the edges of Ω_r, where it is used.

$\lambda_z^+ \approx 580$ for $Re_\tau \approx 730$ for similar β explored here. Note that the spectra in the latter study are not the spectra of the simulations for b1n, b2n, and m18n. Although the prediction of the wall-normal location of the secondary peak from the linear analysis agrees with the location of the premultiplied energy spectra, the value of λ_z^+ is under predicted.

The underprediction of λ_z^+ in the near-wall peaks in Figure 4.14 compared to data and the near-wall peaks of Section 4.3 is likely due to a change in length scale. Both $\ell_\nu(x)$ and $\delta_{99}(x)$ vary significantly for the APG TBLs. In Figures 4.12 and 4.13, it was shown that $\boldsymbol{\phi}$ for the small scales is localized within Ω_r and localized near the inlet for the large scales due to the convective non-normality. This suggests that for the large scales, the length scales of interest $(\ell'_\nu, \delta'_{99})$ are defined upstream. This corresponds to $\ell'_\nu > \ell_\nu(x_c)$ and $\delta'_{99} < \delta_{99}(x_c)$. This is shown in Figure 4.15 for $\lambda_z^+ = 100$, $\lambda_t^+ = 100$ where $\psi_{u,1}$ and $\phi_{v,1}$ are computed using a domain of length $L_x = 4$, the full domain with $\langle \cdot, \cdot \rangle_f = \langle \cdot, \cdot \rangle_r$, and the inner product used in the sweeps for b2n. If $\boldsymbol{\phi}$ and $\boldsymbol{\psi}$ are restricted using either a small domain size or a smaller interrogation window for the inner product, the resolvent modes are found near the wall and represent small scales. When the forcing is not restricted, the resolvent modes have support in the outer region of the flow. $\boldsymbol{\phi}_1$ has the largest amplitude near the inlet. If δ'_{99} is computed at the inlet, then $\lambda_z^d/\delta'_{99} = 1.2$ suggesting that

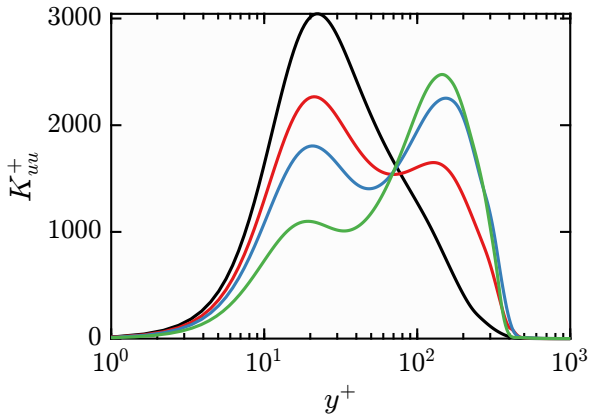

Figure 4.16: K^+_{uu} at $x = x_c$ for the sweeps using the mean flow field color coded in Table 4.2.

this $\lambda^+_z = 100$ mode behaves like an outer scaled mode near the inlet. This outer scaled behavior is seen in Figures 4.15(e,f) where the wall-normal extent of the mode extends to the edge of the boundary layer. Because the $\lambda^+_z \approx 100$ modes are no longer supported near the wall, they are absent in the near-wall peak. The only modes present near the wall are the smaller λ^+_z modes like the one plotted in Figure 4.12. For the outer peak, since the large scale modes are also forced by the inlet, they likely scale with δ'_{99} as opposed to $\delta_{99}(x_c)$ to account for the smaller boundary layer thickness. As a result, the outer peak corresponds to $\lambda_z < .5\delta_{99}(x_c)$ unlike the $\lambda_z \gtrsim .8\delta_{99}(x_c)$ reported in the literature. The discrepancies in the length scale could be accounted for by incorporating a streamwise varying λ^d_z and ω^d as was done in Chapter 3 and Section 4.3, but since the near-wall region and outer region are governed by different scales, the scale would have to be k_z and ω dependent. Despite the changes in the scale, the sweep is able to identify two distinct peaks corresponding to the near-wall cycle and the outer scales.

In Figure 4.16, the K^+_{uu} are plotted for the different sweeps. K^+_{uu} has a single peak for S0 while b1n, b2n and m18n have two peaks. The lack of a secondary peak in S0 is expected since the Re_τ is too small to observe energetic fluctuations in the outer region of the flow in turbulent flows. Since these sweeps did not account for the streamwise development of the inner scales within the domains, there is a lack of inner scaled collapse in the near-wall peak. Furthermore, the secondary peaks increase in magnitude as $\overline{\beta}$ increases. The secondary peak is larger than the near-wall peak for b2n and m18n. The existence of a secondary peak that increases with β and can surpass the inner peak in the streamwise fluctuations has been observed in various studies (Bobke et al., 2017; Pozuelo et al., 2022; J. H. Lee, 2017; Monty,

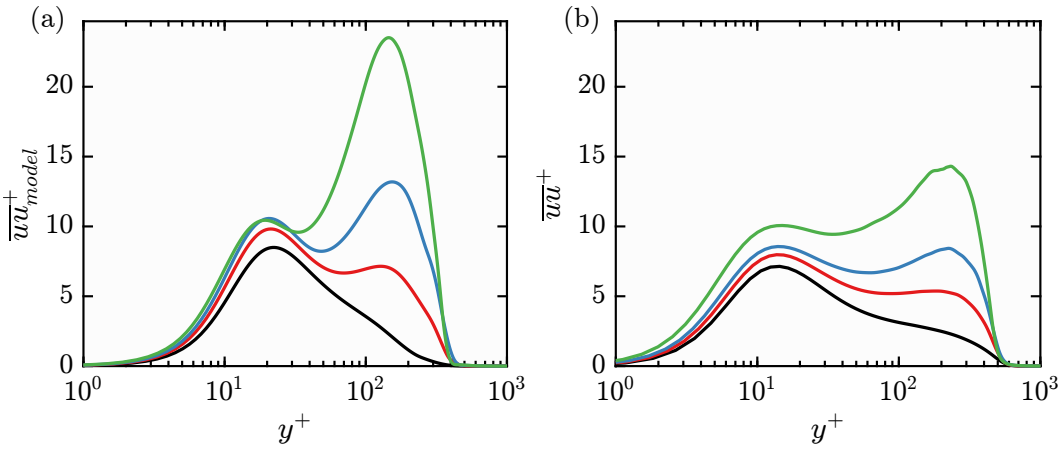

Figure 4.17: $\overline{uu}^+_{model}$ (a) and $\overline{uu}^+$ from the LES datasets (b) at $x = x_c$.

Harun, and Marušić, 2011). This effect is predicted in the optimal responses of the linear operator without the use of nonlinear weights or eddy viscosity.

To compare the linear results quantifiably to turbulent data, an assumption will be made on the linear weights. It is assumed that the velocity fluctuations are defined as a rank-1 model with, $\widehat{\mathbf{q}}(x, y; \omega, k_z) = \sigma_1(\omega, k_z)\xi_1(\omega, k_z)\boldsymbol{\psi}_1(x, y; \omega, k_z)$, where $\xi_1(\omega, k_z)$ is the nonlinear weight of the leading response mode at each frequency-wavenumber pair. ξ_1 will be the same for all ω and k_z and positive so that its value will simply make $\sigma_1(\omega, k_z)\xi_1(\omega, k_z)\boldsymbol{\psi}_1(x, y; \omega, k_z)$ have units of velocity. The units of ξ_1^d are $\left[U^3/\sqrt{L}\right]$. It will be assumed that the modeled velocity fluctuations, $\widehat{u}^d$, scale with $\sqrt{u_\tau U_\infty}$, which has been used as a scaling for the inner peak of the streamwise turbulent intensity (Marušić and Kunkel, 2003; Aubertine and Eaton, 2005). Assuming this scaling, $\xi_1^d = u_\tau^3\sqrt{u_\tau/\nu}\xi_1^+$, where $\xi_1^+ = 1/\sqrt{15}Re/Re_\tau$. The factor Re/Re_τ, where $Re = \delta_{99}U_\infty/\nu$, accounts for the assumed mixed scaling while $1/\sqrt{15}$ is a normalization constant. The rank-1 modeled turbulence intensity is then

$$\begin{aligned}\overline{uu}^+_{model}(x, y) &= \int_{k^+_{z,min}}^{k^+_{z,max}} \int_{\omega^+_{min}}^{\omega^+_{max}} \left|\xi_1^+\sigma_1^+(k_z^+, \omega^+)\psi^+_{u,1}(x, y; k_z^+, \omega^+)\right|^2 d\omega^+ dk_z^+ \\ &= \int_{k^+_{z,min}}^{k^+_{z,max}} \int_{\omega^+_{min}}^{\omega^+_{max}} \left|\frac{Re}{\sqrt{15}Re_\tau}\sigma_1^+(k_z^+, \omega^+)\psi^+_{u,1}(x, y; k_z^+, \omega^+)\right|^2 d\omega^+ dk_z^+.\end{aligned} \tag{4.10}$$

In Figure 4.17, $\overline{uu}^+_{model}$ is compared with $\overline{uu}^+$ from the LES datasets at the $x = x_c$. By using the modeled scaling for ξ_1, the magnitudes of $\overline{uu}^+_{model}$ increase with $\overline{\beta}$ as in $\overline{uu}^+$. The secondary peaks are over predicted with this model, but they follow a similar trend as the data. The weights, ξ_1 were determined using only arguments

Domain	Re_τ range	$\beta(x_r)$	$\overline{\beta}$	β range	$\overline{\beta}_\infty$	Color
m13nH	$(507, 840)$	0.91	1.01	$(1.23, 0.69)$	1.01	—
b1nH	$(535, 832)$	0.78	0.86	$(1.00, 0.32)$	0.88	—
m18nH	$(368, 952)$	2.09	3.27	$(3.80, -1.05)$	3.25	—
m16nH	$(417, 873)$	1.66	2.09	$(2.77, 0.39)$	2.10	—
b2nH	$(451, 869)$	1.56	1.82	$(2.18, 0.10)$	1.91	—
P14H	$(553, 826)$	1.65	1.54	$(1.25, 1.64)$	1.34	—
S0IH	$(654, 804)$	0	0	$(0, 0)$	0	—

Table 4.4: Names of the mean flow fields in the subdomains with flow parameters and labels. Here, Re_τ range and β range denote the values of Re_τ and β at the inlet and outlet of the subdomains. The domain length is $L_x = 15.89$ and $Re_\tau(x_r) = 777$.

for the near-wall peak. A more complete model ought to include a ω, k_z dependent weighting that accounts for the scaling of the outer peaks, but is not investigated further.

4.5 History Effects on the Amplification of Large Scale Structures

APG TBL are locally parameterized by Re_τ, β, and the streamwise history of the APG, denoted by $\beta(x)$ here. In Section 4.3, the effects of Re_τ and β were investigated for the small scales. In Section 4.4, the effect of β on the large scales was investigated for low Re_τ flows. Here, the effect of $\beta(x)$ on the large scale amplification is studied. The APG TBL datasets are from Pozuelo et al. (2022) and Bobke et al. (2017) where several mean flow fields have similar values of β at $Re_\tau(x_r) = 777$. The relevant length and velocity scales are defined at x_r and variables without superscripts denote quantities nondimensionalized by $\delta_{99}(x_r)$ and $U_e(\delta_{99})$. The domains are chosen to be the same size, where $x \in [x_r - .81L_x, x_r + .19L_x]$ and $L_x = 15.89$. The domains have a larger upstream region relative to x_r to incorporate the upstream $\beta(x)$ effects. The computational details are $y_{max} = 5$, $y_{min} = 0.2257$, $N_y = 251$, $N_x = 450$, and $\epsilon_s = 30$ for all the domains of interest. There is no masking applied in the inner products so that the resolvent modes are weighted across the entire domain. Details for each of the datasets are in Table 4.4.

In Figure 4.18(a), the $Re_\tau(x)$ and $\beta(x)$ of the APG TBL mean flow fields are plotted. The datasets m13nH and b1nH have similar values of $\beta(x)$ and $\beta(x_r)$ across the domain, with their values diverging near the inlet and outlets of the domains. The datasets m16nH, b2nH, and P14H have similar values of $\beta(x_r)$ but different $\beta(x)$. Datasets m16nH and b2nH have decreasing $\beta(x)$, and similar $\beta(x)$ for a few δ_{99} upstream of x_r, while P14H has increasing $\beta(x)$. While m18nH and S0IH have

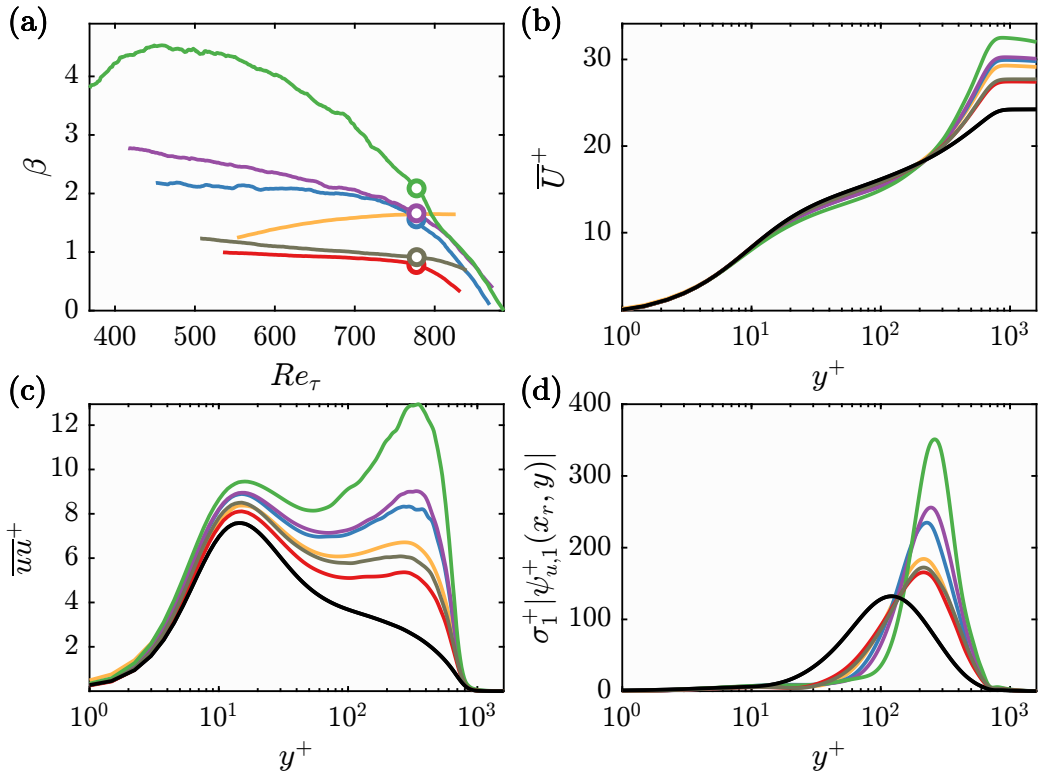

Figure 4.18: β and Re_τ for the domains described in Table 4.4 (a). The circles denote $Re_\tau(x_r)$. $\overline{U}^+(x_r, y^+)$ (b), $\overline{uu}^+(x_r, y^+)$ (c), and $\left|\sigma_1^+\psi_{u,1}(x_r, y^+)\right|$ for $\lambda_z = 2, \lambda_t = 4.48$. The colors are color coded according to Table 4.4.

different values of $\beta(x)$ than the other datasets, they are used to investigate the effects of large β and $\beta = 0$, respectively, on the large scales. m18nH and m16nH have similar values of $\beta(x)$ near the outlet of the domain, but these regions are not compared since they are close to the fringe regions in the LES of Bobke et al. (2017) where the statistics of the flow are expected to be contaminated. These downstream fringe regions are treated with the sponges in the analysis described here.

In Figure 4.18(b), $\overline{U}^+(x_r, y^+)$ is plotted for the different datasets. The datasets with similar $\beta(x_r)$ have similar $\overline{U}^+(x_r, y^+)$ (Bobke et al., 2017), which is unsurprising considering that β is an integral measure of $\overline{U}$. On the other hand, $\overline{uu}^+(x_r, y^+)$ is sensitive to $\beta(x)$ in the outer region of the flow. For example, $\overline{uu}^+$ of b2nH and m16nH are almost matched while for P14H, $\overline{uu}^+$ is significantly lower in the outer region. The changes in $\overline{uu}^+$ have been argued to be an effect of the accumulated $\beta(x)$ upstream of x_r (Bobke et al., 2017). $\beta(x)$ is almost identical for about $6\delta_{99}$ upstream of x_r for b2nH and m16nH while P14H experiences lower $\beta(x)$ values upstream of x_r. For the datasets used here, the relative magnitudes of $\overline{uu}^+$ in the outer region

increased with $\overline{\beta}$, the streamwise averaged β. Comparing $\sigma_1^+\left|\psi_{u,1}^+(x_r, y^+)\right|$ for a representative large scale, $\lambda_z = 2, \lambda_t = 4.48$, reveals a similar trend in the peaks in Figure 4.18(d). For increasing $\overline{\beta}$, the peak also moves further from the wall. $\sigma_1^+\left|\psi_{u,1}^+(x_r, y^+)\right|$ for S0IH also demonstrates smaller amplification closer to the wall indicative of different linear amplification in the wake as was shown in Figure 4.2.

The use of a streamwise averaged $\beta(x)$ to reflect the accumulated effects of the history has been explored in Vinuesa et al. (2017) as a parameter in an empirical correction of the skin friction coefficient correlation for ZPG TBL, $C_f(Re_\theta)$m to incorporate APG effects. In that study, the streamwise averaged β denotes

$$\overline{\beta}_V(Re_\theta) = \frac{1}{Re_\theta - Re_{\theta,0}} \int_{Re_{\theta,0}}^{Re_\theta} \beta(Re_\theta) dRe_\theta, \tag{4.11}$$

where $Re_{\theta,0}$ is a reference Re_θ. The use of $\overline{\beta}_V(Re_\theta)$ helped compare local quantities in the TBLs and accounted for the effect of upstream history effects. Here, the history effects are studied for σ_1, the global linear amplification of the domain. As a result, $\overline{\beta}$ is an average over the entire domain rather than a streamwise varying quantity such that

$$\overline{\beta} = \frac{1}{L_x} \int_0^{L_x} \beta(x) dx. \tag{4.12}$$

An average over Re_θ is not used since the momentum thickness was not considered as a length scale nor was Re_θ used to parameterize the domains.

As described in Equation 1.1, β is defined with respect to dP/dx defined at δ_{99}. Although this is a good measure for the pressure gradient in the freestream for experiments, this is not the pressure gradient imposed in the freestream as a boundary condition in simulations (Pozuelo et al., 2022). Here, $\beta_\infty = \delta^*/\tau_w dP_\infty/dx$ where dP_∞/dx is the pressure gradient at $y^d = 2\delta_{99}(x_r)$ will be used for the remainder of the section since it accounts for the pressure gradient in the freestream. $y^d = 2\delta_{99}(x_r)$ is approximately the edge of the computational domain in the LES studies of Bobke et al. (2017). The difference between $\overline{\beta}$ and $\overline{\beta}_\infty$ are most significant in P14H since the original LES used a significantly taller computational domain than the other simulations causing U_e and U_∞ to differ most significantly.

In Figure 4.19, σ_1 is plotted for some k_z and ω representative of large scale structures for the different $\overline{\mathbf{U}}$ described in Table 4.4. In Figures 4.19(a,b), monotonic growth in σ_1 is observed with both $\overline{\beta}$ and $\overline{\beta}_\infty$. These Figures include lines of best fit between σ_1 and $\overline{\beta}$ or $\overline{\beta}_\infty$ for the APG cases. σ_1 from S0H is not included in the linear fit since

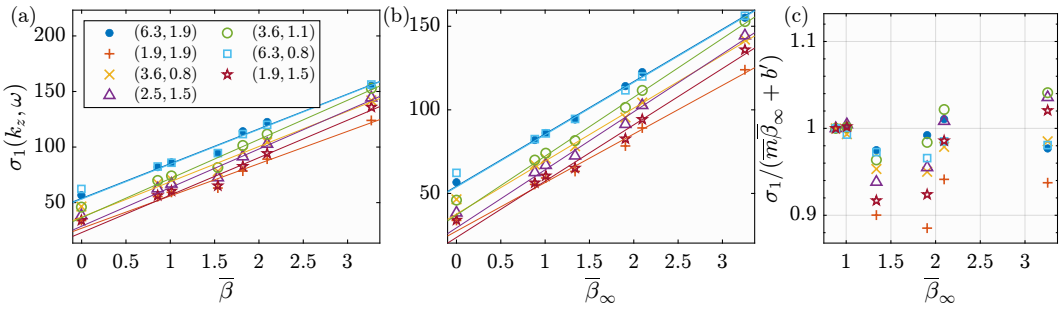

Figure 4.19: σ_1 for the (k_z, ω) labeled in the legend against $\overline{\beta}$ (a) and $\overline{\beta}_\infty$ (b). The lines are the lines of best fit for each k_z, ω, fitted for σ_1 with $\overline{\beta} > 0$. $\sigma_1(k_z, \omega)$ normalized by $\overline{m}\overline{\beta}_\infty + b'(k_z, \omega)$ for $\overline{\beta} > 0$ (c).

the large scale modes follow different amplification mechanisms, as was shown in Figure 4.18. The $\sigma_1(k_z, \omega)$ of P14H falls below the empirical linear growth of the other datasets when plotted using $\overline{\beta}$. On the other hand, using $\overline{\beta}_\infty$ shifts $\sigma_1(k_z, \omega)$ computed with the P14H dataset so that the linear fit improves, which may be due to $\overline{\beta}_\infty$ accounting for the changes in $\overline{\mathbf{U}}$ imposed by the freestream boundary conditions. The norm of residuals, averaged over the (k_z, ω) plotted in Figures 4.19(a,b), is 9.7 using $\overline{\beta}$ and 5.1 using $\overline{\beta}_\infty$ demonstrating an improved linear fit with $\overline{\beta}_\infty$. The lines of best fit, $\tilde{\sigma}(\overline{\beta}_\infty, k_z, \omega) = m(k_z, \omega)\overline{\beta}_\infty + b(k_z, \omega)$, have k_z and ω dependent slopes and intercepts. To mitigate the scale dependence, the lines are consolidated into

$$\overline{\sigma}(\overline{\beta}_\infty, k_z, \omega) = \overline{m}\left(\overline{\beta}_\infty - \overline{\beta}_{\infty,0}\right) + \sigma_{1,0}(k_z, \omega), \tag{4.13}$$

where $\overline{m}$ denotes the k_z and ω averaged $m(k_z, \omega)$ and $\overline{\beta}_{\infty,0}$ and $\sigma_{1,0}(k_z, \omega)$ denote the $\overline{\beta}_\infty$ and $\sigma_1(k_z, \omega)$ computed using the b1nH mean flow field. The reference dataset is arbitrary. In Figure 4.19(c), $\sigma_1(k_z, \omega)/\overline{\sigma}(\overline{\beta}_\infty, k_z, \omega)$ showing that the consolidated line of best fit agrees with the actual values to around 90% accuracy.

In Figure 4.20, $\left|\sigma_1(k_z, \omega)/\overline{\sigma}(\overline{\beta}_\infty, k_z, \omega) - 1\right|$ is plotted to visualize the λ_z and λ_t that deviate from the proposed linear growth. $\overline{\sigma}$ agrees best with σ_1 for $\lambda_z > 1$. It is expected that the agreement would deteriorate for smaller scale modes since they have more support closer to the wall, away from the wake where the amplification mechanisms are most sensitive to APG effects. For these scales, using a scale dependent slope in $\overline{\sigma}$ would be most appropriate. It was checked that the growth in $\sigma_1(k_z, \omega)$ was monotonic with $\overline{\beta}_\infty$ for the range of k_z and ω tested here.

The linear growth observed in σ_1 with $\overline{\beta}_\infty$ is related to the y dependent hybrid velocity scale,

$$U_h^2(y) = u_\tau^2 + \frac{y^d}{\rho^d}\frac{dP^d}{dx^d} = u_\tau^2\left(1 + \frac{y}{\delta^*}\beta\right), \tag{4.14}$$

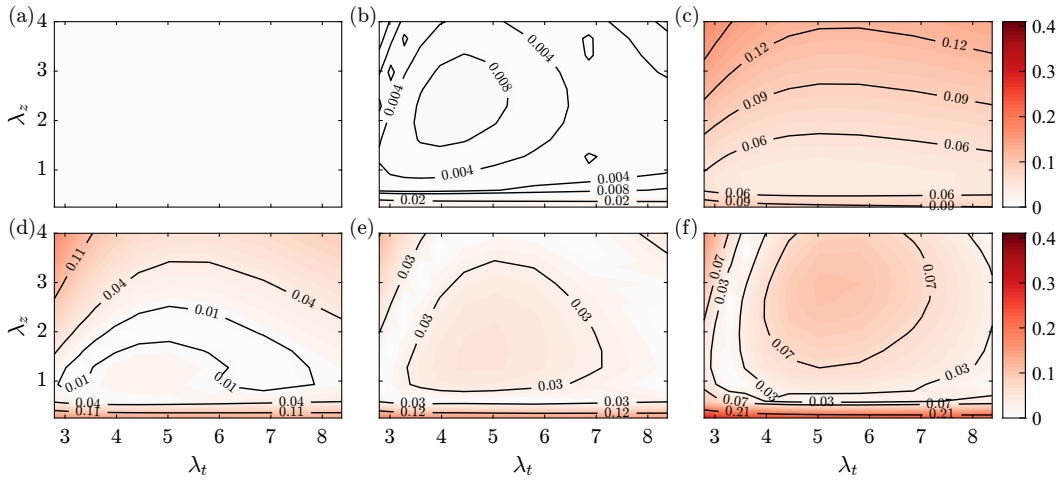

Figure 4.20: Contour maps of $\left|\sigma_1(k_z,\omega)/\overline{\sigma}(\overline{\beta}_\infty,k_z,\omega)-1\right|$ against λ_z and λ_t. (a-f) denote b1nH, m13nH, P14H, b2nH, m16nH, m18nH. The color axis is fixed in all the plots.

which has been shown to suppress the secondary peaks in $\overline{uu}$ (Romero et al., 2022; Sekimoto et al., 2019). Here, a global hybrid velocity scale analogous to U_h is defined as

$$U_{hyb}^2(y;\overline{\beta}_\infty)=\overline{u}_\tau^2\left(1+\frac{y}{\overline{\delta^*}}\overline{\beta}_\infty\right), \tag{4.15}$$

where $\overline{u}_\tau$ and $\overline{\delta^*}$ are the streamwise averages of u_τ and δ^*. Note that U_{hyb} does not come from the mean momentum equation since U_{hyb}^2 is not the streamwise average of U_h^2. This velocity scale can be shown to relate to $\overline{\sigma}$ by setting $\sigma_{1,0}-\overline{m}\overline{\beta}_{\infty,0}=b'$ in Equation 4.13 and manipulating $\overline{\sigma}$ as

$$\overline{\sigma}=b'\left(\frac{\overline{m}}{b'}\overline{\beta}_\infty+1\right). \tag{4.16}$$

By identifying $\overline{m}/b'$ as $y_m/\overline{\delta^*}$ for some wall-normal distance y_m and using Equation 4.15, Equation 4.16 can be written as

$$\overline{\sigma}=b'\frac{U_{hyb}^2(y_m;\overline{\beta}_\infty)}{\overline{u}_\tau^2}. \tag{4.17}$$

The linear growth is related to U_{hyb}^2 at $y_m/\delta^*=\overline{m}/b'$. This ratio is independent of $\overline{\beta}_\infty$ and is k_z,ω dependent because of $\sigma_{1,0}$ in b'.

Due to the similarities between $\overline{\sigma}$ and U_{hyb}, a model for the amplification is constructed as

$$\overline{\sigma}_m(\overline{\beta}_\infty,k_z,\omega)=\sigma_{1,0}(k_z,\omega)\left(\frac{1+\overline{\beta}_\infty}{1+\overline{\beta}_{\infty,0}}\right)=\sigma_{1,0}\frac{\overline{u}_{\tau,0}^2U_{hyb}^2(\delta^*,\overline{\beta}_\infty)}{\overline{u}_\tau^2U_{hyb}^2(\delta_0^*,\overline{\beta}_{\infty,0})}, \tag{4.18}$$

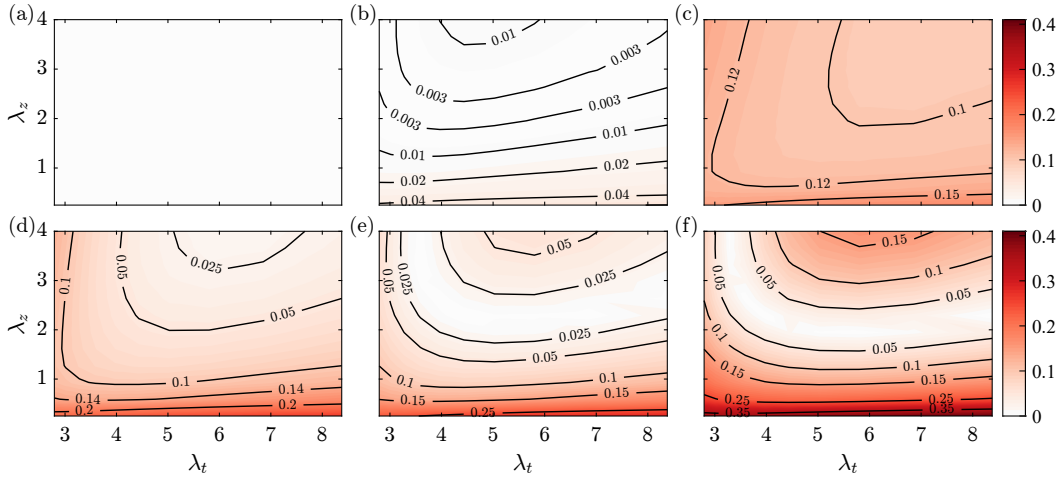

Figure 4.21: Contour maps of $\left|\sigma_1(k_z,\omega)/\overline{\sigma}_m(\overline{\beta}_\infty,k_z,\omega)-1\right|$ against λ_z and λ_t. (a-f) denote b1nH, m13nH, P14H, b2nH, m16nH, m18nH. The color axis is fixed in all the plots.

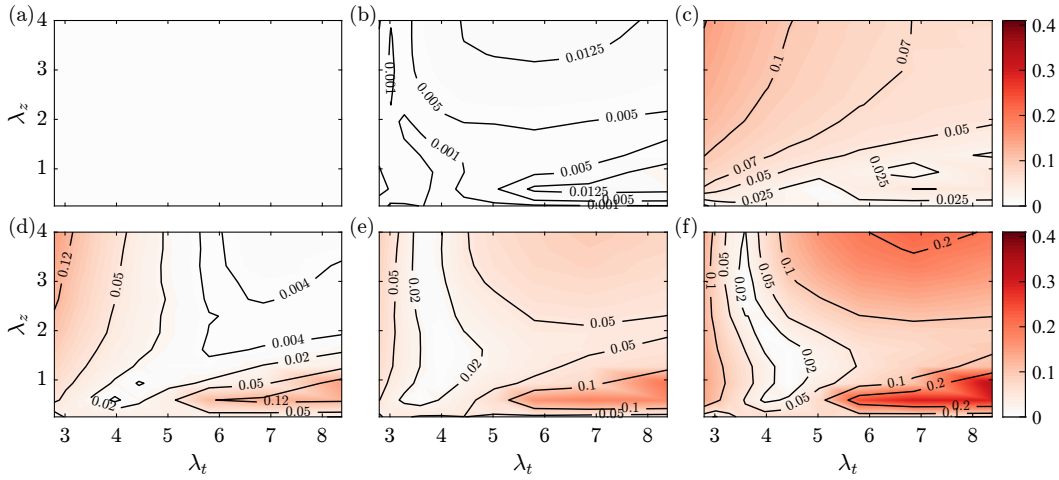

Figure 4.22: Contour maps of $\left|\sigma_1(k_z,\omega)/\tilde{\sigma}_m(\overline{\beta}_\infty,k_z,\omega)-1\right|$ against λ_z and λ_t. (a-f) denote b1nH, m13nH, P14H, b2nH, m16nH, m18nH. The color axis is fixed in all the plots.

where $\overline{u}_{\tau,0}$ and δ_0^* are evaluated from b1nH. This model does not require any fitting, it depends on quantities computed from the mean flow field and $\sigma_{1,0}$. The ratio uses U_{hyb} evaluated at δ^* rather than a suitably defined y_m.

In Figure 4.21, $\left|\sigma_1(k_z,\omega)/\overline{\sigma}_m(\overline{\beta}_\infty,k_z,\omega)-1\right|$ is plotted. Once again, $\lambda_z < 1$ have the worst agreement because a scale-independent slope is used. Overall, the scaling with $\overline{\sigma}_m$ is worse than using $\overline{\sigma}$ however the latter requires fitting to the computed σ_1 for the different $\overline{\beta}$.

Using a well defined y_m instead of δ^* produces a scale dependent slope for $\overline{\beta}_\infty$ as was used in Figure 4.19(b) that can improve the predictions. $y_m(k_z, \omega)$ is chosen as the wall-normal location of the maximum of $\left|\psi_{u,1}(x, y; k_z, \omega)\right|$ of b1nH. The model in Equation 4.18 is altered such that

$$\tilde{\sigma}_m(\overline{\beta}_\infty, k_z, \omega) = \sigma_{1,0}(k_z, \omega)\left(\frac{1 + \frac{y_m(k_z,\omega)}{\delta^*}\overline{\beta}_\infty}{1 + \frac{y_m(k_z,\omega)}{\delta^*}\overline{\beta}_{\infty,0}}\right). \tag{4.19}$$

The performance of the $\tilde{\sigma}_m$ model is plotted in Figure 4.22. Using $\tilde{\sigma}_m$ provides a slight improvement from $\overline{\sigma}_m$. Notably it mitigates the disagreements for $\lambda_z < 1$. The models described in Equations 4.18 and 4.19 require no fitting to reasonably predict the amplification at larger $\overline{\beta}_\infty$. They also illustrate the linear growth of σ_1 with $\overline{\beta}_\infty$. Using $\tilde{\sigma}_m$ also highlights the importance of incorporating a scale-dependent slope to accurately capture the linear growth.

The scaling of σ_1 with u^2_{hyb} indicates that U_{hyb} may be an appropriate velocity scale for the linear amplification. Here, the scaling was investigated for mean flow fields with similar Re_τ distributions and matched outer scaled k_z and ω, but different $\overline{\beta}_\infty$. It is possible that a different choice of scaling for k_z and ω may improve the scaling with U_{hyb} similar to how appropriate scalings were investigated in Chapter 3. However, U_{hyb} only helps remove APG-related features in the outer region of the Reynolds stresses and does not necessarily collapse the statistics nor terms in the RANS (Sekimoto et al., 2019; Romero et al., 2022). Furthermore, the analysis does not present an appropriate outer length scale to couple with U_{hyb}. Romero et al. (2022) notes that U_h and U_m from Section 4.2 are related. However, the WK outer scaling used $U_e - U_m$ as the velocity scale. These issues suggest that scaling for k_z and ω to produce a self-similar linear operator using U_{hyb} is unlikely.

U_{hyb} is used as a velocity scale for K^+_{uu} from Section 4.4 since the outer scaled peak increased with $\overline{\beta}$ and is related to the increased amplification in $\sigma_1(k_z, \omega)$ for modes in the outer region. Since K^+_{uu} has $\sigma^2_1(k_z, \omega)$ in the integrand, it is rescaled by $u^4_\tau/U^4_{hyb}(y)$. Figure 4.16 is replotted and rescaled in Figure 4.23. $K^+_{uu}u^4_\tau/U^4_{hyb}$ demonstrates suppressed secondary peaks much like how rescaling $\overline{uu}$ with $U_h(y)$ suppresses the secondary peaks (Sekimoto et al., 2019; Romero et al., 2022). Although $\overline{uu}$ is rescaled by U^2_h, K^+_{uu} is rescaled by U^4_{hyb} due to the σ^2_1 dependence on K^+_{uu}. Recovering the U^2_h scaling for K^+_{uu} in the outer region requires the choice of an appropriate weight, ξ. Nonetheless, Figure 4.23 demonstrates that a pressure related scaling from U_{hyb}, or $1 + \overline{\beta}_\infty$, explains the increased linear amplification with $\overline{\beta}_\infty$ in the outer region.

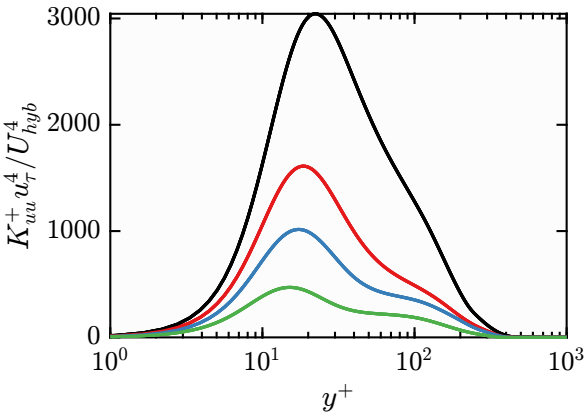

Figure 4.23: K^+_{uu} from Figure 4.16 rescaled with $u^4_\tau/U^4_{hyb}(y)$.

Finally, it is important to note that the results shown here used a limited set of datasets, primarily with small Re_τ. Furthermore, the β variation throughout the domain is small. These results are expected to hold for APG TBL in near-equilibrium conditions with $U_\infty(x) \sim (x - x_0)^m$ where $m \in (-1/3, 0)$ (Bobke et al., 2017). As a result, history effects from sudden variations in U_∞ or upstream favourable pressure gradients were not considered. For flows near separation, as τ_W approaches 0, β can exhibit significant streamwise variation. This case was also outside of the scope of this study. Future work will need to consider $\overline{\mathbf{U}}$ outside of the near-equilibrium conditions where the nonequilibrium effects are more severe.

4.6 Chapter Summary

The linear amplification in APG TBL flows was studied and demonstrated different physical behaviors from the ZPG TBL. This was demonstrated in Section 4.2 where the scaling identified by Wei and Knopp (2023) was shown to admit scaling for k_x, k_z, and ω that produced self-similar resolvent modes and gains over a range of Re_τ and β. Due to the difference in the amplification of the Reynolds shear stresses in the outer region of the flow between the ZPG TBL and the APG TBL, Wei and Knopp (2023)'s scaling did not apply to the mean flow fields of the ZPG TBL. As a result, the ZPG TBL resolvent modes and gains do not collapse to the APG TBL results indicating different mechanisms in the outer scaled amplification. Wei and Knopp (2023) and Gungor et al. (2016) suggest that the APG makes the outer region of the flow behave like a planar shear layer, which in turn changes the nature of the linear amplification in that region. For mild APG TBL, the effect of the PG is negligible in the near-wall region of the flow. The inner scaling of the resolvent modes was studied for APG TBL flows in Section 4.3. To achieve self-similarity in these flows,

the streamwise evolution of the length and time scales must be accounted for and is more prominent in these low Re_τ APG TBL flows than the ZPG TBL. At high Re_τ, the effects of the PG on the inner region are negligible due to the scale separation in the flows. For smaller Re_τ, these effects become more apparent because of the lack of scale separation. An increase in APG strength increases the amplification of the large scale structures further from the wall. The location of the near-wall cycle was approximated well in E^+_{uu}, peaking for $y^+ \approx 30$ and $\lambda^+_z \approx 100$. For these studies, secondary peaks were not observed because the domains were too small to support large scale structures.

To investigate the effect of the APG on the large scale structures, larger streamwise domains were considered in Section 4.4. By performing a sweep over k_z and ω, it was shown that E^+_{uu} and K^+_{uu} demonstrate a near-wall peak and a secondary peak that is absent when using the ZPG TBL dataset. The amplitude of the secondary peaks increase with $\overline{\beta}$ due to the increase in amplification of the large scale structures. The near-wall peak is at $y^+ \approx 20$ and $\lambda^+_z \approx 65$. The smaller λ^+_z identified for the near-wall peak are related to the streamwise evolution of the inner length scales which treated the $\lambda^+_z \approx 100$ modes as large scale modes near the inlet of the domain in the APG TBL datasets.

In Section 4.5, the effects of the nonequilibrium APG history on the large scales were investigated. An accumulated APG strength, $\overline{\beta}_\infty$, was used to parameterize the history effects. Accumulated APG effects were used in the study of Vinuesa et al. (2017) as empirical corrections to commonly used correlations in ZPG TBL, albeit with a different definition for the accumulated history effect. Here, $\overline{\beta}_\infty$ was used to parameterize the resolvent amplification since these are both metrics integrated across the domain. It was shown that σ_1 grows linearly with $\overline{\beta}_\infty$, consistent with the increase in amplification of the outer region with increase in β seen in Section 4.4. This linear growth was shown to be related to a hybrid velocity scale used to suppress the secondary peaks in $\overline{uu}$ (Romero et al., 2022; Sekimoto et al., 2019). Using U_{hyb}, a scale dependent y_m is proposed that can scale the increase in amplification with $\overline{\beta}_\infty$ without any fitting.

The APG effects studied in Sections 4.4 and 4.5 were performed with low Re_τ TBL datasets with mild APGs in near-equilibrium conditions (Bobke et al., 2017; Pozuelo et al., 2022). Furthermore, these LES simulations were chosen because they had long, well-resolved streamwise domains to allow for the streamwise evolution of large scale modes. As a result, the APG TBL parameters represent a small subset of

the full parameter space. Notably, these results were not applied to APG TBLs with favorable pressure gradients, sudden variations in U_∞, rapid variations in β in near-separation conditions, large APG strengths, and large Re_τ TBLs since datasets with these conditions over large streamwise domains are absent. Future work would need to assess if the observations made in Sections 4.4 and 4.5 can extend to flows outside of the studied parameter space. Deshpande et al. (2023) observed that the influence of the APG on the turbulent statistics diminished with increasing Re_τ. The LES of Pozuelo et al. (2022) was used to study the inner scaling of APG TBL with high Re_τ, but was not used for the studies on the amplification of large scales since there is only one β to compare with at these Re_τ. Future studies would need to be done at larger Re_τ to investigate the β effects on linear amplification with larger Re_τ. These future studies can only be done when such datasets become available. Additionally, there is a growing need for the study of turbulent statistics in nonequilibrium APG TBLs away from the near-equilibrium conditions.

An avenue of future work will involve the nonlinear closure. The model used in Equation 4.10 was constructed using a single nonlinear weight independent of k_z and ω designed with only the scaling of the inner peak in mind. Due to this scaling, the amplitudes of the outer region were overpredicted, compared to the LES data. A more encompassing scaling will have to take into account the outer scaling of the outer region of the flow by incorporating a scale-dependent nonlinear weight. One option for the scaling of the large scale modes is to ensure that the modeled $\overline{uu}$ scales with U_h^2 in the outer region as in Romero et al. (2022).

Chapter 5

RESOLVENT ANALYSIS OF HIGH ENTHALPY BOUNDARY LAYERS

5.1 Introduction

In this section, the focus will shift away from incompressible flow to consider hypersonic flows. For the flow to be hypersonic, the relevant Mach number, Ma, must be greater than about 5, though this requirement is debated by many researchers (Anderson Jr., 2006; Edwards, 1992). The supersonic flow, with $Ma > 1$, is categorized by compressibility effects, as well as increased temperatures within the boundary layer (Spina, Smits, and Robinson, 1994). As Ma increases, the temperature, and thermal heating to the wall, increase. To account for the thermodynamics, the supersonic flow models the air as a calorically perfect gas (CPG) while the effects of compressibility on the turbulent statistics can mostly be explained by accounting for the temperature-dependent thermophysical properties (Griffin, Fu, and Moin, 2021; Morkovin, 1962). When $Ma \geq 5$, the temperature raises to a point where the CPG assumption fails. These hypersonic flows require the incorporation of various real gas effects as the Ma continues to increase. Modeling these real gas effects adds various nonlinear terms into the governing equations which strain analytical and computational methods. Along with the temperature-related real gas effects, the increased temperature within the boundary layer increases the viscosity and decreases the density which both serve to make the boundary layer thicker.

The CPG assumption begins to fail at temperatures around 600 K because of vibrational excitation (Anderson Jr., 2006). As the temperatures increase with increasing Ma, the vibrational effects become increasingly important for hypersonic TBLs. The effects of vibrational excitation change the specific heat capacities of the air, making them temperature-dependent. This requires the use of a calorically imperfect gas (CIG) assumption where the specific heats can be described using empirical relationships, like the McBride (2002) polynomials.

As the temperatures increase further, chemistry effects become important. For temperatures larger than 2000K, O_2 begins to dissociate which creates the presence of O and NO in the air (Anderson Jr., 2006). For temperatures exceeding 4000K, N_2 also begins to dissociate into N (Anderson Jr., 2006). The presence of these

components in the air changes its thermodynamic state and the thermophysical properties. These chemical reactions do not occur instantaneously as they require time for the reactions to occur. The air may be convected downstream while the reactions take place. This is related to the Damköhler number, Da, which represents the ratio of the reaction rate to the convective transport rate. If $Da \gg 1$, then the flow is in equilibrium as the reactions effectively occur instantaneously. This means that chemical diffusion can be neglected and any effects from the species are accounted for as changes to the thermophysical properties (Malik and Anderson, 1991). On the other hand, when Da is moderate, the time for chemical reaction and transport processes are comparable. This means that the changes in concentration of the chemical species due to chemical production and chemical diffusion must be accounted for. As a result, the flow requires the modeling of the various species (here N_2, O_2, NO, N, and O) and their chemistry terms. This was studied using linear stability in Franko, MacCormack, and Lele (2010).

The chemical nonequilibrium from the high-temperature real gas effects strain the development of analytic tools since they require a state vector with an increased number of state variables and additional terms in the governing equations that depend nonlinearly on the state vector. Computationally, such terms increase the operation count in simulations as the transport and thermal properties of the mixture are calculated over the entire flow field at each time instance using models requiring polynomials, fits, and look-up tables, whose dimensionality can be large depending on the number of considered species (Edwards, 1992). Otherwise, these properties can be computed using kinetic theory, which requires algebraic solutions of systems of equations, and depends on the assumptions made on the intermolecular forces. Furthermore, uncertainty in the models can also affect the validity of the computations since many of the calculations require experimental measurements at high temperatures with large uncertainties (Anderson Jr., 2006). As these experiments improve, the uncertainties associated with these measurements will decrease. Nonetheless, the chemistry model used to compute the thermophysical properties can significantly affect linear stability results, which in turn affects the location of the laminar-turbulent transition (Franko, MacCormack, and Lele, 2010).

Linear stability theory has been applied to hypersonic flows in the past (Malik and Anderson, 1991; Franko, MacCormack, and Lele, 2010). Linear stability theory can provide much insight on the transition of laminar flows. However, since it fundamentally ignores nonlinearities in the flow, its applicability to turbulent flows is

not valid. In this chapter, the high temperature gas effects in hypersonic TBL will be incorporated into the resolvent analysis which treats the nonlinearities as uncorrelated forcing inputs. The resolvent operator is created by only considering the linear terms of the governing equations, much like the linear operator in linear stability theory. This means that the resolvent modes and amplifications are independent of the true nonlinear nature of the real gas effects. However, the resolvent analysis is by definition an input-output approach. The nonlinearities, here treated as forcing, are treated as inputs to the linear resolvent operator where the outputs are fluctuations. Resolvent analysis then identifies the optimal inputs and outputs, subject to the norm chosen. A limitation of this approach is that the nonlinearities are, in actuality, correlated and restricted based on physically realizeable states. These issues can be partially accounted for by using the strategy described in Towne, Schmidt, and Colonius (2018) by weighing the input forcing with a matrix proportional to the turbulent statistics to bias the forcing inputs to spatial regions where the nonlinearities are active, although this is not applied in this study. The leading resolvent modes can identify physical mechanisms by preferentially amplifying forcing inputs in the direction of the optimal response modes when the resolvent operator is low rank (Abreu, Cavalieri, et al., 2020) while the resolvent amplification gives insight into the forcing inputs, length scales, and frequencies that are most amplified by the linear dynamics.

Similar to how Franko, MacCormack, and Lele (2010) studied the effects of different chemistry models on linear stability theory, in this chapter, differences in the resolvent analysis due to different modeling assumptions for the real gas effects will be investigated. This will give insight as to which structures can be suitably modeled with a simpler modeling approach, such as using chemical equilibrium as opposed to chemical nonequilibrium in the analysis. Performing resolvent analysis with a mixture of gases allows the linear amplification from certain species components to be isolated. This helps identify the length scales where the chemistry terms are active. Furthermore, the analysis will study what phenomena are amplified by the linear terms in a hypersonic TBL and comparisons will be made with data, where possible.

The structure of this chapter is as follows. First, the resolvent analysis will be compared using the CPG and CIG assumptions to identify which length scales are most affected by the vibrational excitation. Then, the resolvent analysis will be formulated to describe a 5 species mixture of ideal gases in chemical nonequilibrium,

which model dissociated air. The results from resolvent analysis using chemical nonequilibrium assumption will be compared to resolvent analysis using a chemical equilibrium assumption. Comparisons will be made using a laminar boundary layer similarity solution under chemical nonequilibrium and a similarity solution using the CPG at matched *Re*, freestream temperature, and wall temperature. Following this, the resolvent analysis will be examined for a hypersonic TBL in chemical nonequilibrium. Finally, the correlations in the resolvent modes of the TBL will be shown to agree qualitatively with data for modes representative of the near-wall cycle.

5.2 Resolvent Formulation for an Ideal Gas

The effects of a CIG or CPG assumption on the linear amplification will be studied through the use of local (1D) resolvent analysis. As such, the analysis will consider a parallel flow assumption, resolving only the wall-normal direction, to reduce the computational costs in the analysis. This will help identify the length scales most affected by the vibrational excitation.

The governing equations are nondimensionalized with the streamwise velocity, U_e, temperature, T_e, boundary layer thickness, δ_{99}, density, ρ_e, dynamic viscosity, μ_e, thermal conductivity, k_e, specific heat capacity at constant volume, $c_{v,e}$, and speed of sound, a_e where all the quantities with subscripts e are evaluated at the local δ_{99}. The specific heat capacity at constant pressure is nondimensionalized with $c_{p,e} = R + c_{v,e}$, where R is the specific gas constant These quantities define the Reynolds number, $Re = U_e\rho_e\delta_{99}/\mu_e$, Mach number, $Ma = U_e/a_e$, Prandtl number, $Pr = \mu_e c_{p,e}/k_e$, and the ratio of specific heats, $\gamma_e = c_{p,e}/c_{v,e}$. In this section, the Pr is assumed to be a constant equal to 0.71 through the boundary layer and freestream. Hereafter, any variable with a breve ($\breve{\cdot}$) denotes the full instantaneous quantity, i.e., the sum of its mean and fluctuation.

For a single species ideal gas, the governing equations are

$$\breve{\rho}\frac{D\breve{\mathbf{u}}}{Dt} = -\frac{1}{\gamma_e Ma^2}\boldsymbol{\nabla}\breve{p} + \frac{1}{Re}\boldsymbol{\nabla}\cdot\breve{\tau}, \tag{5.1}$$

$$\breve{\rho}\breve{c}_v\frac{D\breve{T}}{Dt} = -(\gamma_e - 1)p\boldsymbol{\nabla}\cdot\breve{\mathbf{u}} + \gamma_e(\gamma_e - 1)\frac{Ma^2}{Re}\breve{\tau} : \boldsymbol{\nabla}\breve{\mathbf{u}} + \frac{\gamma_e}{PrRe}\boldsymbol{\nabla}\cdot\left(\breve{k}\boldsymbol{\nabla}\breve{T}\right), \tag{5.2}$$

$$\frac{D\breve{\rho}}{Dt} = -\breve{\rho}\boldsymbol{\nabla}\cdot\breve{\mathbf{u}}, \tag{5.3}$$

$$\breve{p} = \breve{\rho}\breve{T}, \tag{5.4}$$

$$\breve{\tau} = \breve{\mu}\left(\boldsymbol{\nabla}\breve{\mathbf{u}} + \boldsymbol{\nabla}\breve{\mathbf{u}}^T - \frac{2}{3}(\boldsymbol{\nabla}\cdot\breve{\mathbf{u}})\mathcal{I}\right), \tag{5.5}$$

where Equation 5.1 is the momentum equation, Equation 5.2 is the internal energy equation, Equation 5.3 is the continuity equation, Equation 5.4 is the equation of state for an ideal gas, and Equation 5.5 is the expression for the stress tensor for a Newtonian fluid using Stokes' assumption for the second coefficient of viscosity. $D(\cdot)/Dt$ denotes the material derivative, $\partial_t + \breve{u}_i\partial_{x_i}$ of a quantity $(\cdot)$. In Equation 5.2, the colon, :, denotes the double dot product between two tensors such that $\mathbf{A} : \mathbf{B} = A_{ij}B_{ij}$ using Einstein indicial notation. The state variable is chosen as $\breve{\mathbf{q}} = \left[\breve{\mathbf{u}}, \breve{T}, \breve{\rho}\right]$. The velocity follows the usual no-slip boundary condition at the wall and a problem-specific temperature boundary condition.

The viscosity is assumed to follow Sutherland's law such that

$$\breve{\mu} = \breve{T}^{3/2}\left(\frac{T_e + S}{\breve{T}T_e + S}\right), \tag{5.6}$$

where $S = 110.4$ K. If the CPG is assumed, then $\breve{c}_p = 7c_{v,e}/(2R)$. When a CIG is assumed, $\breve{c}_p(\breve{T})$ is computed using the 9-coefficient NASA polynomials for a gas mixture of 79% N_2 and 21% O_2 on a molar basis and the same value of R (McBride, 2002; Di Renzo et al., 2022). γ_e is equal to 1.4 for the CPG and 1.387 for the CIG. Due to the constant Pr assumption, $\breve{k} = \breve{\mu}\breve{c}_p$.

Assuming a known mean flow state, $\overline{\mathbf{q}}$, $\breve{\mathbf{q}}(\mathbf{x}, t) = \overline{\mathbf{q}}(y) + \mathbf{q}(\mathbf{x}, t)$ where the mean flow field is assumed to be parallel. Only state variables with an overbar, $(\bar{\cdot})$, denote mean quantities. Any other quantity with an overbar is computed using $\overline{\mathbf{q}}$. For example, $\overline{p} = \overline{\rho}\overline{T}$. The fluctuations $\mathbf{q}(\mathbf{x}, t)$ are assumed to be stationary in time and homogeneous in the streamwise and spanwise directions as in Bae, Dawson, and McKeon (2020). The homogeneity in x is an approximation for the boundary layers studied in this chapter. See the previous chapters for discussions on the influence of

spatial development on incompressible TBLs. Following Section 2.2, the linear and nonlinear terms of Equations 5.1, 5.2, and 5.3 are separated and $\mathbf{q}$ is approximated as a normal mode such that $\mathbf{q}(\mathbf{x}, t) = \widehat{\mathbf{q}}(y) \exp(-i\omega t + k_x x + k_z z)$, where ω, k_x, and k_z are the temporal frequency, streamwise wavenumber, and spanwise wavenumber, respectively. The fluctuations of a quantity $\breve{g}$ are treated as

$$\widehat{g} = \sum_{i}^{n_s} \left.\frac{\partial \breve{g}}{\partial q_i}\right|_{\overline{\mathbf{q}}} \widehat{q}_i. \tag{5.7}$$

$\widehat{\mathbf{q}}$ is governed by

$$\widehat{\mathbf{q}} = \left(-i\omega + \widehat{\mathcal{L}}\right)^{-1} \mathcal{B}\widehat{\mathbf{f}}, \tag{5.8}$$

where $\widehat{\mathbf{f}}$ denotes the forcing, $\widehat{\mathcal{L}}$ is the LNS operator, and $\mathcal{B}$ is introduced to apply component-wise masking of the forcing. $\widehat{\mathbf{u}}$ satisfies the no-slip boundary condition at the wall and $\widehat{T} = 0$ at the wall, despite the boundary conditions for $\overline{T}$ at the wall (Malik, 1990).

The form of $\widehat{\mathcal{L}}$ is specified as a block matrix,

$$\widehat{\mathcal{L}} = \begin{bmatrix} L_{1,1} & L_{1,2} & L_{1,3} & L_{1,4} & L_{1,5} \\ L_{2,1} & L_{2,2} & L_{2,3} & L_{2,4} & L_{2,5} \\ L_{3,1} & L_{3,2} & L_{3,3} & L_{3,4} & L_{3,5} \\ L_{4,1} & L_{4,2} & L_{4,3} & L_{4,4} & 0 \\ L_{5,1} & L_{5,2} & L_{5,3} & L_{5,4} & L_{5,5} \end{bmatrix}, \tag{5.9}$$

where the blocks, $L_{i,j}$, are specified in Appendix E. The index $i = 1, 2, 3, 4$, and 5 corresponds to the linearized u momentum, v momentum, w momentum, internal energy, and continuity equations and the index $j = 1, 2, 3, 4$, and 5 corresponds to the blocks that act on the u, v, w, T, and ρ components. The diagonal blocks have the convective $k_x\overline{U}$ terms and dissipative terms. The off-diagonal terms are responsible for the component-wise non-normal amplification. Although all the blocks are functions of $\overline{\mathbf{q}}$, only the $L_{4,i}$ blocks are explicitly affected by the variable specific heat used in the CIG assumption.

To perform the resolvent analysis, a suitable inner product must be chosen. The inner products are chosen to be equal so that $\mathcal{W} = \mathcal{W}_r = \mathcal{W}_f$ enforce the Chu (1965) norm,

$$\mathcal{W} = \mathrm{diag}\left(\overline{\rho}, \overline{\rho}, \overline{\rho}, \frac{\overline{c}_v \overline{\rho}}{Ma^2 \gamma_e (\gamma_e - 1)\overline{T}}, \frac{\overline{T}}{\gamma_e Ma^2 \overline{\rho}}\right). \tag{5.10}$$

T_e	T_w	Ma	Re	Re_τ
500 K	1600 K	5	3×10^4	250

Table 5.1: Local properties of the mean flow profiles from the simulations of Di Renzo et al. (2022). T_e and T_w denote the freestream and wall temperatures.

The form of $\mathcal{W}$ is derived by eliminating the compression work related terms (Hanifi, Schmid, and Henningson, 1996). The form of $\mathcal{W}$ differs from the form studied in Bae, Dawson, and McKeon (2020) and Hanifi, Schmid, and Henningson (1996) because $\overline{c}_v$ is not assumed to be a constant.

The equations are discretized using the SBP scheme with grid stretching described in Section 2.3 that has been used in other compressible studies (Madhusudanan and McKeon, 2022; Kamal et al., 2020; Malik, 1990). Half the points are clustered below y_{min} while the other half are between y_{min} and y_{max}. In this case, $y_{min} = 1$ to cluster the points below the boundary layer as in Madhusudanan and McKeon (2022) and $y_{max} = 5$. $N_y = 501$ points are used to discretize the equations. Isothermal and no-slip boundary conditions are applied at the wall. In the freestream, a damping layer and artificial viscosity are applied at the last 5% of the domain to absorb any reflections (Appelö and Colonius, 2009). Due to the damping, the freestream boundary conditions are set as Dirichlet boundary conditions for $\widehat{\mathbf{u}}$ and $\widehat{T}$ at y_{max}. The adjoint matrix is computed using the conjugate-transpose approach rather than the discretized adjoint approach. As such, Algorithm 2 is used with at most 300 iterations and stops if σ_{10} has converged to within 10^{-6}.

5.3 Influence of CPG/CIG Assumption on Linear Amplification

In this section, the mean flow fields will first be discussed. Following this discussion, comparisons will be made between the σ_1, $\boldsymbol{\psi}_1$, and $\boldsymbol{\phi}_1$ using the CPG or CIG assumptions.

Description of the Mean Flow Fields

The mean flow fields are obtained from the DNSs of Di Renzo et al. (2022), in the flat plate region upstream of the compression ramp where nonparallel effects are assumed to be negligible. The two mean flow fields that are studied were computed using the CPG and CIG assumptions. Under the parallel flow assumption, $\overline{\mathbf{q}}(y) = [\overline{U}(y), 0, 0, \overline{T}(y), \overline{\rho}(y)]$. The streamwise location where the mean flow profiles are taken is about $4.5\delta_{99}$ upstream of the start of the ramp so any nonparallel

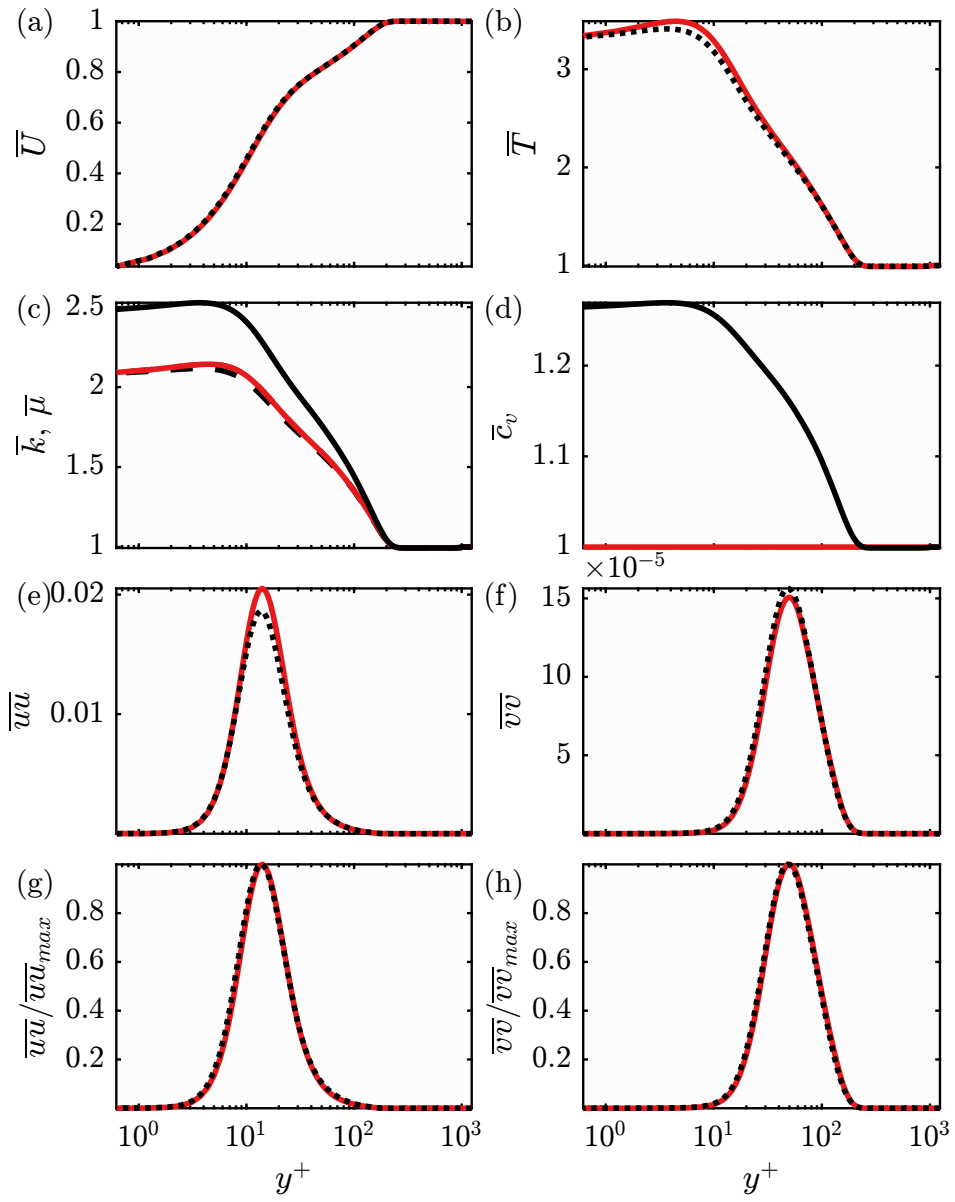

Figure 5.1: $\overline{U}$ (a), $\overline{T}$ (b), $\overline{k}$ (c), $\overline{c}_v$ (d), $\overline{uu}$ (e), $\overline{vv}$ (f), $\overline{uu}/\max\overline{uu}$ (g), and $\overline{vv}/\max\overline{vv}$ (h) from the CPG (red) and CIG (black) DNS. In (c), the black dashed line denotes μ for the CIG. Note that $\mu = k$ for the CPG.

effect from the changing geometry is neglected. The properties that characterize the mean flow profiles are listed in Table 5.1.

In Figure 5.1, the mean flow fields are plotted along with some relevant thermodynamic quantities. The temperature dependence in c_v negligibly affects $\overline{U}$, but changes $\overline{T}$ within the near-wall region where $\overline{T}$ is largest. The difference in T is expected since the change in the thermodynamic variables affects the heat transfer to the wall while the small change in $\overline{\mu}$ hardly affects the viscous diffusion in the

Case	Mean	LNSE
i	CPG	CPG
ii	CIG	CIG
iii	CPG	CIG

Table 5.2: CPG and CIG denote the assumption used for the mean flow field and the LNSE.

momentum. Despite the negligible changes to $\overline{U}$, the streamwise and wall-normal velocity fluctuations, $\overline{uu}$ and $\overline{vv}$ differ appreciably near the wall. The differences are likely because U_e is not a suitable velocity scale for the near-wall region where the temperature is largest (Griffin, Fu, and Moin, 2021). This is investigated briefly in Figures 5.1(g,f) where the fluctuations normalized by their local maxima demonstrate good collapse.

Three cases are studied which differ in the assumption of the gas properties in either the DNS used to compute the mean or in the LNSE for the resolvent analysis. Cases i and ii use the CPG and CIG assumptions, respectively, for both the mean and LNSE. Case iii uses the CPG mean flow field and a CIG for the LNSE. Although case iii uses a different assumption for the gas in the LNSE than the one used in the NSE of the mean flow field, case iii will be used to investigate how the linear amplification changes when only the thermodynamic properties are varied in the LNSE. This removes the differences in the shear-driven amplification from $\partial\overline{\mathbf{q}}/\partial y$ terms when different $\overline{\mathbf{q}}$ are used. These cases are summarized in Table 5.2.

Differences in the Optimal Resolvent Modes and Amplification Using the CPG/CIG Assumptions

The resolvent analysis is computed over a range of k_x and k_z with a fixed wavespeed, c, for the three different cases. The effect of the modeling choice on the amplification is studied by comparing $\sigma_1^2 k_x k_z$ for the three cases. The wavespeed is chosen as $c = \overline{U}(y^+ = 15) \approx 5.75$, where $y^+ = 15$ corresponds to the location of the largest $\overline{uu}$. k_x and k_z each sweep over 80 logarithmically spaced points between $2\pi/.025$ and $2\pi/100$.

The results of the sweep for the three cases are plotted in Figure 5.2. The discontinuity in the amplification, separated by the thick black solid line, is due to the excitation of supersonic modes with support in the freestream. The characteristics

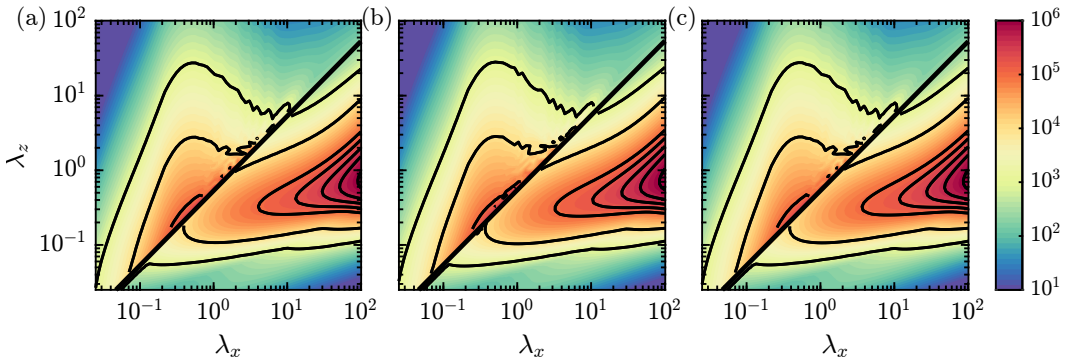

Figure 5.2: $\sigma_1^2 k_x k_z$ for case i (a), case ii (b), and case iii (c). The thick black line corresponds to the sonic line. The black contour lines correspond to $\sigma_1^2 k_x k_z = 10^3$, 10^4, 10^5, 1.75×10^5, 3×10^5, 5×10^5, 10^6.

of these modes are categorized by the value of the freestream relative Mach number,

$$\overline{Ma} = \frac{k_x}{\left(k_x^2 + k_z^2\right)} \frac{Ma(\overline{U} - c)}{\overline{T}^{1/2}}, \tag{5.11}$$

where $\overline{U}$ and $\overline{T}$ are evaluated at the freestream (Mack, 1984; Bae, Dawson, and McKeon, 2020). To gain some insight on $\overline{Ma}$, consider

$$\mathbf{M}_r = \frac{Ma(\overline{U} - c)}{\overline{T}^{1/2}} \mathbf{e}_x = \frac{\overline{U} U_e - c U_e}{\overline{T}^{1/2} a_e} \mathbf{e}_x, \tag{5.12}$$

as the mean velocity relative to the wavespeed, normalized by the mean speed of sound, $\overline{T}^{1/2} a_e$, and the unit vector in the direction of the wavenumber,

$$\mathbf{e}_k = \frac{k_x \mathbf{e}_x + k_z \mathbf{e}_z}{\left(k_x^2 + k_z^2\right)}. \tag{5.13}$$

$\overline{Ma}$ is thus the dot product between $\mathbf{M}_r$ and $\mathbf{e}_k$, in other words, the Mach number relative to the wavespeed projected onto the direction of the wavenumber (Schmid and Henningson, 2002). When the value of $\overline{Ma} \geq 1$, the modes are considered supersonic. The freestream component of these modes resemble acoustic phenomena that radiate out of the boundary layer. $\overline{Ma} = 1$ denotes the sonic line, the location of the discontinuity. Subsonic modes, characterized by $\overline{Ma} < 1$, resemble the incompressible counterparts, albeit with variable viscosity and density (Madhusudanan and McKeon, 2022; Bae, Dawson, and McKeon, 2020). The oscillations in the contours in the supersonic region are due to the limited resolution in the sweep.

Despite differences in the temperature dependence of the specific heats, the linear amplification is only mildly affected. This is shown in Figure 5.3(a) where contour

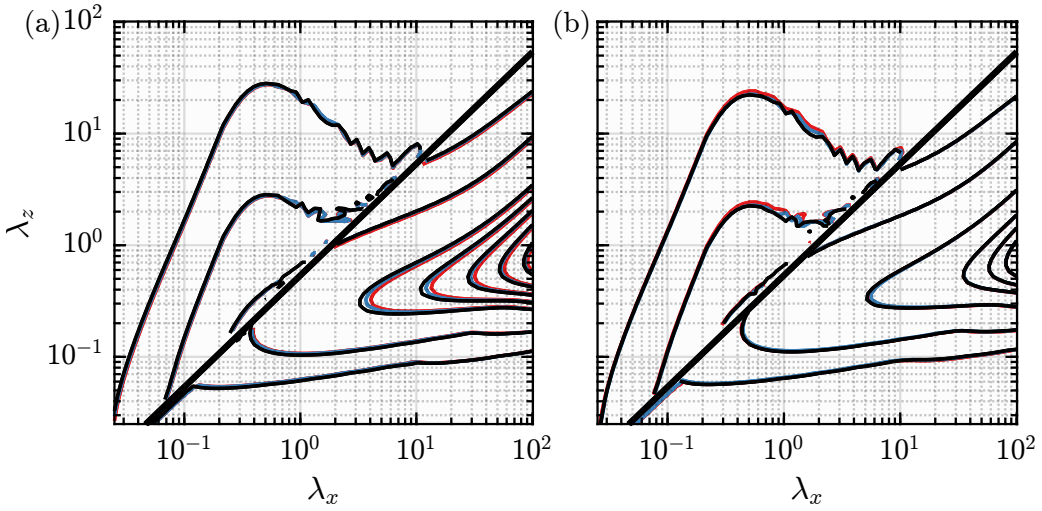

Figure 5.3: Contours of $\sigma_1^2 k_x k_z$ for case i (red), ii (black), and iii (blue) using $c = \overline{U}(y^+ = 15)$. The contours denote $\sigma_1^2 k_x k_z = 10^3$, 10^4, 10^5, 1.75×10^5, 3×10^5, 5×10^5, 10^6 in (a) and .1%, 1%, 10%, 30%, 50%, and 75% of the local maxima of $\sigma_1^2 k_x k_z$ in (b). The thick black line denotes the sonic line.

lines of $\sigma_1^2 k_x k_z$ are plotted at specified values. Owing to the freestream support of the supersonic modes where $\overline{T}$ is smallest, the amplification with $\overline{Ma} > 1$ are unaffected by the differences in the specific heats or $\overline{\mathbf{q}}$ within the boundary layer. Although the supersonic modes are triggered within the boundary layer (Bae, Dawson, and McKeon, 2020), the boundary layer encompasses only a fifth of the integration region in the inner products. The subsonic modes demonstrate sensitivity to the change in thermodynamic properties since these modes have support within the boundary layer. Case ii has the largest amplification, followed by case iii, and then case i. The amplification in case ii is largest because it has access to increased non-normal amplification due to case ii having the largest $\overline{U}_y$ near the wall. The thermal diffusivity, $\overline{k}/\left(\overline{\rho c}_p\right)$, is largest in case i and smallest in case ii. As a result, case i has the smallest amplification because of the increased thermal diffusion while case ii has increased non-normal amplification from $\overline{U}_y$.

In Figure 5.3(b), the contour lines of $\sigma_1^2 k_x k_z$ are plotted at percentages of the maxima of each case. Just as the fluctuations in Figures 5.1(g,h) demonstrated collapse when rescaled by their local maxima, the same is true for the linear amplification in the subsonic region. This suggests that normalization with a set of appropriate variables may collapse the linear amplification, despite the real gas effects. In Figure 5.3(a), the amplification of the supersonic modes is relatively unchanged for the three cases since these modes are excited in the freestream, where the mean flow field and

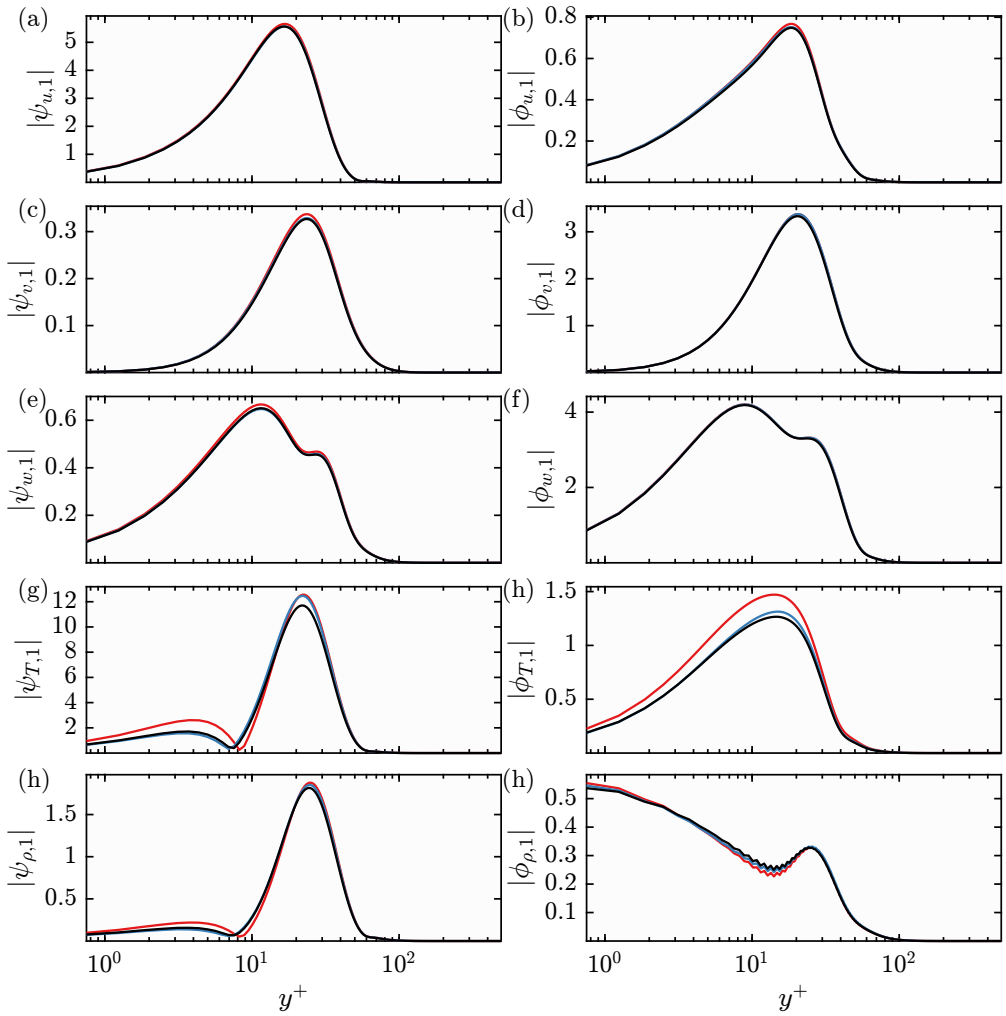

Figure 5.4: $|\psi_{u,1}|$ (a), $|\phi_{u,1}|$ (b), $|\psi_{v,1}|$ (c), $|\phi_{v,1}|$ (d), $|\psi_{w,1}|$ (e), $|\phi_{w,1}|$ (f), $|\psi_{T,1}|$ (g), $|\phi_{T,1}|$ (h), $|\psi_{T,1}|$ (i), $|\phi_{T,1}|$ (j) for representative subsonic modes ($k_x = 2\pi/4$, $k_z^+ = 2\pi/.4$, $c = \overline{U}(y^+ = 15)$. Case i, ii, and iii are in red, black, and blue solid lines.

thermophysical properties are the same. This suggests that the freestream variables can parameterize the amplification of the supersonic modes well. In Figure 5.3(b), the supersonic modes exhibit some variation because the local maxima used to define the contours occur in the subsonic region.

The real gas effects on the resolvent modes are compared for representative subsonic modes with $\lambda_x = 4$ ($\lambda_x^+ = 1000$), $\lambda_z = .4$ ($\lambda_z^+ = 100$), and $c = \overline{U}(y^+ = 15)$ for the three cases in Figure 5.4. $\boldsymbol{\phi}_1$ has large wall-normal and spanwise components, indicative of the lift-up mechanism's role in these shear driven flows (Symon et al., 2018). $\phi_{T,1}$ has a non-negligible component because of the non-normality introduced by the off-diagonal terms in the LNSE due to the pressure gradient, $\boldsymbol{\nabla}\check{p}$,

in blocks $L_{i,4}$ (see Appendix E.2). Physically, the lift-up mechanism redistributes the near-wall fluid up away from the wall and the fluid from outer region down to the wall. This creates the low-speed streaks with a temperature fluctuation whose sign depends on $\overline{T}_y$. The terms responsible for the non-normality are the $\overline{U}_y v$ term in the momentum equation ($L_{1,2}$) and the $\overline{T}_y v$ term in the energy equation ($L_{4,2}$). Although not plotted, $\psi_{u,1}$ and $\psi_{T,1}$ are out-of-phase above $y^+ \approx 10$, the location of maximum $\overline{T}$. Physically, this corresponds to the lift-up mechanism sweeping cooler, high-momentum fluid closer to the wall and ejecting hotter, low-momentum fluid away from the wall above $y^+ \approx 10$ (Pirozzoli and Bernardini, 2011; Kong, Choi, and J. S. Lee, 2000). Due to the non-monotonicity in $\overline{T}$, the $\psi_{u,1}$ and $\psi_{T,1}$ become in phase for $y^+ \leq 10$ because $\overline{T}$ increases away from the wall due to the wall cooling. The velocity components of $\boldsymbol{\psi}_1$ and $\boldsymbol{\phi}_1$ are hardly affected by the change in the thermodynamic properties or $\overline{T}$ unlike the temperature and density components. Lastly, the saw-tooth nature in $\phi_{\rho,1}$ is a numerical artifact that is a consequence of the conjugate-transpose used for the adjoint and limited near-wall resolution (Chandler et al., 2012). Increasing the wall-normal resolution near the wall mitigates these saw-tooth oscillations, but does not affect the value of σ_1.

In the freestream, the unforced, inviscid LNSE with $\overline{Ma} > 1$ have eigenvectors with an eigenvalue of 0 as described by Mack (1984), and here termed Mack modes. Since the freestream inviscid LNSE define a normal operator, these Mack modes are also singular vectors of the inviscid LNSE in the freestream with a singular value of 0. As a result, the inviscid LNSE has a singularity in the freestream when $\overline{Ma} > 1$ (Madhusudanan and McKeon, 2022). This singularity is similar to the critical layer singularity in an inviscid flow (Schmid and Henningson, 2002). When the full viscous LNSE are used, viscous terms can regularize the singularities and make the LNSE invertible. However the inviscid singularities from the Mack modes or the critical layer are still sources of large resolvent amplification. The inviscid singularity from the Mack modes is present in the equation for $\widehat{p} = \overline{T}\widehat{\rho} + \overline{\rho}\widehat{T}$. As a result, the temperature and density components of ψ_1 and ϕ_1 are large in the freestream, resembling the Mack modes, to excite the amplification from the freestream inviscid singularity. This freestream region also supports the existence of velocity disturbances in the freestream (Schmid and Henningson, 2002; Madhusudanan and McKeon, 2022).

Representative supersonic modes with $\lambda_x = 1$, $\lambda_z = 10$, and $c = \overline{U}(y^+ = 15)$ are plotted in Figure 5.5. These modes have non-negligible support in the freestream,

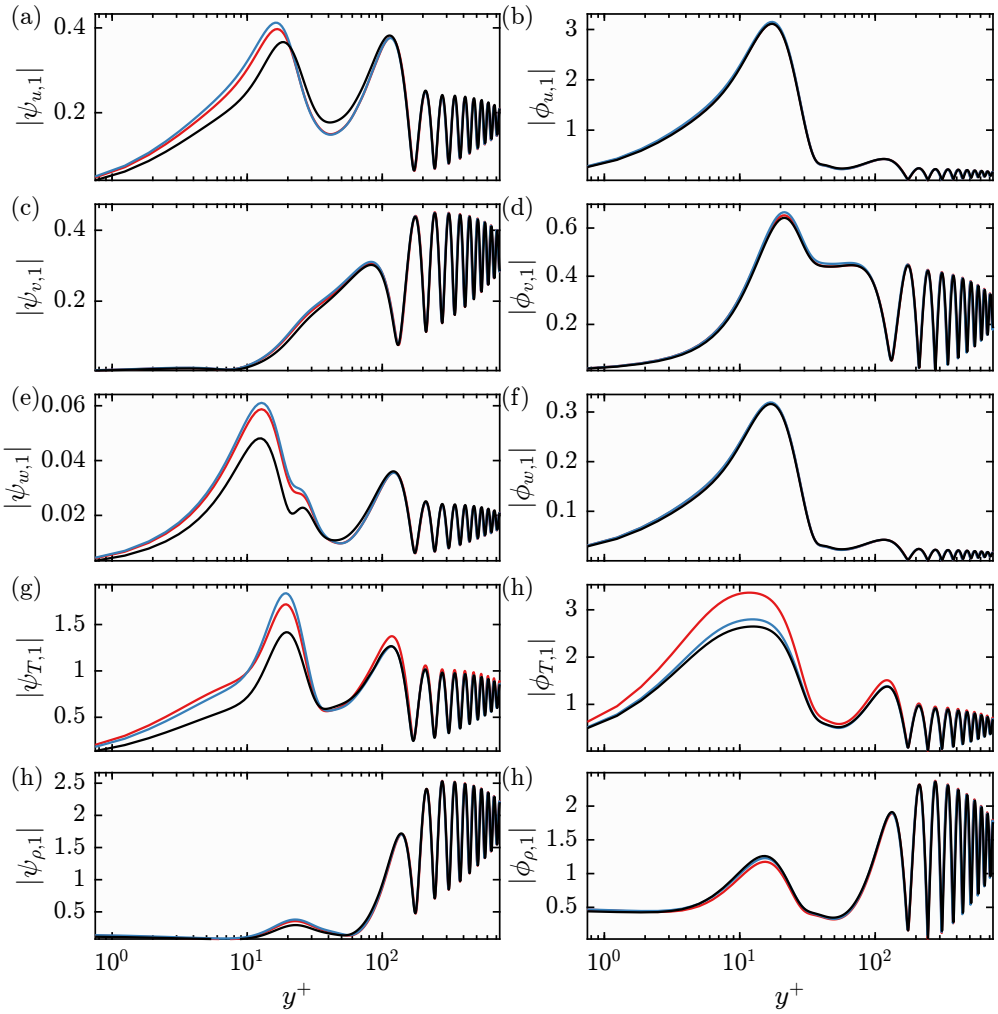

Figure 5.5: $|\psi_{u,1}|$ (a), $|\phi_{u,1}|$ (b), $|\psi_{v,1}|$ (c), $|\phi_{v,1}|$ (d), $|\psi_{w,1}|$ (e), $|\phi_{w,1}|$ (f), $|\psi_{T,1}|$ (g), $|\phi_{T,1}|$ (h), $|\psi_{T,1}|$ (i), $|\phi_{T,1}|$ (j) for representative supersonic modes ($k_x = 2\pi/1$, $k_z = 2\pi/10$, $c = \overline{U}(y^+ = 15)$. Case i, ii, and iii are in red, black, and blue solid lines.

characteristic of Mack modes excited in the freestream. The freestream components are independent of the changes in $\overline{T}$ and thermodynamic properties because of the cooler temperatures in the freestream as the vibrational excitation is nonexistent for mean temperatures less than 600 K (Anderson Jr., 2006). Because of the small differences in γ_e, $\psi_{T,1}$ for case i has slightly larger magnitude. Near the wall, the changes amongst each of the cases are more appreciable. The amplification of these supersonic modes takes advantage of the inviscid singularity in the freestream rather than the shear driven mechanisms within the boundary layer. The supersonic modes require $k_x > k_z$, which are not amplified by the lift-up mechanism through $\overline{U}_y$ within the boundary layer (Abreu, Cavalieri, et al., 2020). The forcing components with

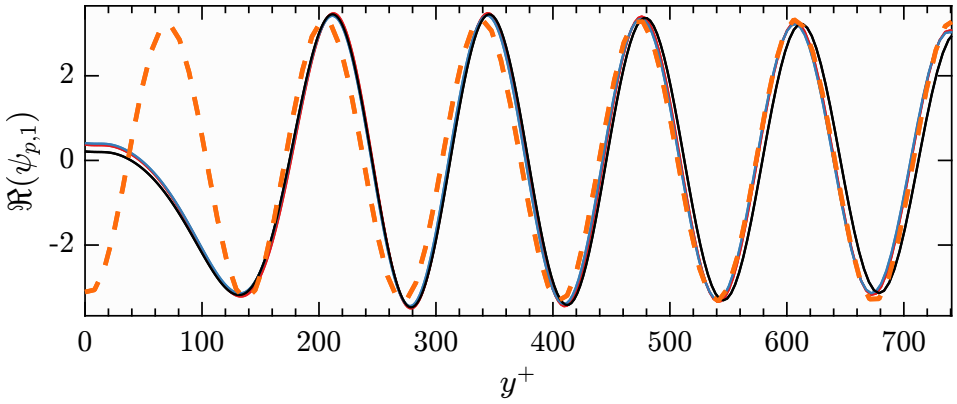

Figure 5.6: Real part of $\psi_{p,1}$ for the representative supersonic modes ($k_x = 2\pi/1$, $k_z = 2\pi/10$, $c = \overline{U}(y^+ = 15)$. Case i, ii, and iii are in red, black, and blue solid lines. The dotted orange line denotes $\widehat{p}_M$, where its amplitude and phase angle is matched to $\psi_{p,1}$ at $y^+ = 350$.

the largest magnitude within the boundary layer are $\phi_{u,1}$, $\phi_{T,1}$, and $\phi_{\rho,1}$ which excite large response components in $\psi_{T,1}$ and $\psi_{\rho,1}$. Hence, within the boundary layer, the linear amplification is primarily through the temperature and density components. These excite terms that are influenced by the change in the thermodynamic properties within the boundary layer. Since the temperature and density components are much larger for the supersonic mode, the difference in γ, $\overline{T}$, and $\overline{\rho}$ in the Chu norm of Equation 5.10 also plays a role in setting the mode shape since the modes need to be orthonormal with respect to the Chu norm. Regardless, the changes within the boundary layer only affect the near-wall region and does not affect the amplification as was shown in Figure 5.3.

In Figure 5.6, the pressure component of $\boldsymbol{\psi}_1$, $\psi_{p,1} = \overline{T}\psi_{T,1} + \overline{\rho}\psi_{\rho,1}$, is plotted for the three cases. This is compared with Mack (1984)'s unforced, inviscid freestream solution,

$$\widehat{p}_M = i\gamma_e Ma^2 k_x \left(\frac{1-c}{\sqrt{k_x^2 + k_z^2}} \right) \exp\left(-\sqrt{k_x^2 + k_z^2}\sqrt{1 - \overline{Ma}^2}\, y \right). \tag{5.14}$$

Note that this solution only holds in the freestream region if viscous effects are assumed to be negligible. The solution agrees well with $\psi_{p,1}$ in the freestream, despite the viscous dissipation and presence of the boundary layer (Madhusudanan and McKeon, 2022). $\psi_{p,1}$ for cases i and iii match well near the wall despite the differences in thermodynamic properties. This may indicate that the pressure component is most influenced by changes to the mean shear, rather than changes to the thermophysical properties.

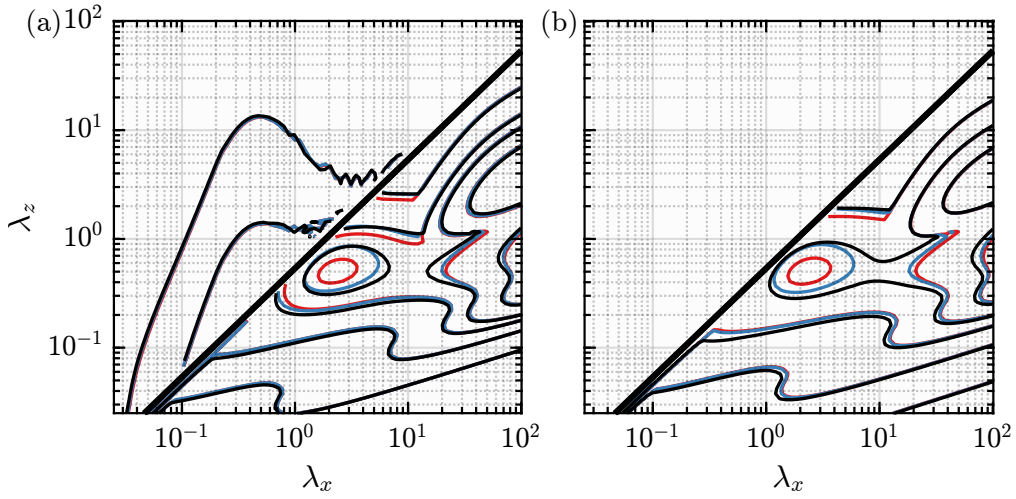

Figure 5.7: Contours of $\sigma_1^2 k_x k_z$ for case i (red), ii (black), and iii (blue) using $c = \overline{U}(y^+ = 15)$ and forcing from only the temperature and density components to investigate the effect of differences in the thermodynamic properties within the boundary layer on the linear amplification. The thick black line denotes the sonic line. The contour lines above the sonic line correspond to $\sigma_1^2 k_x k_z = 790$ and 9600 and below the sonic line correspond to $\sigma_1^2 k_x k_z = 100$, 316, 550, 710, and 1000 in (a). In (b), the contour lines denote .1%, 1%, 10%, 30%, 50%, and 75% of the local maximum of $\sigma_1^2 k_x k_z$ below the sonic line. The contour lines above the sonic line are omitted in (b) to highlight the differences within the subsonic region.

Since the temperature and density components of the forcing were affected by the thermodynamics, component wise masking is applied to the forcing to only allow forcing from ϕ_T and ϕ_ρ. The sweep is recomputed using the same parameters as Figure 5.2 and the results are plotted in Figure 5.7. The absence of hydrodynamic forcing causes the subsonic region ($\overline{Ma} < 1$) to be three orders of magnitude less amplified than the full forcing at their respective peak values. The forcing in the supersonic region amplifies similar regions in spectral space as the full forcing since the supersonic region is amplified by freestream acoustics (Madhusudanan and McKeon, 2022). Furthermore, the change in the thermodynamic properties and $\overline{T}$ within the boundary layer once again does not affect the amplification of these supersonic modes.

On the other hand, the subsonic modes are affected by the component wise forcing since these modes have support within the boundary layer where the changes are more severe. The length scales that demonstrate most sensitivity to the real gas effects are representative of the near-wall cycle with $\lambda_x \approx 1000/Re_\tau, \lambda_z \approx 100/Re_\tau$, contrasting with Figure 5.3 where $\lambda_x \gg \lambda_z$ demonstrated the most sensitivity.

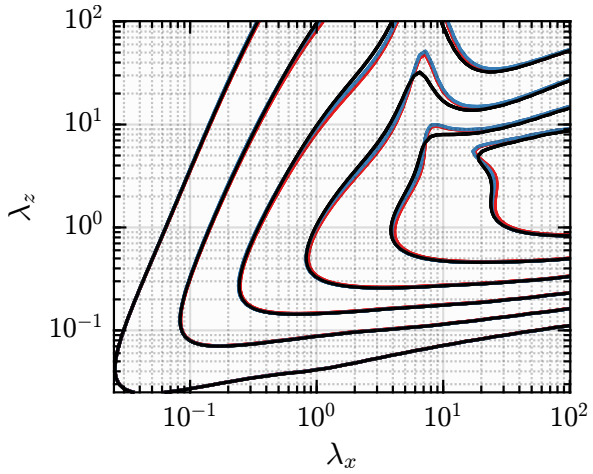

Figure 5.8: Contours of $\sigma_1^2 k_x k_z$ for case i (red), ii (black), and iii (blue) using $c = \overline{U}(y^+ = 100)$. The contour lines correspond to $\sigma_1^2 k_x k_z = 10^3$, 10^4, 10^5, 10^6, 10^7, 10^8.

Plotting the contours as a percent of the local maxima in the subsonic region for each case in Figure 5.7(b) does not collapse the amplification. This may point to the amplification mechanisms of temperature and density forcing lacking self-similarity due to the complex temperature variation in the thermodynamic variables. Case i has the smallest amplification while case iii has the largest amplification in the subsonic region. This again points to the reduction of linear amplification with thermal diffusivity, which is decreased with real gas effects.

Lastly, the sweep is computed using the full forcing for $c = \overline{U}(y^+ = 100) \approx .9$ and plotted in Figure 5.8. Relatively supersonic modes are not possible with this c and Ma since $\overline{Ma} < 1$ for all wavenumbers. As a result, the modes are all relatively subsonic and exhibit no discontinuity in the amplification. The choice of wavespeed ensures that the modes are localized by the critical layer at $y^+ = 100$ (McKeon and Sharma, 2010). At $y^+ = 100$, $\overline{T}$ and $\overline{U}$ are approximately the same between the CPG and CIG. However, $\overline{c}_v$ and $\overline{k}$ vary due to the CIG assumption. The $\lambda_z < 1$ modes have amplification that is independent of the CPG and CIG assumptions. These modes are localized at the critical layer, and have a minimal footprint at the wall. On the other hand, the $\lambda_z > 5$ are affected by the real gas effects since these modes have support close to the wall where $\overline{T}$ differs the most. Case i and iii have similar amplification despite their differences in the thermodynamic properties. The amplification of these modes are then due to the changes in $\overline{T}$ and $\overline{\rho}$ between the CPG and CIG.

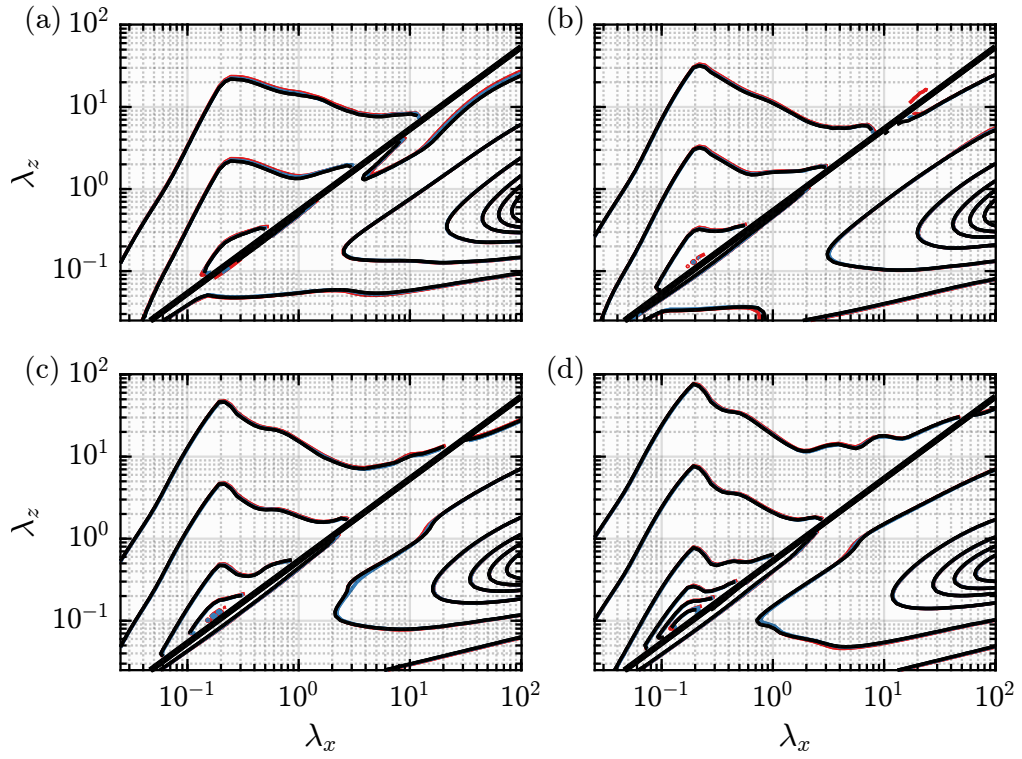

Figure 5.9: Contours of $\sigma_i^2 k_x k_z$ for case i (red), ii (black), and iii (blue) using $c = \overline{U}(y^+ = 15)$. The contour lines denote .1%, 1%, 10%, 30%, 50%, and 75% of the local maximum of $\sigma_i^2 k_x k_z$ below the sonic line. i = 2, 3, 4, and 5 are plotted in (a), (b), (c), and (d).

Differences in the Sub-optimal Resolvent Gains Using the CPG/CIG Assumptions

Up to now, the discussion has focused on the leading response modes and σ_1. Briefly, the discussion will now focus on the higher order modes by primarily looking at $\sigma_i^2 k_x k_z$ for the three different cases. These are plotted using the same sweep that was used to compute Figure 5.2 for i = 2, 3, 4, and 5 in Figure 5.9. For each $\sigma_i^2 k_x k_z$, the contours are plotted at percentages of the maxima of each case. Plotting these resolvent gains demonstrates negligible variations in the amplification of the higher order modes, consistent with what was plotted in Figure 5.3(b) for $\sigma_1^2 k_x k_z$. In fact the variations of the higher order amplifications amongst the different cases is smaller than the variation in the optimal amplification. Although not plotted, the higher order modes show small variations with the different cases consistent with the observations made for the optimal modes.

Finally, for reference, the maximum $\sigma_i^2 k_x k_z$ is listed for each case in Table 5.3. The optimal amplification is an order of magnitude larger than the sub-optimal

Case	1	2	3	4	5
i	1.11×10^6	2.89×10^5	1.22×10^5	5.40×10^4	2.50×10^4
ii	1.24×10^6	3.20×10^5	1.31×10^5	5.77×10^4	2.66×10^4
iii	1.21×10^6	3.05×10^5	1.28×10^5	5.64×10^4	2.60×10^4

Table 5.3: Maximum $\sigma_i^2 k_x k_z$ for each case in the subsonic region

amplification within the subsonic region. This is consistent with the low-rank behavior seen in the resolvent operator (McKeon and Sharma, 2010).

Summary of the Differences in Resolvent Amplification Using the CPG/CIG Assumptions

The real gas effects mostly change the linear amplification within the near-wall region of the flow, where the $\overline{T}$ are largest. The real gas effects were shown to increase the linear amplification of the flow, largely because of the temperature and density components of $\boldsymbol{\psi}_1$ and $\boldsymbol{\phi}_1$. The vibrational excitation decreases the thermal diffusivity which limits the temperature diffusion allowing for more amplification. The lack of collapse in $\overline{uu}$ and σ_1 in Figure 5.3(a) suggest that a velocity scale that accounts for the change in thermodynamic properties may be more appropriate (Bae, Dawson, and McKeon, 2020). In the supersonic region, the real gas effects did not affect the amplification due to the freestream excitation of these modes. The mode shapes, however, differ near the wall. The sub-optimal σ_i were shown to have slight deviations with the different cases, similar to σ_1.

5.4 Resolvent Formulation for a Mixture of Ideal Gases in Chemical Nonequilibrium

At large temperatures, chemical nonequilibrium effects in air become relevant as N_2 and O_2 dissociate into NO, O, and N (Anderson Jr., 2006). The effect of the chemistry terms on the resolvent amplification will now be studied. Accounting for the products and reactants in the dissociation of air requires a larger state vector with extra terms in the LNSE. These extra terms produce sources of shear and dissipation not present in a single species, non-reacting ideal gas.

Here, the fluid is assumed to be a mixture of ideal gases in chemical nonequilibrium and thermal equilibrium as in the simulation of Di Renzo and Urzay (2021). The species in the mixture are N_2, O_2, NO, N, and O, where ionization is neglected. The equations are nondimensionalized with the same variables in Section 5.2, with the

addition of the diffusion coefficients, $D_{i_s,e}$, of species i_s. In this section, subscripts e denote dimensional values defined at the freestream, rather than the local boundary layer edge. The governing equations are then

$$\breve{\rho}\frac{D\breve{\mathbf{u}}}{Dt} = -\frac{1}{\gamma_e Ma^2}\boldsymbol{\nabla}\breve{p} + \frac{1}{Re}\boldsymbol{\nabla}\cdot\breve{\tau}, \tag{5.15}$$

$$\begin{aligned}\breve{\rho}\breve{c}_v\frac{D\breve{T}}{Dt} = &-(\gamma_e-1)\breve{p}\boldsymbol{\nabla}\cdot\breve{\mathbf{u}} + \gamma_e(\gamma_e-1)\frac{Ma^2}{Re}\breve{\tau}:\boldsymbol{\nabla}\breve{\mathbf{u}} + \frac{\gamma_e}{PrRe}\boldsymbol{\nabla}\cdot\left(\breve{k}\nabla\breve{T}\right) + \\ &\sum_{i_s}^{N_s}\left[\frac{\overline{M}_e}{M_{i_s}}\frac{\gamma_e-1}{Re}\breve{T}\boldsymbol{\nabla}\cdot\left(\breve{\rho}_{i_s}\breve{\mathbf{V}}_{i_s}\right) - \breve{e}_{i_s}\breve{\omega}_{i_s} - \frac{\gamma_e}{Re}\breve{c}_{p,i_s}\boldsymbol{\nabla}\breve{T}\cdot\breve{\rho}_{i_s}\breve{\mathbf{V}}_{i_s}\right]\end{aligned}, \tag{5.16}$$

$$\frac{D\breve{\rho}_{i_s}}{Dt} = -\breve{\rho}_{i_s}\boldsymbol{\nabla}\cdot\breve{\mathbf{u}} - \frac{1}{Re}\boldsymbol{\nabla}\cdot\left(\breve{\rho}_{i_s}\breve{\mathbf{V}}_{i_s}\right) + \breve{\omega}_{i_s}, \tag{5.17}$$

$$\breve{p} = \breve{T}\sum_{i_s}^{N_s}\frac{\overline{M}_e}{M_{i_s}}\breve{\rho}_{i_s}, \tag{5.18}$$

$$\breve{\tau} = \breve{\mu}\left(\boldsymbol{\nabla}\breve{\mathbf{u}} + \boldsymbol{\nabla}\breve{\mathbf{u}}^T - \frac{2}{3}(\boldsymbol{\nabla}\cdot\breve{\mathbf{u}})\mathcal{I}\right), \tag{5.19}$$

where Equation 5.15 is the momentum equation, Equation 5.16 is the internal energy equation, Equation 5.17 is the continuity equation for each species, Equation 5.18 is the equation of state, and Equation 5.19 is the stress tensor. The subscripts $i_s = 1,\ldots,5$ denote N_2, O_2, NO, N, and O, respectively. Note that Equation 5.16 is expressed in terms of internal energy transport to ease comparisons with Equation 5.2 and to avoid time derivatives of $\breve{p}$ present when considering enthalpy transport (Malik and Anderson, 1991). Each species has its own density, $\breve{\rho}_{i_s}$, specific heat capacity at constant pressure, $\breve{c}_{p,i_s}$, internal energy, e_{i_s}, and chemical rates of mass production, $\breve{\omega}_{i_s}$. M_{i_s} is the molecular weight of each species, while $\overline{M}_e$ is the molecular weight of the mixture in the freestream. The diffusive flux is defined as

$$\breve{\rho}_{i_s}\breve{\mathbf{V}}_{i_s} = \sum_{k=1}^{N_s}\left(-\frac{\breve{D}_{i_s}}{Sc_{i_s}}\frac{\breve{\rho}_k M_{i_s}}{M_k}\nabla\breve{X}_{i_s} + \breve{Y}_{i_s}\sum_{j=1}^{N_s}\frac{\breve{D}_j}{Sc_j}\frac{\breve{\rho}_k M_j}{M_k}\nabla\breve{X}_j\right), \tag{5.20}$$

where $\breve{D}_{i_s}$, $\breve{Y}_{i_s} = \breve{\rho}_{i_s}/\breve{\rho}$ and $\breve{X}_{i_s} = \left(\breve{\rho}_{i_s}/M_{i_s}\right)/\left(\sum_{k=1}^{N_s}\breve{\rho}_k/M_k\right)$ are the mass diffusivity, mass fraction, and mole fraction of species i_s, respectively. $Sc_{i_s} = \mu_e/(\rho_e D_{i_s,e})$ is the Schmidt number of species i_s. By definition, Equation 5.20 ensures that $\sum_{i_s}^{N_s}\breve{\rho}_{i_s}\breve{\mathbf{V}}_{i_s} = \mathbf{0}$. Additionally, $\sum_{i_s}^{N_s}\breve{\omega}_{i_s} = 0$. Performing a summation of Equation 5.16 over i_s recovers the continuity equation of the mixture,

$$\frac{D\breve{\rho}}{Dt} = -\breve{\rho}\boldsymbol{\nabla}\cdot\breve{\mathbf{u}}, \tag{5.21}$$

though only the individual species continuity equations are used in the analysis. More details on the transport and thermal coefficients are reported by Di Renzo, Fu, and Urzay (2020). The wall is treated with no-slip, isothermal, and non-catalytic boundary conditions to match the simulation in Di Renzo and Urzay (2021).

The state vector is $\breve{\mathbf{q}} = \left[\breve{\mathbf{u}}, \breve{T}, \breve{\rho}_{N_2}, \breve{\rho}_{O_2}, \breve{\rho}_{NO}, \breve{\rho}_N, \breve{\rho}_O\right]$ while the thermodynamic state is $\breve{\theta} = \left[\breve{T}, \breve{\rho}_{N_2}, \breve{\rho}_{O_2}, \breve{\rho}_{NO}, \breve{\rho}_N, \breve{\rho}_O\right]$. $\breve{\mathbf{q}}$ is decomposed into a mean state, $\overline{\mathbf{q}}(y)$, and fluctuating state, $\mathbf{q}(\mathbf{x}, t)$, using the approximation of the parallel flow assumption as in Franko, MacCormack, and Lele (2010). The parallel flow assumption here models flow structures with characteristic length and time scales. Using a streamwise homogeneous and temporally stationary chemically reacting flow, as implied by the parallel flow assumption, can not capture the streamwise-varying heat loss from the endothermic reactions nor the boundary layer growth. Due to these nonparallel effects, this analysis is expected to hold primarily for the smallest scales with $\lambda_x \ll U_e^{-1}\, \partial U_e/\partial x$ and $\lambda_t \ll \partial U_e/\partial x$. Just as in Section 5.2, $\mathbf{q}$ is treated as a normal mode and the linear terms are separated from the nonlinear terms in the governing equations. These nonlinear terms are treated as an uncorrelated forcing. This creates the linear input-output relationship,

$$\widehat{\mathbf{q}} = \left(-i\omega\mathcal{I} + \widehat{\mathcal{L}}\right)\mathcal{B}\widehat{\mathbf{f}}. \tag{5.22}$$

The same convention from Section 5.2 is used for the overbar. Due to the complex relationship between the thermophysical properties, g, and $\breve{\theta}$, partial derivatives, $\partial\overline{g}/\partial\theta_i$, are computed numerically using centered finite differences. The fluctuations of quantities other than the state variables are defined using Equation 5.7. This is useful for defining the p, Y_{i_s}, or X_{i_s} components of the resolvent modes, for example. At the wall, $\widehat{\mathbf{q}}$ satisfies the no-slip, isothermal, and linearized non-catalytic boundary condition,

$$\partial_y \widehat{Y}_{i_s} = \partial_y\left(\frac{\widehat{\rho}_{i_s}}{\overline{\rho}} - \overline{Y}_{i_s}\frac{\widehat{\rho}}{\overline{\rho}}\right) = 0, \tag{5.23}$$

where $\widehat{\rho} = \sum_{i_s=1}^{N_s} \widehat{\rho}_{i_s}$.

For brevity, $\widehat{\mathcal{L}}$ is given as a block diagonal matrix as

$$\widehat{\mathcal{L}} = \begin{bmatrix} L_{1,1} & L_{1,2} & L_{1,3} & L_{1,4} & L_{1,5} & \cdots & L_{1,9} \\ L_{2,1} & L_{2,2} & L_{2,3} & L_{2,4} & L_{2,5} & \cdots & L_{2,9} \\ L_{3,1} & L_{3,2} & L_{3,3} & L_{3,4} & L_{3,5} & \cdots & L_{3,9} \\ L_{4,1} & L_{4,2} & L_{4,3} & L_{4,4} & L_{4,5} & \cdots & L_{4,9} \\ L_{5,1} & L_{5,2} & L_{5,3} & L_{5,4} & L_{5,5} & \cdots & L_{5,9} \\ \vdots & \vdots & \vdots & \vdots & \vdots & \ddots & \vdots \\ L_{9,1} & L_{9,2} & L_{9,3} & L_{9,4} & L_{9,5} & \cdots & L_{9,9} \end{bmatrix}, \tag{5.24}$$

where the blocks $L_{i,j}$ follow a similar convention as in Equation 5.9, except the indices from 1 to 9 denote u, v, w, T, ρ_{N_2}, ρ_{O_2}, ρ_{NO}, ρ_N, and ρ_O. $L_{j,i}$ with $j \geq 5$ denote terms of the linearized jth species continuity equation acting on $\mathbf{q}_i$. The explicit terms are listed in Appendix E.3. Just as in Equation 5.9, the diagonal terms include dissipative terms and the convective term, while the off-diagonal terms include component-wise amplification mechanisms from shear. $L_{4,4}$ can be expanded as

$$L_{4,4} = L^e_{4,4} + L^n_{4,4}, \tag{5.25}$$

where $L^e_{4,4}$ has the same terms as the single species CIG case would have while $L^n_{4,4}$ denotes all the terms related to the chemical nonequilibrium and molecular diffusion. All of the blocks have terms influenced by the mixture due to the dependence of the transport and thermophysical properties' dependence on the thermodynamic state. The blocks that directly include terms related to the chemical nonequilibrium or molecular diffusion are the $L_{i,j}$ blocks with $i \geq 5$, the $L_{i,j}$ blocks with $j \geq 5$, and the $L_{4,4}$ block.

The inner products are chosen such that $\mathcal{W}_r = \mathcal{W}_f = \mathcal{W}$ removes the influence of $p\nabla\cdot\mathbf{u}$ terms in the inner product as in the Chu norm (Chu, 1965; Hanifi, Schmid, and Henningson, 1996; Franko, MacCormack, and Lele, 2010). Explicitly, the weight matrix is

$$\mathcal{W} = \text{diag}\left(\overline{\rho}, \overline{\rho}, \overline{\rho}, \frac{\overline{\rho c}_v}{\overline{T} Ma^2 \gamma_e (\gamma_e - 1)}, \frac{\overline{M}_e \overline{T}}{M_1 \gamma_e Ma^2 \overline{\rho}_1}, \ldots, \frac{\overline{M}_e \overline{T}}{M_5 \gamma_e Ma^2 \overline{\rho}_5}\right). \tag{5.26}$$

There is a discrepancy with the Chu norm used by Franko, MacCormack, and Lele (2010) and Equation 5.26 due to the treatment of the $\left(\overline{\rho}_{i_s}\right)^{-1}$ terms. The former uses $\overline{\rho}$ rather than $\overline{\rho}_{i_s}$ to avoid division by zero in the freestream where the densities of NO, N, and O vanish. Here, regularization is applied by using $(\overline{\rho}_{i_s} + \epsilon_r)^{-1}$, with $\epsilon_r = 10^{-13}$, instead of $\left(\overline{\rho}_{i_s}\right)^{-1}$. Maintaining the $\overline{\rho}_{i_s}$ terms ensures that the

compressive work terms are neglected to allow for a direct comparison with the single species Chu-norm in Equation 5.26. See Appendix F for a comparison of results using the inner product in Equation 5.26 and the one described in Franko, MacCormack, and Lele (2010).

The equations are discretized using SBP with $N_y = 501$ grid points (Mattsson and Nordström, 2004). The grid points are stretched as $y_j = y_{max} \sinh\left(5.1\widehat{y}_j\right)/\sinh(5.1)$, where $\widehat{y}_j \in [0, 1]$ for $j = 1, \ldots, N_y$ are equispaced and $N_y = 501$. This grid stretching was employed in Di Renzo and Urzay (2021), though the value of N_y and y_{max} differ to allow for a larger freestream region and increased resolution. The same strategies as in Section 5.2 are used for the freestream boundary conditions, damping, and resolvent decomposition. The adjoint of the LNSE is treated using the conjugate transpose approach described in Section 2.2 which is known to create grid-to-grid oscillations as in Chandler et al. (2012). Although using increased resolution can mitigate these oscillations, the large state vector make this a computationally intensive approach. Instead, a spatial filter is used to remove the small scale oscillations near the wall (Lele, 1992). See Algorithm 2 for details on the implementation of the filter in the Arnoldi algortithm.

The effects of chemical nonequilibrium on the resolvent analysis will then be studied for a laminar base flow and a turbulent mean flow field. The laminar flow study compares the use of different base flows and gas modeling assumptions in the LNSE. It is shown that the supersonic modes are hardly affected by the changes in the base flow and modeling assumptions while the subsonic modes, with most support near the wall, are sensitive to the changes in the modeling assumptions. Due to the larger wall-normal extent of the $\lambda_x \to \infty$ modes, these modes are also most sensitive to the use of a chemical nonequilibrium assumption. For the turbulent flow fields, the use of chemical equilibrium and chemical nonequilibrium in the LNSE are contrasted. For the optimal modes, all the components of the response and forcing modes under chemical nonequilibrium, agree with those from the chemical equilibrium approach, except for the species density components. This is because the chemical equilibrium can not resolve the changes in concentration predicted by the resolvent modes in chemical nonequilibrium. The linear amplification through chemistry effects in the chemical nonequilibrium assumption creates non-negligible differences in the velocity and temperature components of the sub-optimal modes.

T_e	T_w	Ma	Re_{δ^*}	Pr
1040 K	1700 K	10.2	5.7×10^4	0.71

Table 5.4: Properties of the laminar similarity solutions. Here, $Re_{\delta^*} = \rho_e \delta^* U_e / \mu_e$ and T_e and T_w denote the freestream and wall temperatures.

5.5 Effects of Chemical Nonequilibrium on Resolvent Amplification in Laminar Flow

The resolvent analysis of a mixture of ideal gases in chemical nonequilibrium will now be investigated using laminar similarity solutions as the mean flow fields. The similarity solutions have matched properties, though one is computed using a CPG assumption while the other is computed assuming chemical nonequilibrium. First, the mean flow fields will be described. Following this, the resolvent analysis will then be used to compare results using the CIG, chemical equilibrium, and chemical nonequilibrium assumptions.

Description of the Laminar Similarity Solutions

CPG and chemical nonequilibrium similarity solutions are studied with their characteristic properties and imposed temperatures defined in Table 5.4. Although Re_{δ^*} is matched between the two flows, the Re differ. The chemical nonequilibrium case has $Re = 7.3 \times 10^4$ while the CPG has $Re = 7.0 \times 10^4$. Re_{δ^*} was matched since it is an integral measure of the velocity. The similarity solution of a CPG is computed using $\breve{\mu} = \breve{T}^{2/3}$ as opposed to the Sutherland law. To derive the similarity solution for the CPG, the following variables are defined as

$$\xi(x) = \int_0^x \rho_e \mu_e U_e dx \tag{5.27}$$

and

$$\eta(x, y) = \frac{U_e \rho_e}{\sqrt{2\xi}} \int_0^y \breve{\rho} dy. \tag{5.28}$$

Note that for the ZPG case studied here, $\xi(x) = \rho_e \mu_e U_e x$. A similarity variable, $f(\eta)$, is introduced such that

$$u = f' \tag{5.29}$$

and

$$v = -\frac{1}{U_e \breve{\rho}} \left(\frac{\rho_e \mu_e U_e}{\sqrt{2\xi}} f + \frac{\partial \eta}{\partial x} \sqrt{2\xi} f' \right). \tag{5.30}$$

Case	Mean	LNSE
i	CPG	CIG
ii	CNE	CE
iii	CNE	CNE

Table 5.5: CIG, CE (chemical equilibrium), and CNE (chemical nonequilibrium) denote the assumption used for the mean flow field and the LNSE.

These expressions ensure that the continuity equation in Equation 5.3 holds. Taking the thin boundary layer assumptions, the streamwise momentum equation becomes

$$(Cf'')' + ff'' = 0, \tag{5.31}$$

where $C = \breve{\rho}(\eta)\breve{\mu}(\eta)$. The similarity variables and thin boundary layer equations are then used in Equation 5.2 to arrive at

$$\left(\frac{C}{Pr}g'\right)' + fg' + C\frac{u_e^2}{h_e}(f'')^2 = 0, \tag{5.32}$$

where $g = \breve{T}$, h_e is the enthalpy at the freestream, and the assumption that the Prandtl number is constant across the boundary layer is invoked. Equations 5.31 and 5.32 are closed with the addition of the boundary conditions $f(0) = 0$, $f'(0) = 0$, $g(0) = T_w/T_e$, $\lim_{\eta\to\infty} f = 1$, and $\lim_{\eta\to\infty} g = 1$. More details on the derivation can be found in Anderson Jr. (2006).

The similarity solution for a hypersonic boundary layer with a mixture of ideal gases in chemical nonequilibrium is described in the appendix of Di Renzo and Urzay (2021). The strategy for the similarity solution is similar, except with the addition of 5 equations for the species continuity equations, additional terms in Equation 5.32 related to the energy flux from diffusion, and different constitutive relations for the thermophysical properties. Furthermore, they require the boundary conditions $Y_{N_2} = 0.767$, $Y_{O_2} = 0.233$, $Y_{NO} = 0$, $Y_N = 0$, and $Y_O = 0$ at the freestream and $d_\eta Y_{N_2} = d_\eta Y_{O_2} = d_\eta Y_{NO} = d_\eta Y_N = d_\eta Y_O = 0$ at the wall to satisfy the non-catalytic boundary conditions.

Three cases are studied to investigate the effect of chemical nonequilibrium on the linear amplification. Case i uses the CPG base flow while case ii uses a base flow under chemical nonequilibrium. These two cases use a single species ideal gas for the LNSE where the thermophysical properties are computed using the mean thermodynamic state, $\overline{\theta}$ (Edwards, 1992; Malik and Anderson, 1991). The base flow and the LNSE of case i use different thermophysical properties. Despite the

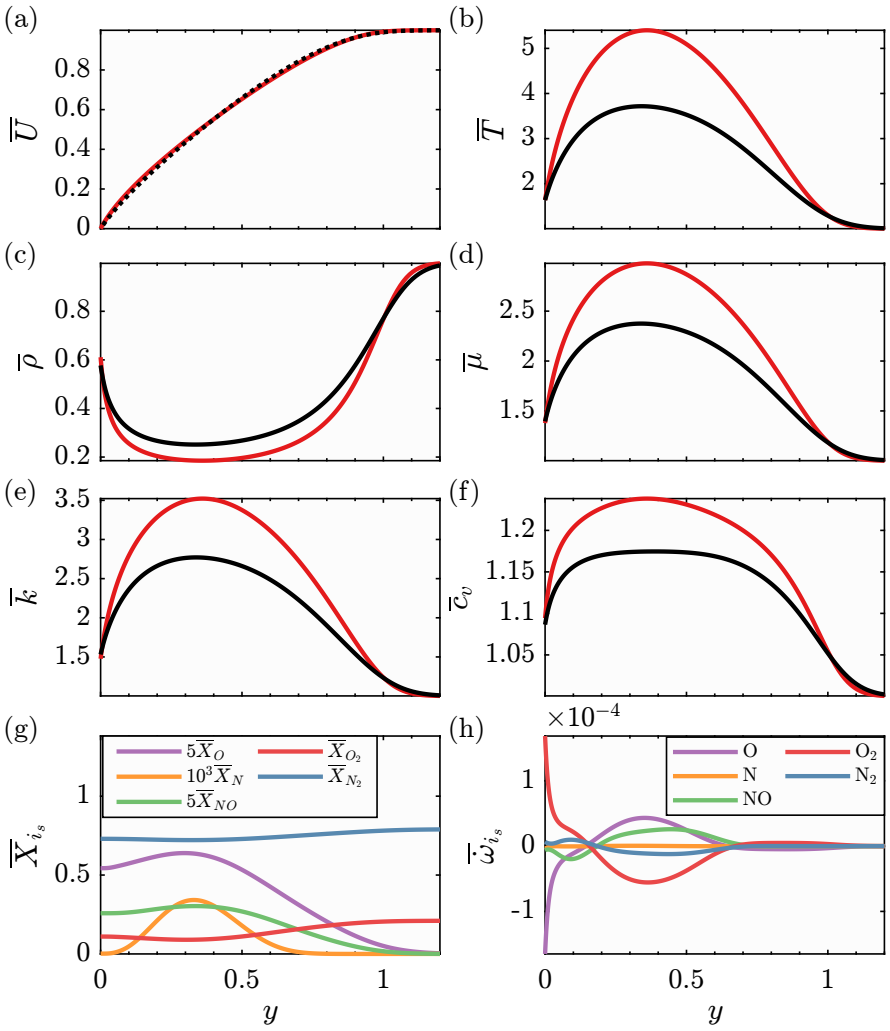

Figure 5.10: $\overline{U}$ (a), $\overline{T}$ (b), $\overline{\rho}$ (c), $\overline{\mu}$ (d), $\overline{k}$ (e), and $\overline{c}_v$ (f) for the CPG (in red) and CNE (in black) similarity solutions. $\overline{X}_{i_s}$ (g), and $\dot{\overline{\omega}}_{i_s}$ (h) are plotted with their colors labeled in the legend. Note that the $\overline{X}_{i_s}$ of the dissociated components are rescaled in (g) for visualization.

discrepancy, case i is primarily used to compare the differences in the mean flow field as opposed to the thermophysical properties. Case i uses a CIG assumption throughout the boundary layer with thermophysical properties computed using the local $\overline{T}$ while case ii uses chemical equilibrium, with the thermophysical properties in the LNSE computed locally using the mass fractions and $\overline{T}$ from the similarity solution in chemical nonequilibrium. Both cases i and ii use a single species gas. Case iii uses chemical nonequilibrium in the base flow and the LNSE. These are summarized in Table 5.5. This is similar to what was studied in Section 5.3, except here the effects of chemical nonequilibrium are studied.

The base flows are plotted in Figure 5.10. The chemical nonequilibrium effects on $\overline{U}$ in the similarity solution are negligible. The chemical nonequilibrium effects are most evident in $\overline{T}$ and $\overline{\rho}$ due to the changes in the thermodynamics. $\overline{k}$, $\overline{\mu}$, and $\overline{c}_v$ differ significantly due to the change in thermodynamic state, primarily because of the $\overline{T}$ differences. $\overline{X}_N$ is largest where $\overline{T}$ peaks. $\overline{X}_{NO}$ and $\overline{X}_O$ also reach their largest values where $\overline{T}$ peaks. The mean chemical rates of mass production, $\overline{\dot{\omega}}_{i_s}$, are plotted in Figure 5.10(h). They peak locally where $\overline{T}$ peaks, but for O and O_2, they have large values near the wall. Since differences in $\overline{U}$ are negligible between the three cases, comparisons using case i will demonstrate the differences in the resolvent modes and amplification due to differences in $\overline{\theta}$. Case ii and iii will illustrate differences in the modelling approaches.

Comparison of the Resolvent Analysis Results Using Laminar Similarity Solutions

The linear amplification of the three cases is studied by performing a sweep over 80 logarithmically spaced points between $2\pi/.025$ and $2\pi/100$ for both k_x and k_z. The wavespeed, c, is fixed at $c = .5$. c is chosen such that $c = \overline{U}(y_T)$, where y_T it the location of maximum temperature. This is the region where chemical nonequilibrium effects are most apparent as the temperature is large enough to sustain dissociation of O_2, the nitrogen oxidation via the Zel'dovich mechanism, and slight dissociation of N_2 (Anderson Jr., 2006; Di Renzo and Urzay, 2021). In this sweep, amplification from different components of the forcing are investigated through component-wise masking with $\mathcal{B}$. The sweeps consider forcing from the full forcing vector, temperature, density, or species density components. The density forcing is only studied in case iii which supports chemical nonequilibrium. The forcing from the density component entails forcing from all the species density components such that $\mathcal{B}\boldsymbol{\phi} = [0, 0, 0, 0, \phi_{\rho_{N_2}}, \phi_{\rho_{O_2}}, \phi_{\rho_{NO}}, \phi_{\rho_N}, \phi_{\rho_O}]$.

In Figure 5.11, the contours of $\sigma_1^2 k_x k_z$ are compared for the three cases using the full forcing vector. A visible discontinuity is present at $\overline{Ma} = 1$ in all three cases indicating that freestream supersonic phenomena are supported even under chemical nonequilibrium. This is expected since these modes are primarily amplified by a singularity in the freestream (Madhusudanan and McKeon, 2022; Mack, 1984), where chemical nonequilibrium effects are negligible due to the smaller $\overline{T}$ (Di Renzo and Urzay, 2021). As a result, cases ii and iii have small differences in the supersonic region for $\lambda_x < 50$. Case i has similar contour shapes, although the amplification is

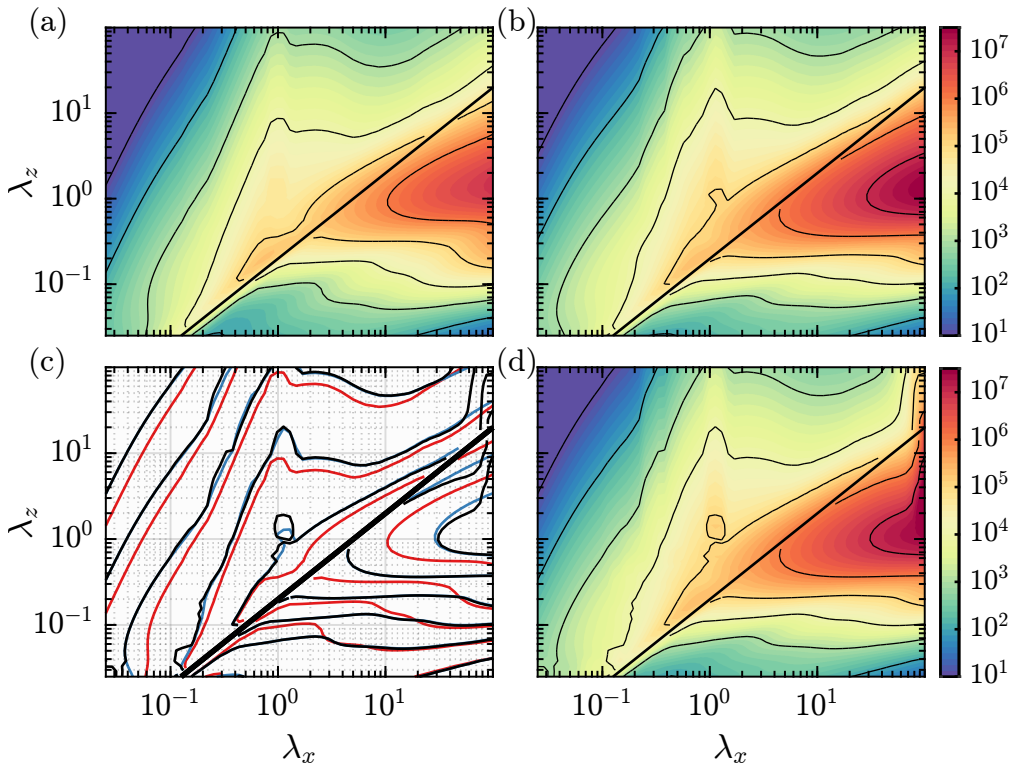

Figure 5.11: Contours of $\sigma_1^2 k_x k_z$ for case i (a), case ii (b), and case iii (d). The contour lines denote $\sigma_1^2 k_x k_z = 10^1, 10^2, \ldots, 10^7$. These contours are all plotted in (c) where case i, ii, and iii are in red, blue, and black. The solid black line denotes the sonic line.

smaller than in cases ii and iii, likely because of the increased temperature diffusivity within the boundary layer. In the subsonic region, the differences between case i and cases ii and iii are most evident because of the differences within the boundary layer. Case i once again has decreased amplification due to the reduction in the $\overline{T}_y$ and increased temperature diffusivity.

The linear amplification in Figure 5.11 of cases ii and iii differs the most for streak-like modes with $\lambda_x > 50, \lambda_z > 1$ with case iii having increased amplification. The streaky structures have support near the wall, where they are amplified by non-normal, off-diagonal terms in the LNSE due to the chemistry components. These terms can be large near the wall for the laminar flow, as shown in Figure 5.10(h). When chemical equilibrium is assumed, these chemistry related terms are neglected resulting in a decrease in amplification. Compared to Figure 5.2, the jump across $\overline{Ma} = 1$ in Figure 5.11 is smaller. This is a Ma related effect, likely due to increased viscous dissipation with Ma^2 in the energy equations which regularize the singularities that generate acoustic modes.

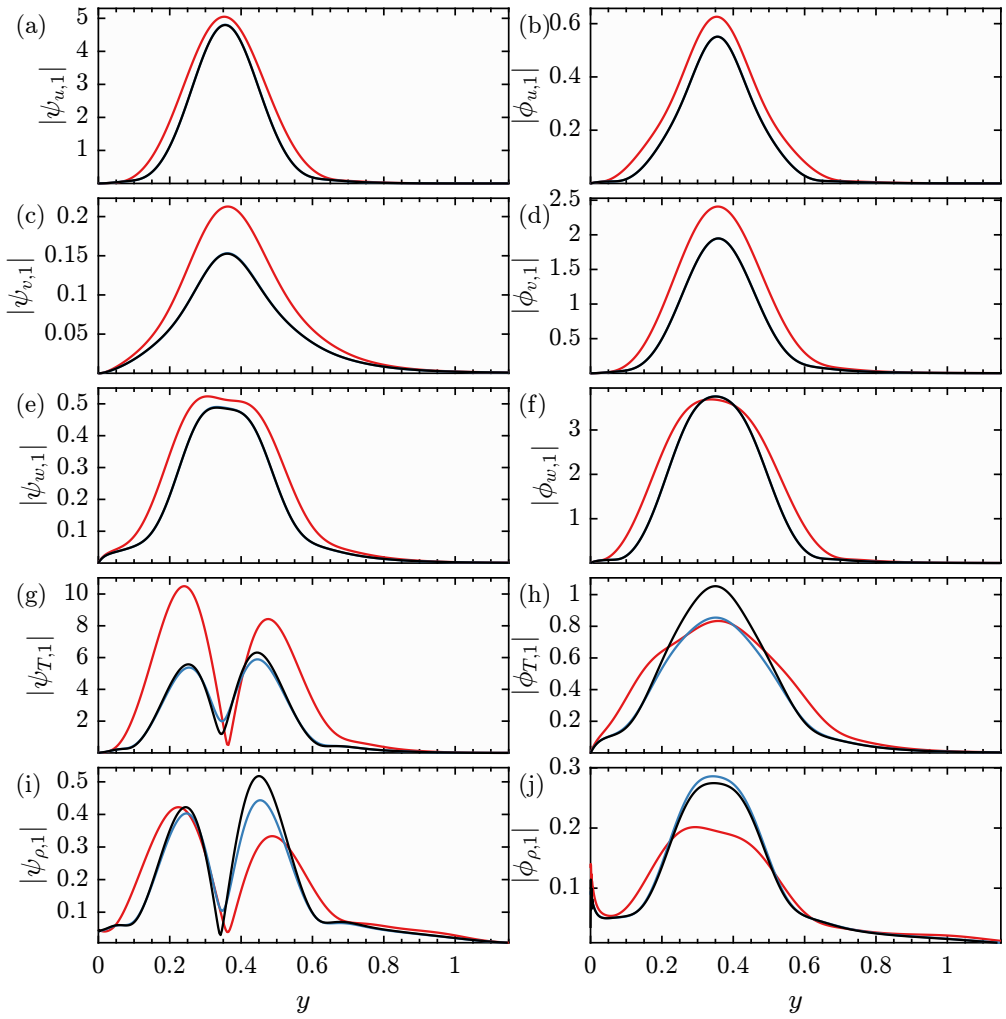

Figure 5.12: $|\psi_{u,1}|$ (a), $|\phi_{u,1}|$ (b), $|\psi_{v,1}|$ (c), $|\phi_{v,1}|$ (d), $|\psi_{w,1}|$ (e), $|\phi_{w,1}|$ (f), $|\psi_{T,1}|$ (g), $|\phi_{T,1}|$ (h), $|\psi_{T,1}|$ (i), $|\phi_{T,1}|$ (j) for representative subsonic modes ($k_x = 2\pi/10$, $k_z = 2\pi/1$, $c = .5$). Case i, ii, and iii are in red, blue, and black solid lines.

In Figure 5.12, the velocity, temperature, and density components of $\boldsymbol{\psi}_1$ and $\boldsymbol{\phi}_1$ are compared for all three cases for a representative subsonic mode with $k_x = 2\pi/10$, $k_z = 2\pi/1$, and $c = .5$. Due to the differences between $\overline{T}$ and $\overline{\rho}$ within the boundary layer, the resolvent modes of case i differ significantly. The velocity components between cases ii and iii are unaffected by the chemical nonequilibrium effects. $\phi_{T,1}$ and $\phi_{\rho,1}$ differ between case ii and iii because the LNSE of case iii have thermodynamic state-dependent off-diagonal terms from the chemical nonequilibrium and molecular diffusion that are not present in case ii. These effects then change $\psi_{T,1}$ and $\psi_{\rho,1}$.

Since case ii assumes chemical equilibrium, a single species of gas is assumed. To compare the species components of case iii with the chemical equilibrium approach,

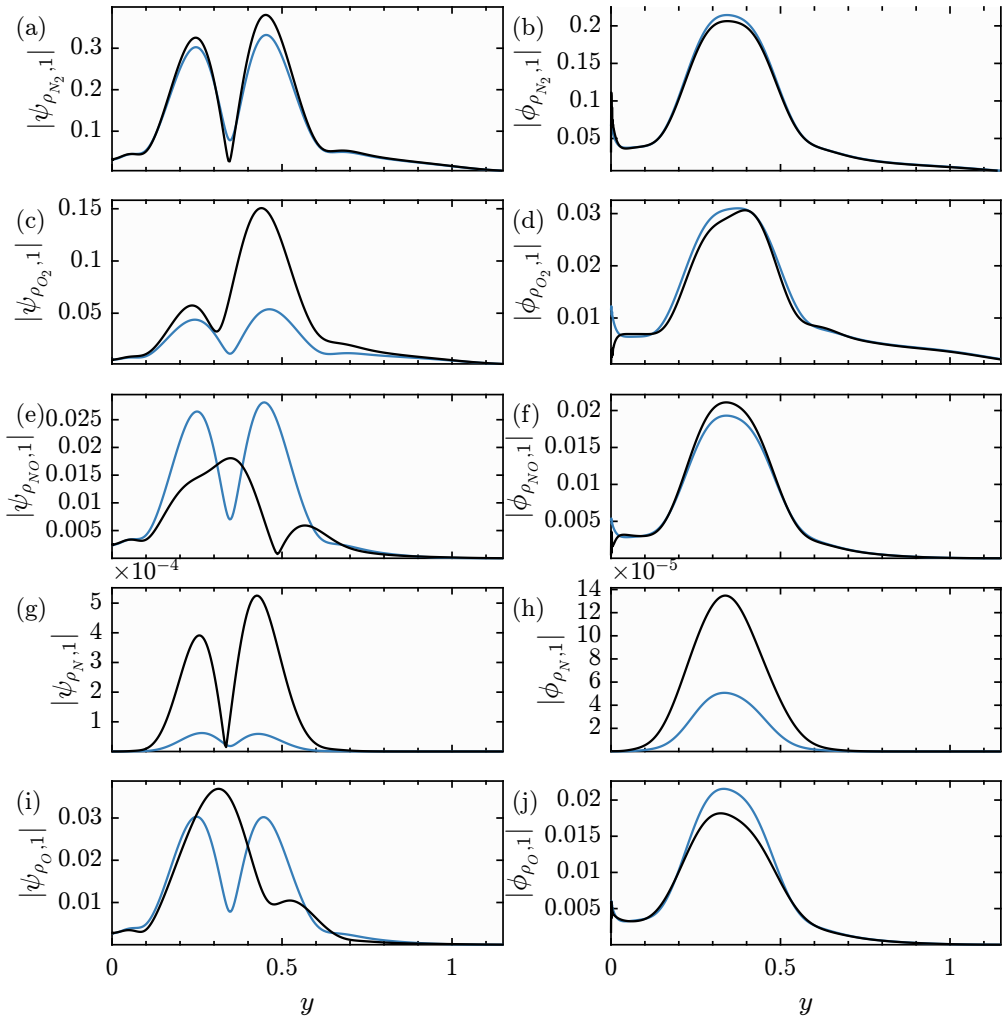

Figure 5.13: $\left|\psi_{\rho_{N_2},1}\right|$ (a), $\left|\phi_{\rho_{N_2},1}\right|$ (b), $\left|\psi_{\rho_{O_2},1}\right|$ (c), $\left|\phi_{\rho_{O_2},1}\right|$ (d), $\left|\psi_{\rho_{NO},1}\right|$ (e), $\left|\phi_{\rho_{NO},1}\right|$ (f), $\left|\psi_{\rho_N,1}\right|$ (g), $\left|\phi_{\rho_N,1}\right|$ (h), $\left|\psi_{\rho_O,1}\right|$ (i), $\left|\phi_{\rho_O,1}\right|$ (j) for representative subsonic modes ($k_x = 2\pi/10$, $k_z = 2\pi/1$, $c = .5$). Case ii and iii are in blue and black solid lines.

the species components of case ii are defined as $\psi_{\rho_{i_s},1} = \overline{Y}_{i_s}\psi_{\rho,1}$ and $\phi_{\rho_{i_s},1} = \overline{Y}_{i_s}\phi_{\rho,1}$. In case iii, these species components are computed explicitly and account for fluctuations in the mass fractions from the species continuity equations. Following the definition of $\psi_{\rho_{i_s},1}$ in case ii, the species component $\psi_{\rho_{i_s},1}$ in case iii is equivalent to $\overline{Y}_{i_s}\psi_{\rho,1} + \overline{\rho}\psi_{Y_{i_s},1}$. The species components are compared in Figure 5.13. The N_2 and O_2 density components are largest, as one would expect, since these species are most abundant within the boundary layer. The density components of NO and O are also larger than the density component of N since the mean temperature within the boundary layer and freestream is less than 4000 K, which is too small to support significant dissociation of N_2 (Anderson Jr., 2006). Furthermore, any

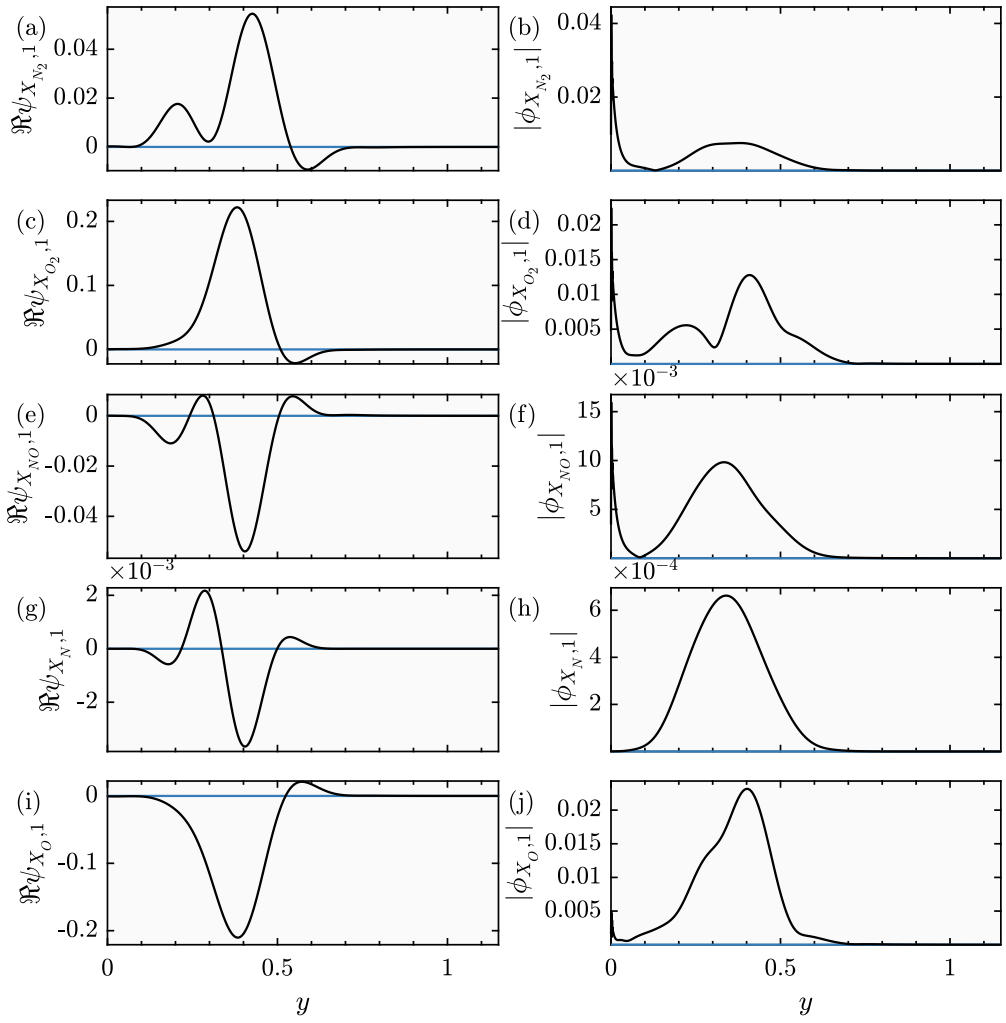

Figure 5.14: Real part of $\psi_{X_{N_2},1}$ (a), $\psi_{X_{O_2},1}$ (c), $\psi_{X_{NO},1}$ (e), $\psi_{X_N,1}$ (g), and $\psi_{X_O,1}$ (i) and magnitude of $\phi_{X_{N_2},1}$ (b), $\phi_{X_{O_2},1}$ (d), $\phi_{X_{NO},1}$ (f), $\phi_{X_N,1}$ (h), and $\phi_{X_O,1}$ (j) for representative subsonic modes ($k_x = 2\pi/10$, $k_z = 2\pi/1$, $c = .5$). Case ii and iii are in blue and black solid lines.

production of N is rapidly consumed by the Zel'dovich mechanism, limiting its support. The ρ_{N_2} components are well approximated in case ii, likely because there is less dissociation of N_2 for these temperatures so $\psi_{Y_{N_2},1}$ is small in case iii. Case ii computes a double peaked shape of $\left|\psi_{\rho_{O_2},1}\right|$, though with an overestimation of the amplitudes. This is consistent with the dissociation of O_2 at these temperatures that makes $\psi_{Y_{O_2},1}$ non-negligible. The dissociated components, NO, N, and O, are completely misrepresented in the response modes in both shape and amplitude. Notably for $\psi_{\rho_N,1}$, the chemical equilibrium approach provides amplitudes almost an order of magnitude larger than in the chemical nonequilibrium approach. The forcing modes agree better between cases ii and iii than the response modes in

both shape and amplitude. Since the species components in case ii are computed without accounting for fluctuations in Y_{i_s}, this suggests that forcing from changes in concentration is not optimal. Rather, ϕ_{ρ_1} may take advantage of a component-wise amplification mechanism for ρ.

The mole fractions are functions of the temperature and the mass fractions, which can only change if a mixture of gases is used. Using a single-species gas assumption, the mole fraction fluctuations in the resolvent modes are 0. In Figure 5.14, the mole fractions are plotted for the chemical nonequilibrium in case iii. $\psi_{X_{O_2},1}$ is anticorrelated with $\psi_{X_O,1}$ since a decrease in O_2 results in an increase in O. With the Zel'dovich mechanism, N_2 and O produce NO and N. N is then rapidly consumed with O_2 to create NO and O. As a result, increases in $\psi_{X_{O_2},1}$ and $\psi_{X_{N_2},1}$ lead to decreases in $\psi_{X_{NO},1}$ and negligible contributions of $\psi_{X_N,1}$ from the Zel'dovich mechanism. This causes the peak of $\psi_{X_{N_2},1}$ to be also anticorrelated with the peaks of $\psi_{X_N,1}$ and $\psi_{X_{NO},1}$. $\psi_{X_N,1}$ is the smallest since the temperatures do not support significant production of N. In the forcing modes, $\phi_{X_{i_s},1}$ have large amplitudes near the wall to force the large shear terms in the chemical terms, such as $\overline{\dot{\omega}}_{i_s}$ in Figure 5.10(g). The small values of $\phi_{X_{i_s},1}$ further explain why using the chemical equilibrium approximation for the forcing resulted in good approximations of $\phi_{\rho_{i_s},1}$ in Figure 5.13.

Now the resolvent modes are compared for a representative supersonic mode with $k_x = 2\pi/5$, $k_z = 2\pi/10$, and $c = .5$. Figure 5.15 compares the velocity, temperature, and density components of $\boldsymbol{\psi}_1$ and $\boldsymbol{\phi}_1$. Despite the presence of chemical nonequilibrium effects, the freestream radiating acoustics are still excited. Case i differs because of the change in $\overline{T}$ within the boundary layer, though it is interesting to note that $\psi_{u,1}$ is almost unchanged between the three cases. The differences between case ii and iii are negligible, except for the boundary layer region of $\phi_{T,1}$. Similarly to Section 5.3, these modes are excited by freestream phenomena, where the chemical nonequilibrium effects are negligible.

In Figure 5.16, the densities of the species components are plotted. The ρ_{N_2} and ρ_{O_2} components are responsible for the pressure oscillations in the freestream acoustics, while the ρ_N, ρ_O, and ρ_{NO} components are nonexistent in the freestream. In the freestream, the mean temperature is too small to support dissociated components, and this is captured with the linear analysis. Here, the chemical equilibrium assumption agrees well with for the ρ_{N_2} and ρ_{O_2} components, even within the boundary layer. This is a stark contrast from what was seen in Figure 5.13. However, the

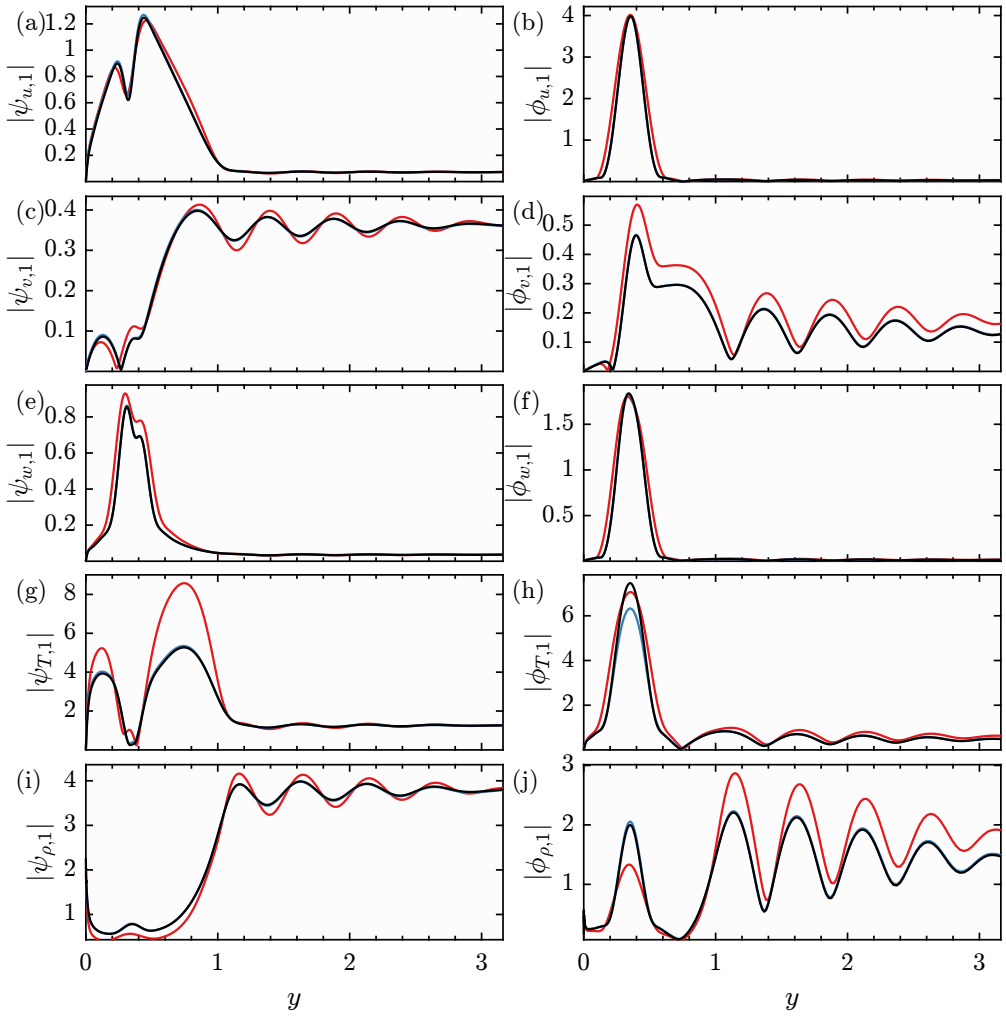

Figure 5.15: $|\psi_{u,1}|$ (a), $|\phi_{u,1}|$ (b), $|\psi_{v,1}|$ (c), $|\phi_{v,1}|$ (d), $|\psi_{w,1}|$ (e), $|\phi_{w,1}|$ (f), $|\psi_{T,1}|$ (g), $|\phi_{T,1}|$ (h), $|\psi_{T,1}|$ (i), $|\phi_{T,1}|$ (j) for representative supersonic modes ($k_x = 2\pi/5$, $k_z = 2\pi/10$, $c = .5$). Case i, ii, and iii are in red, blue, and black solid lines.

dissociated components are not predicted well, with the biggest difference occurring for the ρ_N component. The $\phi_{\rho_{i_s},1}$ components are once again predicted well using the chemical equilibrium approach. These supersonic modes require excitation of a freestream singularity in pressure rather than forcing of chemistry terms through changes in concentration.

Finally, the molar fractions of the response modes are compared in Figure 5.17. Just as in the subsonic mode, the anticorrelations observed in $\psi_{X_{i_s},1}$ are reflected in this mode. In the freestream, $\psi_{X_{i_s},1} \approx 0$ because the small temperatures do not support chemical nonequilibrium. As a result, changes to the concentrations in the mixture are not supported in the freestream, despite the fluctuations in the density. This helps explain why the ρ_{N_2} and ρ_{O_2} components of the resolvent modes agreed well

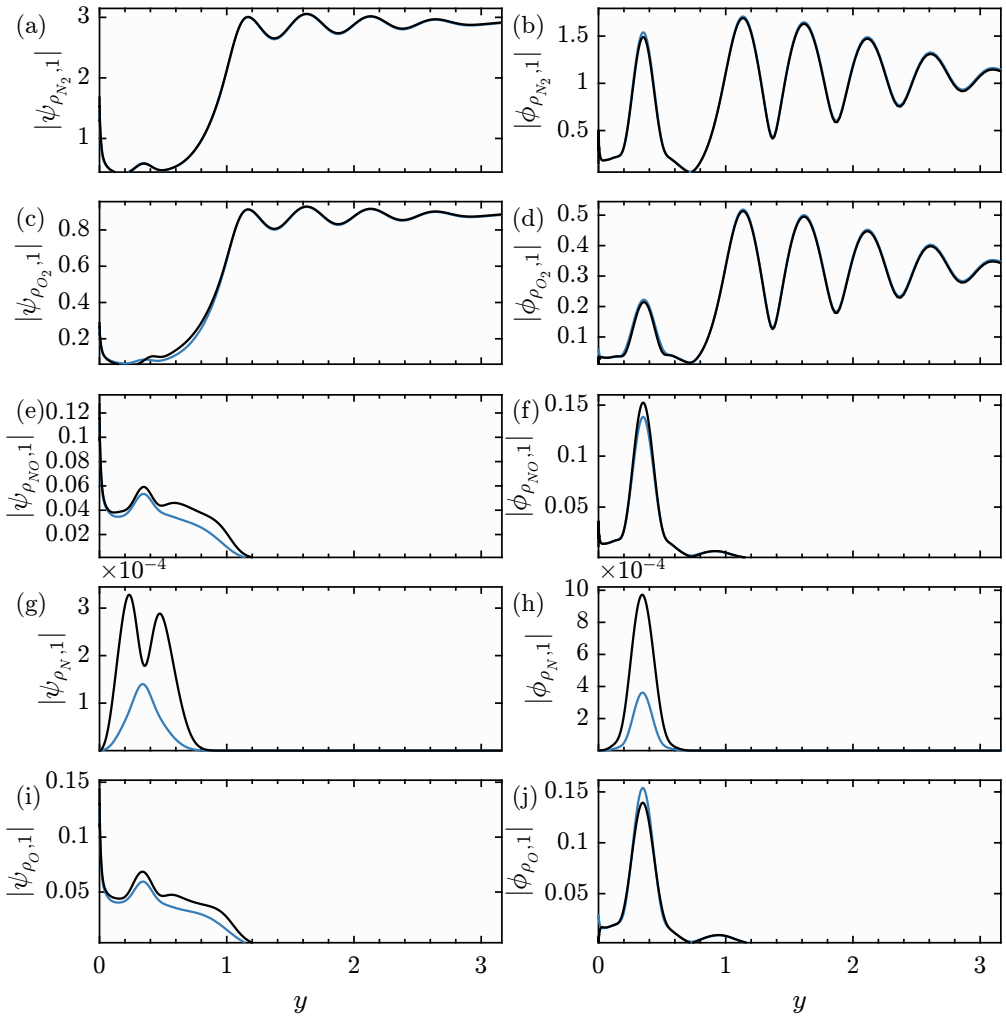

Figure 5.16: $\left|\psi_{\rho_{N_2},1}\right|$ (a), $\left|\phi_{\rho_{N_2},1}\right|$ (b), $\left|\psi_{\rho_{O_2},1}\right|$ (c), $\left|\phi_{\rho_{O_2},1}\right|$ (d), $\left|\psi_{\rho_{NO},1}\right|$ (e), $\left|\phi_{\rho_{NO},1}\right|$ (f), $\left|\psi_{\rho_{N},1}\right|$ (g), $\left|\phi_{\rho_{N},1}\right|$ (h), $\left|\psi_{\rho_{O},1}\right|$ (i), $\left|\phi_{\rho_{O},1}\right|$ (j) for representative supersonic modes ($k_x = 2\pi/5$, $k_z = 2\pi/10$, $c = .5$). Case ii and iii are in blue and black solid lines.

between cases ii and iii for the representative supersonic modes. In Di Renzo and Urzay (2021), the freestream was also absent of any change in concentration. The small components of $\phi_{X_{i_s},1}$ confirm why $\phi_{\rho_{i_s},1}$ in case ii agreed well with case iii just like in the subsonic mode.

The representative modes plotted corresponded to regions in spectral space where the amplification showed little discrepancy when incorporating the chemical nonequilibrium effects. The mode shapes between cases ii and iii were also hardly affected. A representative streaky mode with $k_x = 2\pi/100$, $k_z = 2\pi/5$, and $c = .5$, characteristic of the region in Figure 5.11 where amplification differs the most, is plotted in Figures 5.18. This mode is significantly affected by the chemical nonequilibrium

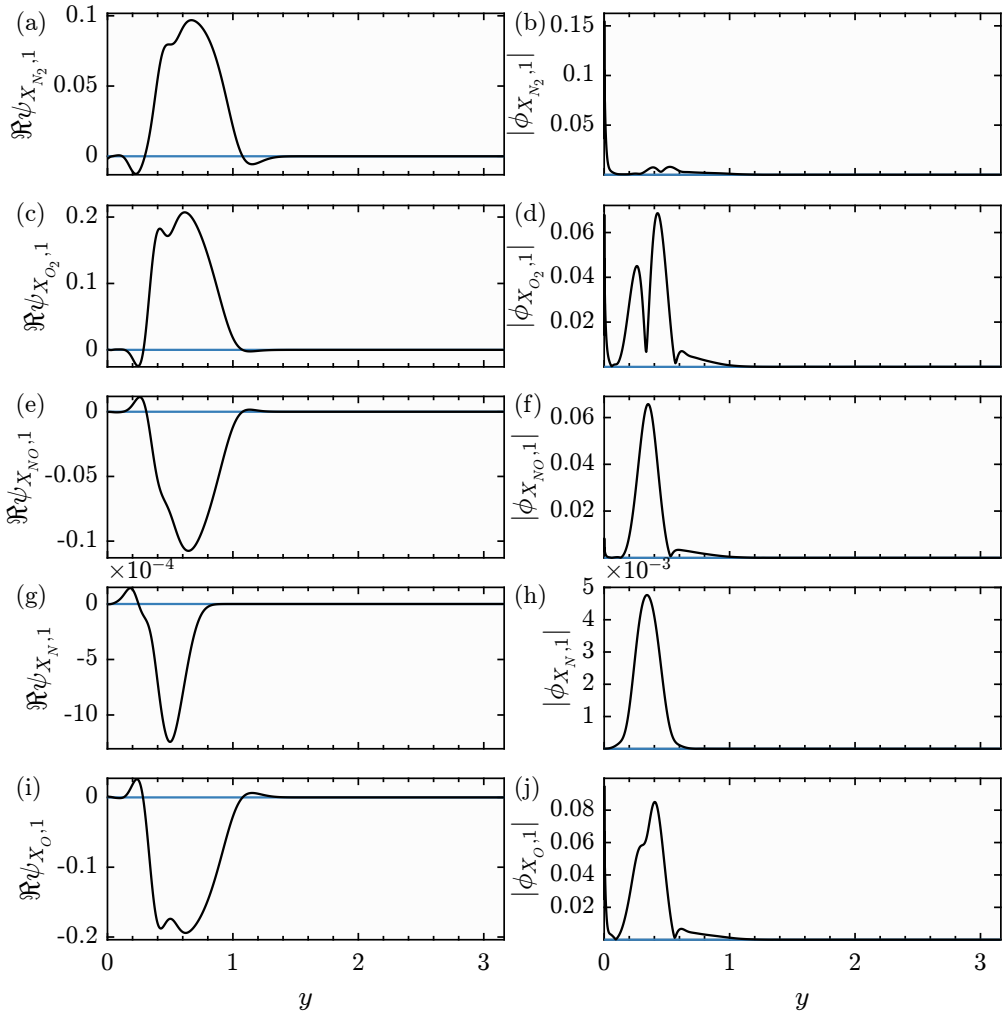

Figure 5.17: Real part of $\psi_{X_{N_2},1}$ (a), $\psi_{X_{O_2},1}$ (c), $\psi_{X_{NO},1}$ (e), $\psi_{X_N,1}$ (g), and $\psi_{X_O,1}$ (i) and magnitude of $\phi_{X_{N_2},1}$ (b), $\phi_{X_{O_2},1}$ (d), $\phi_{X_{NO},1}$ (f), $\phi_{X_N,1}$ (h), and $\phi_{X_O,1}$ (j) for representative supersonic modes ($k_x = 2\pi/5$, $k_z = 2\pi/10$, $c = .5$). Case ii and iii are in blue and black solid lines.

effects as $\boldsymbol{\psi}_1$ and $\boldsymbol{\phi}_1$ differ substantially from case ii. In fact, $\boldsymbol{\psi}_1$ for cases i and ii are more similar than case iii, despite their differences in mean flow fields. Unlike the subsonic modes plotted in Figure 5.12, these streaky modes are able to extend over a wide wall-normal extent of the flow, reaching down to the wall. The large shear terms in the chemistry terms caused by the cooling by the wall create sources of amplification for these modes that reach down to the wall. This can be seen in the temperature and density components of $\boldsymbol{\phi}_1$ for case iii which differs significantly from the other cases. Forcing from the velocity components do not show such extreme variations when using the chemical nonequilibrium approach, suggesting that this mode is amplified by differences in the thermodynamics.

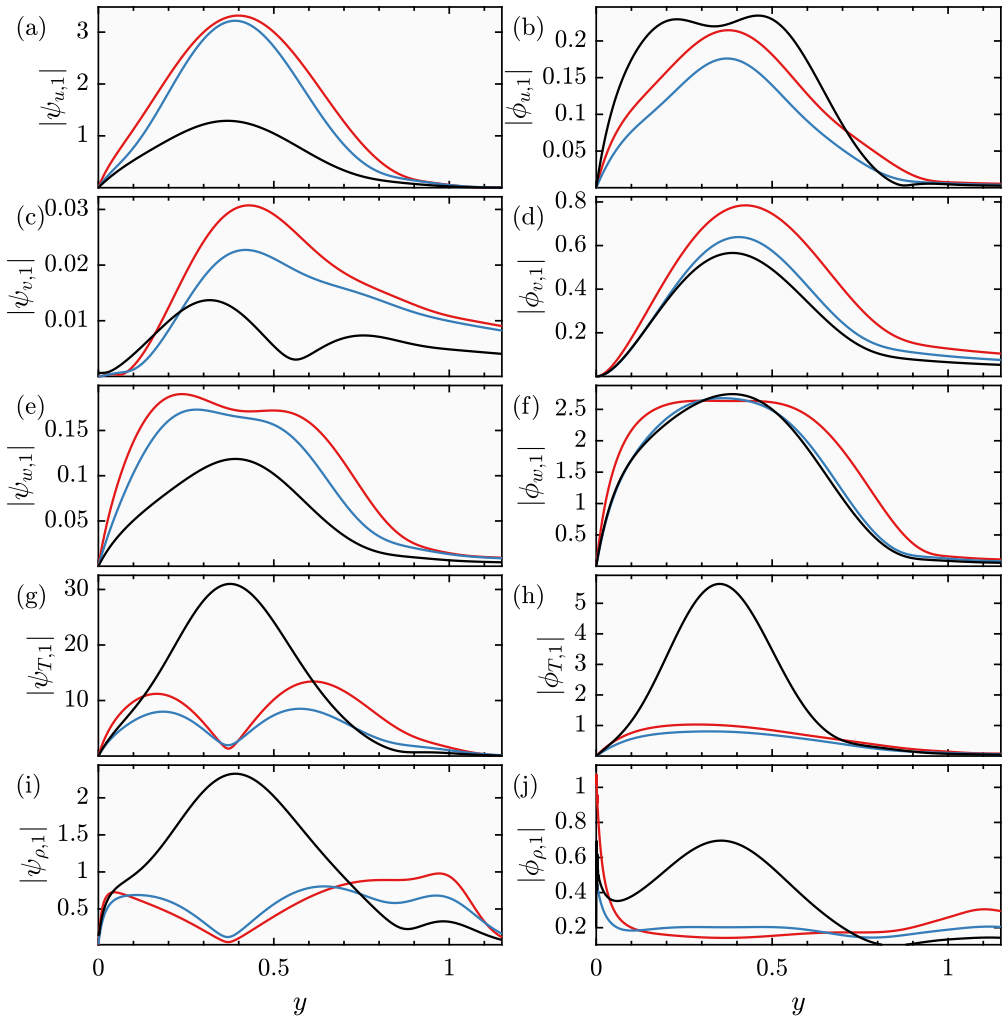

Figure 5.18: $|\psi_{u,1}|$ (a), $|\phi_{u,1}|$ (b), $|\psi_{v,1}|$ (c), $|\phi_{v,1}|$ (d), $|\psi_{w,1}|$ (e), $|\phi_{w,1}|$ (f), $|\psi_{T,1}|$ (g), $|\phi_{T,1}|$ (h), $|\psi_{T,1}|$ (i), $|\phi_{T,1}|$ (j) for representative subsonic streaky modes ($k_x = 2\pi/100$, $k_z = 2\pi/5$, $c = .5$). Case i, ii, and iii are in red, black, and blue solid lines.

The chemical nonequilibrium components of the streaky mode are queried in Figures 5.19 and 5.20. The $\psi_{\rho_{i_s},1}$ components of case i differ significantly from the chemical equilibrium approach in case ii. This is likely brought upon by the difference in ϕ_ρ and ϕ_T. Here, $\phi_{\rho_{i_s},1}$ is shown to differ from the chemical equilibrium approach since $\phi_{\rho,1}$ already differed substantially. In Figure 5.20 the X_{i_s} components are plotted. Notably, $\phi_{X_{O_2},1}$ and $\phi_{X_O,1}$ are large indicating substantial effects from chemical concentration-related forcing.

Since thermodynamic state-dependent chemistry terms are the only difference between case ii and iii, the forcing is masked to consider only linear amplification from ϕ_T. The sweep over k_x and k_z is recomputed using only temperature-component forcing and is plotted in Figure 5.21. The temperature forcing excites supersonic

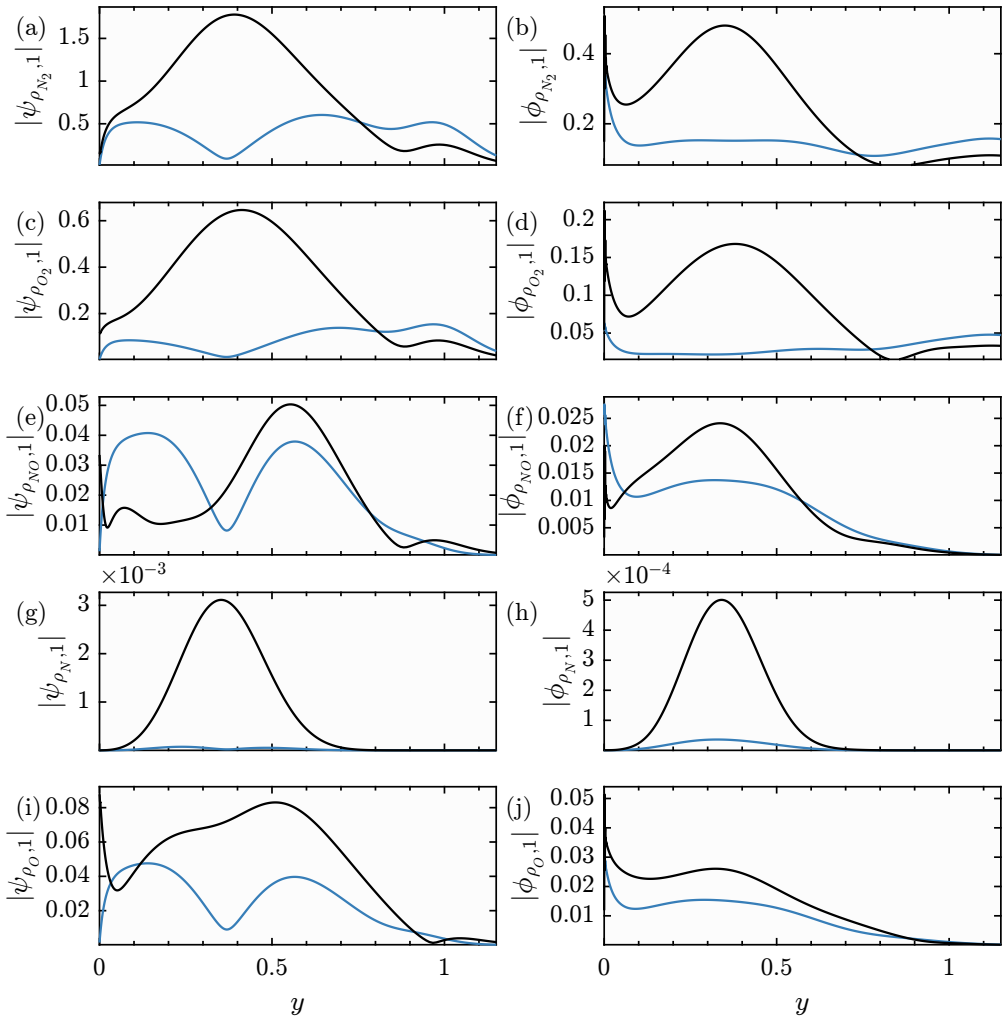

Figure 5.19: $\left|\psi_{\rho_{N_2},1}\right|$ (a), $\left|\phi_{\rho_{N_2},1}\right|$ (b), $\left|\psi_{\rho_{O_2},1}\right|$ (c), $\left|\phi_{\rho_{O_2},1}\right|$ (d), $\left|\psi_{\rho_{NO},1}\right|$ (e), $\left|\phi_{\rho_{NO},1}\right|$ (f), $\left|\psi_{\rho_N,1}\right|$ (g), $\left|\phi_{\rho_N,1}\right|$ (h), $\left|\psi_{\rho_O,1}\right|$ (i), $\left|\phi_{\rho_O,1}\right|$ (j) for representative subsonic streaky modes ($k_x = 2\pi/100$, $k_z = 2\pi/5$, $c = .5$). Case ii and iii are in blue and black solid lines.

phenomena whose qualitative behavior is relatively unchanged from the full forcing in Figure 5.11. This is because the temperature component is able to excite the radiating pressure modes in the freestream. On the other hand, the subsonic region is less amplified since it lacks forcing from the shear-driven lift-up mechanism. Differences between case ii and iii are observed for larger λ_x and λ_z which correspond to modes that are able to reach down to the wall. The amplification from the streaky structures is also uniquely observed in case iii, being completely absent in cases i and ii. This increase in amplification is also observed to permeate more into the supersonic region, caused by the forcing from the thermodynamic state.

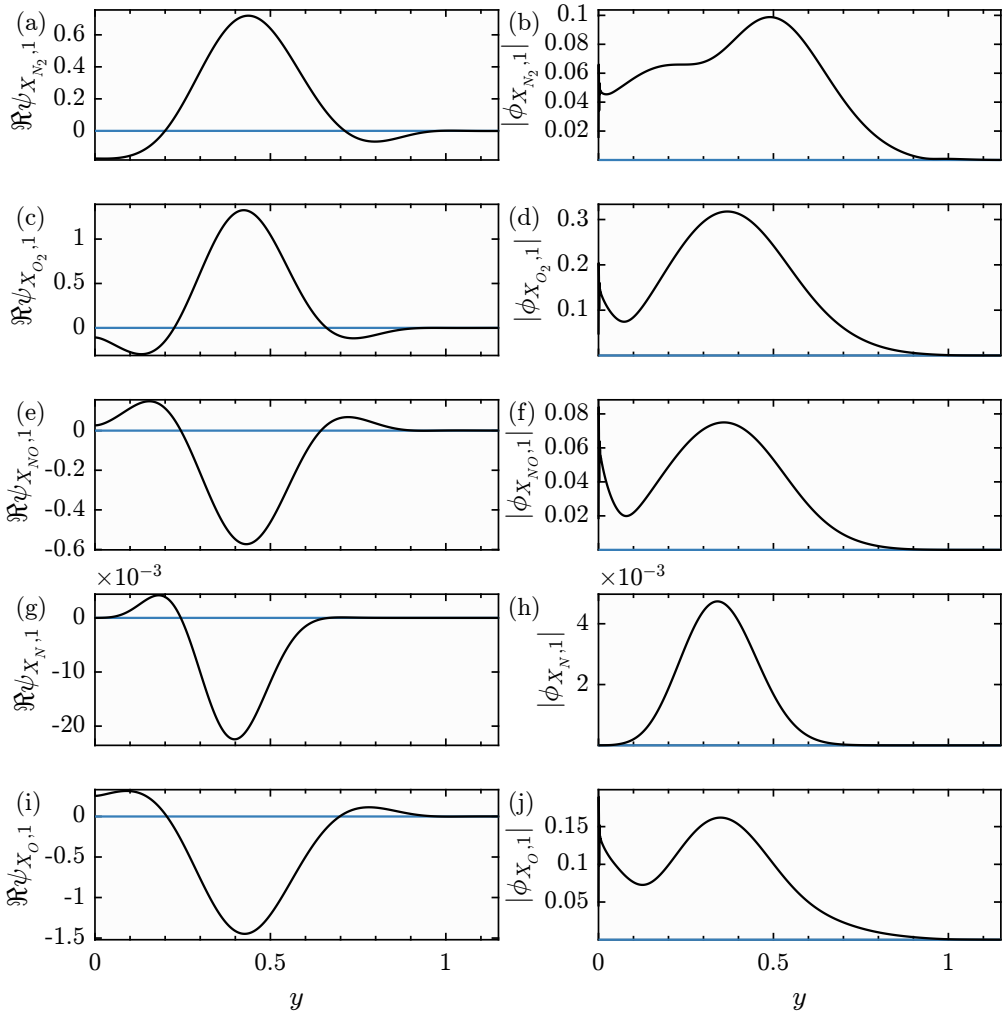

Figure 5.20: Real part of $\psi_{X_{N_2},1}$ (a), $\psi_{X_{O_2},1}$ (c), $\psi_{X_{NO},1}$ (e), $\psi_{X_N,1}$ (g), and $\psi_{X_O,1}$ (i) and magnitude of $\phi_{X_{N_2},1}$ (b), $\phi_{X_{O_2},1}$ (d), $\phi_{X_{NO},1}$ (f), $\phi_{X_N,1}$ (h), and $\phi_{X_O,1}$ (j) for representative subsonic streaky modes ($k_x = 2\pi/100$, $k_z = 2\pi/5$, $c = .5$). Case ii and iii are in blue and black solid lines.

Continuing with the effects of component-wise forcing, chemical nonequilibrium allows the study of forcing from individual species components. Here the forcing is masked to consider the forcing from $\phi_{\rho_{i,s}}$ and ϕ_ρ for case iii. The same parameters are used for this sweep and the resulting amplification is plotted in Figure 5.22. Forcing from ϕ_ρ produces similar amplification as forcing from ϕ_T in that the supersonic region is relatively unchanged, the subsonic region is less amplified, and an increase in amplification for the larger λ_x and λ_z modes. Considering forcing from $\phi_{\rho_{N_2}}$ and $\phi_{\rho_{O_2}}$ reveals similar results as forcing from ϕ_ρ. This is expected as N_2 and O_2 are the most abundant species in the mixture, responsible for the majority of the density. Compared to the amplification from ϕ_ρ, the amplification from $\phi_{\rho_{N_2}}$

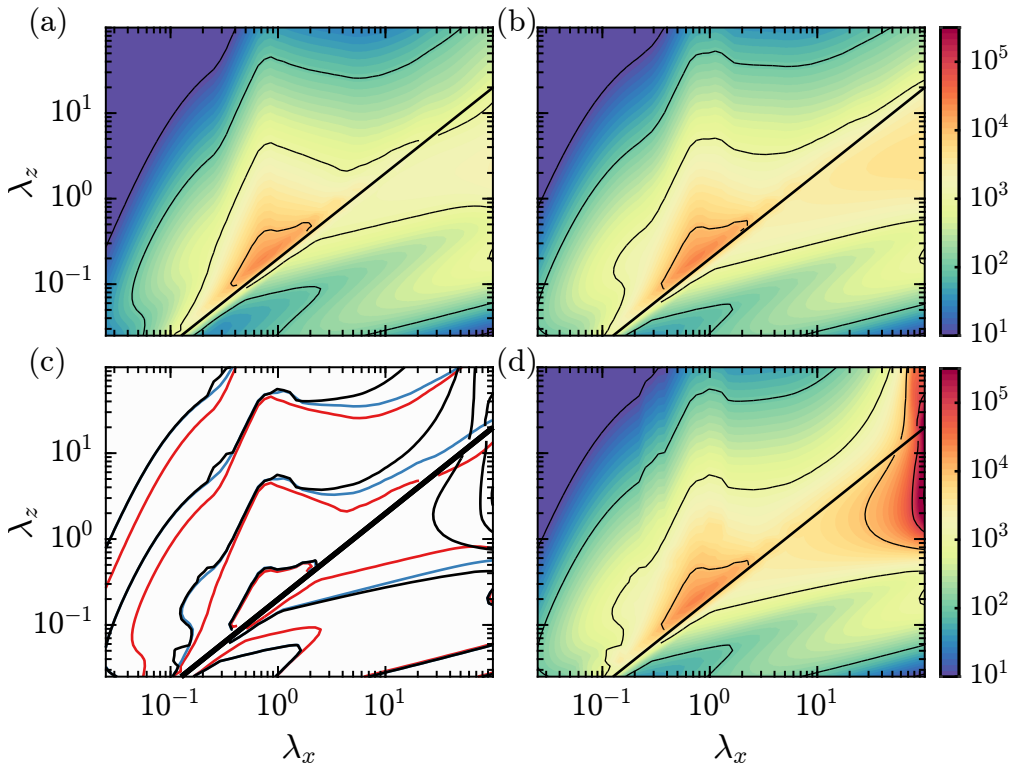

Figure 5.21: Contours of $\sigma_1^2 k_x k_z$ for case i (a), case ii (b), and case iii (d) where only forcing from the T component is considered. The contour lines denote $\sigma_1^2 k_x k_z = 10^1, 10^2, \ldots, 10^5$. These contours are all plotted in (c) where case i, ii, and iii are in red, blue, and black. The solid black line denotes the sonic line.

and $\phi_{\rho_{O_2}}$ is smaller because they are portions of the full density.

Considering forcing from the dissociated components, $\phi_{\rho_{NO}}$, ϕ_{ρ_N} and ϕ_{ρ_O}, reveals that the discontinuity across the relative sonic line is absent. This is because the temperature in the freestream is too small to support the dissociated components. As a result, these dissociated components can not excite the relevant acoustic phenomena that generates the supersonic modes. The forcing contours still identify the presence of large amplification of the streaky structures signaling that these modes are excited by the thermodynamic effects. The forcing from ϕ_{ρ_N} creates amplification mostly by these streaky structures, with some components in the smallest scales.

Differences in the Sub-optimal Resolvent Gains Using the Laminar Similarity Solution

Now, the differences in the higher order singular values will be compared between cases ii and iii. Case i is not considered as it has already been shown that changes in

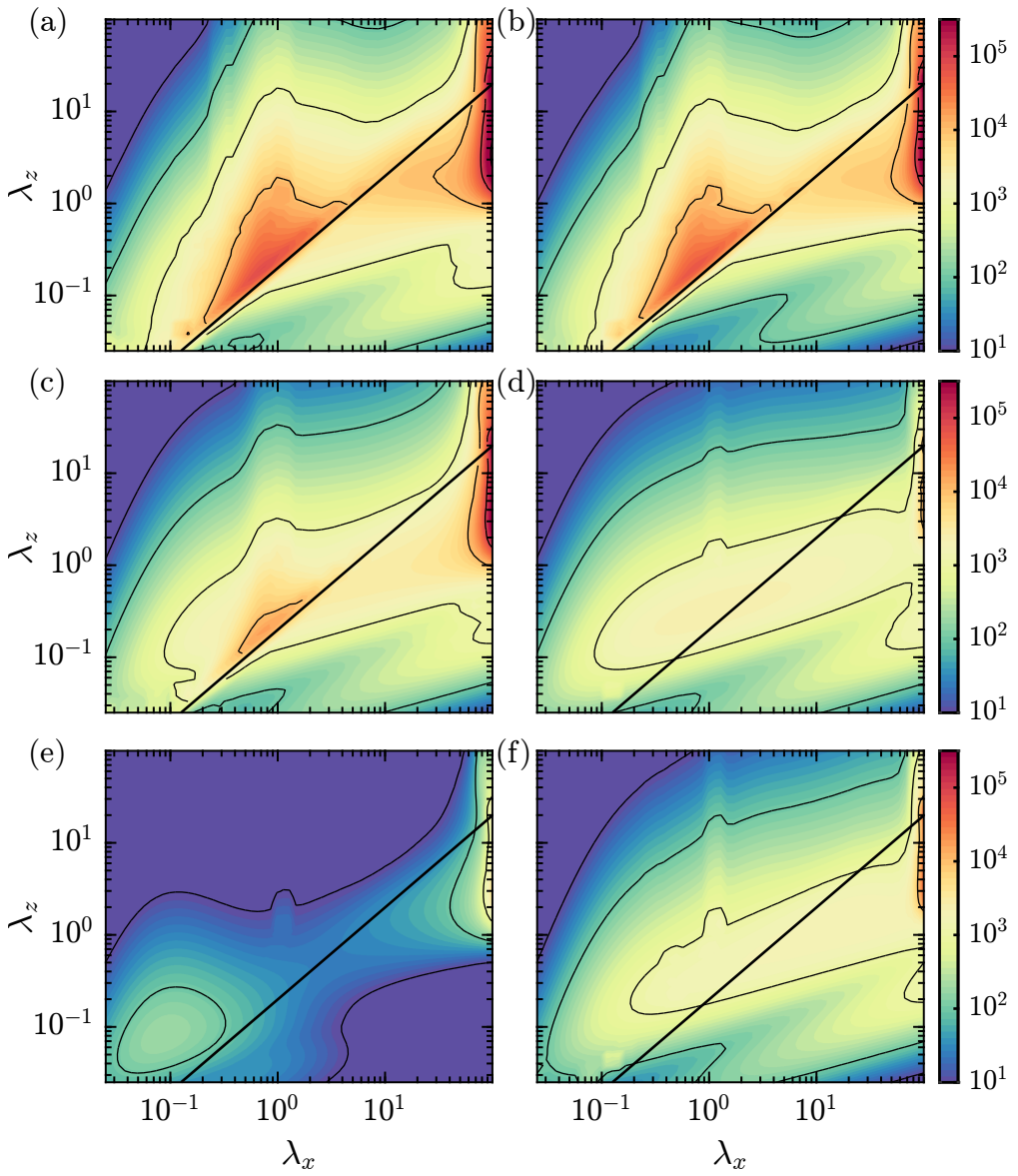

Figure 5.22: Contours of $\sigma_1^2 k_x k_z$ for case iii where forcing from ρ (a), ρ_{N_2} (b), ρ_{O_2} (c), ρ_{NO} (d), ρ_N (e), ρ_O (f) is considered through masking. The contour lines denote $\sigma_1^2 k_x k_z = 10^1, 10^2, \ldots, 10^5$. The diagonal black line denotes the sonic line.

Case	1	2	3	4	5
ii	3.13×10^7	1.75×10^6	6.17×10^5	2.81×10^5	1.43×10^5
iii	1.20×10^8	1.73×10^6	6.04×10^5	2.73×10^5	1.39×10^5

Table 5.6: Maximum $\sigma_i^2 k_x k_z$ for cases ii and iii.

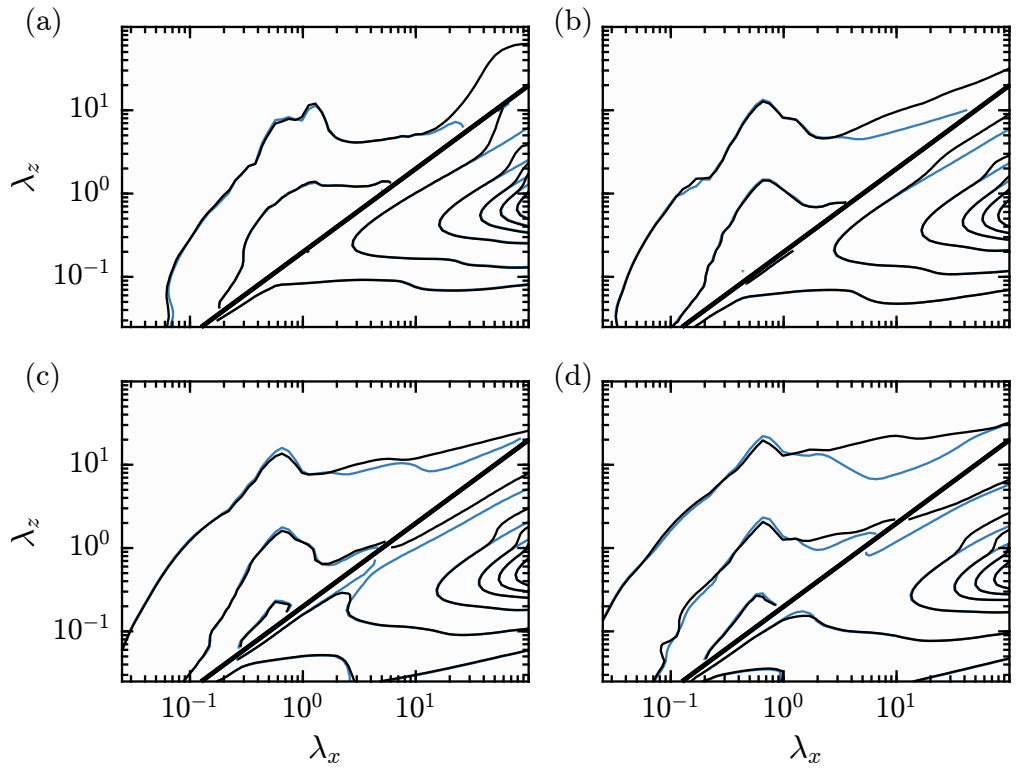

Figure 5.23: Contours of $\sigma_i^2 k_x k_z$ for case ii (blue) and iii (black). The contour lines denote .1%, 1%, 10%, 30%, 50%, and 75% of the local maximum of $\sigma_i^2 k_x k_z$ for each case. i = 2, 3, 4, and 5 are plotted in (a), (b), (c), and (d).

the mean flow field were the primary cause of the differences in the amplification. As such, only differences in the assumption of chemical equilibrium or chemical nonequilibrium in the LNSE will be considered. $\sigma_i^2 k_x k_z$ are plotted from the sweep used in Figure 5.11 for i = 2, 3, 4, and 5. The contours are plotted as percentages of the maxima of $\sigma_i^2 k_x k_z$ for each case. $\sigma_1^2 k_x k_z$ displayed large amplification for the streak-like modes with large λ_z in case iii that was absent in case ii. The difference in amplification for those streak-like modes is reflected in $\sigma_2^2 k_x k_z$ as they are sources of amplification for the i = 2 modes in case iii. For $i > 3$, those large λ_x streak-like modes also contribute to the changes in the amplification contours. For all the other length scales, the change in amplification is small as evidenced by the amplification contours overlapping. In Table 5.6, the maximum of $\sigma_i^2 k_x k_z$ over the sweep is listed for cases ii and iii. For i = 1, the amplification in case iii is an order of magnitude larger than case ii because of the streak-like modes. For the higher order modes, the difference in maximum amplification between the two cases is small. This is because the local maxima of $\sigma_i^2 k_x k_z$ for $i \geq 2$ occurs at $k_z = 2\pi$ and $k_x = 2\pi/100$, which is not representative of the streak-like modes that contributed to the differences in the

T_e	T_w	Ma	Re_{δ^*}	Re	Re_τ	Pr
1070 K	1700 K	10	4.28×10^4	9.2×10^4	1104	0.71

Table 5.7: Properties of the hypersonic TBL. Here, $Re_{\delta^*} = \rho_e \delta^* U_e / \mu_e$ and T_e and T_w denote the freestream and wall temperatures. This mean profile corresponds to the streamwise station furthest downstream presented in Di Renzo and Urzay (2021).

amplification. The maximum of $\sigma_1^2 k_x k_z$ is at least an order of magnitude larger than $\sigma_2^2 k_x k_z$, once again highlighting the low-rank behavior in the resolvent operator. A discussion on the higher order resolvent modes for the laminar case is omitted and will be presented instead for the turbulent case in the next section.

5.6 Effects of Chemical Nonequilibrium on Resolvent Amplification in a TBL

In the previous section, the laminar similarity solution was used to compare the effects of chemical nonequilibrium on resolvent amplification. In hypersonic boundary layers, the turbulent flow has shear stresses and heat fluxes an order of magnitude larger than the laminar case (Van Driest, 1956). This leads to increased $\overline{U}_y$ and $\overline{T}_y$ in the near-wall region of the TBL. This causes the peak $\overline{T}$ variation to be concentrated in the near-wall region for a TBL while the peak $\overline{T}$ variation is diffused across the entire laminar boundary layer. Due to the differences in the two flows, the effects of chemical nonequilibrium on the resolvent analysis will be studied using the TBL. First, a description of the mean flow field will be provided and then results will be shown.

Description of the Hypersonic TBL Mean Flow Field

The mean flow from the DNS of Di Renzo and Urzay (2021) is used to gauge the effects of chemical nonequilibrium on the linear amplification. The mean flow field parameters are described in Table 5.7. Here, the effects of the linear amplification will be compared by considering the linear amplification using either chemical nonequilibrium or chemical equilibrium as in cases ii and iii in Section 5.5, though with a turbulent mean flow field. Comparisons will not be done with a CPG mean flow field since a CPG turbulent flow with parameters similar to Di Renzo and Urzay (2021) are not readily available. If one were available, the results in Section 5.5 suggest that the differences in amplification will be attributed to differences in the mean thermodynamic state as opposed to the chemical nonequilibrium present in the LNSE.

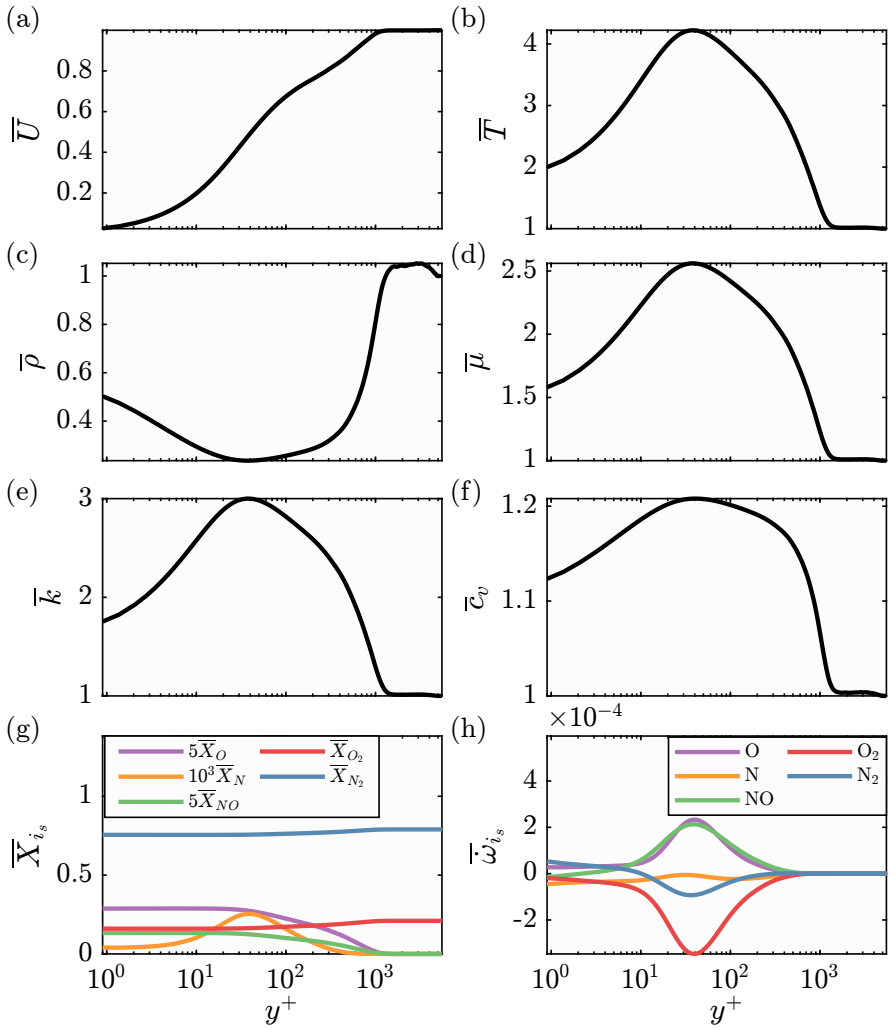

Figure 5.24: $\overline{U}$ (a), $\overline{T}$ (b), $\overline{\rho}$ (c), $\overline{\mu}$ (d), $\overline{k}$ (e), and $\overline{c}_v$ (f) for TBL assuming chemical nonequilibrium. $\overline{\rho}_{i_s}$ (g), and $\dot{\overline{\omega}}_{i_s}$ (h) are plotted with their colors labeled in the legend. Note that the densities of the dissociated components are rescaled in (g) for visualization.

The turbulent mean flow fields are plotted in Figure 5.24 against y^+, where the viscous length scale is defined with the mean properties at the wall. $\overline{U}$ demonstrates multiscale behavior, with the near-wall region indicative of viscous sublayer and the presence of a log region which emerges under an appropriate scaling (Griffin, Fu, and Moin, 2021). The peak $\overline{T}$ is larger for the turbulent flow than the similarity solution due to the increase in viscous heating in the turbulent flow. Apart from the changes in $\overline{T}$, the turbulence changes the chemical composition of the flow, especially in the near-wall region. Notably, $\overline{X}_N$ is nonzero at the wall. The values of $\overline{X}_O$ and $\overline{X}_{NO}$ at the wall are also reduced by a factor of almost 2, resulting in an increase in $\overline{X}_{O_2}$. The changes in chemical composition at the wall are responsible

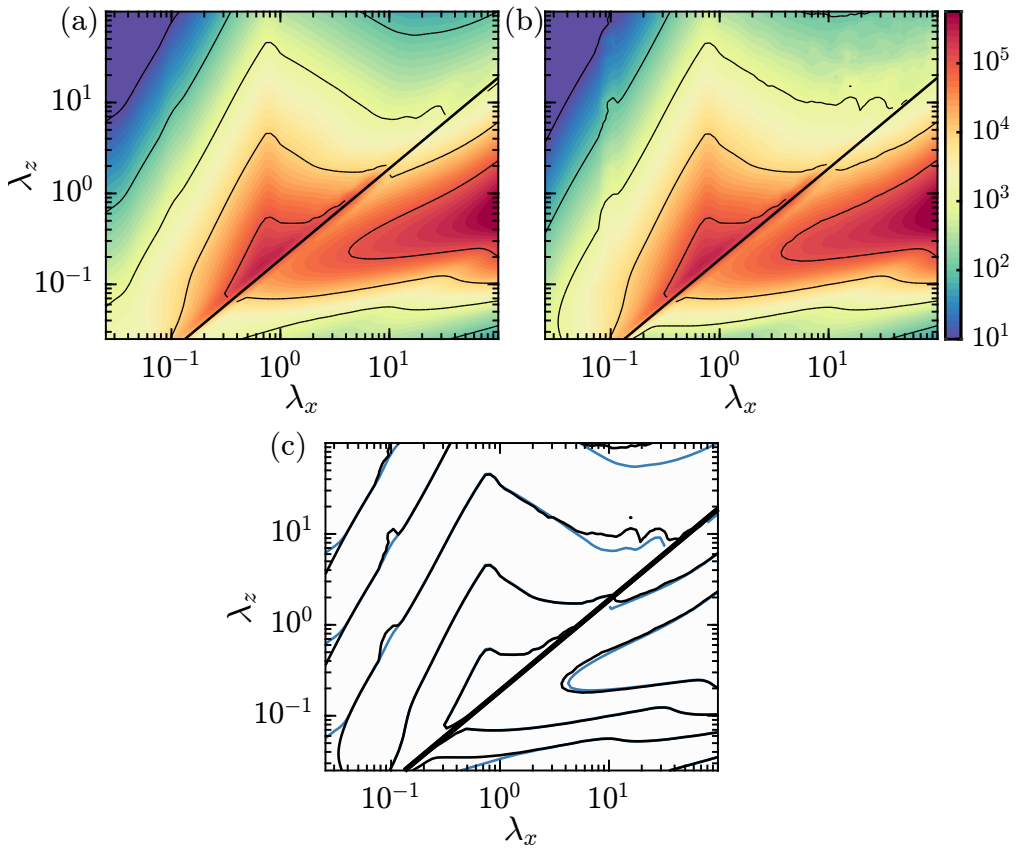

Figure 5.25: Contours of $\sigma_1^2 k_x k_z$ assuming chemical equilibrium (a) and chemical nonequilibrium (b). The contour lines denote $\sigma_1^2 k_x k_z = 10^1, 10^2, \ldots, 10^7$. These contours are all plotted in (c) where blue and black denote chemical equilibrium and nonequilibrium. The solid black line denotes the sonic line.

for the change in the chemical rates of mass production, $\overline{\dot{\omega}}_{i_s}$, in the near-wall region. Here, the peaks of $\overline{\dot{\omega}}_{i_s}$ are near the location of largest $\overline{T}$, with these peaks being almost twice as large as in the similarity solution. The value of $\overline{\dot{\omega}}_N$ is also nonzero at the wall. Finally, since these mean flow fields are plotted in logarithmic units, the peak variation in these quantities occurs within 10% of the boundary layer making this flow subject to stronger shear terms.

Comparison of Resolvent Modes and Amplification Using a Hypersonic TBL Under Chemical Nonequilibrium

A sweep over 80 logarithmically-spaced k_x and k_z spanning $2\pi/.025$ to $2\pi/100$ is computed with fixed $c \approx .48$ for the chemical equilibrium and chemical nonequilibrium cases. The same parameters are used for the other sweeps in this section. This wavespeed corresponds to the $\overline{U}$ where $\overline{T}$ is the largest, located at $y^+ \approx 30$.

The results of this sweep are plotted in Figure 5.25. The use of a turbulent mean state does not remove the presence of the discontinuity at the sonic line. The most amplified structures in the subsonic region are modes with $\lambda_x > \lambda_z$ and $.1 \geq \lambda_z \leq 1$. For the laminar case, the most amplified structures had a λ_z about an order of magnitude larger. The differences in the amplified structures are due to the differences in $\overline{U}_y$ and $\overline{T}_y$ in the turbulent flow as these are large primarily in the near-wall region. This essentially creates a constraint on the preferential wall-normal length scales which relates to the preferential λ_x and λ_z. Comparing the amplification between the chemical nonequilibrium and chemical equilibrium approaches reveal only slight differences in the amplification. The similarities in the amplification are likely because of the increased non-normal amplification from the $\overline{U}_y$ and $\overline{T}_y$ components which are unchanged if a mixture or a single species is considered. The biggest differences occur for the largest scales like in the laminar case of figure 5.11.

Since the amplifications are so similar, it is worth considering how the mode shapes differ. First, subsonic modes are considered with $k_x^+ = 2\pi/1000$ ($k_x = 2\pi/.9$), $k_z^+ = 2\pi/100$ ($k_z = 2\pi/.09$), and $c = .48$ as scales representative of the near-wall cycle. The velocity, temperature, and density components of $\boldsymbol{\psi}_1$ and $\boldsymbol{\phi}_1$ are plotted in Figure 5.26. Owing to the amplification via the lift-up effect through $\overline{U}_y$, the velocity components are independent of the chemical nonequilibrium effects. Similar to Section 5.3, the large $\psi_{u,1}$ is forced by large $\phi_{v,1}$ and $\phi_{w,1}$. There is also a large $\psi_{T,1}$ response, though it is also unchanged save for the region closest to the wall. A similar observation is made for $\psi_{\rho,1}$. The most discernible differences between the two modes is in $\phi_{T,1}$, likely because of the increase in temperature-dependent chemical nonequilibrium and molecular diffusion terms which become more important near the wall. The jaggedness in $\phi_{\rho,1}$ is because of the limited resolution near the wall which creates sharp gradients in the mean chemistry terms.

The species components of the subsonic mode are plotted in Figure 5.27. The ρ_{N_2} and ρ_{O_2} components of $\boldsymbol{\psi}_1$ are well approximated with the chemical equilibrium approach. The peak amplitudes of the ρ_{NO} and ρ_O components are also predicted well, although their shape differs. The chemical equilibrium approach predicts a zero crossing that is not observed in the chemical nonequilibrium approach. The lack of the zero crossing is likely because of the production of ρ_N in $\boldsymbol{\psi}_1$ which is underpredicted in the chemical equilibrium approach. The sharp gradients in $\phi_{\rho_{i_s},1}$ were also reflected in $\phi_{\rho,1}$. The $\phi_{\rho_{i_s},1}$ terms are large near the wall to account for the increased shear in the chemistry terms not present in the chemical equilibrium

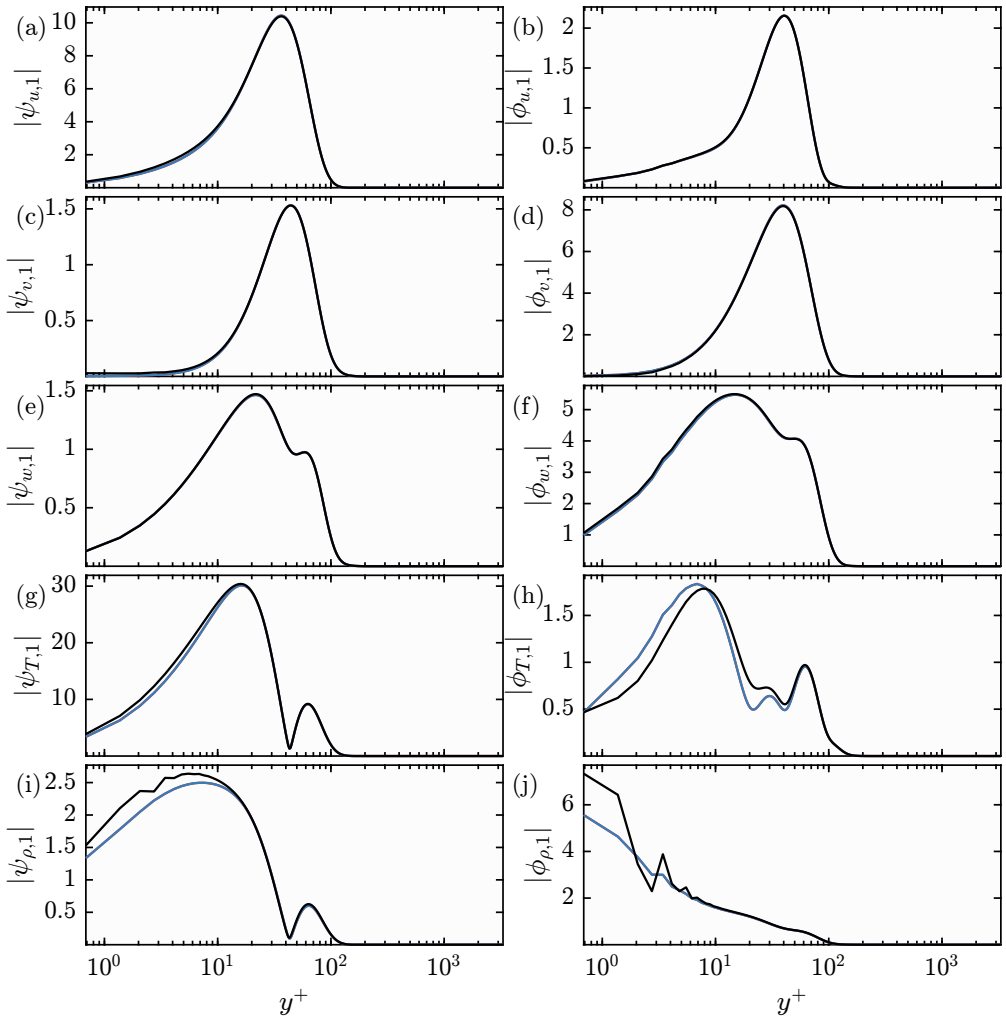

Figure 5.26: $|\psi_{u,1}|$ (a), $|\phi_{u,1}|$ (b), $|\psi_{v,1}|$ (c), $|\phi_{v,1}|$ (d), $|\psi_{w,1}|$ (e), $|\phi_{w,1}|$ (f), $|\psi_{T,1}|$ (g), $|\phi_{T,1}|$ (h), $|\psi_{T,1}|$ (i), $|\phi_{T,1}|$ (j) for representative subsonic modes ($k_x = 2\pi/.9$, $k_z = 2\pi/.09$, $c = .48$). The chemical nonequilibrium and equilibrium modes are in black and blue.

approach. Although $\phi_{\rho,1}$ for the two approaches are similar, the differences in $\phi_{\rho_{i_s},1}$ suggests differences in concentration.

The X_{i_s} components of the subsonic optimal modes are plotted in Figure 5.28. The anticorrelation that was discussed in Section 5.5 is seen clearly in the real part of the X_{N_2}, X_{O_2}, X_{NO}, and X_O components of $\boldsymbol{\psi}_1$. An increase in concentration of N_2 and O_2 correlates with a decrease in concentration of NO and O. $\psi_{X_N,1}$ is the smallest component of the response since the temperature is too small within the boundary layer to support large scale dissociation of N_2 (Anderson Jr., 2006). The forcing components, $\phi_{X_{i_s},1}$, are large and non-negligible near the wall owing to the differences seen in $\phi_{\rho_{i_s},1}$.

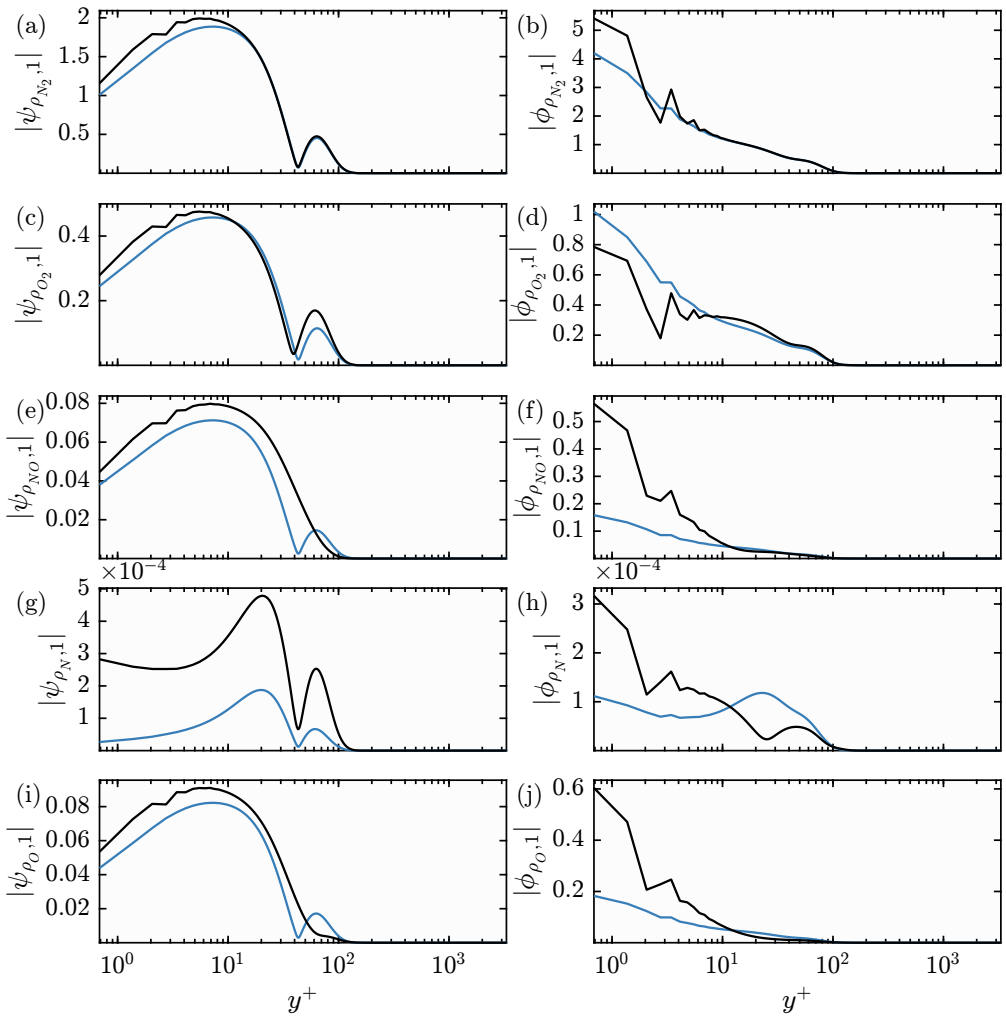

Figure 5.27: $\left|\psi_{\rho_{N_2},1}\right|$ (a), $\left|\phi_{\rho_{N_2},1}\right|$ (b), $\left|\psi_{\rho_{O_2},1}\right|$ (c), $\left|\phi_{\rho_{O_2},1}\right|$ (d), $\left|\psi_{\rho_{NO},1}\right|$ (e), $\left|\phi_{\rho_{NO},1}\right|$ (f), $\left|\psi_{\rho_N,1}\right|$ (g), $\left|\phi_{\rho_N,1}\right|$ (h), $\left|\psi_{\rho_O,1}\right|$ (i), $\left|\phi_{\rho_O,1}\right|$ (j) for representative subsonic modes ($k_x = 2\pi/.9$, $k_z = 2\pi/.09$, $c = .48$). The chemical nonequilibrium and equilibrium modes are in black and blue.

A representative supersonic mode with $k_x = 2\pi/5$, $k_z = 2\pi/10$, and $c = .48$ is considered as this is corresponds to the spectral region where the amplification differs between the chemical nonequilibrium and equilibrium approaches. From Figure 5.31, the structure of the modes in the freestream are largely unchanged, except for $\phi_{v,1}$. Note however that $\phi_{v,1}$ is significantly smaller than $\phi_{\rho,1}$ and $\phi_{T,1}$ in the freestream, so its difference in amplitude is negligible. The differences in the modes in the freestream are likely caused within the boundary layer where the chemical nonequilbrium effects are more appreciable. In this region, the mode shapes differ slightly, but there is agreement in the amplitudes of the resolvent modes' components.

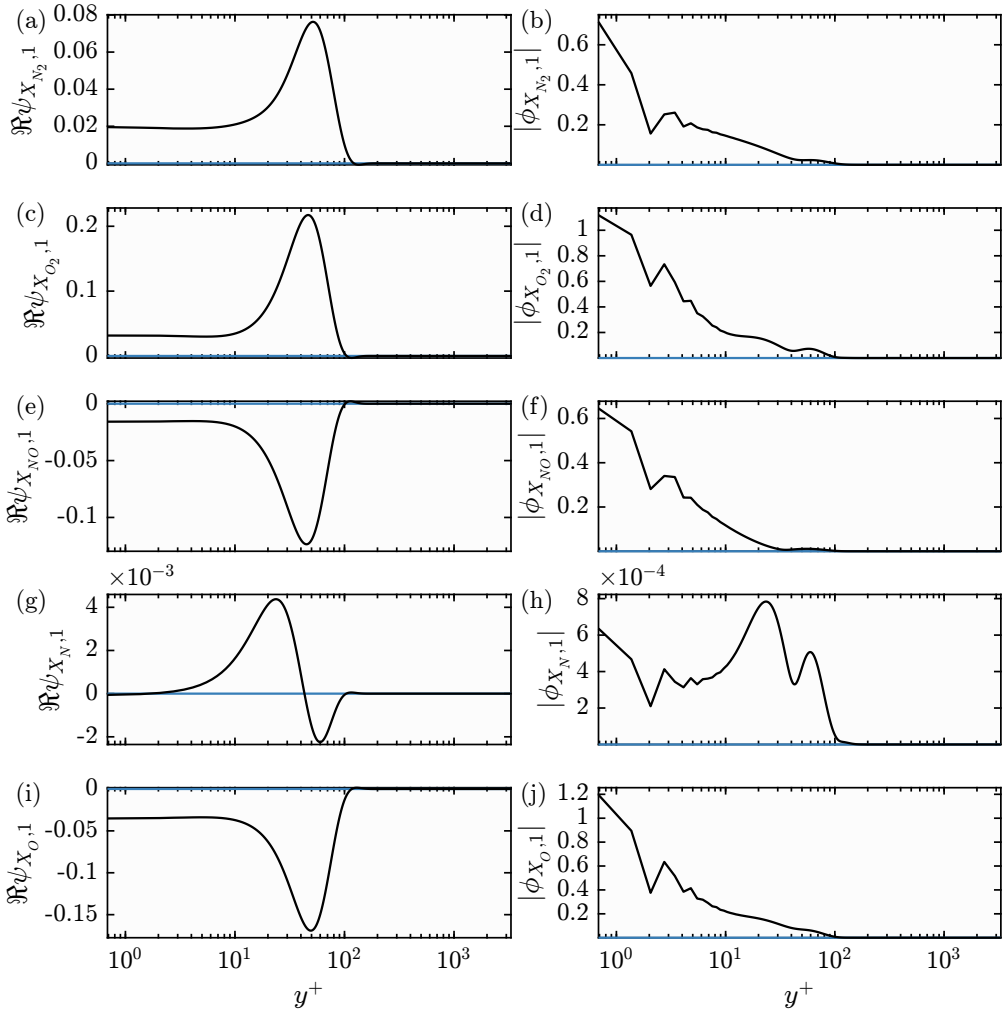

Figure 5.28: Real part of $\psi_{X_{N_2},1}$ (a), $\psi_{X_{O_2},1}$ (c), $\psi_{X_{NO},1}$ (e), $\psi_{X_N,1}$ (g), and $\psi_{X_O,1}$ (i) and magnitude of $\phi_{X_{N_2},1}$ (b), $\phi_{X_{O_2},1}$ (d), $\phi_{X_{NO},1}$ (f), $\phi_{X_N,1}$ (h), and $\phi_{X_O,1}$ (j) for representative subsonic modes ($k_x = 2\pi/.9$, $k_z = 2\pi/.09$, $c = .48$). The chemical nonequilibrium and equilibrium modes are in black and blue.

The ρ_{i_s} components of the supersonic mode are plotted in Figure 5.30. These demonstrate the differences between the two approaches within the boundary layer. The mode shapes of the $\psi_{\rho_{i_s},1}$ components within the boundary layer using the chemical equilibrium approach agree poorly with those computed using the chemical nonequilibrium approach, especially for the dissociated components. On the other hand, within the freestream region, the $\psi_{\rho_{N_2},1}$ and $\psi_{\rho_{O_2},1}$ components are in agreement since the effects of chemical nonequilibrium are negligible in the freestream. The dissociated components are absent in the freestream. $\phi_{\rho_{i_s},1}$ in the near-wall region is also not approximated well within the near-wall region.

The X_{i_s} components are plotted in Figure 5.31. These components only have support

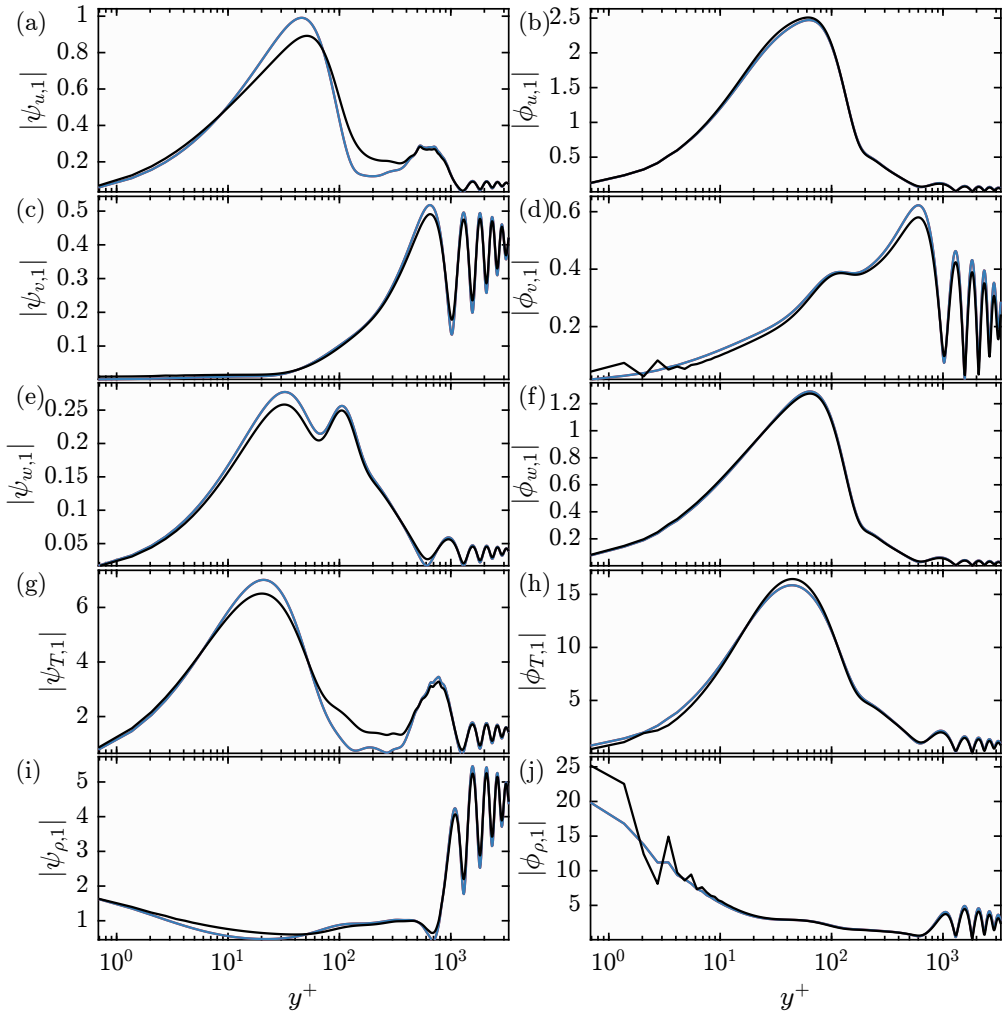

Figure 5.29: $|\psi_{u,1}|$ (a), $|\phi_{u,1}|$ (b), $|\psi_{v,1}|$ (c), $|\phi_{v,1}|$ (d), $|\psi_{w,1}|$ (e), $|\phi_{w,1}|$ (f), $|\psi_{T,1}|$ (g), $|\phi_{T,1}|$ (h), $|\psi_{T,1}|$ (i), $|\phi_{T,1}|$ (j) for representative supersonic modes ($k_x = 2\pi/5$, $k_z = 2\pi/10$, $c = .48$). The chemical nonequilibrium and equilibrium modes are in black dotted and blue solid lines.

within the boundary layer, where the chemistry is active. There are no changes to the concentrations in the freestream. The correlations between the X_{N_2}, X_{O_2}, X_{NO}, and X_O components of $\boldsymbol{\psi}_1$ from the subsonic mode are also recovered here. The large near-wall forcing in $\phi_{X_{i_s},1}$ once again illustrates the importance of the shear in the chemistry-related terms at the wall.

Masking is now considered to investigate the differences in amplification. First, the amplification from ϕ_T is investigated in Figure 5.32. Unlike in Figure 5.21, the effects from the chemical nonequilibrium terms in the linear operator lead to small changes when considering forcing from ϕ_T. The differences in Figure 5.21 mostly stemmed from the influence of the large scale streaky that reached down

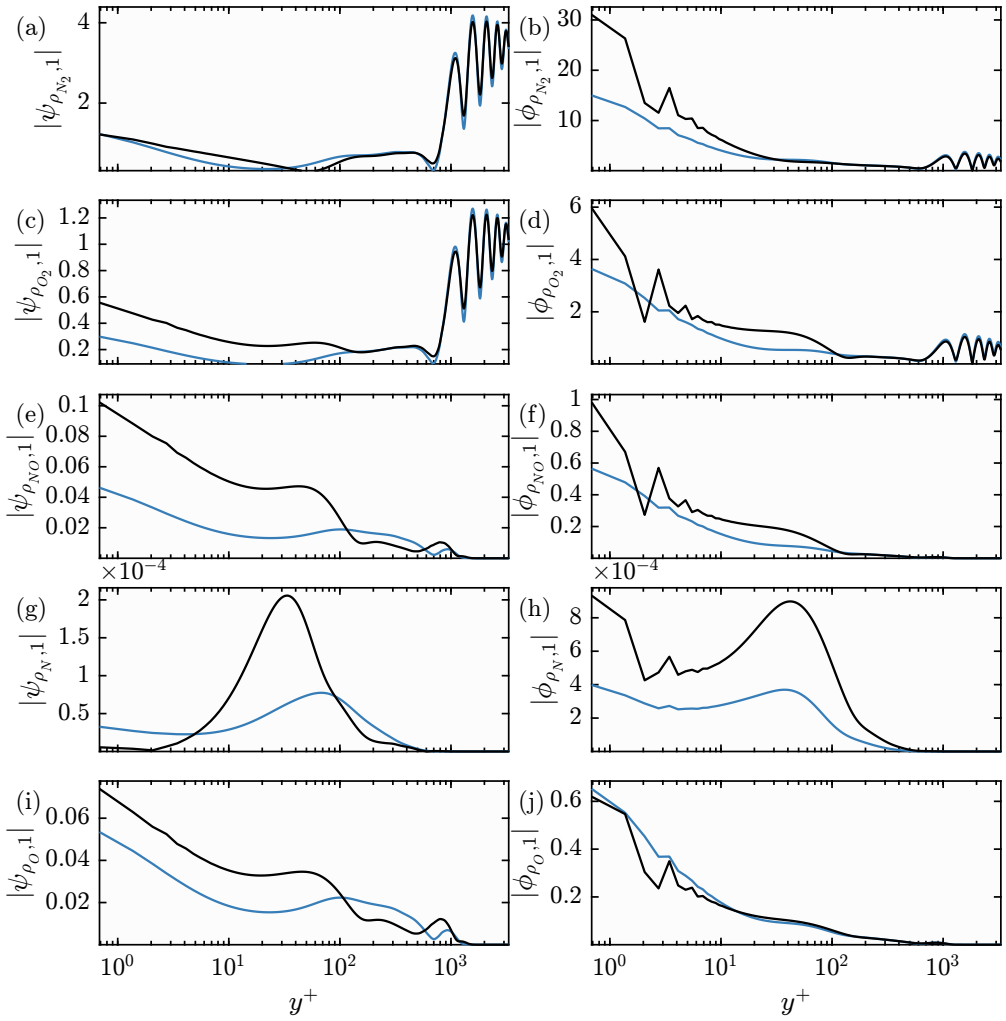

Figure 5.30: $\left|\psi_{\rho_{N_2},1}\right|$ (a), $\left|\phi_{\rho_{N_2},1}\right|$ (b), $\left|\psi_{\rho_{O_2},1}\right|$ (c), $\left|\phi_{\rho_{O_2},1}\right|$ (d), $\left|\psi_{\rho_{NO},1}\right|$ (e), $\left|\phi_{\rho_{NO},1}\right|$ (f), $\left|\psi_{\rho_N,1}\right|$ (g), $\left|\phi_{\rho_N,1}\right|$ (h), $\left|\psi_{\rho_O,1}\right|$ (i), $\left|\phi_{\rho_O,1}\right|$ (j) for representative supersonic modes ($k_x = 2\pi/5$, $k_z = 2\pi/10$, $c = .48$). The chemical nonequilibrium and equilibrium modes are in black dotted and blue solid lines.

to the wall. This is reflected in the top right corner of Figure 5.32(c), though the influence of these large scale modes on the subsonic region is not as apparent for this sweep. The lack of amplification for these large scale modes in the turbulent flow is likely because the large shear region is constrained to the near-wall-region unlike the laminar case. This limits the amplification from the shear since only the near-wall portion of the mode can contribute to the non-normal amplification. The slight differences in the optimal amplification considering forcing from only ϕ_T suggest that the $L_{i,4}$ and $L^n_{4,4}$ terms play a negligible role in the linear amplification.

Finally, a sweep is done to compare the amplification from the density components,

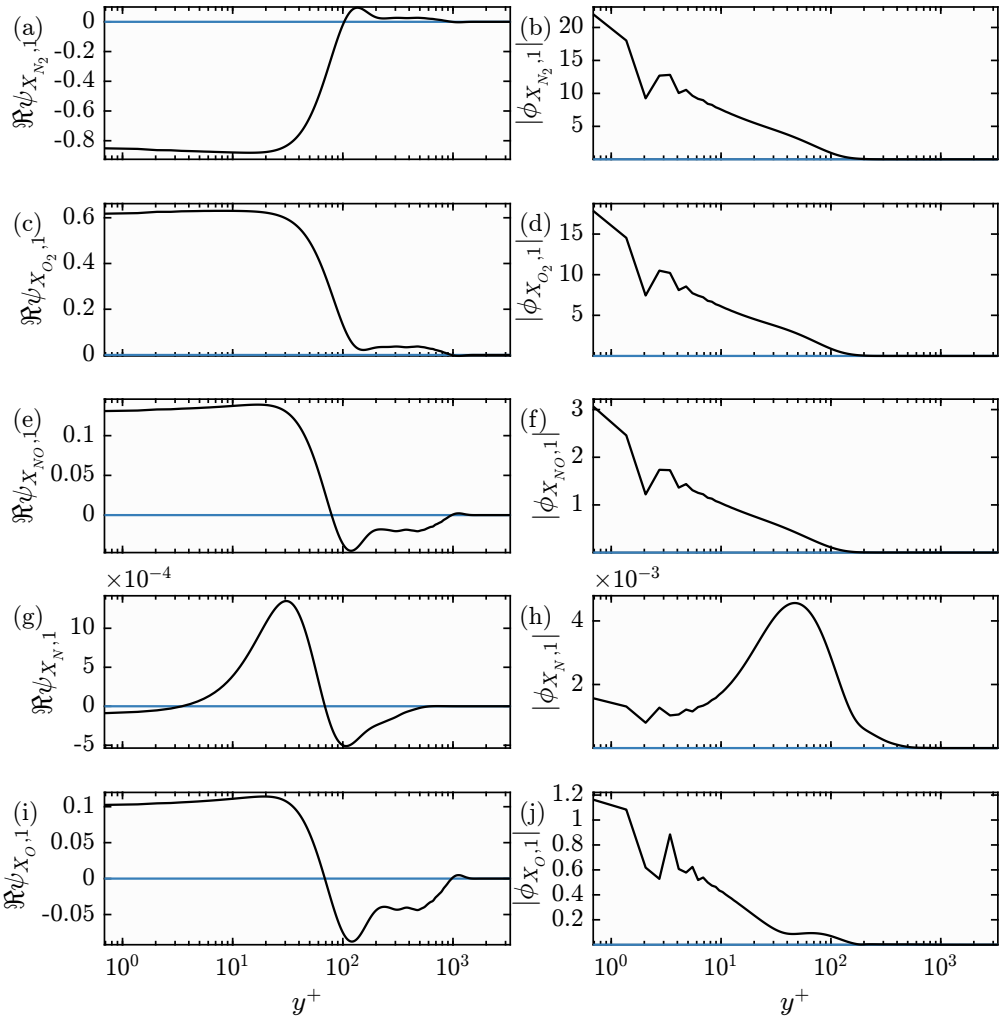

Figure 5.31: Real part of $\psi_{X_{N_2},1}$ (a), $\psi_{X_{O_2},1}$ (c), $\psi_{X_{NO},1}$ (e), $\psi_{X_N,1}$ (g), and $\psi_{X_O,1}$ (i) and magnitude of $\phi_{X_{N_2},1}$ (b), $\phi_{X_{O_2},1}$ (d), $\phi_{X_{NO},1}$ (f), $\phi_{X_N,1}$ (h), and $\phi_{X_O,1}$ (j) for representative supersonic modes ($k_x = 2\pi/5$, $k_z = 2\pi/10$, $c = .48$). The chemical nonequilibrium and equilibrium modes are in black and blue solid lines.

ϕ_ρ and $\phi_{\rho_{i_s}}$ in Figure 5.33. Just as in the laminar case in Figure 5.22, the forcings from ϕ_ρ, $\phi_{\rho_{N_2}}$, and $\phi_{\rho_{O_2}}$ result in the amplification of a supersonic region while the forcing from $\phi_{\rho_{NO}}$, ϕ_{ρ_N}, and ϕ_{ρ_O} reveal no discontinuity across the sonic line. This again occurs because the forcing from the dissociated components can not excite the freestream acoustics as they are not present in the freestream. The amplification of streak-like modes seen in Figure 5.22 is not present for the turbulent case. The relative amplification between the supersonic region and the subsonic region using forcing from ϕ_ρ, $\phi_{\rho_{N_2}}$, and $\phi_{\rho_{O_2}}$ is larger for the turbulent case than the laminar case. This likely occurs because the shear-driven amplification from the boundary layer is constrained to the near-wall region which forms less than a tenth of the boundary

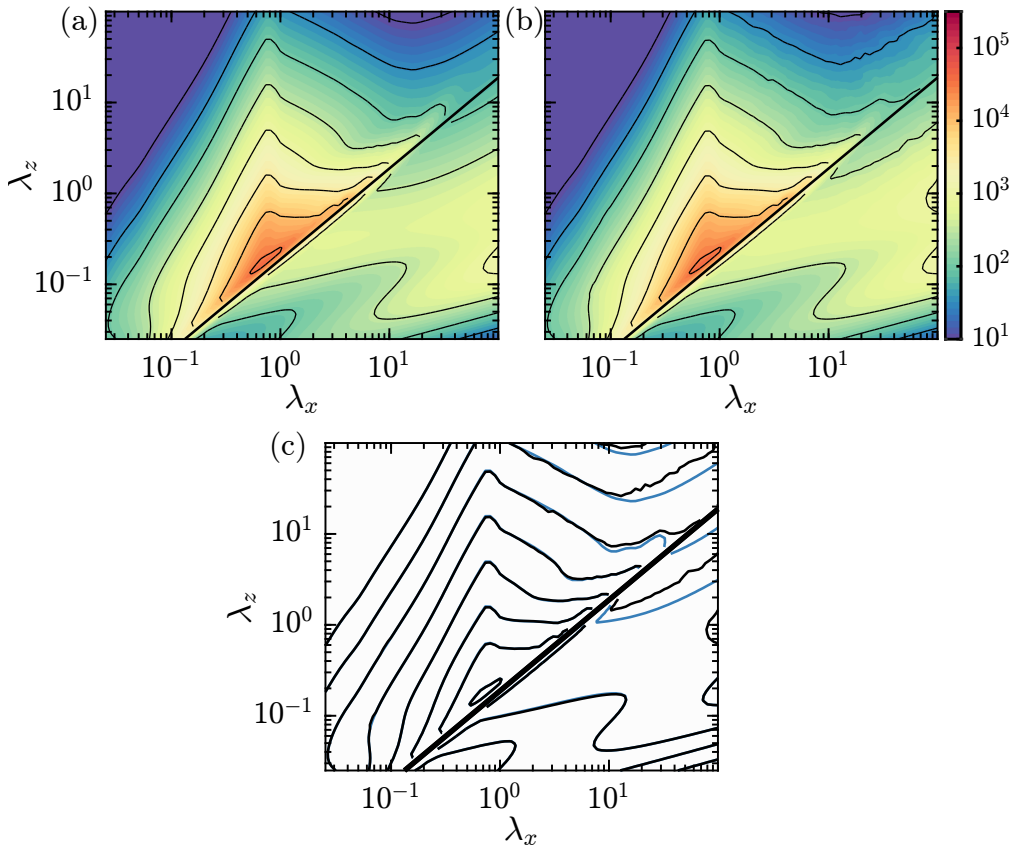

Figure 5.32: Contours of $\sigma_1^2 k_x k_z$ assuming chemical equilibrium (a) and chemical nonequilibrium (b) where only forcing from the T component is considered. The contour lines denote $\sigma_1^2 k_x k_z = 10^1, 10^{1.5}, 10^2, \ldots, 10^{4.5}, 10^5$. These contours are all plotted in (c) where blue and black denote chemical equilibrium and nonequilibrium. The solid black line denotes the sonic line.

Chemistry	1	2	3	4	5
equilib.	7.68×10^5	2.56×10^5	1.46×10^5	9.57×10^4	6.44×10^4
nonequilib.	7.78×10^5	2.61×10^5	1.48×10^5	9.75×10^4	6.57×10^4

Table 5.8: Maximum $\sigma_i^2 k_x k_z$ using the chemical equilibrium or chemical nonequilibrium assumptions.

layer in the turbulent case while the shear is present throughout the entire boundary layer in the laminar case.

Differences in the Sub-optimal Resolvent Gains Using the TBL

In Figure 5.34, contours of $\sigma_i^2 k_x k_z$ for $i \geq 2$ are plotted as percentages of their maximum for the chemical equilibrium and chemical nonequilibrium assumptions. The regions with largest amplification are largely unaffected by the assumption used

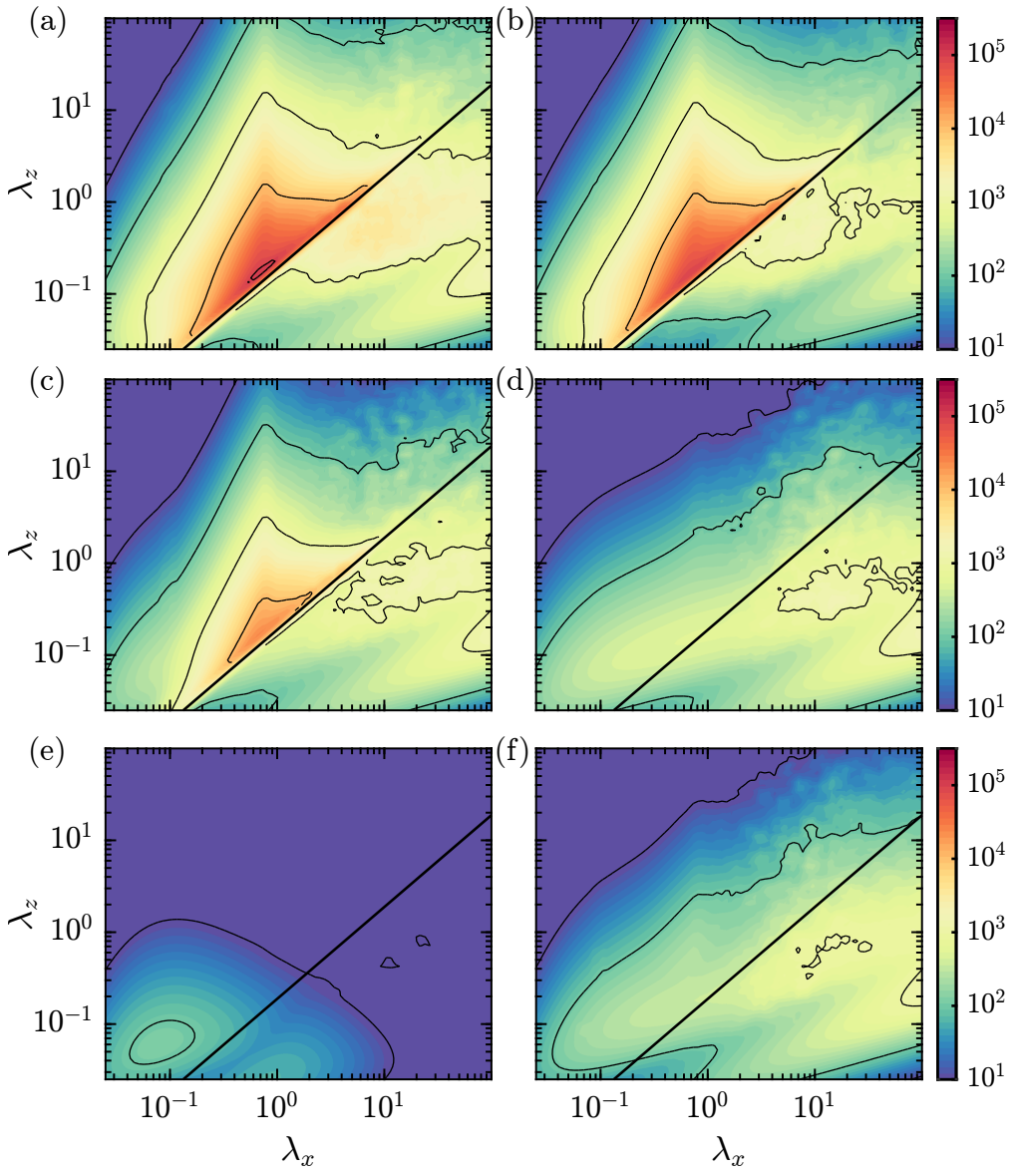

Figure 5.33: Contours of $\sigma_1^2 k_x k_z$ for case iii where forcing from ρ (a), ρ_{N_2} (b), ρ_{O_2} (c), ρ_{NO} (d), ρ_N (e), ρ_O (f) is considered through masking for the turbulent mean flow field. The contour lines denote $\sigma_1^2 k_x k_z = 10^1, 10^2, \ldots, 10^5$. The diagonal black line denotes the sonic line.

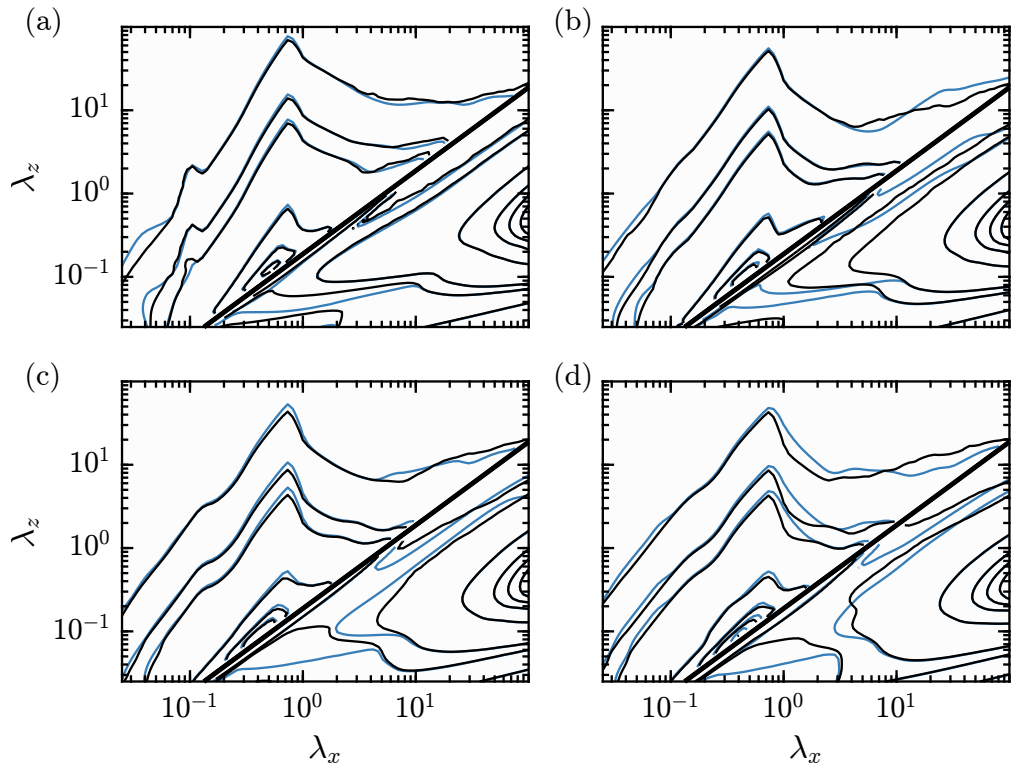

Figure 5.34: Contours of $\sigma_i^2 k_x k_z$ using chemical equilibrium (blue) and chemical nonequilibrium (black). The contour lines denote .1%, .5%, 1%, 10%, 30%, 50%, and 75% of the local maximum of $\sigma_i^2 k_x k_z$ for each case. i = 2, 3, 4, and 5 are plotted in (a), (b), (c), and (d).

in the chemistry of the LNSE. This is reflected in Table 5.8 where the maximum of $\sigma_i^2 k_x k_z$ is listed for each assumption used and display only minor variation. The differences in the amplification of the supersonic modes is also small. The biggest differences in amplification occur in the subsonic region for the smallest λ_x and λ_z. These small scales were the scales amplified in Figure 5.33 when only forcing from the dissociated components was considered. This suggests that the higher order modes with small length scales are amplified by sub-optimal mechanisms related to forcing from the species components. Accurately capturing the higher order mode behavior is important because the nonlinearities in true turbulent flows have projection onto the higher order modes. This can affect flow reconstructions and predictions from flow actuation.

The components of a sub-optimal response and forcing mode are plotted for the representative subsonic mode studied in this section. The variations in the i = 2 and i = 3 modes are not plotted because the differences are small between the two assumptions on the chemistry, similar to the i = 1 mode. The small

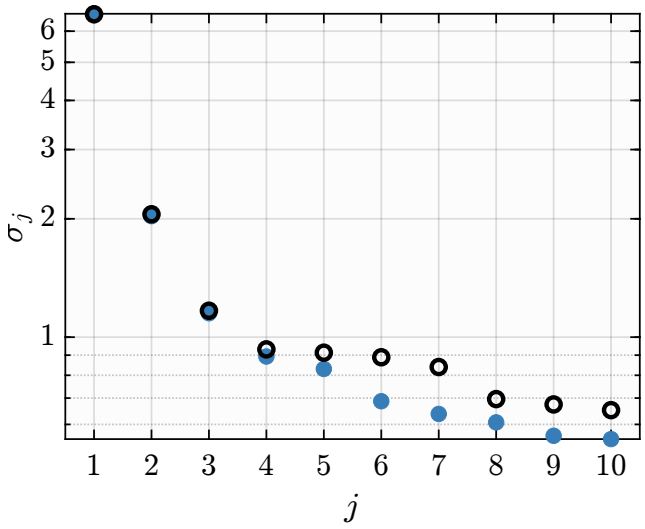

Figure 5.35: The first ten σ_j for the chemical nonequilibrium (black open circles) and chemical equilibrium (blue filled cirlces) approaches using $k_x = 2\pi/.9$, $k_z = 2\pi/.09$, $c = .48$, represenative of the subsonic region. The y axis is in log-scale.

variation in the mode shape can be intuited by comparing the contour shapes of the amplification near $\lambda_x = .9$ and $\lambda_z = .09$ in Figure 5.34(a,b). Although the magnitude of the amplification changes, the amplified length scales are still similar, indicating similar amplification mechanisms for these modes. Significant deviations in the contour shapes of the amplification near the representative subsonic length scales occur for $i = 4$ and $i = 5$ in Figure 5.34(c,d). The difference in the amplified length scales using either the chemical equilibrium or chemical nonequilibrium assumptions are due to the different amplification mechanisms in the sub-optimal resolvent modes. The σ_j are compared for the representative subsonic length scales in Figure 5.35. It is interesting to note that the hypersonic resolvent gains have considerably less separation between σ_1 and σ_2 than the incompressible counterpart. It is likely that this is caused by the increased dissipation with a larger Ma. The study of Bae, Dawson, and McKeon (2020) demonstrated that the supersonic resolvent modes identified low-rank wavenumbers in the subsonic region, similar to Moarref, Sharma, et al. (2013). The similar low-rank behavior in the supersonic TBL and the incompressible TBL can be predicted by the Morkovin hypothesis (Morkovin, 1962), which states that for moderate Ma, the compressible dynamics follow the incompressible dynamics in a TBL if the density variations are accounted for. Since the hypersonic TBL has a Ma significantly larger than the supersonic TBL studied in Bae, Dawson, and McKeon (2020), it is likely that the compressible effects are too large to separate from the incompressible behavior. They further support that

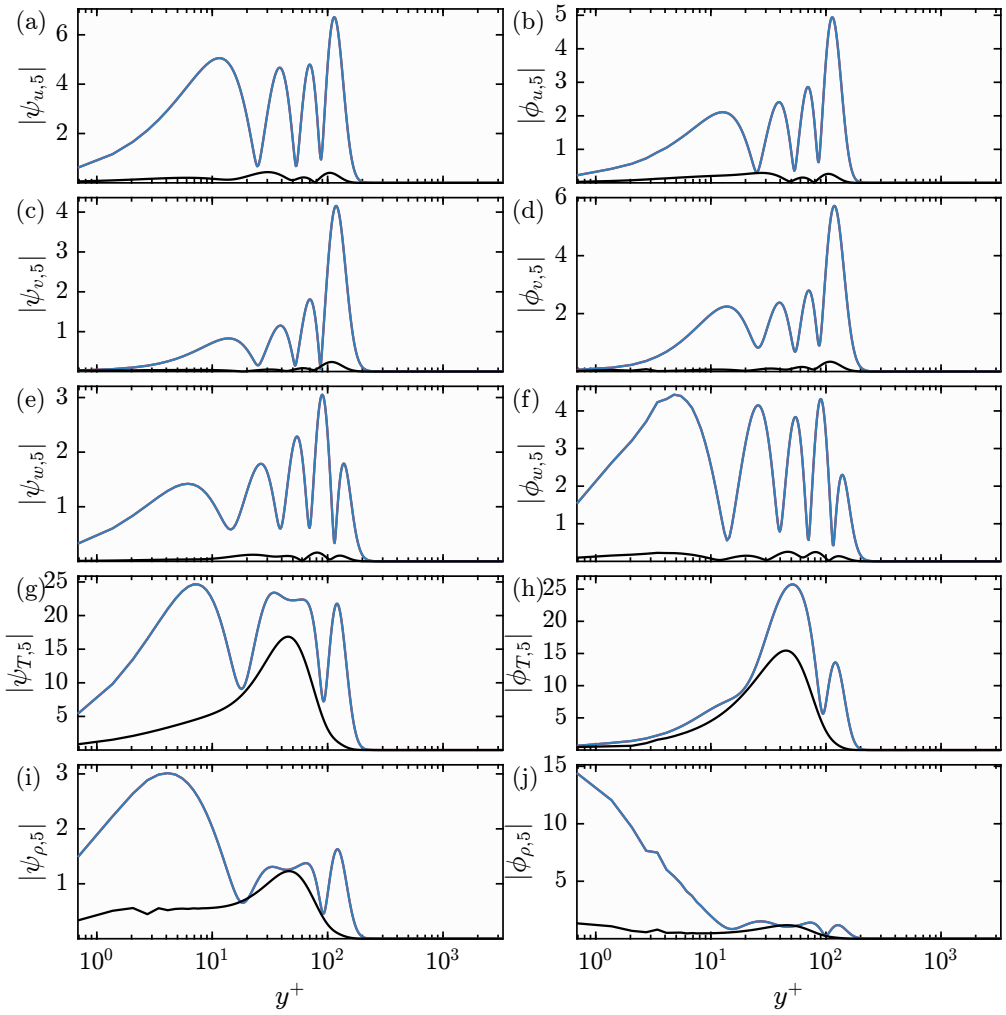

Figure 5.36: $|\psi_{u,5}|$ (a), $|\phi_{u,5}|$ (b), $|\psi_{v,5}|$ (c), $|\phi_{v,5}|$ (d), $|\psi_{w,5}|$ (e), $|\phi_{w,5}|$ (f), $|\psi_{T,5}|$ (g), $|\phi_{T,5}|$ (h), $|\psi_{T,5}|$ (i), $|\phi_{T,5}|$ (j) for representative subsonic modes ($k_x = 2\pi/.9$, $k_z = 2\pi/.09$, $c = .48$). The chemical nonequilibrium and equilibrium modes are in black and blue.

the first three modes have minor differences since the σ_i are almost the same. For $i > 4$, the σ_j begin to vary depending on how the chemistry is modeled. To study the differences in the amplification mechanisms due to the chemistry, Figures 5.36, 5.37, and 5.38 compare the components of $\boldsymbol{\psi}_5$ and $\boldsymbol{\phi}_5$.

First, the u, v, w, ρ, and T components of $\boldsymbol{\psi}_5$ and $\boldsymbol{\phi}_5$ are compared in Figure 5.36. Unlike the optimal mode, the differences using the chemistry assumptions are severe in both mode shape and relative amplitudes. The multiple-peaked structure in $\boldsymbol{\psi}_5$ and $\boldsymbol{\phi}_5$ using chemical equilibrium is consistent with the orthonormality constraint of the resolvent modes. Similar behavior is observed in the $i = 2$ and $i = 3$ modes in both the chemical equilibrium and nonequilibrium approach, albeit with less peaks

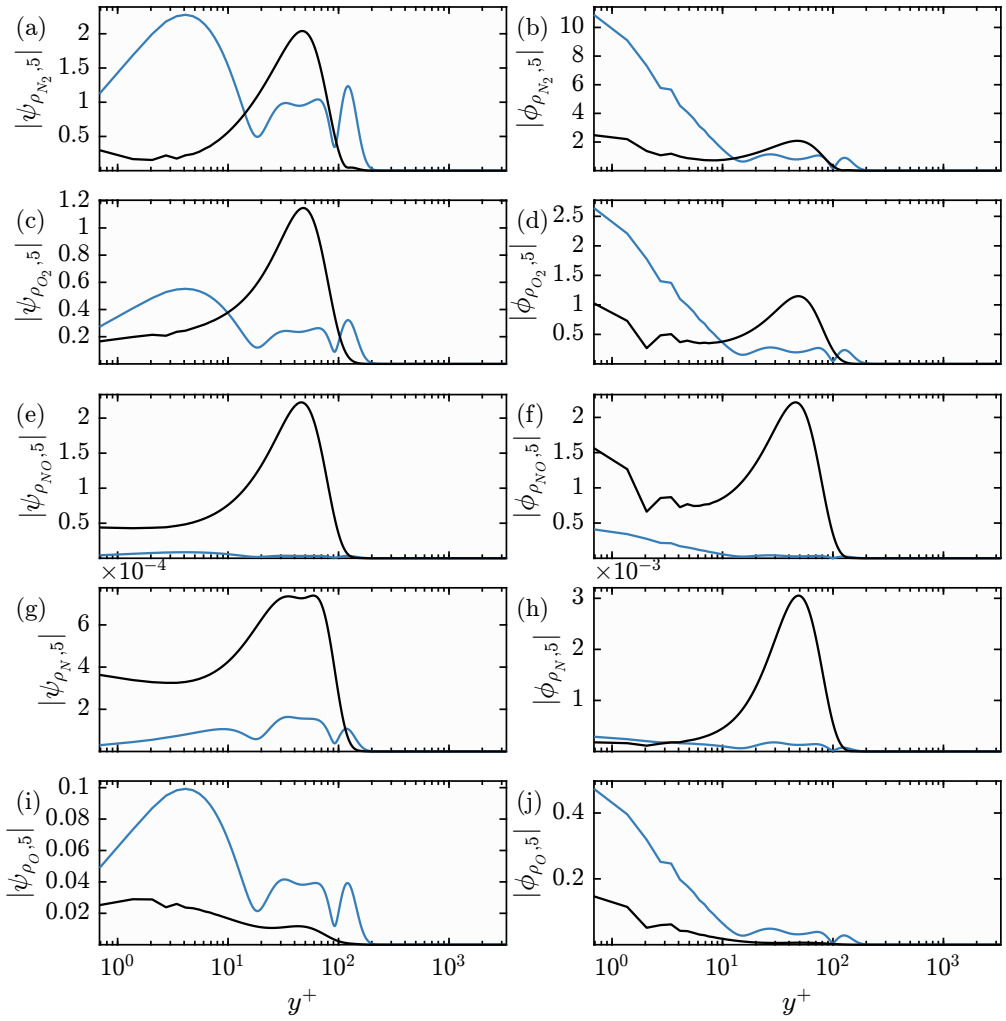

Figure 5.37: $\left|\psi_{\rho_{N_2},5}\right|$ (a), $\left|\phi_{\rho_{N_2},5}\right|$ (b), $\left|\psi_{\rho_{O_2},5}\right|$ (c), $\left|\phi_{\rho_{O_2},5}\right|$ (d), $\left|\psi_{\rho_{NO},5}\right|$ (e), $\left|\phi_{\rho_{NO},5}\right|$ (f), $\left|\psi_{\rho_N,5}\right|$ (g), $\left|\phi_{\rho_N,5}\right|$ (h), $\left|\psi_{\rho_O,5}\right|$ (i), $\left|\phi_{\rho_O,5}\right|$ (j) for representative subsonic modes ($k_x = 2\pi/.9$, $k_z = 2\pi/.09$, $c = .48$). The chemical nonequilibrium and equilibrium modes are in black and blue.

in the components (not plotted). Since the T and ρ components of $\boldsymbol{\psi}_5$ and $\boldsymbol{\phi}_5$ in the chemical nonequilibrium approach have only a single peak, this suggests that the orthonormality is enforced via a change in the component-wise amplification of the mode rather than a change in the spatial structure of modes to maintain the same component-wise amplification seen in the chemical equilibrium sub-optimal modes. Indeed, this can be seen by comparing the u, v, and w components of $\boldsymbol{\psi}_5$ and $\boldsymbol{\phi}_5$. The chemical equilibrium approach continues to have large hydrodynamic components in both the forcing and response due to amplification from $\overline{U}_y$. These components in the chemical nonequilibrium approach are an order of magnitude smaller indicating that this hydrodynamic amplification is not favored in the presence of chemistry.

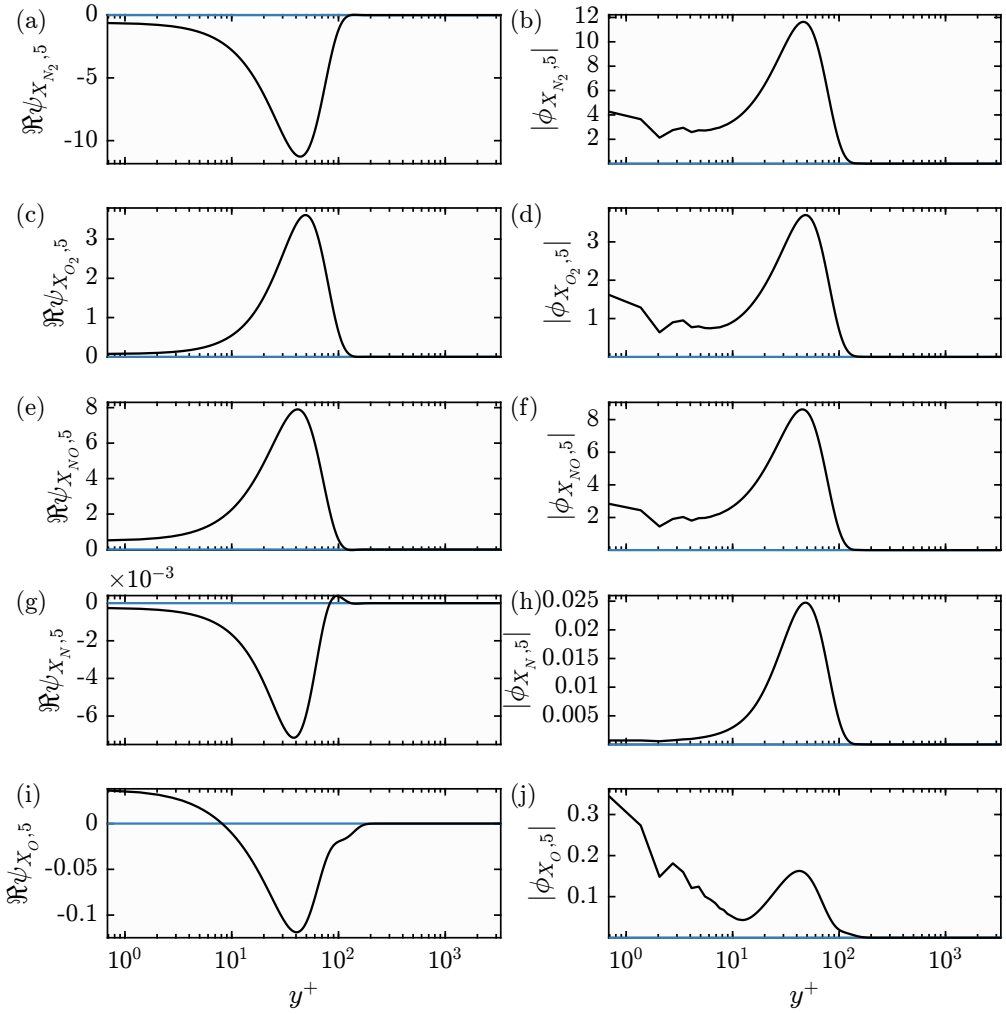

Figure 5.38: Real part of $\psi_{X_{N_2},5}$ (a), $\psi_{X_{O_2},5}$ (c), $\psi_{X_{NO},5}$ (e), $\psi_{X_N,5}$ (g), and $\psi_{X_O,5}$ (i) and magnitude of $\phi_{X_{N_2},5}$ (b), $\phi_{X_{O_2},5}$ (d), $\phi_{X_{NO},5}$ (f), $\phi_{X_N,5}$ (h), and $\phi_{X_O,5}$ (j) for representative subsonic modes ($k_x = 2\pi/.9$, $k_z = 2\pi/.09$, $c = .48$). The chemical nonequilibrium and equilibrium modes are in black and blue.

The differences in the shape of $\phi_{\rho,5}$, notably the presence of a singular peak in the near-wall region using chemical nonequilibrium, further suggest that forcing from the species components is causing the changes in this mode.

Now the ρ_{i_s} components are plotted in Figure 5.37. Unlike in the optimal mode, modelling the ρ_{i_s} components of $\boldsymbol{\psi}_5$ and $\boldsymbol{\phi}_5$ with the chemical equilibrium approach leads to significant disagreements with the chemical nonequilibrium approach. The chemical nonequilibrium has singular peaks for $\psi_{\rho_{i_s},5}$ and $\phi_{\rho_{i_s},5}$ at $y^+ = 50$, unlike the chemical equilibrium approach. The singular peaks in $\psi_{\rho_{i_s},5}$ and $\phi_{\rho_{i_s},5}$ contrast with the optimal modes, as they peak closer to the wall. Component-wise, the O_2 and NO components of $\psi_{\rho_{i_s},5}$ and $\phi_{\rho_{i_s},5}$ are much larger than in the optimal

mode. The ρ_N component remains the smallest response component since the mean temperature is too small to support large concentrations of N. However, the $\phi_{\rho_N,5}$ component has an amplitude an order of magnitude larger than what was observed in the optimal mode. $\boldsymbol{\psi}_5$ supports the production of primarily NO, with N_2 and O_2 playing a role in its production, as expected.

Next the X_{i_s} components of $\boldsymbol{\psi}_5$ and $\boldsymbol{\phi}_5$ are compared in Figure 5.38. The first thing to note is that the magnitudes of these components are significantly larger than the magnitudes plotted in Figure 5.28 for the optimal modes. The $\psi_{X_N,5}$ component has the smallest amplitude once again, in accordance with the relatively small mean temperature. The $\phi_{X_{i_s},5}$ components also have peaks at $y^+ = 50$ that are not observed in the optimal mode. The presence of these peaks in $\phi_{X_{i_s},5}$ and $\phi_{\rho_{i_s},5}$ serve as sources away from the wall in the species continuity equations that were almost nonexistent in the optimal mode. The forcing occurs primarily in N_2, O_2, and NO. These components in turn have the largest components in the response. Interestingly an O forcing or response is about two of orders of magnitude smaller than the other N_2, O_2, and NO components. In the response mode, the X_{N_2} component is anticorrelated with the X_{NO} while the X_{O_2} and X_{NO} components are correlated. Since the X_{i_s} components are so large, this implies that linear mechanisms that force the species components drive the amplification of this sub-optimal mode, unlike the optimal mode. This further explains why the chemical equilibrium approach does not agree with the chemical nonequilibrium approach in the higher order modes. The source of this component-wise non-normality stems from $\partial\overline{\dot{\omega}}_{j_s} \Big/ \partial\rho_{i_s}$ terms in the L_{4,i_s} and L_{j_s,i_s} blocks in the LNS operator.

When the dominant amplification mechanism is shear driven or caused by acoustic phenomena, the chemical equilibrium and chemical nonequilibrium approaches amplify dominant modes with similar mode structure. For the mean flow field studied here, amplification via chemical nonequilibrium mechanisms only becomes important in the higher order modes. It is likely that for a TBL with a larger mean temperature, the chemical nonequilibrium mechanisms can affect even the optimal modes because the temperatures can support more dissociation and compete with the shear driven or acoustic amplification mechanisms. This could increase the magnitude of the $\partial\overline{\dot{\omega}}_{j_s} \Big/ \partial\rho_{i_s}$ terms and increase the role of the component-wise non-normality. Finally, it is stressed that the behavior of these modes is influenced by the choice of inner product, which sets the condition for the orthonormality.

5.7 Correlations in the Chemical Nonequilibrium Response Mode Components

In the previous sections, most of the behavior of in the response modes was inferred by comparing the absolute value of certain components. Here, the difference in phase between different components of a single mode will be compared to infer any correlations. Comparisons between the phases of resolvent modes have been used in the past to investigate the large scale modulation on small scale signals using a reduced-order model (Sharma and McKeon, 2013). In that study, the cosine of the differences in phase between a set of triadically-consistent resolvent modes was used as a model for the correlation coefficient. In a similar vein, the correlation coefficient between the i and j components of the leading response mode, $\boldsymbol{\psi}_1$, is defined here as

$$R_{i,j} = \cos\left(\alpha_i - \alpha_j\right), \tag{5.33}$$

where α_i and α_j are the phase angles of $\psi_{i,1}$ and $\psi_{j,1}$. $R_{i,j}$ can also be defined as

$$R_{i,j} = \frac{\Re\left(\psi^*_{i,1}\psi_{j,1}\right)}{\left|\psi_{i,1}\right|\left|\psi_{j,1}\right|}, \tag{5.34}$$

where the real part is chosen so that $R_{i,j}$ remains symmetric. $R_{i,j}$ is bounded by $[-1, 1]$, with negative values denoting anticorrelation and positive values denoting correlation. $R_{i,j}$ close to 0 means that components i and j of $\boldsymbol{\psi}_1$ are not correlated. In real measurements, the correlation coefficient, $C_{i,j}$ of two signals i and j is the ratio of their cross correlation normalized by the products of their standard deviations. Here, $R_{i,j}$ is simply a comparison of the phase of two different components of the leading response mode. Although $R_{i,j}$ can be computed with higher order modes, the leading mode is chosen because it has a single-peaked structure with less zero crossings compared to the higher order modes. This makes the interpretation of the changes in phase easier to interpret for the leading mode.

The correlation is examined using the same turbulent mean flow field from Section 5.6, with modes focused on the subsonic region. The c is chosen as .4817 which corresponds to $\overline{U}(y^+ \approx 40)$. Although there are many choices for $R_{i,j}$ that can be plotted, the $R_{i,j}$ that are considered are $R_{u,Y_{i_s}}$, $R_{v,Y_{i_s}}$, $R_{u,T}$, $R_{v,T}$, $R_{T,Y_{i_s}}$, and R_{X_i,X_j}. The first four are chosen to compare with the correlation coefficients computed in Di Renzo and Urzay (2021) and plotted in Figure 5.39. $R_{T,Y_{i_s}}$ is used to investigate how the mass fractions correlate with the temperature in the linear analysis. R_{X_i,X_j} is used to investigate the correlation between the mole fractions. In particular, this

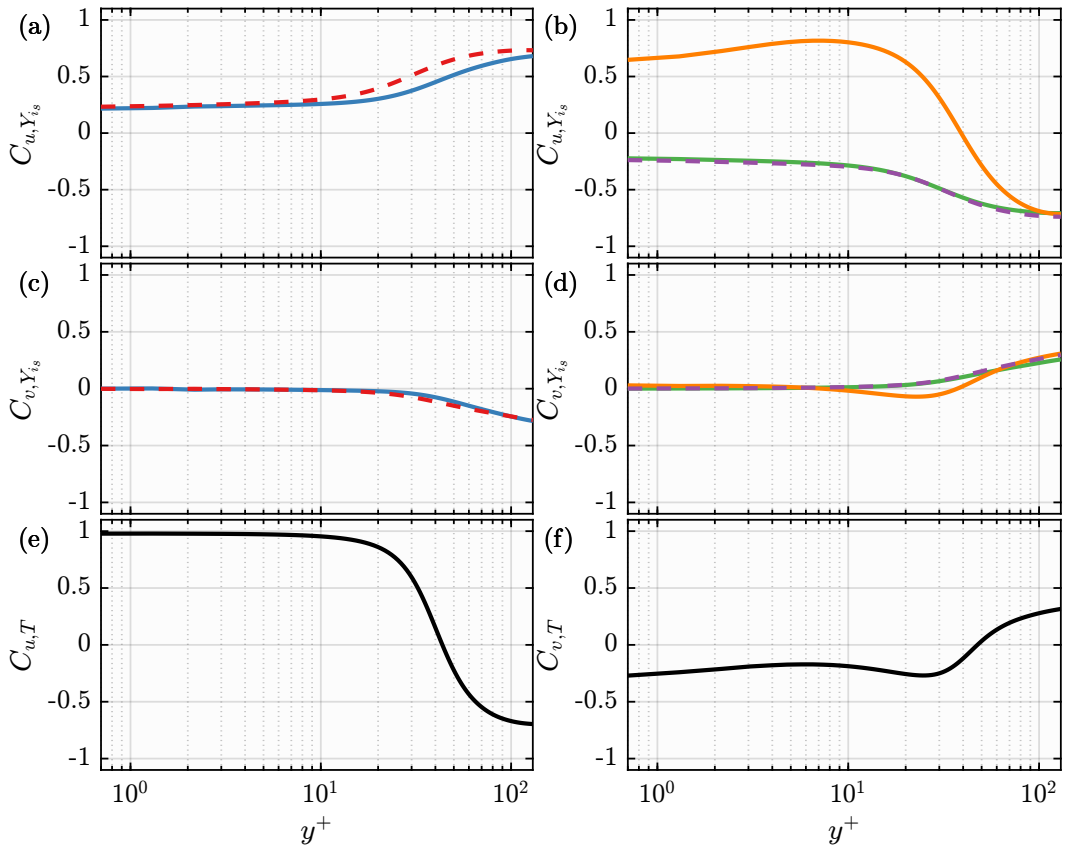

Figure 5.39: $C_{i,j}$ from the DNS of Di Renzo and Urzay (2021). (a) and (b) plot $C_{u,Y_{i_s}}$, (c) and (d) plot $C_{v,Y_{i_s}}$, (e) plots $C_{u,T}$, and (f) plot $C_{u,T}$. The blue, red, green, orange, and purple curves denote i_s =N_2, O_2, NO, N, and O. The dashed lines are used to distinguish the different curves. Note that only the region $y^+ < 130$ is shown to compare the regions where $\boldsymbol{\psi_1}$ is supported for small scale modes.

is used to test how the X_{N_2} and X_{O_2} components correlate with the X_{NO}, X_N, and X_O components.

Before discussing $R_{i,j}$, a summary of the $C_{i,j}$ computed in Di Renzo and Urzay (2021) is presented and plotted in Figure 5.39. Recall that $C_{i,j}$ is computed with the full temporal signal of the data unlike $R_{i,j}$ which is computed based on the phase of different component of $\boldsymbol{\psi}_i$. $C_{u,T}$ is equal to 1 near the wall and changes sign near the location of the maximum $\overline{T}$. From that location to the rest of the boundary layer, $C_{u,T}$ remains negative. The opposite is true for $C_{v,T}$ as it begins negative near the wall and changes sign away from the wall for the rest of the boundary layer. The change in sign of $C_{u,T}$ and $C_{v,T}$ is related to the sweeps and ejections that moves fluid in the wall-normal directions coupled with the non-monotonicity of $\overline{T}$. More details on this will be provided below, when the results of $R_{i,j}$ are presented. $C_{u,Y_{i_s}}$ remains positive for N_2 and O_2 and negative for NO and O throughout the boundary layer.

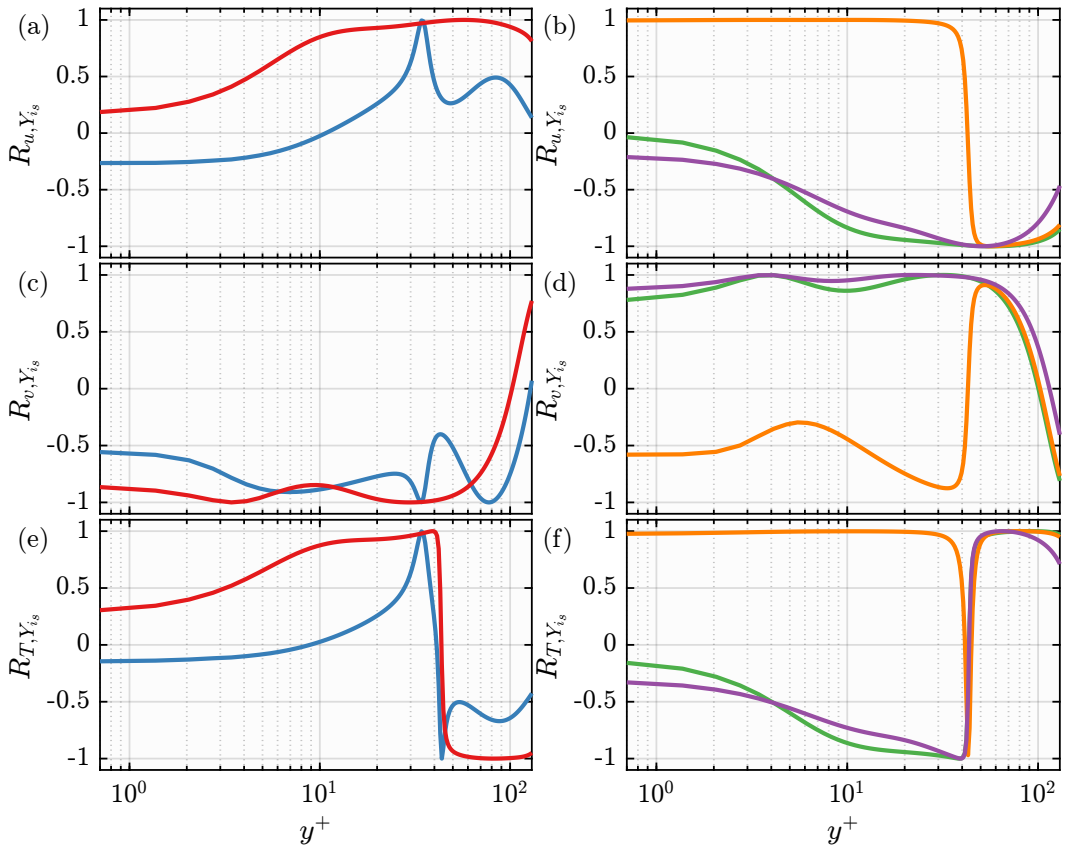

Figure 5.40: $R_{i,j}$ for a subsonic mode with $k_x = 2\pi/.9$, $k_z = 2\pi/.09$, and $c = .48$. (a) and (b) plot $R_{u,Y_{i_s}}$, (c) and (d) plot $R_{v,Y_{i_s}}$, and (e) and (f) plot $R_{T,Y_{i_s}}$. The blue, red, green, orange, and purple curves denote i_s =N_2, O_2, NO, N, and O. Note that only the region $y^+ < 130$ is shown since $\boldsymbol{\psi_1}$ has negligible support in the outer region of the flow.

For N, $C_{u,Y_{i_s}}$ begins positive near the wall and becomes negative away from the flow like $C_{u,T}$. This behavior in $C_{u,Y_{i_s}}$ can also be explained with the sweeps and ejections as $\overline{Y}_{N_2}$ and $\overline{Y}_{O_2}$ monotonically increase while $\overline{Y}_{NO}$ and $\overline{Y}_O$ monotonically decrease with away from the wall. $\overline{Y}_N$, like $\overline{T}$, is non-monotonic with the peak $\overline{Y}_N$ and $\overline{T}$ occuring at the same wall-normal location. Since Y_N tracks T, N is mostly in steady state as the chemical production and consumption occurs faster than its molecular diffusion (Di Renzo and Urzay, 2021). Since $C_{u,Y_{i_s}}$ does not change sign across the boundary layer for the other species components like $C_{u,T}$, the other species are not in steady state and have significant transport due to diffusion in the near-wall region. In the outer region of the flow, $C_{v,Y_{i_s}}$ is positive for the dissociated components and negative for the undissociated components. Near the wall, $C_{v,Y_{i_s}}$ is approximately 0 for all the species components. This indicates that the mole fractions in the near-wall region are dominated by molecular diffusion.

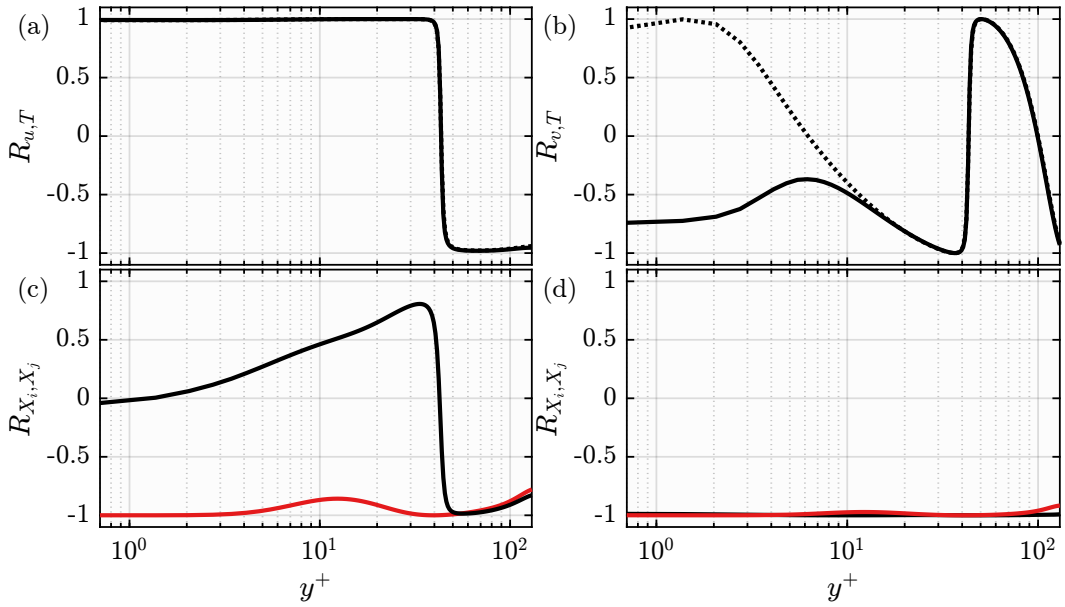

Figure 5.41: $R_{i,j}$ for a subsonic mode with $k_x = 2\pi/.9$, $k_z = 2\pi/.09$, and $c = .48$. $R_{u,T}$ and $R_{v,T}$ are plotted in (a) and (b). The solid lines are computed using the chemical nonequilibrium approach and the dotted lines are computed using the chemical equilibrium approach. (c) plots $R_{X_{N_2},X_N}$ and $R_{X_{N_2},X_{NO}}$ in black and red. (d) plots $R_{X_{O_2},X_{NO}}$, and $R_{X_{O_2},X_O}$ in black and red. Note that only the region $y^+ < 130$ is shown since $\boldsymbol{\psi_1}$ has negligible support in the outer region of the flow.

In Figures 5.40 and 5.41, the correlation coefficients are compared for the subsonic mode plotted in Figures 5.26, 5.27, and 5.28 which is representative of the structures in the near-wall cycle, albeit with a faster convective velocity. Figures 5.40(a,b) demonstrate that $\psi_{u,1}$ is positively correlated with $\psi_{Y_{N_2},1}$ throughout the near-wall region. $\psi_{u,1}$ and $\psi_{Y_{O_2},1}$ are positively correlated only in the region $y^+ \in (10, 100)$. $\psi_{u,1}$ is anticorrelated with $\psi_{Y_{NO},1}$ and $\psi_{Y_O,1}$. The correlation between $\psi_{u,1}$ and $\psi_{Y_N,1}$ changes sign around the location of maximum temperature, with them being anticorrelated away away from the wall. Figures 5.40(c,d) show that $\psi_{v,1}$ is correlated with $\psi_{Y_{N_2},1}$, $\psi_{Y_{O_2},1}$, and $\psi_{Y_N,1}$ and anticorrelated with $\psi_{Y_{NO},1}$ and $\psi_{Y_O,1}$ near the wall. Away from the wall, $R_{v,Y_{i_s}}$ changes signs for all the species, except N. R_{v,Y_N} tracks $R_{v,Y_{NO}}$ and R_{v,Y_O} above the $\overline{T}$ maximum.

The sign of $R_{u,Y_{i_s}}$ is similar to the sign of the correlation coefficients from the DNS plotted in Figure 5.39, including the change in sign of R_{u,Y_N} in the near-wall region. This is unsurprising as sweeps ($-v$) are responsible for convecting undissociated components (N_2 and O_2) and high momentum fluid ($+u$) down closer to the wall. The ejections ($+v$) convect dissociated components (NO, and O) and low momentum fluid ($-u$) away from the wall. As a result, the high speed streaks have increased

Y_{N_2} and Y_{O_2} while the low speed streaks have decreased Y_{NO} and Y_O. The change in sign in the correlations with Y_N near the wall are because the N are in steady state and follow T variations (Di Renzo and Urzay, 2021). This causes $\overline{Y}_N$ to be non-monotonic, like $\overline{T}$, which changes the N distributions through the sweeps and ejections depending if they occur below or above the $\overline{T}$ maximum. One thing not captured in this analysis is the lack of correlation between $\psi_{v,1}$ and $\psi_{Y_{i_s},1}$ in the near-wall region. This is likely because the linear mechanisms near the wall are optimally amplified by the lift-up mechanism. The linear coupling between the v and Y_{i_s} components is likely saturated when nonlinear terms, or nonlinear interactions, are included in the full simulation. In the outer region, the sign of $R_{u,Y_{i_s}}$ matches the sign in $C_{u,Y_{i_s}}$.

Next the correlations between $\psi_{T,1}$ and $\psi_{Y_{i_s},1}$ are plotted in Figures 5.40(e,f). Near the wall, below the critical layer, $R_{T,Y_{i_s}}$ tracks $R_{u,Y_{i_s}}$. $R_{T_{Y_N}} \approx 1$ throughout the boundary layer, except at the critical layer where the value of $\psi_{T,1}$ drops to 0. The correlation between $\psi_{T,1}$ and $\psi_{Y_N,1}$ agrees with the observation that N is in steady state (Di Renzo and Urzay, 2021). Further from the wall, $R_{T,Y_{i_s}}$ changes sign and is the opposite of $R_{u,Y_{i,s}}$ for all the components except N. This change in sign relative to $R_{u,Y_{i,s}}$ is explained by the change in sign of $R_{u,T}$ across the $\overline{T}$ maximum in Figure 5.41(a). Below the $\overline{T}$ maximum, the ejections bring cool, low momentum fluid up while the sweeps bring hot, high momentum fluid down. Above the $\overline{T}$ maximum, the picture is flipped as the ejections now bring hot, low momentum fluid up and the sweeps bring cool, high momentum fluid down. The change in sign of $\overline{T}_y$ is thus responsible for the phase jump. The sweeps and ejections also explain the correlation $R_{v,T}$ in Figure 5.41(b) which has the opposite sign of $R_{u,T}$ for $y^+ < 100$. The velocity-temperature correlations are qualitatively similar to the correlations from the DNS plotted in Figure 5.39, even capturing the change in sign at the $\overline{T}$ maximum. Note that $R_{u,T}$ and $R_{v,T}$ track R_{u,Y_N} and R_{v,Y_N} due to the almost perfect correlation between $\psi_{T,1}$ and $\psi_{Y_N,1}$.

$R_{u,T}$ and $R_{v,T}$ are compared for the chemical equilibrium case. $R_{u,T}$ both agree. $R_{v,T}$ differs substantially only in the near-wall region where the chemical equilibrium case predicts correlation between $\psi_{T,1}$ and $\psi_{v,1}$. Although this change is large, it may be a symptom of the small amplitudes in the viscous sub-layer as $\boldsymbol{\psi}_1$ matches the no-slip and isothermal boundary conditions as visual inspection of the modes does not reveal a significant phase change. It is worth noting that resolvent analysis assuming chemical equilibrium would not be able to predict any correlations involving mass

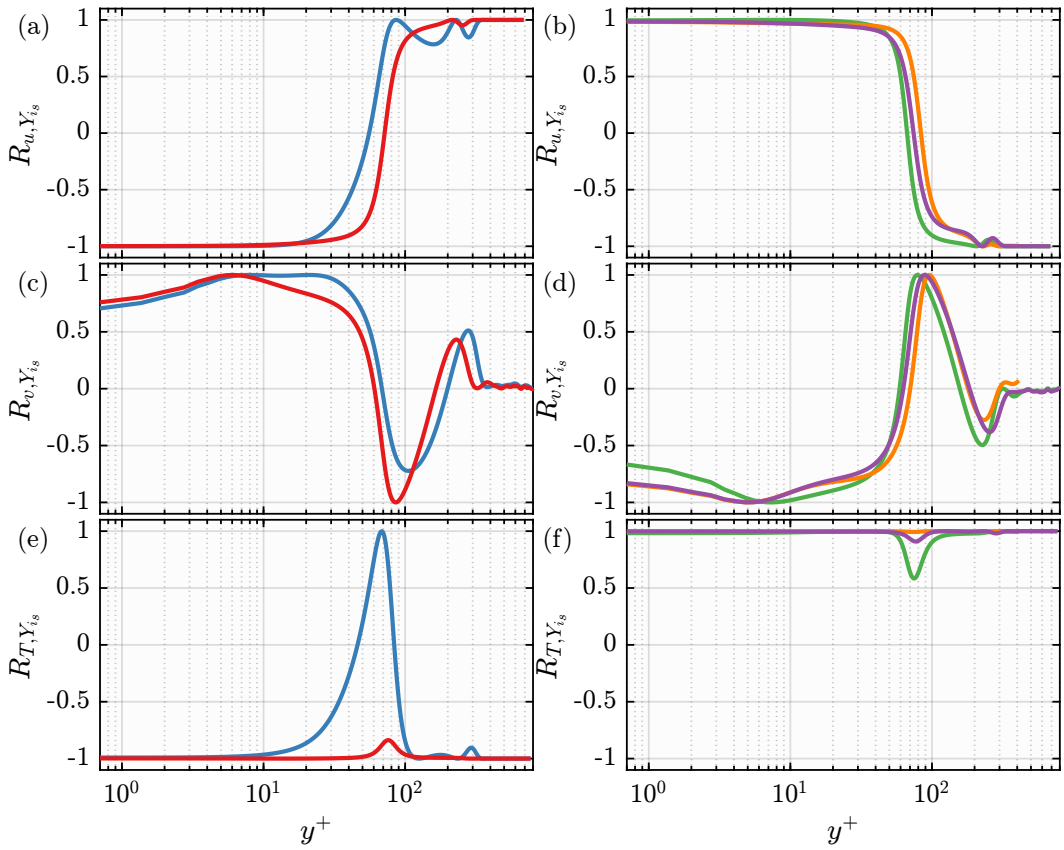

Figure 5.42: $R_{i,j}$ for a subsonic mode with $k_x = 2\pi/10$, $k_z = 2\pi/1$, and $c = .48$. The colors and linestyles are the same as in Figure 5.40.

fractions or mole fractions since the changes in concentration are 0, by construction.

The correlations between the mole fractions of the undissociated components and the dissociated components are plotted in Figures 5.41(c,d). As was alluded to in the plots of $\psi_{X_{i_s},1}$ in Sections 5.5 and 5.6, $\psi_{X_{N_2},1}$ is anticorrelated to $\psi_{X_{NO},1}$ and $\psi_{X_{O_2},1}$ is anticorrelated to $\psi_{X_{NO},1}$ and $\psi_{X_O,1}$ as the values of $R_{X_i,X_j} \approx -1$ throughout. This is expected because a decrease in undissociated components leads to an increase in dissociated components. The $\psi_{X_{N_2},1}$ and $\psi_{X_N,1}$ are not anticorrelated since dissociation of N_2 primarily leads to NO. Furthermore, the production of N is more correlated to the temperature fluctuations (Di Renzo and Urzay, 2021).

In Figures 5.42 and 5.43, the same correlations are plotted for a larger mode with $k_x = 2\pi/10$ and $k_z = 2\pi/1$, with the same c. For this large scale mode, $\psi_{T,1}$ and $\psi_{Y_{i_s},1}$ are correlated to the dissociated components and anticorrelated for N_2. $\psi_{T,1}$ and $\psi_{Y_{O_2},1}$ are correlated for most of the domain, except near the temperature peak. This accompanies a slight change in the correlations with $\psi_{Y_{NO},1}$ and $\psi_{Y_O,1}$. $\psi_{Y_{i_s},1}$ mostly tracks $\psi_{T,1}$ since the chemical activity in this mode is in steady-state,

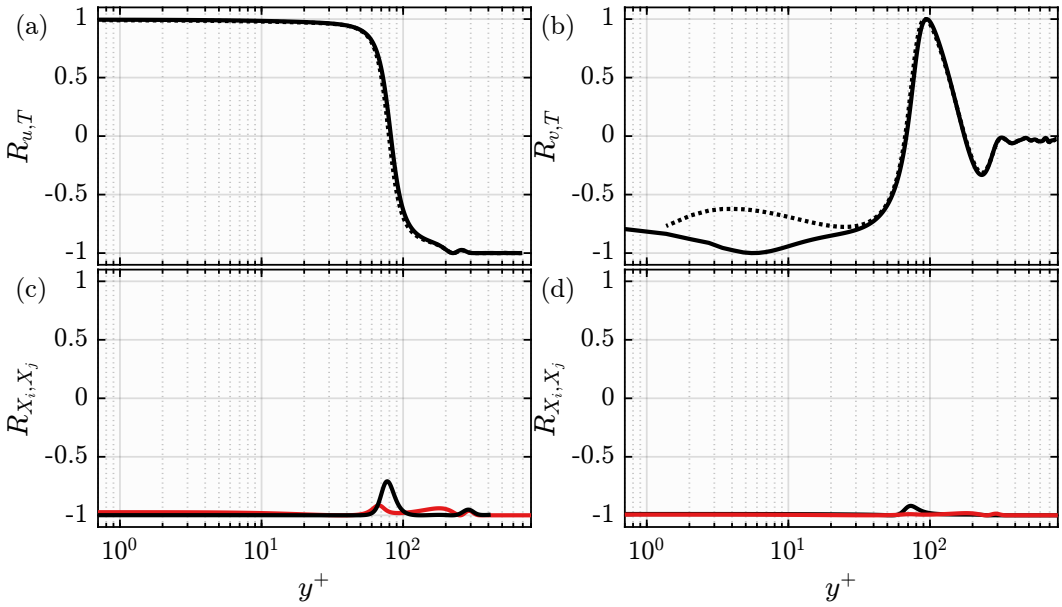

Figure 5.43: $R_{i,j}$ for a subsonic mode with $k_x = 2\pi/10$, $k_z = 2\pi/1$, and $c = .48$. The colors and linestyles are the same as in Figure 5.41.

as was the case for N in the small scale mode. This suggests that for this mode, chemical diffusion plays a negligible role. The chemical diffusion in Equation 5.17 introduces spatial second derivatives to the mole fractions which decrease the influence of the chemical diffusion on the large scale modes. The $\psi_{Y_{O_2},1}$ component is likely more susceptible to chemical nonequilibrium effects because it is easier to create large concentrations of O_2 with the relevant temperatures in the TBL. Due to the correlations between $\psi_{Y_{i_s},1}$ and $\psi_{T,1}$, the profiles of $R_{u,Y_{i_s}}$ and $R_{v,Y_{i_s}}$ follow $R_{u,T}$ and $R_{v,T}$. Lastly, $R_{X_i,X_j} \approx -1$ between the undissociated components and the dissociated components with no variation for N.

The correlations of the small scale mode agree qualitatively with the correlations from the DNS data of Di Renzo and Urzay (2021) plotted in Figure 5.39. The correlations with the large scale mode result in correlations that differ from the data, notably because the species mass fractions follow the temperature component of the leading mode. Although the large scale mode is more amplified in the local analysis, modes with those scales are not typically energetic in the near-wall region of the flow. Cogo et al. (2022)'s premultiplied energy spectra of a single species compressible TBL reports a near-wall cycle centered at $y^+ \approx 20$ and $\lambda_z^+ \approx 100$, while scales similar to the large scale mode in Figures 5.42 and 5.43 are only energetic in the outer region of the flow. The chemical nonequilibrium flow of Passiatore et al. (2022) also demonstrates a near-wall peak with $\lambda_z^\star \sim 300$, where $\star$ denotes

rescaling with semilocal length scale $\overline{\mu^d}/\sqrt{\overline{\rho}^d \tau_w^d}$. The small scale structures play an important role in the near-wall turbulent dynamics while the small scale resolvent modes reflect the qualitative behavior in the near-wall region.

The correlations made with the small scale mode are only relevant where the small scale mode has non-negligible support. Furthermore, they only apply for a single wavenumber triplet. In order to extend the correlations further from the wall, and to improve the quantitative agreement with the full data, more modes need to be included with their nonlinear weights chosen to respect the nonlinearity in the full turbulent flow. This is also true for the incompressible TBL, as was investigated by Moarref, Jovanović, et al. (2014). Extending the results used in the incompressible flow to supersonic or hypersonic flows requires an understanding that the interactions are no longer triadic since the nonlinear terms are not quadratic for hypersonic TBL.

5.8 Chapter Summary and Future Work

The real gas effects that are relevant to hypersonic TBLs such as vibrational excitation and chemical nonequilibrium were examined to see what is captured by the linear amplification and enable comparisons with real flows. For the flows studied here, these effects were relevant only within the boundary layer region where the temperatures were largest. This caused the most appreciable changes in the thermophysical properties. The linear amplification of the supersonic modes were hardly changed by the modeling assumptions due to them being excited in a cooler region of the flow where the real gas effects are negligible.

It was shown that vibrational excitation, modeled through a CIG assumption, lead to slight changes in the resolvent amplification, even using the same mean flow fields, in the subsonic region. The change in amplification is likely because of the differences in thermal diffusivity caused by the CIG assumption. The mode shapes within the boundary layer were not changed substantially, although there were differences in the amplitudes of the modes examined. Since the amplification in the subsonic region was shown to collapse when rescaled with the local maxima, it may suggest that the resolvent analysis can be rescaled by accounting for the local variation in the thermodynamic properties as in Bae, Dawson, and McKeon (2020). The most relevant changes to the amplification were found when the forcing was constrained to ϕ_T and ϕ_ρ. This revealed sensitivity of the near-wall cycle to the CIG assumption when forced through the thermodynamic variables. This can have implications for the control of the near-wall cycle if temperature related effects

are used as a control mechanism. In Di Renzo et al. (2022), the effects of a CIG assumption were shown to be most relevant near the oblique shock, where the CIG assumption affected relevant frequencies near the shock location. An oblique shock is outside the realm of validity for a local approach. Future work would need to develop the biglobal approach described earlier to a compressible flow and account for the changes in coordinates with the ramp to capture these effects.

The effects of chemical nonequilibrium were investigated for both a turbulent flow and a laminar flow. The analysis with the laminar flow found that the amplification differed the most with the large-scale streak-like modes that can reach down to the wall. These streak like modes were uniquely amplified and were not present in the chemical equilibrium approach. These modes also illustrated different amplification mechanisms, primarily through ϕ_T and ϕ_ρ. In the case of the turbulent flow, the large $\overline{U}_y$ and $\overline{T}_y$ terms created sources of amplification that dominated the chemical nonequilibrium and molecular diffusion terms. As a result, the $\mathbf{u}$, T, and ρ components of the leading resolvent modes differed slightly for the small scale modes amplified by the shear. With chemical nonequilibrium, the largest observed differences were when the ρ_{i_s} and X_{i_s} components were compared as the chemical equilibrium approach can not account for changes in concentration. The presence of the streaky mode seen in the laminar case was not observed in the turbulent case. The higher order modes for the hypersonic TBL under chemical nonequilibrium demonstrated amplification through the chemistry terms that are absent in the chemical equilibrium approach. This changed the structure and amplification of the higher order modes.

The use of chemical nonequilibrium allows concentrations of the species to differ in the linear analysis. A unique aspect of this approach is that it also allows for forcing from certain species components. Forcing from $\phi_{\rho_{N_2}}$ and $\phi_{\rho_{O_2}}$ led to the energization of supersonic modes while forcing from $\phi_{\rho_{NO}}$, ϕ_{ρ_N}, and ϕ_{ρ_O} demonstrated no discontinuity from the supersonic phenomena as these components are not present in the freestream. This forcing can be used to consider the linear response to forcing from a catalytic wall which can blow species components into the boundary layer. Furthermore, the analysis described here can be used to describe how a change to the chemistry model can affect the linear amplification and which length scales are expected to be affected, to first order.

The correlations in the small-scale chemical nonequilibrium resolvent modes were shown to agree qualitatively well with the correlations from the data of Di Renzo

and Urzay (2021). This was due to the importance of the lift-up effect in these modes. The large scale modes were shown to have correlations that did not agree with the full data because the large scales did not allow for molecular diffusion. Future work will require nonlinear closure by finding coefficients for the resolvent basis described herein.

The resolvent analysis framework is not able to capture the true nonlinear dynamics in a hypersonic TBL for a number of reasons. One limitation of this approach is that the turbulence is multiscale, whereas this approach considers the linear amplification of a single wavenumber-frequency triad. It does not account for the true nonlinear nature in the full TBL or the nonlinear interactions present in the chemical effects. Furthermore, the results are depend on the choice of a 2-norm based on the Chu energy norm (Chu, 1965), which may not be an appropriate measure of energy for a hypersonic TBL. Despite these limiations, resolvent analysis provides predictions of the most linearly amplified length and time scales in a hypersonic TBL. This can help predict which structures are most affected by changes in the chemistry modelling, similar to the study of Franko, MacCormack, and Lele (2010). Furthermore, the qualitative agreement in the correlations of the small scale modes with the DNS correlations suggest that resolvent analysis can capture amplification mechanisms that are present in the turbulent data with chemical nonequilibrium. Such effects would not be captured if chemical equilibrium was used in the analysis. Future work will have to account for the multiscale nature of the TBL by incorporating closure arguments and properly modeling the nonlinear forcing terms.

Lastly, the freestream temperatures described in this problem allowed for no relevant chemical effects in the freestream. Future work will study how a larger T_e, which can sustain the freestream dissociation, affects the linear amplification described herein. It is likely that a larger T_e may change the supersonic region when the dissociated components have non-negligible concentrations in the freestream. Within the boundary layer, hotter temperatures lead to more dissociation of the air, and as a result, larger chemical terms. These may create substantial effects that differ from the chemical equilibrium approach. As T_e increases, incorporating a vibrational temperature model as in Franko, MacCormack, and Lele (2010) in the resolvent analysis will also a topic of future work.

Chapter 6

EFFICIENT METHODS FOR RESOLVENT ANALYSIS: SAMPLING AND APPROXIMATIONS

6.1 Introduction

Computationally, n, the number of degrees of freedom in the state vector $\breve{\mathbf{q}}$, is equal to the number of state variables, n_s, times the number of grid points, N. Increasing n increases the computational cost of computing resolvent analysis since the matrix inversion and SVD are both $\mathcal{O}(n^3)$ operations. Because history effects from a streamwise varying β affect the turbulent statistics in a nonequilibrium APG TBL, the streamwise development needs to be accounted for, requiring $n = 4N_xN_y$ compared to a parallel flow assumption which can use $n = 4N_y$. To account for chemical nonequilibrium effects in high temperature air, the local analysis uses $n = 9N_y$ to account for 5 reacting species in mixture while the chemical equilibrium assumption uses $n = 5N_y$. As a result, the biglobal resolvent analysis is N_x^3 times as expensive as the local analysis while including the different gas species in a hypersonic TBL makes the operator at least 5 times as expensive as the single species calculations. Although the analyses already take advantage of sparse differentiation schemes, Arnoldi iterations, and efficient LU decompositions to avoid the explicit storage and calculation of the inverse, the calculations are still expensive, even requiring parallel architecture in a high performance computer for the biglobal case.

In this chapter, efficient methods to approximate the resolvent modes will be discussed along with a sampling algorithm that autonomously identifies the large amplification regions in the parameter space. The approximate methods could have been used in Chapters 3 and 4 to decrease the computation time of the large parameter sweeps. In Chapter 5, the adaptive search algorithm could have been applied to find and increase the resolution of regions in spectral space where the resolvent amplification differed the most, as opposed to distributing the samples equally.

The autonomous sampling uses ideas embedded in Bayesian Optimization (BO) to identify the most energetic regions of the parameter space. The main idea of this can be garnered by considering a real world example. Suppose an oil company has a suspicion that its land sits on a deposit of oil. The company wants to place a well where it is likely to retrieve the most oil. Because it costs money to drill, the

company is only willing to make as few holes as possible to sample the oil levels below. Since samples are limited, the company will need to figure out where to place the next samples in regions where it can learn the most (reduce the uncertainty) about the oil field topology while also finding the regions with the most oil. Although the underlying oil field topology may be smooth, gradient descent approaches to find the optimal placement are not applicable for this task since the true topology is unknown and samples are too sparse to calculate any gradients. Instead, this problem can be tackled with BO. BO is a black box method for identifying optimal parameters that develops a surrogate model with uncertainty using Gaussian Process Regression (GPR) from the sampled points. The next points to sample are determined based on an acquisition function which balances decreasing the uncertainty and finding the maxima of the surrogate model. Each subsequent sample improves the GPR and the prediction from BO.

In many ways, the oil well problem is similar to finding optimal parameters in resolvent analysis which lead to the largest amplification. As described earlier, calculating resolvent analysis for a new set of samples can be computationally expensive. Often times, because of scale separation in turbulent flows, there may be multiple regions in spectral space with different amplification mechanisms. In those cases, the interest is not to simply identify the largest amplification, but to sample the various local maxima of the amplification in the parameter space. In Gomez et al. (2022), a method denoted adaptive resolvent analysis (ARA) was described which uses BO to identify and sample the large amplification regions in high enthalpy TBL. This scheme, compared to a fixed-grid parameter search, was able to increase the resolution of the various large amplification regions. A description of that work is described in Section 6.2.

While the work in Gomez et al. (2022) described optimal ways of sampling the parameter space, the calculation of each sample can still be prohibitively expensive. In Barthel, Gomez, and McKeon (2022b), a method coined VRA was described which approximates resolvent modes using an inverse free approach. Using calculus of variations, an Euler-Lagrange equation can be derived that computes the resolvent modes and singular values as the eigenvectors and eigenvalues of the linearized Navier Stokes (LNS) operator, $\left(-i\omega + \widehat{\mathcal{L}}\right)$. This avoids the use of the resolvent operator, $\left(-i\omega + \widehat{\mathcal{L}}\right)^{-1}$. Describing the resolvent modes as a sum of r basis elements allows the eigenvalue problem to be projected onto an $r \times r$ matrix. More on this will be describe in Section 6.3.

While the VRA approach of Barthel, Gomez, and McKeon (2022b) leads to computational savings by avoiding any inversions, the LNS operator does not act as a directional amplifier like the resolvent operator. The resolvent operator amplifies responses in the direction of $\boldsymbol{\psi}_1$, since it has the largest gain, σ_1. On the other hand, the singular values of the LNS operator are $1/\sigma_j$, the reciprocal of the gains of the resolvent operator. As a result, the LNS operator amplifies in the direction of the highest order modes, $\boldsymbol{\phi}_n$, which are often spurious (Theofilis, 2011). To take advantage of the directional amplification of the resolvent operator, the ideas in Barthel, Gomez, and McKeon (2022b) are applied to the biglobal resolvent operator by using r basis elements to approximate the forcing modes. This leads to a projection of Equation 2.13 onto an $r \times r$ eigenvalue problem. This eigenvalue problem now does not require the use of an Arnoldi iteration to solve. This is described in 6.4.

In this chapter, Section 6.2 will first give a description of GPR and BO to then explain the ARA algorithm. Examples will be presented to show that the ARA can increase the resolution of the large amplification regions compared to an equispaced parameter search. In Section 6.3, the VRA approach will be described. Examples will be presented to show how the choice of basis functions affect the results. Section 6.4 will describe how an approximation for the forcing modes can lead to an Arnoldi-free algorithm for resolvent analysis. Conclusions will be presented at the end of the chapter.

6.2 Preliminaries for Bayesian Optimization

The ARA uses a modification of BO to sample the large amplification regions of the parameter space. BO builds a surrogate model with uncertainty by using a GPR. To describe ARA, these two topics will be succinctly described.

Gaussian Process Regression

A Gaussian Process is defined as a collection of random variables that have a joint Gaussian distribution. In GPR, it is assumed that there is a probability distribution over all possible functions. The samples of these functions act as the random variables and are jointly Gaussian distributed. The regression from the GPR is the mean function calculated from the probability of all possible functions, given the samples. The variance of this probability is the uncertainty in the regresssion. As more samples are included, the mean function and its uncertainty are updated.

A Gaussian Process assumes that the measurements $f(\mathbf{x})$ of samples $\mathbf{x}$ are specified by the mean function, $\mu_m(\mathbf{x})$, and covariance, $k(\mathbf{x}, \mathbf{x}')$, as

$$\begin{aligned} \mu_m(\mathbf{x}) &= \mathbb{E}[f(\mathbf{X})], \\ k(\mathbf{x}, \mathbf{x}') &= = \mathbb{E}[(f(\mathbf{X}) - \mu_m(\mathbf{x}))(f(\mathbf{X}') - \mu_m(\mathbf{x}'))], \end{aligned} \tag{6.1}$$

where $\mathbb{E}$ denotes the expectation of all possible measurements (Williams and Rasmussen, 2006). Thus, it is assumed that $f(\mathbf{x})$ is drawn from a joint Gaussian distribution with mean μ_m and covariance k. Per convention, μ_m is set to 0 such that the Gaussian Process is determined only by k, such that

$$f \sim \mathcal{N}(0, k), \tag{6.2}$$

where $\mathcal{N}$ denotes a normal distribution. Since the covariance is a symmetric function, k is described as a user-defined kernel function. k may depend on hyperparameters that specify its behavior. k describes how two points in the sample space, $\mathbf{x}$ and $\mathbf{x}'$, are correlated.

It is assumed that j samples, $\mathbf{X} = \left[\mathbf{x}_1, \ldots, \mathbf{x}_j\right]$, are used to make j measurements, $\mathbf{f} = \left[f(\mathbf{x}_1), \ldots, f\left(\mathbf{x}_j\right)\right]$ for the Gaussian Process f. The predicted measurements, $\mathbf{f}_*$, at samples, $\mathbf{X}_*$, are also defined. Since $\mathbf{f}$ and $\mathbf{f}_*$ form a Gaussian Processes, they form a joint Gaussian distribution,

$$\begin{bmatrix} \mathbf{f} \\ \mathbf{f}_* \end{bmatrix} \sim \mathcal{N}\left(\mathbf{0}, \begin{bmatrix} \mathbf{K}(\mathbf{X}, \mathbf{X}) + \epsilon_n^2 \mathbf{I} & \mathbf{K}(\mathbf{X}, \mathbf{X}_*) \\ \mathbf{K}(\mathbf{X}_*, \mathbf{X}) & \mathbf{K}(\mathbf{X}_*, \mathbf{X}_*) \end{bmatrix}\right), \tag{6.3}$$

where $\mathbf{K}(\mathbf{X}^i, \mathbf{X}^j)$ denotes a matrix formed with entries $K_{p,q} = k\left(\mathbf{x}_p^i, \mathbf{x}_q^j\right)$ and ϵ_n accounts for noisy measurements. The distribution in Equation 6.3 is the prior and includes no information from the observations. $\mathbf{f}_*$ is defined as the predicted measurement at samples $\mathbf{X}_*$ given the measurements $\mathbf{f}$ at samples $\mathbf{X}$. This can be quantified with the distribution conditioned on the observations,

$$\mathbf{f}_* | \mathbf{X}_*, \mathbf{X}, \mathbf{f} \sim \mathcal{N}(\mathbf{m}, \mathbf{\Sigma}), \tag{6.4}$$

where

$$\mathbf{m}(\mathbf{X}_*) = \mathbf{K}(\mathbf{X}_*, \mathbf{X})\left(\mathbf{K}(\mathbf{X}, \mathbf{X}) + \epsilon_n^2 \mathbf{I}\right)^{-1} \mathbf{f}, \tag{6.5}$$

$$\mathbf{\Sigma}(\mathbf{X}_*, \mathbf{X}_*) = \mathbf{K}(\mathbf{X}_*, \mathbf{X}_*) - \mathbf{K}(\mathbf{X}_*, \mathbf{X})\left(\mathbf{X}(\mathbf{X}, \mathbf{X}) + \epsilon_n^2 \mathbf{I}\right)^{-1} \mathbf{K}(\mathbf{X}, \mathbf{X}_*). \tag{6.6}$$

More details on this derivation are available in Williams and Rasmussen (2006). $\mathbf{m}\left(\mathbf{X}_*\right)$ is the GPR of the data, $(\mathbf{X}, \mathbf{f})$, and serves as the prediction, $\mathbf{f}_*$, at samples

$\mathbf{X}_*$. $\mathbf{\Sigma}(\mathbf{X}_*, \mathbf{X}_*)$ is the covariance matrix around $\mathbf{m}(\mathbf{X}_*)$. The uncertainty, $\mathbf{s}(\mathbf{X}_*)$, is then the diagonal of $\mathbf{\Sigma}(\mathbf{X}_*, \mathbf{X}_*)$. $\mathbf{m}$ and $\mathbf{s}$ are vectors organized as $\mathbf{m}(\mathbf{X}_*) = \left[m\left(\mathbf{x}_{*,1}\right), \ldots, m\left(\mathbf{x}_{*,n_p}\right)\right]$ and $\mathbf{s}(\mathbf{X}_*) = \left[s\left(\mathbf{x}_{*,1}\right), \ldots, s\left(\mathbf{x}_{*,n_p}\right)\right]$, where m and s are scalars and n_p is the number of vectors in $\mathbf{X}_*$. If $\epsilon_n = 0$, then $s(x_i) = 0$ and $m(x_i) = f(x_i)$ for every sampled point, x_i.

Although ϵ_n is used to account for noise, here it is used as a regularizer to invert the covariance matrices and serves as an external parameter (Eriksson et al., 2018). The GPR depends on the choice of k and its hyperparameters as well. Here, given a choice of kernel function, its hyperparameters, θ_{hyp}, and ϵ_n are determined as the values that maximize the log-marginal likelihood,

$$\begin{aligned}\log\left(p(\mathbf{f}|\mathbf{X}, \theta_{hyp}, \epsilon_n)\right) = -\frac{1}{2}\Bigg[\mathbf{f}^T\left(\mathbf{K}(\mathbf{X}, \mathbf{X}; \theta_{hyp}) + \epsilon_n^2\mathbf{I}\right)^{-1}\mathbf{f} \\ + \log\left(\det\left(\mathbf{K}(\mathbf{X}, \mathbf{X}; \theta_{hyp}) + \epsilon_n^2\mathbf{I}\right)\right) + j\log(2\pi)\Bigg],\end{aligned} \tag{6.7}$$

over θ and ϵ_n (Williams and Rasmussen, 2006; Eriksson et al., 2018). Here, j is the number of samples. The only modeling choice that enters the GPR used here is the choice of kernel function.

The code used for GPR uses an adapted version of the code described in Eriksson et al. (2018), though their extension using the derivatives of the observations is not used. In Gomez et al. (2022), the derivative approach was used to apply GPR in two separate regions— the relatively subsonic and the relatively supersonic regions. The two separate regions were used because the derivatives are ill-defined at the sonic line and the radial basis function could not properly model the discontinuity. Here, a Matérn $3/2$ kernel is used as a kernel function instead as it can resolve sharp features. This allows for the application of a single GPR across the entire spectral space, requiring no *a priori* knowledge of any discontinuities.

Bayesian Optimization

BO uses GPR to create a surrogate model from the measurements with uncertainties and identifies the next point to sample via an acquisition function. Since it does not require any *a priori* knowledge of the function being optimized, BO is commonly used as a black-box method for optimizing functions that are expensive to compute (Huhn and Magri, 2022).

BO begins by making a few measurements, $\mathbf{f}$, at samples, $\mathbf{X}$. These samples and measurements are then used to calculate the surrogate model, m, and uncertainty, s,

from Equation 6.5 and the diagonal of Equation 6.6, respectively. The next sample point is the maxima of an acquisition function, $a = a(m, s)$, designed to balance exploration and exploitation. Exploration looks for regions of large uncertainty, so a needs to be large when s is large. Exploitation looks for the largest predicted values from the surrogate model. Exploitation requires that a is large when m is large. A description of commonly used acquisition functions in BO can be found in Williams and Rasmussen (2006) and Huhn and Magri (2022). These acquisition functions are not used for the ARA since they focus on identifying the optimal maxima as opposed to sampling several local maxima. With each new sample, $\mathbf{x}_{new}$, a new measurement $f(\mathbf{x}_{new})$ is made as well. These values update $\mathbf{f}$ and $\mathbf{X}$ which then update m and s. With each subsequent sample, the surrogate model improves at modeling f. These steps are repeated until a convergence criterion or desired total number of samples has been met.

Adaptive Resolvent Analysis

Here, the ARA algorithm is described and applied to the high enthalpy TBL using a mixture of ideal gases in chemical nonequilibrium from Section 5.6[1]. The analysis considers k_x and k_z as parameters, given a constant wavespeed, c. c is fixed as $\overline{U}(y^+ \approx 40)$ as in Section 5.6. The analysis can consider any combination of the three parameters, but here, the focus is only on the length scales. The BO is applied to the logarithm of the premultiplied singular values,

$$g(k_x, k_z) = \log_{10}(\sigma_1^2(k_x, k_z, c)k_x k_z). \tag{6.8}$$

The use of the logarithm is two-fold. First, the singular values span several orders of magnitude, which can strain the regressions. The logarithm is able to regularize this issue. Second, while $\sigma_1 \geq 0$, the GPR is not constrained to predict non-negative surrogate models. Since g can be positive and negative, the GPR does not need to be restricted. Since σ_1^2 peaks for the largest length scales, the premultiplied $\sigma_1^2 k_x k_z$ is used to also capture amplification from the smallest length scales. Since the length scales of interest can span several orders of magnitude, the BO is applied in log-space, such that the parameters are $\mathbf{x} = \left[\log_{10}(k_x), \log_{10}(k_z)\right]$.

The acquisition function is defined as

$$a(m, s) = (m - \min(m))s^\alpha + \kappa s, \tag{6.9}$$

[1]This work first appeared in Gomez et al. (2022). S. R. G. provided the formulation for the ARA and developed the hypersonic resolvent schemes. That work has been adapted and reworked into this section. Fruitful discussions and contributions from the coauthors are gratefully acknowledged.

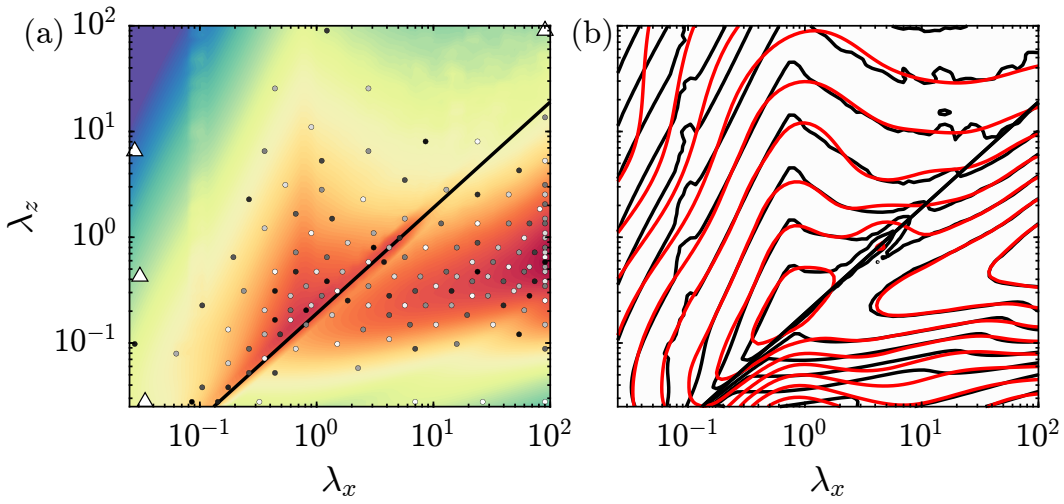

Figure 6.1: $\sigma_1^2 k_x k_z$ for a TBL in chemical nonequilibrium using the same parameters as in Figure 5.25 with the initial samples (triangles) and the samples found using ARA (circles) (a). The order of the identified samples is color coded, beginning with white and ending with black. $\sigma_1^2 k_x k_z$ (black contours) and 10^{m_e} (red contours) where the contour values are $10^{.5}, 10^1, \ldots, 10^6$ (b).

where $\kappa > 0$ and α are used to tune exploration and exploitation. A larger value of κ encourages exploration by weighing s more than m. The value of α is used to influence the neighborhood near the samples where $s \ll 1$. Here, $\alpha = .3$ and $\kappa = .5$. In the first term, m is offset by $\min(m)$ to ensure that $a \geq 0$ and s is set to 0 at sampled points manually so that new points are always sampled.

The discontinuity in σ_1 at the sonic line causes issues when performing regressions across the entire space. The Matérn 3/2 kernel is used to better resolve the discontinuity since it can resolve sharp features (Huhn and Magri, 2022). The Matérn 3/2 kernel is

$$k(\mathbf{x}, \mathbf{x}'; A, \ell) = A\left(1 + \frac{\sqrt{3}}{\ell}\|\mathbf{x} - \mathbf{x}'\|\right)\exp\left(-\frac{\sqrt{3}}{\ell}\|\mathbf{x} - \mathbf{x}'\|\right), \tag{6.10}$$

where A and ℓ are hyperparameters that are determined by maximizing the log-marginal likelihood and $\|\cdot\|$ denotes the Euclidean distance.

Adaptive Resolvent Analysis Results

The same parameters used in Figure 5.25 for the TBL in chemical nonequilibrium are used to compare the results of the ARA. The ARA is initialized with the four points, labeled by triangles in Figure 6.1(a). The ARA identified 148 points to sample, labeled by the grey circles. Although the ARA is initialized with points in the

low amplification regions in the outskirts of the plot, the ARA identifies the largest amplification within a few iterations. The points are all clustered in the regions with largest amplification, with sparse measurements in the low amplification regions. As the large amplification region becomes over sampled, the scheme switches to exploration, noted by the few dark-grey circles in the low-amplification supersonic regions with $\lambda_z > 10$. In Figure 6.1(b), $\sigma_1^2 k_x k_z$ from the full sweep is compared with 10^{m_e}, where m_e is the surrogate model of g based on the 148 samples. $\sigma_1^2 k_x k_z$ and m_e are evaluated at the same k_x and k_z. The large amplification regions overlap well with the surrogate model. The low amplification regions, like the supersonic region with $(\lambda_x \leq 1, \lambda_z \geq 1)$ and subsonic region with $(\lambda_x \leq 10, \lambda_z \leq 0.1)$, are poorly represented with the surrogate model due to limited samples. The GPR assumes that g is continuous so the contours are closed across the sonic line. This limits the modeling of fine features near the sonic line. Nonetheless, the surrogate model is able to represent the large amplification regions well.

To compare a practical use of ARA, a comparison is made with 49 samples from the ARA scheme and 49 equispaced samples. An initial coarse sampling with 12 points is made and the ARA is used to increase the resolution of the large amplification regions. The comparison is done by using the same `scatteredInterpolant` function on MATLAB® with a continuous linear interpolation for the two sets of samples. The interpolant only matches the data at the sampled points and is computed similarly to how the contours are plotted in MATLAB® on an equispaced, regular grid. The interpolants are plotted in Figures 6.2(b,d). Using the ARA, the remaining samples can be concentrated in the large amplification regions. This improves the interpolation in those regions. Using the equispaced sampling leads to less resolution in the regions of interest, causing the large amplifications to be poorly reconstructed with the samples.

Figure 6.2 illustrates a use for ARA when computational resources are limited. By applying ARA, the resolution increases in the large amplification regions. The interpolation using these values can provide a clearer picture of the large amplification regions compared to using a simple equispaced sampling of the parameter space. It is noted that although the ARA was designed to find optimal points to sample in spectral space for resolvent analysis, the scheme can easily be adjusted and applied to other sampling needs. Any BO algorithm can simply replace the acquisition function with Equation 6.9 to convert the algorithm into a sampling algorithm.

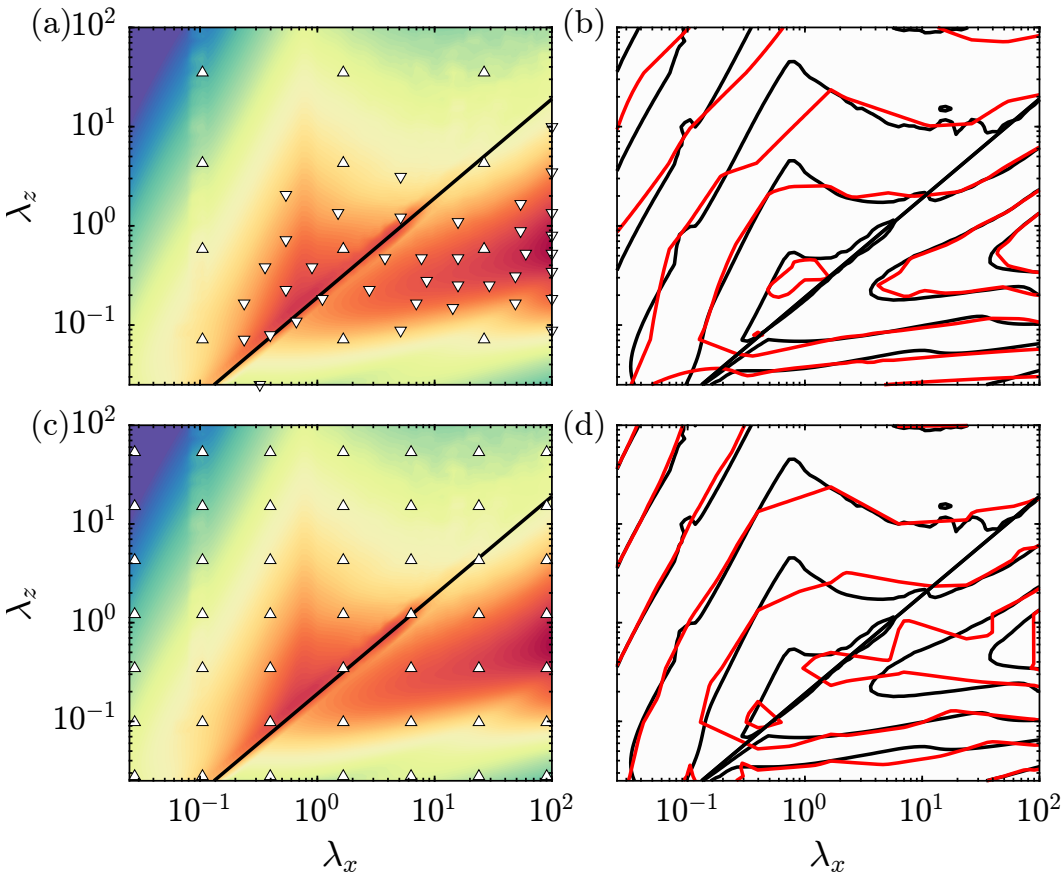

Figure 6.2: The same contours from Figure 6.1 are plotted in (a) and (c). In (a), the upside down triangles denote the points found from the ARA, while the rest denote the initial points. In (c), the triangles denote the sample points, all equispaced. $\sigma_1^2 k_x k_z$ (black contours) is compared with interpolations (red contours) from the ARA samples in (b) and the equispaced samples in (d). The contours are taken at 10^1, 10^2, 10^3, 10^4, 10^5, $10^{5.5}$.

6.3 Variational Resolvent Analysis

The main computational bottleneck with resolvent analysis is dealing with an operator inverse required to create the resolvent operator, $\mathcal{H}$. In practice, the direct calculation and storage of an inverse can be avoided by computing an LU decomposition of the LNS operator, $\mathcal{A}$. The action of $\mathcal{H}$ is then replaced with back-substitution using the LU factors of $\mathcal{A}$, as described in Appendix A (Jeun, Nichols, and Jovanović, 2016; Sipp and Marquet, 2013; Schmidt et al., 2018). Another approach that avoided the direct storage of $\mathcal{H}$ is the work of Ribeiro, Yeh, and Taira (2020), who used back-substitution with $\mathcal{A}$ on a small subset of vectors to sketch $\mathcal{H}$. These strategies reduce the computational cost as $\mathcal{H}$ is never explicitly formed, though the cost of this strategy is the overall cost of an LU decomposition. Other approaches

that avoid the direct calculation of $\mathcal{H}$ are the "matrix-free" approach of Martini et al. (2021) that approximates the action of $\mathcal{H}$ through the transient and steady state responses of the periodically forced linearized system and its corresponding adjoint system. The computational cost of this approach is $O(n)$, though it requires time-integration of the linearized systems. Through different means, the methods described all use different strategies to approximate the action of $\mathcal{H}$ to solve the eigenvalue problem in Equation 2.12. The VRA approach of Barthel, Gomez, and McKeon (2022b), never uses $\mathcal{H}$ as the approach only considers $\mathcal{A}$ in Equation 2.22.

Here, the VRA approach described in Barthel, Gomez, and McKeon (2022b) will first be derived and applied to the Ginzburg-Landau equation and the biglobal resolvent modes. Discussions will be presented to illustrate the effect of the modeling basis on the VRA approximations.[2]

Derivation of the Variational Resolvent Analysis Approach

While resolvent analysis searches for the largest resolvent amplification, mathematically, one can equivalently search for the smallest amplification from the LNS operator (Barthel, Gomez, and McKeon, 2022b). Numerically, this search is ill-conditioned (Saad, 2011; Theofilis, 2011). In Section 2.21, it was shown that the minimum of the cost functional in Equation 2.21,

$$\begin{aligned}\mathcal{J}_m(\mathbf{q}) &= \|\mathcal{A}\mathbf{q}\|_f - \lambda^2\|\mathbf{q}\|_r \\ &= \left\langle \mathbf{q}, \mathcal{A}^\dagger \mathcal{W}_f \mathcal{A}\mathbf{q}\right\rangle - \lambda^2 \left\langle \mathbf{q}, \mathcal{W}_r \mathbf{q}\right\rangle ,\end{aligned} \tag{6.11}$$

is found by the Euler-Lagrange equations described in Equation 2.22,

$$\mathcal{A}^\dagger \mathcal{W}_f \mathcal{A}\boldsymbol{\psi}_i = \lambda_i^2 \mathcal{W}_r \boldsymbol{\psi}_i. \tag{6.12}$$

Since $\mathcal{A}^\dagger\mathcal{W}_f\mathcal{A}$ and $\mathcal{W}_r$ are normal operators, $\lambda_i^2 \geq 0$ and $\boldsymbol{\psi}_i$ are orthonormal with respect to the inner product $\langle\cdot,\cdot\rangle_r$. The index i is ordered in ascending order for λ_i such that $\lambda_i \leq \lambda_{i+1}$. By multiplying both sides of Equation 6.11 by $\mathcal{A}^\dagger\mathcal{W}_f\mathcal{A} = \mathcal{H}\mathcal{W}_f^{-1}\mathcal{H}^\dagger$, one can show using Equation 2.17 that the eigenvectors, $\boldsymbol{\psi}_i$, and reciprocals of the eigenvalues, λ_i^{-1}, are the response modes and singular

[2]The idea for VRA first appeared in Barthel, Gomez, and McKeon (2022b), while the ideas for an optimal modeling basis were investigated in Barthel, Gomez, and McKeon (2022a) to explain the discrepancies in the nonperiodic biglobal resolvent modes using a periodic basis. In Barthel, Gomez, and McKeon (2022a), S. R. G. developed the example for the choice of basis on the Ginzburg-Landau system. In this section, S. R. G. applied the nonperiodic basis to the nonperiodic biglobal resolvent modes. Contributions from the coauthors are greatly appreciated, especially Benedikt Barthel who first created the VRA approach and subsequent comment and discussions.

values of $\mathcal{H}$, respectively. The forcing modes of $\mathcal{H}$ are computed by inverting Equation 2.15 such that

$$\mathcal{A}\boldsymbol{\psi}_i = \sigma_i^{-1}\boldsymbol{\phi}_i. \tag{6.13}$$

Unlike Equation 2.13, the eigenvalue problem in Equation 6.12 does not involve any operator inverses since it does not require $\mathcal{H}$.

This approach is, mathematically, an equivalent representation for resolvent analysis without the use of inverse operations. To compare with resolvent analysis, one needs to find the smallest eigenvalues in Equation 6.12. In practice, this is a difficult problem as many Krylov-space methods to approximate eigenvalues, like the Arnoldi iteration, can converge quickly to the largest eigenvalues, while the smallest eigenvalues are the last to converge. To find the smallest eigenvalues using Krylov-space methods, the matrix, $\mathbf{M}$, and its eigenvalues, p_i, are transformed into $\widetilde{\mathbf{M}}$ and $\widetilde{p}_i$ such that the smallest eigenvalues become the largest. This can be done with shift-and-invert such that $\widetilde{M} = \mathbf{M}^{-1}$ which makes $\widetilde{p}_i = p_i^{-1}$ (Saad, 2011). Arnoldi iteration is then done on $\widetilde{M}$ and the identified eigenvalues are then transformed back to recover the smallest p_i. Thus, to compute the eigenvalues of interest in Equation 6.12, a $n \times n$ matrix inverse is required which removes any of its computational advantages.

To circumvent this limitation, Barthel, Gomez, and McKeon (2022b) considers a projection of Equation 6.12 onto a set of basis elements. The basis elements have physical properties characteristic of the underlying physics in $\mathcal{A}$. For example, the examples using biglobal resolvent analysis in Barthel, Gomez, and McKeon (2022b) used basis elements from a local resolvent approach, which are much cheaper to compute, while Schmid and Henningson (2002) considered the largest transient growth of $\mathcal{A}$ through a projection onto its eigenmodes. The projection removes the influence of the spurious eigenvectors associated with large eigenvalues as they are removed from the span of the projected matrices (Theofilis, 2011). The underlying projected system is then expected to only retain a span representative of the underlying physical mechanisms.

To explain this projection, consider Equation 2.21 for a vector defined as the sum of known basis functions, $\mathbf{b}_i$, with coefficients a_i as

$$\mathbf{q} = \sum_{i=1}^{r} a_i \mathbf{b}_i = \mathbf{B}\mathbf{a}, \tag{6.14}$$

where $\mathbf{B} = [\mathbf{b}_1, \mathbf{b}_2, \ldots, \mathbf{b}_r] \in \mathbb{C}^{n\times r}$ and $\mathbf{a} = [a_1, a_2, \ldots, a_r]^T \in \mathbb{C}^{r\times 1}$. Determining $\mathbf{q}$ requires the determination of its coefficient vector $\mathbf{a}$. Rewriting Equation 2.21 with $\mathbf{q}$ gives

$$\begin{aligned}\mathcal{J}_m(\mathbf{Ba}) &= \|\mathcal{A}\mathbf{Ba}\|_f - \lambda^2\|\mathbf{Ba}\|_r \\ &= \left\langle \mathcal{A}\mathbf{Ba}, \mathcal{W}_f\mathcal{A}\mathbf{Ba}\right\rangle - \lambda^2 \left\langle \mathbf{Ba}, \mathcal{W}_r\mathbf{Ba}\right\rangle \\ &= \left\langle \mathbf{a}, (\mathcal{A}\mathbf{B})^*\mathcal{W}_f\mathcal{A}\mathbf{Ba}\right\rangle - \lambda^2 \left\langle \mathbf{a}, \mathbf{B}^*\mathcal{W}_r\mathbf{Ba}\right\rangle .\end{aligned} \tag{6.15}$$

To find $\mathbf{a}$ that minimizes $\mathcal{J}_m(\mathbf{Ba})$, the stationary points must be found as

$$\frac{d\mathcal{J}_m(\mathbf{Ba} + \epsilon\mathbf{Bh})}{d\epsilon} = 2\Re\left\{\left\langle \mathbf{h}, (\mathcal{A}\mathbf{B})^*\mathcal{W}_f\mathcal{A}\mathbf{Ba}\right\rangle - \lambda^2 \left\langle \mathbf{a}, \mathbf{B}^*\mathcal{W}_r\mathbf{Ba}\right\rangle\right\} = 0. \tag{6.16}$$

Since Equation 6.16 must hold for any $\mathbf{h}$, the Euler-Lagrange equation becomes the eigenvalue problem,

$$(\mathcal{A}\mathbf{B})^*\mathcal{W}_f\mathcal{A}\mathbf{Ba}_i = \mathbf{Qa}_i = \widetilde{\lambda}_i^2\mathbf{B}^*\mathcal{W}_r\mathbf{Ba}_i = \widetilde{\lambda}_i^2\mathbf{Da}_i. \tag{6.17}$$

The $r \times r$ matrices $\mathbf{Q}$ and $\mathbf{D}$ are projections of the operators $\mathcal{A}^\dagger\mathcal{W}_f\mathcal{A}$ and $\mathcal{W}_r$ onto the basis $\mathbf{b}_i$. $\mathbf{Q}$ is also independent of an adjoint operator. Since $\mathbf{Q}$ and $\mathbf{D}$ are Hermitian matrices, Equation 6.17 produces r nonnegative eigenvalues, $\widetilde{\lambda}_i^2$, such that $\widetilde{\lambda}_i \leq \widetilde{\lambda}_{i+1}$. The eigenvectors, $\mathbf{a}_i$ are also orthogonal such that

$$\mathbf{a}_i^*\mathbf{Da}_j = \delta_{ij}, \tag{6.18}$$

where δ_{ij} is the Kroenecker delta. The eigenvectors $\mathbf{a}_i$ are coefficients that optimally approximate $\boldsymbol{\psi}_i$ in the basis $\mathbf{B}$ while the eigenvalues $\widetilde{\lambda}_i^{-1}$ approximate σ_i. The response modes are then

$$\boldsymbol{\psi}_i = \mathbf{Ba}_i. \tag{6.19}$$

Due to Equation 6.18, $\boldsymbol{\psi}_i$ are orthonormal with respect to the inner product $\langle\cdot,\cdot\rangle_r$. By suitably choosing the basis vectors, the projection can identify the amplification mechanisms present in the optimal modes as opposed to spurious behavior in the higher order modes.

Using the approximation for σ_i and $\boldsymbol{\psi}_i$, the forcing modes can be approximated by using Equation 6.13. This was done in Barthel, Gomez, and McKeon (2022b), though it was shown to amplify errors in the approximation of $\boldsymbol{\phi}_i$. This occurs because $\mathcal{A}$ amplifies the higher order modes, as opposed to the optimal modes. This can be seen by the σ_i^{-1} on the right hand side of Equation 6.13.

The necessary r depends on both the efficiency of the model basis and the desired level of accuracy. The derivation does not include any approximations, so if the input

basis is complete, the VRA approximation will converge to the solution computed via an SVD as $r \to \infty$. However, it is desired that r is sufficiently small compared to the number of degrees of freedom in the discretized system, n. If $r \sim O(n)$, it is preferential to use the standard resolvent approach because the eigenvalue problem numerically scales as $O(r)^3$. For the examples described here, r is at several orders of magnitude smaller than n, so computing Equation 6.17 can take seconds.

The approximation in the VRA method is dependent on the choice of basis and r. However, one may not know *a priori* what the optimal basis is nor the r required for satisfactory convergence. In Barthel, Gomez, and McKeon (2022b), this effect was manifest in the modeling of the ZPG TBL resolvent modes. In that study, streamwise-periodic local resolvent modes were used as a modeling basis for biglobal resolvent modes in a ZPG TBL. It was found that the modes closest to the wall could be optimally represented by the modeling basis. Modes further from the wall in the wake, subject to non-periodic effects like the convective non-normality and nonparallel effects from the streamwise evolving flow, lead to poor approximations of the resolvent modes.

Application to the Ginzburg-Landau Equation

To investigate the effects of using a modeling basis that sub-optimally represents the leading response modes, VRA is applied to the simple linear Ginzburg-Landau (GL) equation studied in Bagheri et al., 2009. Here, the GL operator is

$$\mathcal{A} = \left(-i\omega + \widehat{\mathcal{L}}\right) = -i\omega - \nu\partial_x + \gamma\partial_{xx} + \left(\mu_0 - c_\mu^2\right) + \frac{\mu_2}{2}x^2 \tag{6.20}$$

and the resolvent operator is $\mathcal{H} = \mathcal{A}^{-1}$ for $x \in \mathbb{R}$. The coefficients ν, γ, μ_0, and c_μ are chosen to be the same as in Bagheri et al., 2009. Here, ω is set to 2 and μ_2 is -0.01. Finally, the standard inner product over $\mathbb{R}$ is chosen such that

$$\langle a, b\rangle_x = \int_{-\infty}^{\infty} a^*(x)b(x)dx, \tag{6.21}$$

meaning that $\mathcal{W}_r = \mathcal{W}_f = \mathcal{I}$.

Cossu and Chomaz (1997) note that the GL operator has many of the hallmarks seen in the LNS operator. The $-i\omega - \nu\partial_x$ term provides a convective non-normality, parameterized by ν, $\gamma\partial_{xx}$ provides viscous dissipation, and $\mu_2 x^2/2$ provides non-parallel effects. By increasing μ_2, the nonparallel term can be made stronger. The nonparallel term behaves like a potential well, which encourages amplified modes

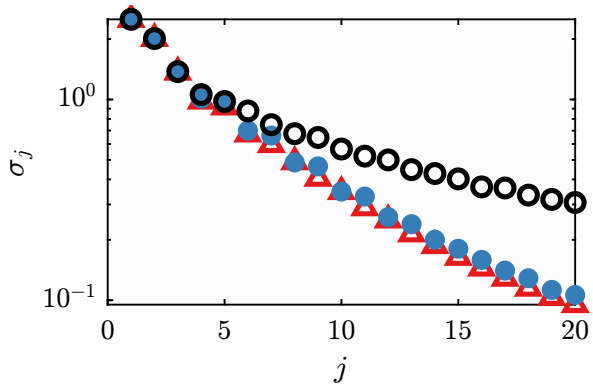

Figure 6.3: Comparison of σ_j using 23 basis elements for the GL system. The red triangles and blue filled circles are the VRA approximated singular values using the Gaussian and Fourier bases, respectively. The black open circles are the singular values computed using the SVD. Note the logarithmic scale in the y axis.

to have the most support near $x = 0$, where the potential well is weakest. This term causes modes to decay in the far field.

$\mathcal{A}$ is discretized into the matrix, $\mathbf{A}$, with a fourth-order, equispaced, SBP scheme (Mattsson and Nordström, 2004) for $x \in [-L, L]$ using $n = 1920$ points using Dirichlet boundary conditions at $|x| = L$. A trapezoidal scheme is used to create the diagonal matrix, $\mathbf{W}$. The matrix inverse and its SVD are computed using the built in functions, `mldivide` and `svd` on MATLAB®.

To investigate the role of the boundary conditions, the VRA is computed with two different modeling bases. The first set of basis elements are created with Gaussians, centered at different locations, to model the effect of a compact basis set. The basis is defined as

$$\mathbf{b}_j^G(x;r) = \frac{1}{\sqrt{2\pi\sigma_r^2}} \exp\left(\frac{(x - x_{r,j})^2}{2\sigma_r^2}\right), \tag{6.22}$$

where r denotes the number of basis elements. Here, $\sigma_r = \frac{2L}{.675r}$ and $x_{r,h} = \frac{2L}{r} j - L$, so that the width and location of the Gaussians depend on the number of basis elements. The second set of basis elements uses a noncompact modeling basis in the form of Fourier modes such that

$$\mathbf{b}_j^F(x;r) = \frac{1}{\sqrt{L}} \exp\left(\frac{2\pi i}{L} jx\right). \tag{6.23}$$

The Fourier basis is similar to the basis set chosen in Barthel, Gomez, and McKeon (2022b).

In Figures 6.3 and 6.4, the resolvent modes and σ_j computed with VRA the two bases using $r = 23$ are compared to those computed with the SVD. The σ_j show

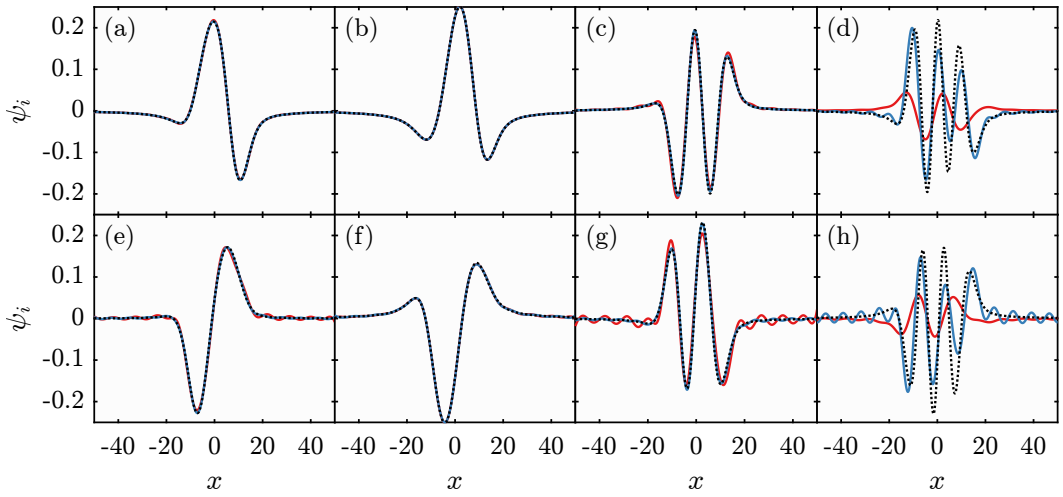

Figure 6.4: Comparison of the real parts of ψ_i (a-d) and ϕ_i (e-f) using 23 basis elements for the GL system. i increases from 1 to 4 from left to right. The red and blue lines are the VRA approximated modes using the Gaussian and Fourier bases, respectively. The black dotted lines are the modes computed from the SVD.

excellent agreement for the first three σ_j, with the approximation deteriorating as j increases. The same is true for ψ_j. Using the Fourier basis leads to worse agreement in ψ_4 than using the Gaussian basis. In the forcing modes, the discrepancies are amplified due to $\mathcal{A}$ directionally amplifying the errors in the approximations. This issue becomes most apparent in ϕ_1 and ϕ_3 using the Fourier basis. The ϕ_4 mode is approximated poorly using the two approaches because of the error in ψ_4. Despite the issues in the higher order modes, the leading modes and amplifications were captured well by using only 23 basis elements.

The convergence of the singular values, response modes, and forcing modes is plotted in Figure 6.5. The error in the singular values is defined as $e_{\sigma,j} = |\sigma_j^S - \sigma_j^V|$, and the error in the forcing modes and response modes is defined as $e_{\phi,j} = ||\phi_j - \tilde{\phi}_j||$ and $e_{\psi,j} = ||\psi_j - \tilde{\psi}_j||$, respectively. The superscript S and V denote if the quantity was computed using the SVD or VRA. For the Gaussian basis, the $e_{\sigma,j}$ and $e_{\psi,j}$ decreases initially, then plateaus for large r. This is similar for $e_{\phi,j}$, except that the error begins to increase. For the Fourier basis, the error continues to decrease as r increases. When r becomes large, the error in the Fourier basis scales as $e_{\sigma,j} \sim O(r^{-1})$, $e_{\psi,j} \sim O(r^{-2})$, and $e_{\phi,j} \sim O(r^{-1})$. In all the cases plotted here, $e_{\phi,j} > e_{\psi,j}$.

The Gaussian basis converges quicker than the Fourier basis because the Fourier basis is not compact whereas the resolvent modes of the Ginzburg Landau operator

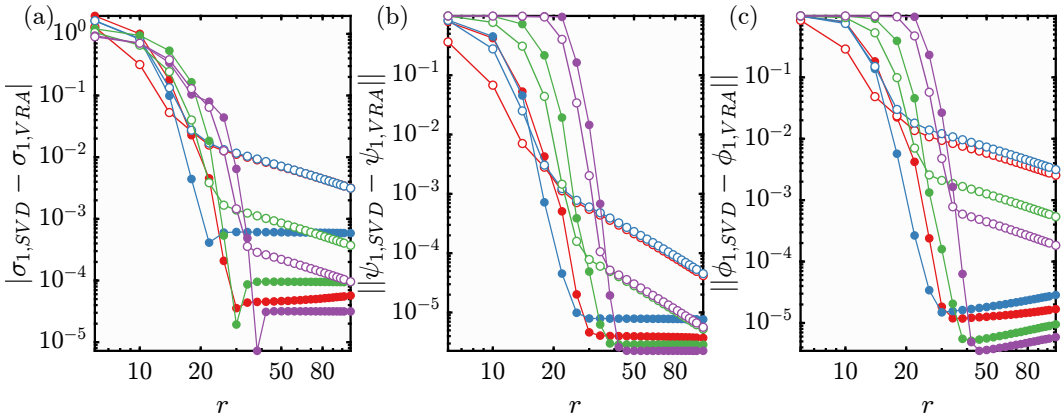

Figure 6.5: The error in the VRA approximations for σ_j (a), ψ_j (b), and ϕ_j (c) relative to the SVD computed modes as r increases. The open circles denote the error using the Fourier basis while the closed circles are the error with the Gaussian basis. The red, blue, green, and purple lines denote $i = 1$, 2, 3, and 4. The black dashed lines are proportional to r^{-1} in (a,c) and proportional to r^{-2} in (b).

are. To resolve the discrepancy, more Fourier modes are required. This is similar to resolving a spatially localized bump with a Fourier series. The Gaussian basis does not have this limitation and it is better able to resolve the spatially compact modes. The plateau in the Gaussian basis likely occurs because the basis elements $\mathbf{b}_j^G(x;r)$ become narrower as r increases, making the basis elements themselves difficult to differentiate. Since the boundary conditions are homogeneous, it is expected that the Fourier basis can eventually completely resolve the mode shapes.

Effect of Basis on VRA Approximation in ZPG TBL

VRA is now applied to a ZPG TBL and two different resolvent modes are considered—one representative of small near-wall structures and the other representative of large scale structures. The basis elements will differ from those used in Barthel, Gomez, and McKeon (2022b). The wall-normal variation of the basis elements will be computed from the local resolvent modes, $\boldsymbol{\psi}_i^{1D}(y;c_j,k_z,\omega)$. The k_z and ω are the same used as those used in the biglobal resolvent modes while c_j are N_c equispaced wavespeeds between c_{min} and c_{max}. The c_j define the streamwise wavenumbers, $k_{x,j} = \omega/c_j$, so that $k_{x,j}$ is dependent on ω. For each c_j, the first N_j resolvent modes are retained so that $r = N_j N_c$. The streamwise structure will nominally be wave-like with a streamwise wavenumber $k_{x,j}$, though nonperiodic features will be incorporated. In Barthel, Gomez, and McKeon (2022b), the basis elements were periodic local resolvent modes, $\boldsymbol{\psi}_i^{1D}(y;c_j,k_z,c_j k_{x,l})\exp\left(\sqrt{-1}k_{x,j}x\right)$, param-

λ_z^+	ω^+	N_x	L	(c_{min}^+, c_{max}^+)	N_c	N_j	r	$n = 4N_xN_y$
100	$2\pi/100$	300	4.5	$(10, 18)$	10	2	20	301250
1537	244	600	20	$(14.75, 25)$	20	9	180	602400

Table 6.1: The computational parameters for the two modes studied here. These modes both use $y_{min} = .24$, $y_{max} = 3.5$, $N_y = 251$, and $\epsilon_s = 30$. The parameters c_{min}^+, c_{max}^+, N_c, N_j, and r are parameters used to define the local mode basis.

eterized with N_{k_x} streamwise wavenumbers, N_c wavespeeds, and N_j sub-optimal modes such that $r = N_{k_x}N_cN_j$. The temporal frequency of the basis modes is different than the temporal frequency of the biglobal modes in that study.

To provide the streamwise structure for the basis elements, two approaches are used. The first allows for streamwise periodicity such that

$$\mathbf{b}_{i+j}^p(x, y) = \boldsymbol{\psi}_i^{1D}(y; c_j k_z, \omega) e^{ik_{x,j}x}. \tag{6.24}$$

The second basis relaxes the streamwise periodicity by allowing for streamwise variation to account for the convective non-normality. The amplitude of these basis elements is augmented so that it increase downstream, starting from 0, to mimic this effect. The nonperiodic basis, $\mathbf{b}_i^n$ is defined as

$$\begin{aligned}
b_{i+j,u}^n(x, y) &= \psi_{i,u}^{1D}(y; c_j k_z, \omega) e^{ik_{x,j}x} f(x) \\
b_{i+j,v}^n(x, y) &= \psi_{i,v}^{1D}(y; c_j k_z, \omega) e^{ik_{x,j}x} f(x) \\
b_{i+j,w}^n(x, y) &= \frac{\sqrt{-1}}{k_z} \frac{\partial b_{i+j,u}^n(x, y)}{\partial x} + \frac{\partial b_{i+j,v}^n(x, y)}{\partial y} \\
b_{i+j,p}^n(x, y) &= \psi_{i,p}^{1D}(y; c_j k_z, \omega) e^{ik_{x,j}x} f(x),
\end{aligned} \tag{6.25}$$

where

$$f(x) = \left(\frac{1 - \exp(-25x/L)}{1 - \exp(-25)} \right)^2, \tag{6.26}$$

creates the nonperiodic structure. The spanwise component of the basis elements, $\mathbf{b}_i^n$, is chosen so the basis elements remain divergence-free. The periodic basis does not need to account for this since the local resolvent modes are divergence free. Since $\mathcal{A}$ assumes that the response and forcing modes are 0 at the inlet and outlet, both sets of basis elements are manually set to be 0 at the inlet and outlet. This ensures that any $\mathbf{q}$ defined as a sum of the basis elements satisfies the correct boundary conditions.

The ZPG TBL is interpolated from the LES of Eitel-Amor, Örlü, and Schlatter (2014). The outlet of each domain is used to compute the reference length scales,

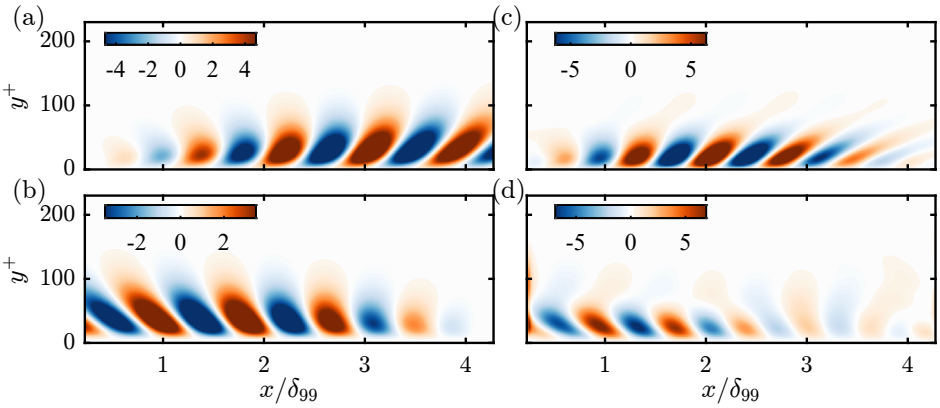

Figure 6.6: Real part of $\psi^S_{u,1}$ (a), $\psi^V_{u,1}$ (c), $\phi^S_{v,1}$ (b), $\phi^V_{v,1}$ (d) using $\lambda_z^+ = 100$. The VRA modes use $\mathbf{b}_i^p$ as the basis.

δ_{99} and ℓ_ν, and velocity scales, U_∞ and u_τ, used to nondimensionalize the problem. At the outlet, each domain has a $Re_\tau = 1537$. The local resolvent modes in the basis elements are computed with the outlet streamwise velocity profile, $\overline{\mathbf{U}}(y) = \overline{U}(L, y)$. The small scale mode uses $\lambda_z^+ = 100$ and $\omega^+ = 2\pi/100$, like the modes plotted in Figure 3.6. The large scale mode uses $\lambda_z = 1$ and $\omega = 1.5$. The parameters used to compute the modes are described in Table 6.1, including their parameters for the VRA.

The resolvent modes and singular values computed with the standard resolvent approach described in Chapter 2 are denoted with an S superscript while those computed using VRA have a V superscript. First, the effect of the periodic basis, $\mathbf{b}_i^p$ on the VRA approximations is shown in Figure 6.6. Here, the periodic basis does a poor job at representing the near-wall mode. Although the periodic basis was able to approximate a similar mode in Barthel, Gomez, and McKeon (2022b), the study differed for two reasons. First, that study used 468 basis elements that varied c and k_x independently. The k_x were chosen to be harmonics of the fundamental wavenumber, $2\pi/L$. This resulted in local modes with a different ω than the biglobal mode. Second, that study used a larger streamwise domain (around $40\delta_{99}$) which allowed the biglobal modes to exhibit streamwise periodic structure while they slowly decay in x due to viscous dissipation within the domain. On the other hand, this streamwise domain is too short to allow for significant viscous dissipation downstream. Furthermore, in this short domain, $\psi^S_{u,1}$ is characterized by transient effects, like the streamwise growth in amplitude characteristic of the convective non-normality and the gradual tilting downstream via the Orr-tilting mechanism. These nonperiodic modes are poorly captured with a periodic basis, especially for

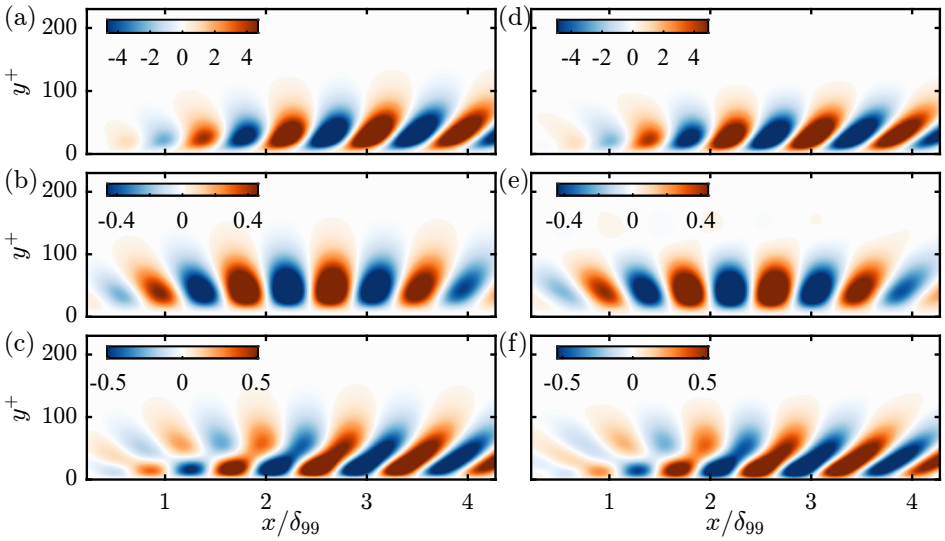

Figure 6.7: Real parts of $\psi^S_{u,1}$ (a), $\psi^S_{v,1}$ (b), $\psi^S_{w,1}$ (c), $\psi^V_{u,1}$ (d), $\psi^V_{v,1}$ (e), and $\psi^V_{w,1}$ (f) using $\lambda_z^+ = 100$.

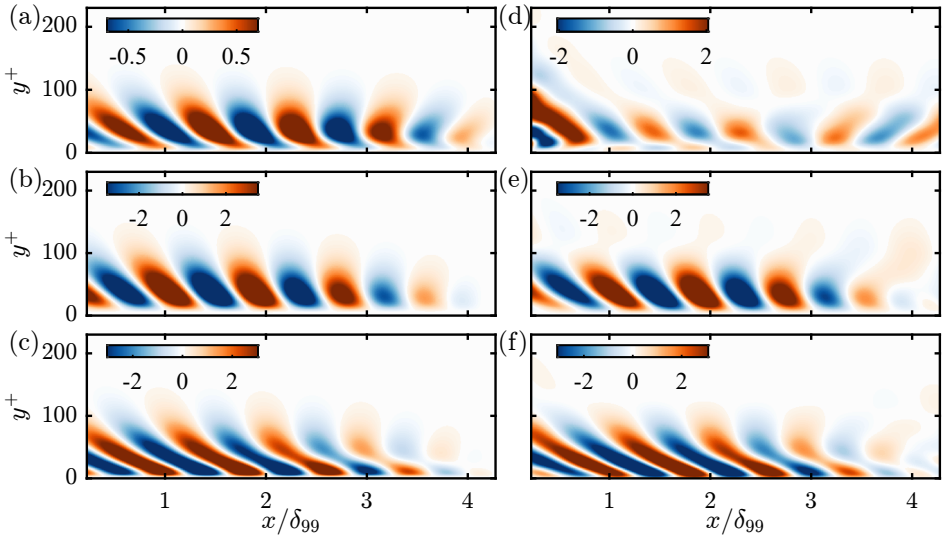

Figure 6.8: Real parts of $\phi^S_{u,1}$ (a), $\phi^S_{v,1}$ (b), $\phi^S_{w,1}$ (c), $\phi^V_{u,1}$ (d), $\phi^V_{v,1}$ (e), and $\phi^V_{w,1}$ (f) using $\lambda_z^+ = 100$.

the r used here. For the rest of this section, the modes presented are computed with the nonperiodic basis.

Figures 6.7 and 6.8 compare the reference modes with $\boldsymbol{\psi}^V_1$ and $\boldsymbol{\phi}^V_1$ using the nonperiodic basis, $\mathbf{b}^n_i$. Using only $r = 20$ nonperiodic basis elements provides an excellent agreement with $\boldsymbol{\psi}^S_1$. The error in the modes is defined in the same way as (Ribeiro,

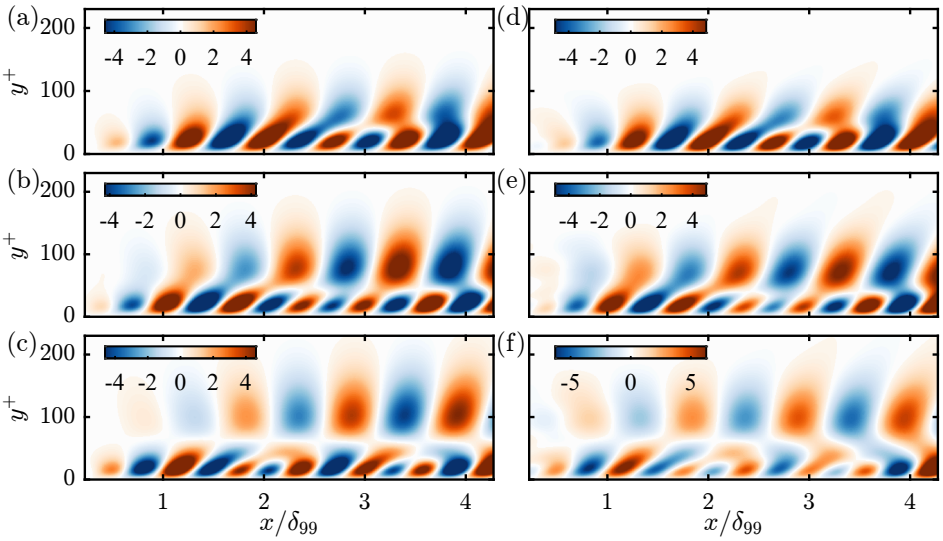

Figure 6.9: Real parts of $\psi^S_{u,2}$ (a), $\psi^S_{u,3}$ (b), $\psi^S_{u,4}$ (c), $\psi^V_{u,2}$ (d), $\psi^V_{u,3}$ (e), and $\psi^V_{u,3}$ (f) using $\lambda_z^+ = 100$.

Yeh, and Taira, 2020) as

$$e^V_{\psi,j} = \left|\left|\left\langle \boldsymbol{\psi}^S_j, \boldsymbol{\psi}^V_j \right\rangle_r\right| - 1\right|, \tag{6.27}$$

$$e^V_{\phi,j} = \left|\left|\left\langle \boldsymbol{\phi}^S_j, \boldsymbol{\phi}^V_j \right\rangle_f\right| - 1\right|, \tag{6.28}$$

where the absolute value accounts for a phase differences between the modes. Here, $e^V_{\psi,1} = .013$, indicating agreement up to around 1%. The forcing modes do not agree as well as the response modes, primarily because of the streamwise forcing components. The wall-normal and spanwise components are approximated well with the VRA approximation. Similar behavior was seen in Barthel, Gomez, and McKeon (2022b), where $\phi^V_{v,1}$ and $\phi^V_{w,1}$ identified similar structure as those computed with the SVD. The agreement in the transverse components of the forcing is likely due to the component-wise amplification in the LNS operator, which connects transverse forcing to streamwise responses. Such streamwise forcing is inactive in the lift-up mechanism (Abreu, Cavalieri, et al., 2020) making it difficult to estimate with the VRA approach. Despite the issues in $\phi^V_{u,1}$, $e^V_{\phi,1} = .046$ indicates agreement to within 5% with only 20 modes.

The agreement with the higher order modes is presented in Figures 6.9 and 6.10, by comparing only $\psi_{u,i}$ and $\phi_{v,i}$ for brevity. Although the response modes agree qualitatively well, their agreement deteriorates as i increases. The error is quantified as $e^V_{\psi,2} = 0.058$, $e^V_{\psi,3} = 0.068$, and $e^V_{\psi,3} = 0.056$. The disagreement in the forcing modes begins near the inlet, where large amplitudes are computed for $\psi_{v,i}$. The

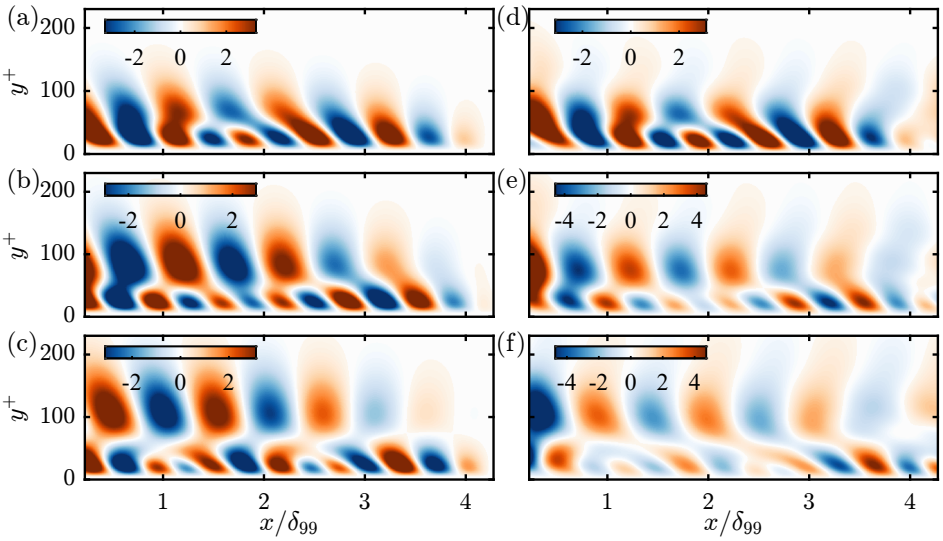

Figure 6.10: Real parts of $\phi^S_{u,2}$ (a), $\phi^S_{u,3}$ (b), $\phi^S_{u,4}$ (c), $\phi^V_{u,2}$ (d), $\phi^V_{u,3}$ (e), and $\phi^V_{u,3}$ (f) using $\lambda_z^+ = 100$.

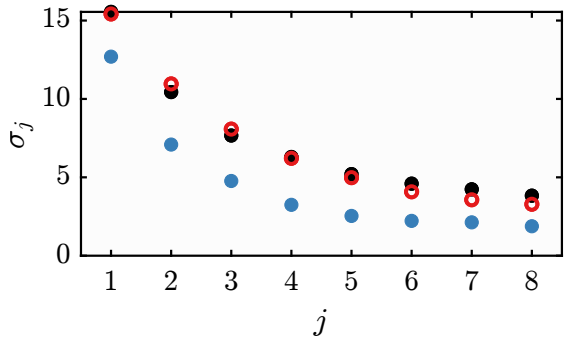

Figure 6.11: σ_j^S (black circles) and σ_j^V using $\lambda_z^+ = 100$. The red open circles are the VRA approximated modes, computed with the nonperiodic basis, while the blue circles are computed with the periodic basis.

multiple peaked structure in the higher order modes occurs to enforce orthogonality and is well captured with VRA. The error is much larger for the higher order forcing modes with $e^V_{\psi,2} = 0.11$, $e^V_{\psi,3} = 0.13$, and $e^V_{\psi,4} = 0.20$.

Finally, the singular values are compared between the reference and the VRA approximations using $\mathbf{b}_i^p$ and $\mathbf{b}_i^n$ in Figure 6.11. Using the latter leads to an underprediction in the singular values. This disagreement could be expected from the difference in mode shape seen in Figure 6.6. Using the nonperiodic basis leads to good agreement in the singular values, which could be expected from the agreement in the resolvent modes. By accounting for the streamwise evolution suggested by the convective non-normality, the VRA can approximate the standard resolvent results from $\mathcal{A}$ using only 20 basis elements.

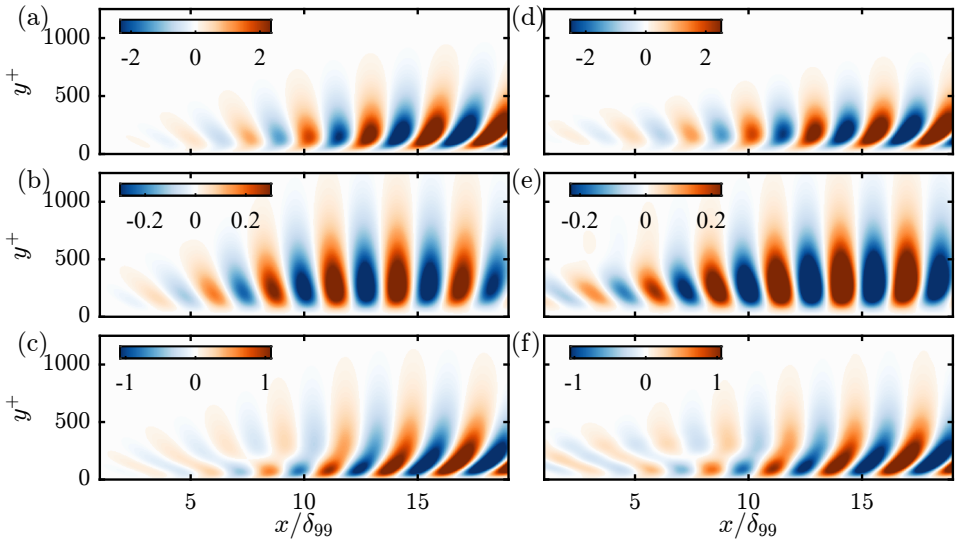

Figure 6.12: Real parts of $\psi^S_{u,1}$ (a), $\psi^S_{v,1}$ (b), $\psi^S_{w,1}$ (c), $\psi^V_{u,1}$ (d), $\psi^V_{v,1}$ (e), and $\psi^V_{w,1}$ (f) using $\lambda_z = 1$.

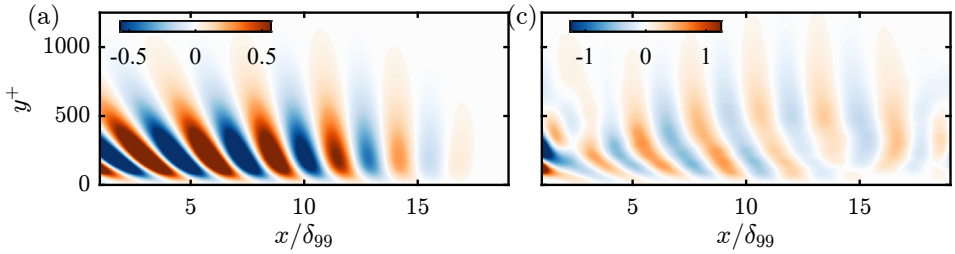

Figure 6.13: Real parts of $\phi^S_{v,1}$ (a) and $\phi^V_{v,1}$ (b) using $\lambda_z = 1$.

Now, the performance of the nonperiodic basis is investigated for the large scale mode in Figures 6.12 and 6.13. In Barthel, Gomez, and McKeon (2022b), using a periodic basis for the large scale modes lead to poor agreement with reference modes. By accounting for the convective non-normality in the response modes, the nonperiodic basis is able to create a $\boldsymbol{\psi}^V_1$ that agrees well with $\boldsymbol{\psi}^S_1$ with only 180 basis elements. With these basis elements, $e^V_{\psi,1} = 0.009$. Despite the agreement in the response modes, the forcing modes are poorly approximated, as evidenced by $\phi^V_{v,1}$. The $\phi^V_{v,1}$ have over predicted amplitudes near the inlet, which is likely caused by the convective non-normality. In $\mathcal{H}$, upstream inputs lead to large downstream outputs. For $\mathcal{A}$, this relationship is reversed causing the large values of $\boldsymbol{\psi}^V_1$ at the outlet to amplify the upstream amplitude of $\phi^V_{v,1}$. Here, $e^V_{\phi,1} = 0.46$.

Components of the higher order resolvent modes are presented in Figures 6.14 and 6.15. The agreement of $\psi^V_{u,i}$ with $\psi^S_{u,i}$ is good, especially in the downstream region. The orthogonality constraint that creates i peaked structures in the wall-normal

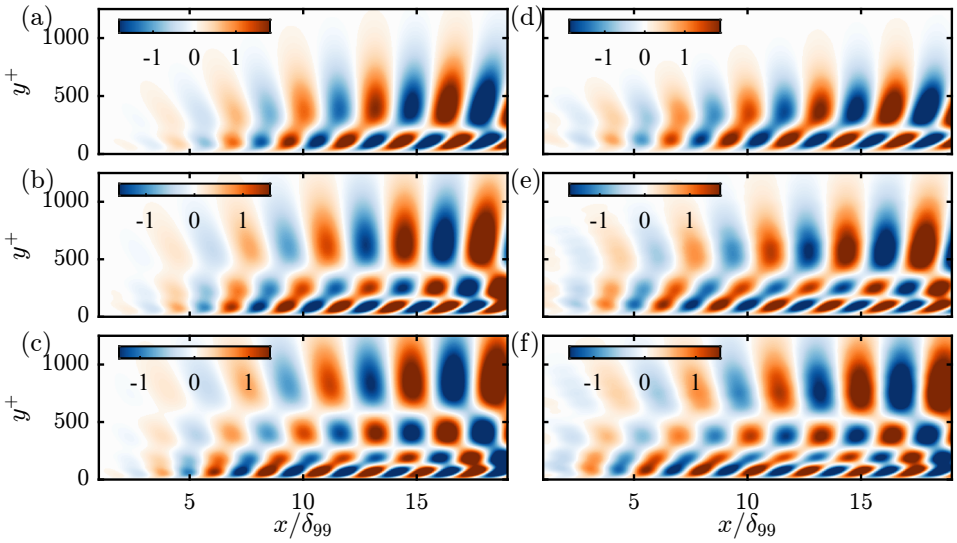

Figure 6.14: Real parts of $\psi^S_{u,2}$ (a), $\psi^S_{u,3}$ (b), $\psi^S_{u,4}$ (c), $\psi^V_{u,2}$ (d), $\psi^V_{u,3}$ (e), and $\psi^V_{u,3}$ (f) using $\lambda_z = 1$.

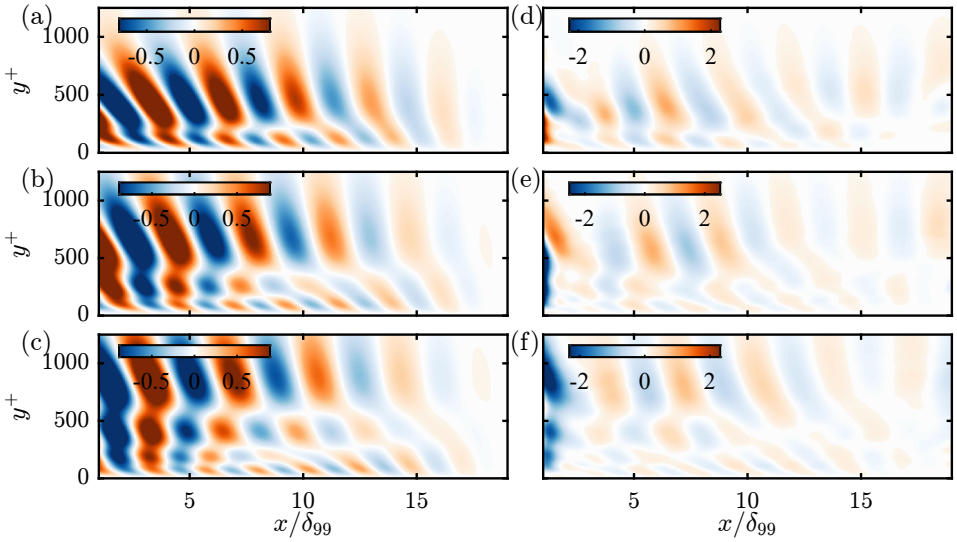

Figure 6.15: Real parts of $\phi^S_{u,2}$ (a), $\phi^S_{u,3}$ (b), $\phi^S_{u,4}$ (c), $\phi^V_{u,2}$ (d), $\phi^V_{u,3}$ (e), and $\phi^V_{u,3}$ (f) using $\lambda_z = 1$.

direction for $\psi^S_{u,i}$ is also recovered in $\psi^V_{u,i}$. Due to the disagreement in the response modes, the higher order $\boldsymbol{\phi}^V_i$ then poorly approximate $\boldsymbol{\phi}^S_i$, as seen in Figure 6.15. They are also categorized by a large amplitude near the inlet. Despite the large amplification near the inlet, there is an underlying structure in the VRA forcing modes that resembles the reference forcing modes. The error increases for the higher order response modes with $e^V_{\psi,2} = 0.04$, $e^V_{\psi,3} = 0.12$, and $e^V_{\psi,4} = 0.18$ while $e^V_{\phi,j} \approx .45$.

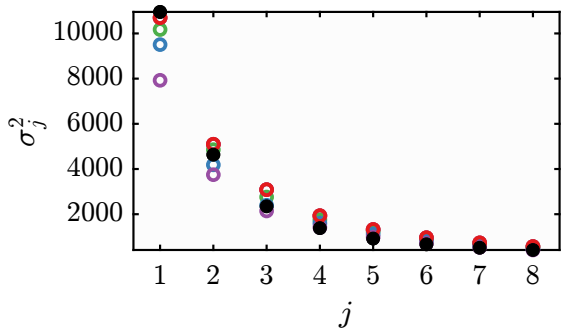

Figure 6.16: σ_j^S (black circles), σ_j^V computed with $N_j = 9$ (red open circles), $N_j = 8$ (green open circles), $N_j = 6$ (blue open circles), and $N_j = 4$ (purple open circles) using $\lambda_z = 1$. The singular values squared are plotted to visualize differences in N_j.

In Figure 6.16, σ_j^S is compared with σ_j^V using the parameters in Table 6.1. As expected from the poor agreement in the forcing modes, the singular values are under predicted. σ_j^V is recomputed using less basis elements by decreasing N_j. Increasing N_j does not increase the cost of computing the basis, since the local resolvent calculation is only computed N_c times. N_j simply increases the amount of retained higher order local modes. Although this increases the cost of the eigenvalue problem, its computational cost is still miniscule compared to the biglobal approach. Since $r = 180$ and $N_y = 251$, calculating a single local response mode takes longer than computing the eigenvalues in Equation 6.17. As $r = N_c N_j$ increases, σ_1^V increases monotonically, improving the agreement in the singular value approximation. Despite the improvement in σ_i^V, $\boldsymbol{\psi}_i^V$ and $\boldsymbol{\phi}_i^V$ are hardly affected. This suggests that a better basis may be possible.

In conclusion, VRA approximates the true resolvent modes well while avoiding a matrix inverse. The projection onto the basis elements helps regularize the problem by projecting away spurious vectors from the range of $\mathcal{A}$. This makes the eigenvalue problem in Equation 6.17 well posed. There is a dependence on the choice of basis used. When the basis does not satisfy the correct boundary conditions, VRA leads to poor approximations. This was seen by the increased error in the Fourier basis for the GL problem and in the lack of agreement using the periodic basis. Incorporating nonperiodicity into the basis elements for the biglobal modes lead to excellent agreement, even for the large scale modes. The nonperiodicity was chosen with *a priori* knowledge of the convective non-normality in the ZPG TBL. Increasing the number of basis elements, r, also lead to better agreements between the results of the reference resolvent analysis and the VRA. A challenge remains in decreasing the error in the forcing modes and determining what the best basis may

be for the nonperiodic flows.

6.4 An Arnoldi-free Resolvent Analysis Approximation

Using the ideas developed for the VRA, a method is described to approximate the resolvent modes using $\mathcal{H}$ that avoids the Arnoldi iteration. The use of $\mathcal{H}$ has the advantageous property that it amplifies responses in the direction of $\boldsymbol{\psi}_1$. Furthermore, the outputs of $\mathcal{H}$ satisfy the correct boundary conditions and are divergence free. However, often times several Arnoldi iterations are required that need to be computed iteratively, which can add computational time. In Ribeiro, Yeh, and Taira (2020), the matrix sketching allowed the action of $\mathcal{H}$ to be applied to r vectors at once, which avoided the need for an Arnoldi iteration. However, it also required the action of $\mathcal{H}^\dagger$ to another set of r vectors. Nonetheless, it saved computational time compared to the Arnoldi algorithm. Here, this method only needs to compute the action of $\mathcal{H}$ to a set of r vectors once.

This method begins by assuming that the forcing $\mathbf{f}$ is described as the sum of r basis elements, $\widetilde{\mathbf{b}}_i$, with coefficients, $\widetilde{a}_j$, as

$$\mathbf{f} = \sum_j^r \widetilde{a}_j \widetilde{\mathbf{b}}_j = \widetilde{\mathbf{B}}\widetilde{\mathbf{a}}. \tag{6.29}$$

Using similar notation as the previous section, $\widetilde{\mathbf{B}} = \left[\widetilde{\mathbf{b}}_1, \ldots, \widetilde{\mathbf{b}}_r\right]$ and $\widetilde{\mathbf{a}} = [\widetilde{a}_1, \ldots, \widetilde{a}_r]^T$. Now the goal is to maximize the cost function, $\mathcal{J}$, in Equation 2.11 for the forcing $\mathbf{f}$. Following the analysis described in Section 6.3, it can be shown that the Euler-Lagrange equation for $\widetilde{\mathbf{a}}$ becomes

$$\left(\mathcal{H}\widetilde{\mathbf{B}}\right)^* \mathcal{W}_r \left(\mathcal{H}\widetilde{\mathbf{B}}\right)\widetilde{\mathbf{a}}_i = \mathbf{Q}_H \widetilde{\mathbf{a}}_i = \widetilde{\lambda}_i^2 \widetilde{\mathbf{B}}^* \mathcal{W}_r \widetilde{\mathbf{B}}\widetilde{\mathbf{a}}_i = \widetilde{\lambda}_i^2 \mathbf{D}_H \widetilde{\mathbf{a}}_i. \tag{6.30}$$

$\mathbf{Q}_H$ and $\mathbf{D}_H$ are $r \times r$ Hermitian matrices. This ensures that $\widetilde{\mathbf{a}}_i$ are orthonormal such that

$$\widetilde{\mathbf{a}}_i^* \mathbf{D}_H \widetilde{\mathbf{a}}_j = \delta_{ij}. \tag{6.31}$$

Furthermore, $\widetilde{\lambda}_i \geq 0$ and $\widetilde{\lambda}_{i+1} \leq \widetilde{\lambda}_i$. The coefficients $\widetilde{\mathbf{a}}_i$ optimally represent $\boldsymbol{\phi}_i$ in the basis $\widetilde{\mathbf{B}}$ while $\widetilde{\lambda}_i$ is an approximation for σ_i. The forcing modes can be reconstructed as

$$\boldsymbol{\phi}_i = \widetilde{\mathbf{B}}\widetilde{\mathbf{a}}_i. \tag{6.32}$$

The response modes are reconstructed using

$$\boldsymbol{\psi}_i = \sigma_i^{-1} \left(\mathcal{H}\widetilde{\mathbf{B}}\right)\widetilde{\mathbf{a}}_i. \tag{6.33}$$

Using $\mathcal{H}$ for this projection scheme requires the solution of $\mathcal{A}\mathbf{x} = \mathbf{y}$, unlike the VRA approach. This creates a large cost for the method proposed here as an LU decomposition is required to solve the linear system. The computational savings of using this approach over the standard resolvent approach is that, due to the projection, the Arnoldi iterations and discretization of an adjoint resolvent operator are no longer necessary. Furthermore, this approach only needs to compute $\mathcal{H}\tilde{\mathbf{B}}$ once since the formulation does not require $\mathcal{H}^\dagger$.

By referencing the algorithms in Appendix 1, if the Arnoldi iteration uses N_i iterations, then the linear systems $\mathcal{A}\mathbf{x}_i = \mathbf{y}_i$ and $\mathcal{A}^\dagger\mathbf{x}_i = \mathbf{y}_i$ are solved N_i times. Assuming that the conjugate-transpose method is used, then the LU decomposition is computed once, which is an $O(n^3)$ operation. Using the LU factors to solve the linear systems is an $O(n^2)$ operation for each triangular system. Thus, the total cost to compute the standard resolvent analysis is $O(n^3 + 4N_i n^2)$. If the adjoint is discretized, then the cost is $O(2n^3 + 4N_i n^2)$ due to the extra LU decomposition for the adjoint operator.

These repeated calculations are avoided in the approach described herein by solving the following system once for all the basis vectors:

$$\mathcal{A}\mathbf{X} = \widetilde{\mathbf{B}}. \tag{6.34}$$

This sets $\mathbf{X} = \mathcal{H}\widetilde{\mathbf{B}}$. Solving this system has a computational complexity of $O(rn^2)$ if $\mathcal{A}$ has already been decomposed into its LU factors. The back substitution is done only once, as opposed to the Arnoldi algorithm which requires the back substitution to be computed sequentially. The cost of this algorithm is $O(n^3 + rn^2)$. Like in the VRA example, r can be small.

The approach is now applied to the same large scale mode from Figure 6.3. Both approaches compute the LU decomposition and the Gaussian elimination using the Intel® oneAPI Math Kernel Library PARDISO (Schenk and Gärtner, 2004). The Arnoldi algorithm described in Algorithm 2 is used to compare the Arnoldi iterations so that the adjoint is treated as a conjugate transpose to not include the LU decomposition of the adjoint operator in the computational cost. The nonperiodic

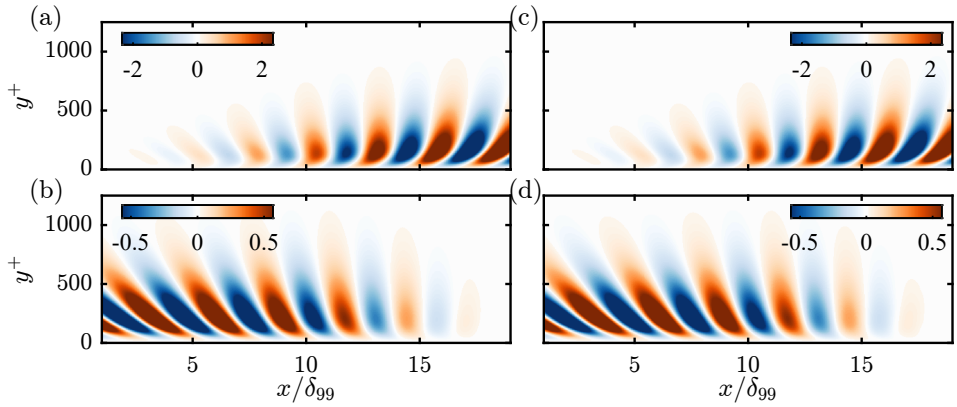

Figure 6.17: Real parts of $\psi^S_{u,1}$ (a), $\phi^S_{v,1}$ (b), $\psi^P_{u,1}$ (c), and $\phi^P_{v,1}$ (d) for the $\lambda_z = 1$ mode described in Section 6.3.

basis, $\widetilde{\mathbf{b}}_i$, is defined as

$$\begin{aligned}
\widetilde{b}_{i+j,u}(x,y) &= \phi^{1D}_{i,u}(y; c_j k_z, \omega) e^{ik_{x,j}x} f(x) \\
\widetilde{b}_{i+j,v}(x,y) &= \phi^{1D}_{i,v}(y; c_j k_z, \omega) e^{ik_{x,j}x} f(x) \\
\widetilde{b}_{i+j,w}(x,y) &= \frac{\sqrt{-1}}{k_z} \frac{\partial \widetilde{b}_{i+j,u}(x,y)}{\partial x} + \frac{\partial \widetilde{b}_{i+j,v}(x,y)}{\partial y} \\
\widetilde{b}_{i+j,p}(x,y) &= 0,
\end{aligned} \tag{6.35}$$

where

$$\widetilde{f}(x) = f\left(-\left(x - \frac{L}{2}\right)\right) = \left(\frac{1 - \exp(-25(L-x)/L)}{1 - \exp(-25)}\right)^2 \tag{6.36}$$

creates the nonperiodic structure. $\widetilde{f}$ is a reflection of f used in Section 6.3 about center of the domain so that large amplitudes in the forcing are in the upstream region. This is inline with the convective non-normality for the forcing modes. $\boldsymbol{\psi}^P_j$, $\boldsymbol{\phi}^P_j$, and σ^P_j will denote the resolvent modes and singular values computed from the eigenvalue problem in Equation 6.30 and $\boldsymbol{\psi}^S_j$, $\boldsymbol{\phi}^S_j$, and σ^S_j are the reference results computed using the standard resolvent approach.

The streamwise component of the response modes and wall-normal components of the forcing modes are plotted in Figure 6.17. The $\phi^P_{v,1}$ compares well with $\phi^S_{v,1}$ with the 180 basis elements used. Due to the directional-amplification of $\mathcal{H}$ in the direction of $\boldsymbol{\psi}_1$ and the good approximation in $\boldsymbol{\phi}_1$, the $\psi^S_{u,1}$ and $\psi^P_{u,1}$ agree well. These components are almost indistinguishable from one another.

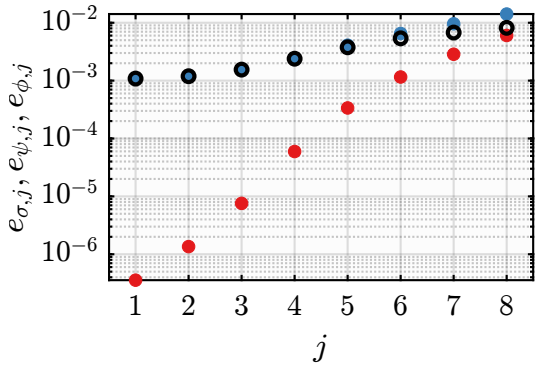

Figure 6.18: Error in response modes, forcing modes, and singular values plotted as $e_{\psi,j}$ (red circles), $e_{\phi,j}$ (blue circles), and $e_{\sigma,j}$ (black open circles) for the mode described in Section 6.3.

To compare the agreement in the higher order modes, the errors are defined as

$$e_{\psi,j} = \left| \left| \left\langle \boldsymbol{\psi}_j^S, \boldsymbol{\psi}_j^P \right\rangle_r \right| - 1 \right|, \tag{6.37}$$

$$e_{\phi,j} = \left| \left| \left\langle \boldsymbol{\phi}_j^S, \boldsymbol{\phi}_j^P \right\rangle_f \right| - 1 \right|, \tag{6.38}$$

$$e_{\sigma,j} = \frac{\left| \sigma_j^S - \sigma_j^P \right|}{\sigma_j^S}. \tag{6.39}$$

The absolute value is used in Equations 6.37 and 6.38 to account for a difference in phase between the two sets of modes. The errors are similar to those used in Ribeiro, Yeh, and Taira (2020). These are plotted in Figure 6.18 for the first 8 modes. The error increases for the higher order modes. $e_{\psi,j}$ being smaller than $e_{\phi,j}$ is a testament to the directional amplification in $\mathcal{H}$, since it preferentially amplifies in the direction of the leading response modes. Since this preferential amplification weakens for the higher order modes, their associated error increases.

To compare this algorithm with the Arnoldi method, Figure 6.19(a) compares the time it takes to use these approaches, using i Arnoldi iterations or i basis elements. The time it takes to compute a single Arnoldi iteration is about a third of the time it takes to compute the projection algorithm with 180 basis elements. The projection algorithm is able to converge σ_4^P to σ_4^S in about 13 seconds, compared to the Arnoldi algorithm, which takes about 25 seconds.

The main benefit of this approach is that the resolvent analysis can be approximated with a single back substitution, as opposed to multiple iterations. Although this method is more computationally expensive than the VRA approach, it is a lot more accurate. The main computational drawback of this approach is that an LU

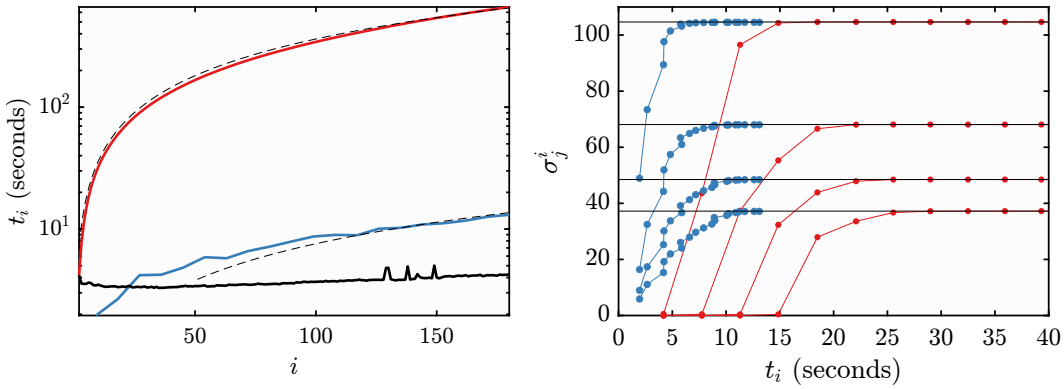

Figure 6.19: Temporal comparison of the Arnoldi algorithm and the resolvent approximation on i basis elements. (a) Time to compute i iterations of the Arnoldi algorithm (blue), the ith Arnoldi iteration (black solid line), and resolvent approximation using i basis elements (red). The dashed lines are proportional to i. (b) The time, t_i, it took to compute the Arnoldi algorithm using i iterations or the projection using i basis elements. σ_j^i is the jth leading singular value computed using i iterations (red) of i basis elements (blue). σ_j^S is denoted by the black solid lines.

decomposition needs to be computed. The LU decomposition for the example shown here takes 26 seconds, which can take longer than the Arnoldi algorithm. Another issue is that this method may be susceptible to the choice of modeling basis, like the VRA approach.

6.5 Chapter Summary

This chapter focused on strategies that can be implemented to save computational resources. ARA illustrated that with appropriate choices of acquisition functions and kernels, the parameter space in the resolvent analysis can be efficiently sampled with augmented BO code. Compared to a fixed grid parameter search, the large amplification regions are sampled with increased resolution. The choice of acquisition function allowed for increased sampling of various regions around the local maxima in the amplification, not just the region with the largest amplification. This approach can easily be applied to other applications where various local maxima need to be well-resolved with few samples.

The VRA approach approximates the resolvent modes without the need for a matrix inverse or solution of a linear system. By assuming that the resolvent modes are a sum of r basis elements, an $r \times r$ eigenvalue problem for the coefficients can be constructed from the Euler-Lagrange equations of Equation 2.21. These eigencoefficients provide the optimal representation of the response modes in the given

basis. Section 6.3 further illustrated that the choice of basis functions can affect the results significantly. By using a basis that models the physical amplification mechanism present in the convective non-normality, the response modes and amplifications can be well-approximated using a small number of basis elements. The most expensive calculations in the VRA approach are the matrix multiplications with the sparsely discretized LNS operator. Unlike the standard resolvent approach applied to the biglobal operator, this can be computed without the need for expensive calculations on parallelized architecture. Despite the computational benefits of the VRA approximation, the forcing modes are often poorly approximated because $\mathcal{A}$ amplifies the errors in the approximated response modes. The VRA can be rederived by using $\mathcal{A}^\dagger$ and an approximation of the forcing modes with r basis elements. This would find eigen-coefficients for the forcing modes, allowing for an approximation for the forcing modes without having to compute the forcing modes through Equation 6.13.

The computational cost for the local resolvent mode basis scales as $O\big(r(4N_y)^3\big)$, compared to the LU decomposition of the biglobal operator which scale as $O\big((4N_xN_y)^3\big)$. If the VRA was applied to a parameter sweep, then the local basis would be computed once and the rest of the expensive calculations would be matrix multiplications. Due to the nonperiodic boundary conditions used in the biglobal resolvent analysis, special care needs to be taken to ensure that the basis elements satisfy the same assumptions as the response modes. It is likely that better basis elements exist that can satisfy these conditions.

Ideas from the VRA approach were used in Section 6.4 to approximate resolvent analysis without using an Arnoldi algorithm. This approach represented the forcing as the sum of r basis elements. The coefficients that lead to the largest resolvent amplification were shown to satisfy the $r \times r$ eigenvalue problem in Equation 6.30. Although this approach still uses the resolvent operator, the action of the resolvent operator on the basis elements is only computed once, unlike the Arnoldi algorithm. This leads to a significant reduction in the calculation time for resolvent analysis. It was shown that the singular values can converge in about half the time as the Arnoldi algorithm. Furthermore, the approximations made with this approach have an error less than a percent, even for the 8th order modes and singular values. Although the method identifies the optimal forcing modes in the given basis, the error in the response modes is smaller than the error in the forcing modes. This occurs because the resolvent operator amplifies the higher response modes.

Chapter 7

CONCLUSIONS AND FUTURE WORK

This work focused on the resolvent analysis of streamwise developing boundary layers and high enthalpy boundary layers with real gas effects. To deal with the increased computational cost associated with larger state vectors, methods were also presented to efficiently sample the parameter space using ideas from Bayesian Optimization and to approximate the resolvent analysis through variational methods. The major findings will be summarized, and future work will also be presented that can extend these results.

The biglobal resolvent operator described and validated in Chapter 2 was applied to ZPG boundary layers in Chapter 3. The scaling relationships of the local resolvent operator studied in Moarref, Sharma, et al. (2013) were shown to extend to the biglobal resolvent operator. While the local analysis can determine the appropriate scaling based on a user-specified wavespeed, the biglobal analysis determines its scaling from k_z. It was shown that modes with large k_z are localized near the wall, taking advantage of the lift up mechanism through the large shear at the wall, while modes with small k_z are further from the wall, taking advantage of the convective non-normality. From this biglobal analysis, it was shown that the scaling identified in Sasaki et al. (2022) for the Blasius boundary layer can be applied to the amplitudes of the resolvent modes and that those results generalize to $\omega \neq 0$. Scaling was presented for the inner layer, mesolayer and outer layer of a ZPG TBL, where it was shown that the scaling improved as Re_τ increased due to the increased scale separation. The inner scaling was shown to hold for a wide range of k_z^+ and ω^+. The premultiplied amplification also identified the presence of self-similar, small-scale, region, with length scales and wall-normal location similar to what is observed in experiment and simulation for the near wall cycle. These scaling relationships can be used to predict the behavior of high Re_τ resolvent modes, which may be computationally intractable if the near-wall modes are desired. A topic of interest is the interactions between small scale and large scale motions, which is predicted to increase with Re_τ (Marušić, Mathis, and Hutchins, 2010a). One to way to understand this is by determining a scaling relationship for the nonlinear weights of the large scale modes that extend down to the wall. Understanding the scaling of the nonlinear weights can also be used to build predictive models of the turbulent statistics.

The biglobal resolvent operator also allowed for the incorporation of nonparallel effects in an APG TBL in Chapter 4. The inner scaling described in Chapter 3 was applied to low Re_τ APG TBLs. Due to the lack of scale separation, the APG effects were shown to adversely affect the near-wall self-similarity. Using an APG TBL with a larger Re_τ, it was shown that the self-similarity in the inner region could be recovered, due to to the increased scale separation between the outer and inner regions and improved self-similarity in $\overline{U}$. Using the premultiplied response, E^+_{uu}, the amplification of the large scale modes was shown to increase with β. These effects are qualitatively similar to the energization of large scale structures seen in simulation (J. H. Lee, 2017; Bobke et al., 2017). Using the biglobal resolvent operator, history effects in the APG can also be studied. It was shown that σ_1 increased linearly with $\overline{\beta}$ for the large scale modes and that this linear growth may be related to a hybrid velocity scaling (Romero et al., 2022; Sekimoto et al., 2019). These effects suggest that changes in the turbulent statistics in an APG TBL can be explained through changes in the linear amplification. When comparing the modeled streamwise fluctuations from the linear analysis to the data, the nonlinear weight was chosen only to enforce an observed mixed velocity scaling in the inner peak (Aubertine and Eaton, 2005) and was not k_z or ω dependent. In order to improve the modeled streamwise fluctuations, a scale-dependent, nonlinear weight that can account for the outer scaling will be necessary.

In Chapter 5, the resolvent operator was augmented to include real gas effects from vibrational excitation using a CIG assumption and chemical nonequilibrium using a mixture of reacting gases. It was shown that the linear amplification from the CIG and CPG assumptions differed most in the subsonic region, where the modes were localized near the large temperature regions. However, by rescaling the subsonic linear amplification, it was shown that the amplification contours were self-similar. This suggests that there may be a scaling that can account for the differences in the thermophysical properties. While the effects of vibrational excitation did not significantly affect the local resolvent modes where the flow could be approximated as a parallel flow, the vibrational effects in simulation were shown to affect the flow near a leading shock (Di Renzo et al., 2022). The effects of an oblique shock can not be modeled with a local approach, so future work will need to extend the biglobal approach to handle these nonparallel flow features.

The resolvent analysis with chemical nonequilibrium effects allowed for concentration and species density variations across the boundary layer through diffusion

and chemical production. These effects are small for the optimal resolvent modes and amplification since they are amplified via shear-driven mechanisms involving $\overline{U}$ and $\overline{T}$. However, higher order modes can take advantage of forcing through the chemistry terms, which lead to substantial differences between the chemical nonequilibrium and chemical equilibrium approaches. For the small-scale resolvent modes in chemical nonequilibrium, it was shown that their correlations agree qualitatively with the data of Di Renzo and Urzay (2021) due to the importance of the lift-up effect. Future work will need to consider larger freestream temperatures that can support increased chemical dissociation of N_2 and O_2, which are predicted to increase the role of the chemical production terms. Furthermore, two-temperature models will also need to be incorporated for cases where the flow is in vibrational nonequilibrium (Franko, MacCormack, and Lele, 2010; Passiatore et al., 2022).

In Chapter 6, the adaptive resolvent analysis scheme was presented. This scheme relies on Bayesian Optimization with an acquisition function designed to sample the large amplification regions. This was applied to the hypersonic resolvent analysis in chemical nonequilibrium. Compared to a fixed-grid sampling, the adaptive resolvent analysis scheme was shown to increase the resolution of the large amplification regions. This approach can be readily applied to other problems. By using a variational approach, Euler-Lagrange equations were found for the coefficients of r basis elements that optimally approximate the resolvent modes and amplifications through an $r \times r$ eigenvalue problem where $r \ll n$. In the VRA approach, this was used to create inverse-free approximation of resolvent analysis, where the projection onto the basis elements removed the spurious vector space from the linear operator. It was shown that incorporating a set of basis elements that model the convective non-normality can better represent the biglobal resolvent modes. While the VRA approach is useful, it can often lead to errors in the forcing mode prediction. Future work will use the adjoint operator to approximate the forcing modes and avoid the detrimental amplification from the LNS operator. An Arnoldi-free approach was also described that can approximate the forcing modes using r basis elements. Although this method requires the operator inverse, it avoids the Arnoldi iterations while retaining accuracy of 99% for even the 8th order modes. As opposed to VRA, this approach does not amplify errors in the approximation of the forcing mode when computing the response mode. Since these two approaches are sensitive to the choice of basis, future work will need to determine *a priori* what an optimal basis is for the problem at hand.

BIBLIOGRAPHY

Abreu, Leandra I., André V. G. Cavalieri, et al. (2020). "Spectral proper orthogonal decomposition and resolvent analysis of near-wall coherent structures in turbulent pipe flows". In: *Journal of Fluid Mechanics* 900, A11.

Abreu, Leandra I., Alvaro Tanarro, et al. (2021). "Spanwise-coherent hydrodynamic waves around flat plates and airfoils". In: *Journal of Fluid Mechanics* 927, A1.

Afzal, Noor (1984). "Mesolayer theory for turbulent flows". In: *AIAA Journal* 22.3, pp. 437–439.

Anderson Jr., John David (2006). *Hypersonic and High-Temperature Gas Dynamics*. 2nd ed. Reston, Virginia: American Institute of Aeronautics and Astronautics.

Appelö, Daniel and Tim Colonius (2009). "A high-order super-grid-scale absorbing layer and its application to linear hyperbolic systems". In: *Journal of Computational Physics* 228.11, pp. 4200–4217.

Aubertine, Carolyn D. and John K. Eaton (2005). "Turbulence development in a non-equilibrium turbulent boundary layer with mild adverse pressure gradient". In: *Journal of Fluid Mechanics* 532, pp. 345–364.

Bae, H. Jane, Scott T. M. Dawson, and Beverley J. McKeon (2020). "Resolvent-based study of compressibility effects on supersonic turbulent boundary layers". In: *Journal of Fluid Mechanics* 883, A29.

Bagheri, Shervin et al. (2009). "Input-output analysis and control design applied to a linear model of spatially developing flows". In: *Applied Mechanics Reviews* 62.2, p. 020803.

Baidya, Rio et al. (2017). "Distance-from-the-wall scaling of turbulent motions in wall-bounded flows". In: *Physics of Fluids* 29.2.

Barthel, Benedikt, Salvador R. Gomez, and Beverley J. McKeon (2022a). "The role of an optimal modeling basis in variational resolvent analysis". In: *Turbulence and Shear Flow Phenomena*. Vol. 12.

Barthel, Benedikt, Salvador R. Gomez, and Beverley J. McKeon (2022b). "Variational formulation of resolvent analysis". In: *Physical Review Fluids* 7.1, p. 013905.

Bobke, Alexandra et al. (2017). "History effects and near equilibrium in adverse-pressure-gradient turbulent boundary layers". In: *Journal of Fluid Mechanics* 820, pp. 667–692.

Candler, Graham V. (2019). "Rate effects in hypersonic flows". In: *Annual Review of Fluid Mechanics* 51, pp. 379–402.

Chandler, Gary J. et al. (2012). “Adjoint algorithms for the Navier–Stokes equations in the low Mach number limit”. In: *Journal of Computational Physics* 231.4, pp. 1900–1916.

Chomaz, Jean-Marc (2005). “Global instabilities in spatially developing flows: non-normality and nonlinearity”. In: *Annual Review of Fluid Mechanics* 37, pp. 357–392.

Chu, Boa-Teh (1965). “On the energy transfer to small disturbances in fluid flow (Part I)”. In: *Acta Mechanica* 1.3, pp. 215–234.

Clauser, Francis H. (1954). “Turbulent boundary layers in adverse pressure gradients”. In: *Journal of the Aeronautical Sciences* 21.2, pp. 91–108.

Cogo, Michele et al. (2022). “Direct numerical simulation of supersonic and hypersonic turbulent boundary layers at moderate-high Reynolds numbers and isothermal wall condition”. In: *Journal of Fluid Mechanics* 945, A30.

Coles, Donald (1956). “The law of the wake in the turbulent boundary layer”. In: *Journal of Fluid Mechanics* 1.2, pp. 191–226.

Cossu, Carlo and Jean-Marc Chomaz (1997). “Global measures of local convective instabilities”. In: *Physical Review Letters* 78.23, p. 4387.

Davis, Timothy B., Ali Uzun, and Farrukh S. Alvi (2019). “Optimal disturbances and large-scale energetic motions in turbulent boundary layers”. In: *Journal of Fluid Mechanics* 860, pp. 40–80.

Dawson, Scott T. M. and Beverley J. McKeon (2019). “On the shape of resolvent modes in wall-bounded turbulence”. In: *Journal of Fluid Mechanics* 877, pp. 682–716.

Deshpande, Rahul et al. (2023). “Reynolds-number effects on the outer region of adverse-pressure-gradient turbulent boundary layers”. In: *arXiv preprint arXiv:2304.08714*.

Di Renzo, Mario, Lin Fu, and Javier Urzay (2020). “HTR solver: An open-source exascale-oriented task-based multi-GPU high-order code for hypersonic aerothermodynamics”. In: *Computer Physics Communications* 255, p. 107262.

Di Renzo, Mario and Javier Urzay (2021). “Direct numerical simulation of a hypersonic transitional boundary layer at suborbital enthalpies”. In: *Journal of Fluid Mechanics* 912.

Di Renzo, Mario et al. (2022). “Stagnation enthalpy effects on turbulent compression corner flow at Mach 5”. In: *Proceedings of the CTR Summer Program*, pp. 367–376.

Edwards, Thomas A. (1992). “Fluid/chemistry modeling for hypersonic flight analysis”. In: *Computers & Mathematics with Applications* 24.5-6, pp. 25–36.

Eitel-Amor, Georg, Ramis Örlü, and Philipp Schlatter (2014). "Simulation and validation of a spatially evolving turbulent boundary layer up to $Re_\theta = 8300$". In: *International Journal of Heat and Fluid Flow* 47, pp. 57–69.

Eriksson, David et al. (2018). "Scaling Gaussian process regression with derivatives". In: *Advances in Neural Information Processing Systems* 31.

Franko, Kenneth, Robert MacCormack, and Sanjiva K. Lele (2010). "Effects of chemistry modeling on hypersonic boundary layer linear stability prediction". In: *40th Fluid Dynamics Conference and Exhibit*, p. 4601.

Gomez, Salvador R. et al. (2022). "Adaptive resolvent analysis with application to high enthalpy flows". In: *Proceedings of the CTR Summer Program*, pp. 87–96.

Gómez, Francisco et al. (2014). "On the origin of frequency sparsity in direct numerical simulations of turbulent pipe flow". In: *Physics of Fluids* 26.10.

Griffin, Kevin Patrick, Lin Fu, and Parviz Moin (2021). "Velocity transformation for compressible wall-bounded turbulent flows with and without heat transfer". In: *Proceedings of the National Academy of Sciences* 118.34, e2111144118.

Gungor, AG et al. (2016). "Scaling and statistics of large-defect adverse pressure gradient turbulent boundary layers". In: *International Journal of Heat and Fluid Flow* 59, pp. 109–124.

Hanifi, Ardeshir, Peter J. Schmid, and Dan S. Henningson (1996). "Transient growth in compressible boundary layer flow". In: *Physics of Fluids* 8.3, pp. 826–837.

Harun, Zambri et al. (2013). "Pressure gradient effects on the large-scale structure of turbulent boundary layers". In: *Journal of Fluid Mechanics* 715, pp. 477–498.

Hoyas, Sergio and Javier Jiménez (2006). "Scaling of the velocity fluctuations in turbulent channels up to Re τ= 2003". In: *Physics of Fluids* 18.1, p. 011702.

Hoyas, Sergio, Martin Oberlack, et al. (2021). *DNS Channel Data $Re_\tau = 10000$*. DOI: 10.48328/tudatalib-658. URL: https://tudatalib.ulb.tu-darmstadt.de/handle/tudatalib/2990.

Huhn, Francisco and Luca Magri (2022). "Gradient-free optimization of chaotic acoustics with reservoir computing". In: *Physical Review Fluids* 7.1, p. 014402.

Jeun, Jinah, Joseph W. Nichols, and Mihailo R. Jovanović (2016). "Input-output analysis of high-speed axisymmetric isothermal jet noise". In: *Physics of Fluids* 28.4, p. 047101.

Jiménez, Javier (2013). "Near-wall turbulence". In: *Physics of Fluids* 25.10.

Jovanović, Mihailo R. and Bassam Bamieh (2005). "Componentwise energy amplification in channel flows". In: *Journal of Fluid Mechanics* 534, pp. 145–183.

Kamal, Omar et al. (2020). "Application of the One-Way Navier-Stokes (OWNS) equations to hypersonic boundary layers". In: *AIAA Aviation 2020 Forum*, p. 2986.

Kitsios, Vassili, Callum Atkinson, et al. (2016). "Direct numerical simulation of a self-similar adverse pressure gradient turbulent boundary layer". In: *International Journal of Heat and Fluid Flow* 61, pp. 129–136.

Kitsios, Vassili, Atsushi Sekimoto, et al. (2017). "Direct numerical simulation of a self-similar adverse pressure gradient turbulent boundary layer at the verge of separation". In: *Journal of Fluid Mechanics* 829, pp. 392–419.

Kong, Hojin, Haecheon Choi, and Joon Sik Lee (2000). "Direct numerical simulation of turbulent thermal boundary layers". In: *Physics of Fluids* 12.10, pp. 2555–2568.

Lee, Jae Hwa (2017). "Large-scale motions in turbulent boundary layers subjected to adverse pressure gradients". In: *Journal of Fluid Mechanics* 810, pp. 323–361.

Lee, Myoungkyu and Robert D. Moser (2015). "Direct numerical simulation of turbulent channel flow up to $Re_\tau \approx 5200$". In: *Journal of Fluid Mechanics* 774, pp. 395–415.

Lele, Sanjiva K. (1992). "Compact finite difference schemes with spectral-like resolution". In: *Journal of Computational Physics* 103.1, pp. 16–42.

Lund, Thomas S., Xiaohua Wu, and Kyle D. Squires (1998). "Generation of turbulent inflow data for spatially-developing boundary layer simulations". In: *Journal of computational physics* 140.2, pp. 233–258.

Mack, Leslie M. (1984). *Boundary-layer linear stability theory*. AGARD Report No 709, Part 3. Jet Propulsion Laboratory, California Institute of Technology.

Madhusudanan, Anagha and Beverley J. McKeon (2022). "Subsonic and supersonic mechanisms in compressible turbulent boundary layers: a perspective from resolvent analysis". In: *arXiv preprint arXiv:2209.14223*.

Malik, Mujeeb R. (1990). "Numerical methods for hypersonic boundary layer stability". In: *Journal of Computational Physics* 86.2, pp. 376–413.

Malik, Mujeeb R. and E. Clay Anderson (1991). "Real gas effects on hypersonic boundary-layer stability". In: *Physics of Fluids A: Fluid Dynamics* 3.5, pp. 803–821.

Martini, Eduardo et al. (2021). "Efficient computation of global resolvent modes". In: *Journal of Fluid Mechanics* 919, A3.

Marušić, Ivan and Gary J Kunkel (2003). "Streamwise turbulence intensity formulation for flat-plate boundary layers". In: *Physics of Fluids* 15.8, pp. 2461–2464.

Marušić, Ivan, Romain Mathis, and Nicholas Hutchins (2010a). "High Reynolds number effects in wall turbulence". In: *International Journal of Heat and Fluid Flow* 31.3, pp. 418–428.

Marušić, Ivan, Romain Mathis, and Nicholas Hutchins (2010b). "Predictive model for wall-bounded turbulent flow". In: *Science* 329.5988, pp. 193–196.

Marušić, Ivan, Jason P. Monty, et al. (2013). "On the logarithmic region in wall turbulence". In: *Journal of Fluid Mechanics* 716, R3.

Marušić, Ivan and Anthony E. Perry (1995). "A wall-wake model for the turbulence structure of boundary layers. Part 2. Further experimental support". In: *Journal of Fluid Mechanics* 298, pp. 389–407.

Mattsson, Ken and Jan Nordström (2004). "Summation by parts operators for finite difference approximations of second derivatives". In: *Journal of Computational Physics* 199.2, pp. 503–540.

McBride, Bonnie J. (2002). *NASA Glenn coefficients for calculating thermodynamic properties of individual species*. Tech. rep.

McKeon, Beverley J. and Ati S. Sharma (2010). "A critical-layer framework for turbulent pipe flow". In: *Journal of Fluid Mechanics* 658, pp. 336–382.

Millikan, Clark B (1938). "A critical discussion of turbulent flows in channels and circular tubes". In: *Proc. Fifth Intern. Congr. Appl. Mech., Cambridge*, pp. 386–392.

Moarref, Rashad, Mihailo R. Jovanović, et al. (2014). "A low-order decomposition of turbulent channel flow via resolvent analysis and convex optimization". In: *Physics of Fluids* 26.5.

Moarref, Rashad, Ati S. Sharma, et al. (2013). "Model-based scaling of the streamwise energy density in high-Reynolds-number turbulent channels". In: *Journal of Fluid Mechanics* 734, pp. 275–316.

Monkewitz, Peter A., Kapil A. Chauhan, and Hassan M. Nagib (2007). "Self-consistent high-Reynolds-number asymptotics for zero-pressure-gradient turbulent boundary layers". In: *Physics of Fluids* 19.11, p. 115101.

Monty, Jason P., Zambri Harun, and Ivan Marušić (2011). "A parametric study of adverse pressure gradient turbulent boundary layers". In: *International Journal of Heat and Fluid Flow* 32.3, pp. 575–585.

Morkovin, Mark V. (1962). "Effects of compressibility on turbulent flows". In: *Mécanique de la Turbulence* 367.380, p. 26.

Nagib, Hassan M., Kapil A. Chauhan, and Peter A. Monkewitz (2007). "Approach to an asymptotic state for zero pressure gradient turbulent boundary layers". In: *Philosophical Transactions of the Royal Society A: Mathematical, Physical and Engineering Sciences* 365.1852, pp. 755–770.

Park, Chul (1990). *Nonequilibrium Hypersonic Aerothermodynamics*. New York: Wiley. ISBN: 9780471510932.

Passiatore, Donatella et al. (2022). "Thermochemical non-equilibrium effects in turbulent hypersonic boundary layers". In: *Journal of Fluid Mechanics* 941, A21.

Pirozzoli, Sergio and Matteo Bernardini (2011). “Turbulence in supersonic boundary layers at moderate Reynolds number”. In: *Journal of Fluid Mechanics* 688, pp. 120–168.

Pope, Stephen B. (2000). *Turbulent Flows*. Cambridge University Press.

Pozuelo, Ramón et al. (2022). “An adverse-pressure-gradient turbulent boundary layer with nearly constant $\beta \simeq 1.4$ up to $Re_\theta \simeq 8,700$”. In: *Journal of Fluid Mechanics* 939, A34.

Ran, Wei et al. (2019). “Stochastic receptivity analysis of boundary layer flow”. In: *Physical Review Fluids* 4.9, p. 093901.

Ribeiro, Jean Hélder Marques, Chi-An Yeh, and Kunihiko Taira (2020). “Randomized resolvent analysis”. In: *Physical Review Fluids* 5.3, p. 033902.

Romero, Sylvia K. et al. (2022). “Stress equation based scaling framework for adverse pressure gradient turbulent boundary layers”. In: *International Journal of Heat and Fluid Flow* 93, p. 108885.

Rosenberg, Kevin Thomas (2018). “Resolvent-based modeling of flows in a channel”. PhD thesis. California Institute of Technology.

Ruan, Joseph Y. (2021). “Streamwise Homogeneous Turbulent Boundary Layers”. PhD thesis. California Institute of Technology.

Saad, Yousef (2011). *Numerical Methods for Large Eigenvalue Problems: Revised Edition*. SIAM.

Sanmiguel Vila, Carlos et al. (2020). “Separating adverse-pressure-gradient and Reynolds-number effects in turbulent boundary layers”. In: *Physical Review Fluids* 5.6, p. 064609.

Sasaki, Kenzo et al. (2022). “Parabolic resolvent modes for streaky structures in transitional and turbulent boundary layers”. In: *Physical Review Fluids* 7.10, p. 104611.

Schenk, Olaf and Klaus Gärtner (2004). “Solving unsymmetric sparse systems of linear equations with PARDISO”. In: *Future Generation Computer Systems* 20.3, pp. 475–487.

Schlatter, Philipp and Ramis Örlü (2010). “Assessment of direct numerical simulation data of turbulent boundary layers”. In: *Journal of Fluid Mechanics* 659, pp. 116–126.

Schmid, Peter J. and Dan S. Henningson (2002). *Stability and Transition in Shear Flows*. Vol. 142. Springer Science & Business Media.

Schmidt, Oliver T. et al. (2018). “Spectral analysis of jet turbulence”. In: *Journal of Fluid Mechanics* 855, pp. 953–982.

Sekimoto, Atsushi et al. (2019). “Outer scaling of self-similar adverse-pressure-gradient turbulent boundary layers”. In: *arXiv preprint arXiv:1912.05143*.

Sharma, Ati S. and Beverley J. McKeon (2013). "On coherent structure in wall turbulence". In: *Journal of Fluid Mechanics* 728, pp. 196–238.

Sipp, Denis and Olivier Marquet (2013). "Characterization of noise amplifiers with global singular modes: the case of the leading-edge flat-plate boundary layer". In: *Theoretical and Computational Fluid Dynamics* 27, pp. 617–635.

Skene, Calum S. et al. (2022). "Sparsifying the resolvent forcing mode via gradient-based optimisation". In: *Journal of Fluid Mechanics* 944, A52.

Smits, Alexander J. and Ivan Marušić (2013). "Wall-bounded turbulence". In: *Physics Today* 66.9, pp. 25–30.

Smits, Alexander J., Beverley J. McKeon, and Ivan Marušić (2011). "High–Reynolds number wall turbulence". In: *Annual Review of Fluid Mechanics* 43, pp. 353–375.

Spina, Eric F., Alexander J. Smits, and Stephen K. Robinson (1994). "The physics of supersonic turbulent boundary layers". In: *Annual Review of Fluid Mechanics* 26.1, pp. 287–319.

Symon, Sean et al. (2018). "Non-normality and classification of amplification mechanisms in stability and resolvent analysis". In: *Physical Review Fluids* 3.5, p. 053902.

Theofilis, Vassilios (2011). "Global linear instability". In: *Annual Review of Fluid Mechanics* 43, pp. 319–352.

Towne, Aaron, Oliver T. Schmidt, and Tim Colonius (2018). "Spectral proper orthogonal decomposition and its relationship to dynamic mode decomposition and resolvent analysis". In: *Journal of Fluid Mechanics* 847, pp. 821–867.

Trefethen, Lloyd N. (1999). *Spectra and Pseudospectra: The Behaviour of Non-normal Matrices and Operators*. Springer.

Trefethen, Lloyd N. et al. (1993). "Hydrodynamic stability without eigenvalues". In: *Science* 261.5121, pp. 578–584.

Van Driest, E. Reginald (1956). "The problem of aerodynamic heating". In.

Vinuesa, Ricardo et al. (2017). "Revisiting history effects in adverse-pressure-gradient turbulent boundary layers". In: *Flow, Turbulence and Combustion* 99, pp. 565–587.

von Kármán, Theodore (1934). "Turbulence and skin friction". In: *Journal of the Aeronautical Sciences* 1.1, pp. 1–20.

von Kármán, Theodore (1939). "The analogy between fluid friction and heat transfer". In: *Transactions of the American Society of Mechanical Engineers* 61.8, pp. 705–710.

Wei, Tie, Paul Fife, et al. (2005). "Properties of the mean momentum balance in turbulent boundary layer, pipe and channel flows". In: *Journal of Fluid Mechanics* 522, pp. 303–327.

Wei, Tie and Tobias Knopp (2023). “Outer scaling of the mean momentum equation for turbulent boundary layers under adverse pressure gradient”. In: *Journal of Fluid Mechanics* 958, A9.

Williams, Christopher K. I. and Carl Edward Rasmussen (2006). *Gaussian Processes for Machine Learning*. Vol. 2. 3. MIT press Cambridge, MA.

Appendix A

ARNOLDI ITERATION ALGORITHMS

A.1 Arnoldi Algorithm for Eigenvalue Problems

Consider the eigenvalue problem of a square matrix, $\mathbf{A} \in \mathbb{C}^{n \times n}$,

$$\mathbf{A}\mathbf{p}_i = \lambda_i \mathbf{p}_i. \tag{A.1}$$

The Arnoldi algorithm looks for approximate eigenvalues, $\tilde{\lambda}_i$, and eigenvectors, $\tilde{\mathbf{p}}_i$, based on an orthogonal projection onto the Krylov subspace,

$$\mathcal{K}_m(\mathbf{A}, \mathbf{v}) = span\left\{\mathbf{v}, \mathbf{A}\mathbf{v}, \mathbf{A}^2\mathbf{v}, ..., \mathbf{A}^{m-1}\mathbf{v}\right\}. \tag{A.2}$$

Following the steps outlined in Saad (2011), a matrix, $\mathbf{V} \in \mathbb{C}^{n,m}$, with orthonormal columns is constructed such that its columns span $\mathcal{K}_m(\mathbf{A}, \mathbf{v}_1)$, where $\mathbf{v}_1$ is a random unit vector. The inner product is chosen as the usual L_2 inner product such that $\langle \mathbf{a}, \mathbf{b} \rangle_2 = \mathbf{a}^*\mathbf{b}$. The Hessenberg matrix, $\mathbf{H}^e \in \mathbb{C}^{m,m} = \mathbf{V}^*\mathbf{A}\mathbf{V}$ is used to approximate the eigenvalues of $\mathbf{A}$. Since $m \ll n$, the eigenvalues of $\mathbf{H}^e$ can be calculated with $\mathcal{O}(m^3)$ operations rather than the than the $\mathcal{O}(n^3)$ operations required to compute the eigenvalues of $\mathbf{A}$. Due to orthogonality of the columns of $\mathbf{V}$, $\mathbf{V}^*\mathbf{V} = \mathbf{I}_m$, where $\mathbf{I}_m$ is the $m \times m$ identity matrix. The eigenvalue problem for $\mathbf{H}^e$ can be expanded as

$$\mathbf{H}^e\mathbf{t}_i = \tilde{\lambda}_i \mathbf{t}_i \tag{A.3}$$

$$\mathbf{V}^*\mathbf{A}\mathbf{V}\mathbf{t}_i = \tilde{\lambda}_i \mathbf{V}^*\mathbf{V}\mathbf{t}_i, \tag{A.4}$$

where $\mathbf{t}_i$ and $\tilde{\lambda}_i$ are the eigenvectors and eigenvalues of $\mathbf{H}^e$. If $m = n$, then $\mathbf{V}\mathbf{t}_i$ and $\tilde{\lambda}_i$ could be identified as the eigenvectors and eigenvalues of $\mathbf{A}$. otherwise, it can be shown (Saad, 2011) that $\tilde{\lambda}_i \to \lambda_i$ and $\mathbf{V}\mathbf{t}_i \to \mathbf{p}_i$ and as $m \to n$ for the first m eigen-pairs in descending $|\lambda_i|$ order. The algorithm is described in Algorithm 1 where the Gram-Schmidt process is used to create the orthonormal columns of $\mathbf{V}$.

A.2 Arnoldi Algorithm for Resolvent Analysis

The eigenvalue problem that is needed to do perform the resolvent analysis is defined in Equation 2.13. The discretized version is

$$\mathbf{W}_f^{-1}\mathbf{H}^\dagger\mathbf{W}_r\mathbf{H}\boldsymbol{\phi}_i = \sigma_i^2\boldsymbol{\phi}_i, \tag{A.5}$$

Algorithm 1 Arnoldi algorithm for eigenvalue problems

Begin with a random $n \times 1$ vector, u
$\mathbf{v}_1 = \mathbf{u}/\|\mathbf{u}\|_2$ ▷ Normalize
for $j = 1 : m - 1$ **do**
  $\mathbf{w} = \mathbf{A}\mathbf{v}_j$
  for $i = 1 : j$ **do**
    $H^e_{i,j} = \langle \mathbf{v}_i, \mathbf{w} \rangle_2$ ▷ Update the Hessenberg matrix
    $\mathbf{w} := \mathbf{w} - H_{i,j}\mathbf{v}_i$ ▷ Gram-Schmidt
  end for
  $H^e_{j+1,j} = \|\mathbf{w}\|_2$ ▷ Update the Hessenberg matrix
  $\mathbf{v}_{j+1} = \mathbf{w}/H^e_{j+1,j}$ ▷ Update and normalize vector
end for
$\mathbf{V} = [\mathbf{v}_1, \ldots, \mathbf{v}_m]$
$\left[\tilde{\lambda}_i, \mathbf{t}_i\right] = \mathrm{eig}(\mathbf{H}^e)$ ▷ Eigenvalues and eigenvectors of Hessenberg matrix
$\tilde{\mathbf{p}}_i = \mathbf{V}\mathbf{t}_i$ ▷ Approximate eigenvectors of $\mathbf{A}$

where $\mathbf{H}^\dagger$ is either the discretized continuous adjoint (DCA) or the conjugate-transpose (CT), $\mathbf{W}_I^{-1}\mathbf{H}^*\mathbf{W}_I$. Due to the prohibitive cost to compute and store $\mathbf{H}$ and $\mathbf{H}^\dagger$, an LU factorization of $(-i\omega\mathbf{I} + \mathbf{L})$ will be used (Jeun, Nichols, and Jovanović, 2016; Sipp and Marquet, 2013; Schmidt et al., 2018), where the LU factorization is computed using the Intel® oneAPI Math Kernel Library PARDISO (Schenk and Gärtner, 2004). This replaces the calculation $\mathbf{w} = \mathbf{H}\mathbf{v}_j$ with the solution of $(-i\omega\mathbf{I} + \mathbf{L})\mathbf{w} = \mathbf{I}_c\mathbf{v}_j$, where $\mathbf{w}$ is solved efficiently by leveraging the LU decomposition that is computed once. Without accounting for the sparse nature of the operators, the LU decomposition is $O(n^3)$ while Gaussian elimination of upper-triangular matrices is $O(n^2)$, which is negligible compared to the LU decomposition if $m \ll n$. The LU decomposition gives

$$(-i\omega\mathbf{I} + \mathbf{L}) = \mathbf{P}_d^T\mathbf{L}_d\mathbf{U}_d \tag{A.6}$$

and

$$\left(i\omega\mathbf{I} + \mathbf{L}^\dagger\right) = \mathbf{P}_a^T\mathbf{L}_a\mathbf{U}_a, \tag{A.7}$$

where $\mathbf{P}_a$ and $\mathbf{P}_d$ are permutation matrices, $\mathbf{L}_a$ and $\mathbf{L}_d$ are lower-diagonal matrices, and $\mathbf{U}_a$ and $\mathbf{U}_d$ are upper-diagonal matrices. Note that Equation A.7 is only used for the DCA matrix. For the CT matrix, the conjugate transpose of Equation A.6 is used.

Conjugate Transpose Adjoint Matrix

Using the CT matrix, Equation A.5 becomes

$$\mathbf{W}_f^{-1}\mathbf{W}_I^{-1}\mathbf{B}^*\mathbf{R}^*\mathbf{C}^*\mathbf{W}_I\mathbf{W}_r\mathbf{CRB}\boldsymbol{\phi}_i = \sigma_i^2\boldsymbol{\phi}_i. \tag{A.8}$$

Algorithm 1 is adapted to perform resolvent analysis in Algorithm 2 by employing the same strategy to solve the eigenvalue problem in Equation A.8. An optional spatial filter described in Lele (1992) is applied at each iteration and to the computed $\boldsymbol{\phi}_i$ and $\boldsymbol{\psi}_i$. The spatial filter is applied on Ω_n for each component q_i of the state vector $\mathbf{q}$ using a block diagonal matrix. If the filter is not used, then it is set to the identity matrix.

Discretized Continuous Adjoint Matrix

Using the DCA matrix, Equation A.5 becomes

$$\mathbf{W}_f^{-1}\mathbf{B}^\dagger\mathbf{R}^\dagger\mathbf{C}^\dagger\mathbf{W}_r\mathbf{CRB}\boldsymbol{\phi}_i = \sigma_i^2\boldsymbol{\phi}_i. \tag{A.9}$$

The algorithm to solve the eigenvalue problem in Equation A.9 is presented in Algorithm 3. Note that compared to Algorithm 2, Algorithm 3 requires two separate LU decompositions. This means that resolvent analysis using DCA is about twice as expensive as the CT approach. A spatial filter can be included in this approach as well, but is omitted since it is not used in this work.

Algorithm 2 Arnoldi algorithm for resolvent analysis using conjugate-transpose adjoint

Perform LU decomposition of $(-i\omega\mathbf{I}+\mathbf{L})$ and store $\mathbf{L}_d$, $\mathbf{U}_d$, and $\mathbf{P}_d$
if Filtering applied **then**
    Set $\mathbf{F}$ as $n_s \times n_s$ block-diagonal matrix where diagonal blocks apply the spatial filtering to each component of state vector
else
    Set $\mathbf{F}$ to identity matrix
end if
Begin with a random $n_s n \times 1$ vector, u
$\mathbf{v}_1 = \mathbf{u}/\|\mathbf{u}\|_2$ ▷ Normalize
for $j = 1 : m-1$ **do**
    $\mathbf{v}'_j = \mathbf{F}\mathbf{v}_j$ ▷ Apply filter
    $\mathbf{w}_1 = (-i\omega\mathbf{I}+\mathbf{L})\backslash\mathbf{I}_c\mathbf{B}\mathbf{v}'_j = \mathbf{U}_d\backslash\left(\mathbf{L}_d\backslash\left(\mathbf{P}_d\mathbf{I}_c\mathbf{B}\mathbf{v}'_j\right)\right)$
    $\mathbf{w}_2 = \mathbf{C}^*\mathbf{W}_I\mathbf{W}_r\mathbf{C}\mathbf{w}_1$
    $\mathbf{w}_3 = (i\omega\mathbf{I}+\mathbf{L}^*)\backslash\mathbf{I}_c^*\mathbf{w}_2 = \mathbf{P}_d^T\left(\mathbf{L}_d^*\backslash\left(\mathbf{U}_d^*\backslash\mathbf{I}_c^*\mathbf{w}_2\right)\right)$
    $\mathbf{w} = \mathbf{W}_f^{-1}\mathbf{W}_I^{-1}\mathbf{B}^*\mathbf{w}_3$ ▷ Calculate $\mathbf{A}\mathbf{v}_i$
    for $i = 1 : j$ **do**
        $H^e_{i,j} = \left\langle \mathbf{v}'_i, \mathbf{w}\right\rangle_2$ ▷ Update the Hessenberg matrix
        $\mathbf{w} := \mathbf{w} - H_{i,j}\mathbf{v}'_i$ ▷ Gram-Schmidt
    end for
    $H^e_{j+1,j} = \|\mathbf{w}\|_2$ ▷ Update the Hessenberg matrix
    $\mathbf{v}_{j+1} = \mathbf{w}/H^e_{j+1,j}$ ▷ Update and normalize vector
end for
$\mathbf{V} = \left[\mathbf{v}'_1, \ldots, \mathbf{v}'_m\right]$
$\left[\tilde{\lambda}_i, \mathbf{t}_i\right] = \mathrm{eig}(\mathbf{H}^e)$ ▷ Eigenvalues and eigenvectors of Hessenberg matrix
$\tilde{\mathbf{p}}_i = \mathbf{V}\mathbf{t}_i$
$\sigma_i = \sqrt{\tilde{\lambda}_i}$ ▷ Singular values of $\mathbf{H}$
$\boldsymbol{\phi}_i = \mathbf{F}\tilde{\mathbf{p}}_i/\|\tilde{\mathbf{p}}_i\|_f$ ▷ Forcing modes of $\mathbf{H}$
$\boldsymbol{\psi}_i = \sigma_i^{-1}\mathbf{F}\mathbf{H}\boldsymbol{\phi}_i$ ▷ Response modes of $\mathbf{H}$

Algorithm 3 Arnoldi algorithm for resolvent analysis using direct continuous adjoint

Perform LU decomposition of $(-i\omega\mathbf{I}+\mathbf{L})$ and store $\mathbf{L}_d$, $\mathbf{U}_d$, and $\mathbf{P}_d$
Perform LU decomposition of $\left(i\omega\mathbf{I}+\mathbf{L}^\dagger\right)$ and store $\mathbf{L}_a$, $\mathbf{U}_a$, and $\mathbf{P}_a$
Begin with a random $n_s n \times 1$ vector, u
$\mathbf{v}_1 = \mathbf{u}/\|\mathbf{u}\|_2$ ▷ Normalize
for $j = 1 : m-1$ **do**
    $\mathbf{w}_1 = (-i\omega\mathbf{I}+\mathbf{L})\backslash\mathbf{I}_c\mathbf{B}\mathbf{v}_i = \mathbf{U}_d\backslash\left(\mathbf{L}_d\backslash\left(\mathbf{P}_d\mathbf{I}_c\mathbf{B}\mathbf{v}_i\right)\right)$
    $\mathbf{w}_2 = \mathbf{C}^\dagger\mathbf{W}_r\mathbf{I}_c\mathbf{C}\mathbf{w}_1$
    $\mathbf{w}_3 = \left(i\omega\mathbf{I}+\mathbf{L}^\dagger\right)\backslash\mathbf{I}_c^\dagger\mathbf{w}_2 = \mathbf{U}_a\backslash\left(\mathbf{L}_a\backslash\left(\mathbf{P}_a\mathbf{I}_c^\dagger\mathbf{w}_2\right)\right)$
    $\mathbf{w} = \mathbf{W}_f^{-1}\mathbf{B}^\dagger\mathbf{w}_3$ ▷ Calculate $\mathbf{A}\mathbf{v}_i$
    for $i = 1 : j$ **do**
        $H^e_{i,j} = \langle\mathbf{v}_i, \mathbf{w}\rangle_2$ ▷ Update the Hessenberg matrix
        $\mathbf{w} := \mathbf{w} - H_{i,j}\mathbf{v}_i$ ▷ Gram-Schmidt
    end for
    $H^e_{j+1,j} = \|\mathbf{w}\|_2$ ▷ Update the Hessenberg matrix
    $\mathbf{v}_{j+1} = \mathbf{w}/H^e_{j+1,j}$ ▷ Update and normalize vector
end for
$\mathbf{V} = [\mathbf{v}_1, \ldots, \mathbf{v}_m]$
$\left[\tilde{\lambda}_i, \mathbf{t}_i\right] = \mathrm{eig}(\mathbf{H}^e)$ ▷ Eigenvalues and eigenvectors of Hessenberg matrix
$\tilde{\mathbf{p}}_i = \mathbf{V}\mathbf{t}_i$
$\sigma_i = \sqrt{\tilde{\lambda}_i}$ ▷ Singular values of $\mathbf{H}$
$\boldsymbol{\phi}_i = \tilde{\mathbf{p}}_i/\|\tilde{\mathbf{p}}_i\|_f$ ▷ Forcing modes of $\mathbf{H}$
$\boldsymbol{\psi}_i = \sigma_i^{-1}\mathbf{H}\boldsymbol{\phi}_i$ ▷ Response modes of $\mathbf{H}$

Appendix B

ADJOINT OF LINEAR DIFFERENTIAL OPERATORS WITH DIRICHLET BOUNDARY CONDITIONS

Equation 2.33 can be rewritten as

$$(\mathcal{A}_1 + \mathcal{A}_2 + \mathcal{A}_3 + \mathcal{A}_4)\widehat{\mathbf{q}} = \mathcal{I}\widehat{\mathbf{f}}, \tag{B.1}$$

where

$$\mathcal{A}_1 = \begin{pmatrix} i\omega\tilde{\mathcal{I}} + \boldsymbol{\nabla}\overline{\mathbf{U}} & 0 \\ 0 & 0 \end{pmatrix}, \tag{B.2}$$

$$\mathcal{A}_2 = \begin{pmatrix} \overline{\mathbf{U}} \cdot \widehat{\boldsymbol{\nabla}} & 0 \\ 0 & 0 \end{pmatrix}, \tag{B.3}$$

$$\mathcal{A}_3 = \begin{pmatrix} 0 & \widehat{\boldsymbol{\nabla}} \\ \widehat{\boldsymbol{\nabla}}\cdot & 0 \end{pmatrix}, \tag{B.4}$$

$$\mathcal{A}_4 = \begin{pmatrix} Re^{-1}\widehat{\nabla}^2 & 0 \\ 0 & 0 \end{pmatrix}, \tag{B.5}$$

and $\tilde{\mathcal{I}}$ denotes the identity operator on $\mathbb{C}^3$. Since the adjoint of a sum is the sum of the adjoints, the adjoints of $\mathcal{A}_i$, $\mathcal{A}_i^\dagger$, are computed with respect to the inner product in Equation 2.9 such that $\langle \mathbf{a}, \mathcal{A}_i\mathbf{b}\rangle = \left\langle \mathcal{A}_i^\dagger \mathbf{a}, \mathbf{b}\right\rangle$. Since $\mathcal{A}_1$ is not a differential operator, $\mathcal{A}_1^\dagger = \mathcal{A}_1^*$. For the others, integration by parts will be used.

Beginning with $\mathcal{A}_2$, one finds

$$\begin{aligned}\int_{\Omega_n} \mathbf{a}_u^*\left(\left(\overline{\mathbf{U}} \cdot \widehat{\boldsymbol{\nabla}}\right)\mathbf{b}_u\right)dV &= \int_{\Omega_n}\left[\widehat{\boldsymbol{\nabla}} \cdot \left(\mathbf{a}_u^*\mathbf{b}_u\overline{\mathbf{U}}\right) + \left(\left(-\overline{\mathbf{U}} \cdot \widehat{\boldsymbol{\nabla}}\right)\mathbf{a}_u\right)^*\mathbf{b}_u\right]dV \\ &= \oint_{\partial\Omega_n}\left(\mathbf{a}_u^*\mathbf{b}_u\overline{\mathbf{U}}\right)\cdot\mathbf{n}dS + \int_{\Omega_n}\left(\left(-\overline{\mathbf{U}} \cdot \widehat{\boldsymbol{\nabla}}\right)\mathbf{a}_u\right)^*\mathbf{b}_u dV. \end{aligned} \tag{B.6}$$

The surface integral in Equation B.6 is 0 if there are periodic boundary conditions or Dirichlet boundary conditions. Here, the latter is assumed at the wall, and at the inlet and outlet in the biglobal approach. In the free stream, the fluctuations are assumed to be compact and thus approach 0 as $y \to y_{max}$. Thus,

$$\mathcal{A}_2^\dagger = \begin{pmatrix} -\overline{\mathbf{U}} \cdot \widehat{\boldsymbol{\nabla}} & 0 \\ 0 & 0 \end{pmatrix}. \tag{B.7}$$

For $\mathcal{A}_3$ one finds

$$\begin{aligned}\int_{\Omega_n}\left(\mathbf{a}_u^*\widehat{\boldsymbol{\nabla}}b_p + a_p^*\widehat{\boldsymbol{\nabla}}\cdot\mathbf{b}_u\right)dV &= \int_{\Omega_n}\Big[\widehat{\boldsymbol{\nabla}}\cdot\left(\mathbf{a}_u^*b_p + a_p^*\mathbf{b}_u\right) - \left(\widehat{\boldsymbol{\nabla}}\cdot\mathbf{a}_u\right)^*b_p \\ &\qquad -\left(\widehat{\boldsymbol{\nabla}}a_p\right)^*\mathbf{b}_u\Big]\,dV \\ &= \oint_{\partial\Omega_n}\left(\mathbf{a}_u^*b_p + a_p^*\mathbf{b}_u\right)\cdot\mathbf{n}dS \\ &\qquad \int_{\Omega_n}\left[\left(-\widehat{\boldsymbol{\nabla}}\cdot\mathbf{a}_u\right)^*b_p + \left(-\widehat{\boldsymbol{\nabla}}a_p\right)^*\mathbf{b}_u\right]dV.\end{aligned} \tag{B.8}$$

Once again the surface integral is 0, thus

$$\mathcal{A}_3^\dagger = \begin{pmatrix} 0 & -\widehat{\boldsymbol{\nabla}} \\ -\widehat{\boldsymbol{\nabla}}\cdot & 0 \end{pmatrix}. \tag{B.9}$$

Finally, $\mathcal{A}_4^\dagger = \mathcal{A}_4$ because $\widehat{\nabla}^2$ is a self-adjoint operator, under the boundary conditions used in this analysis.

Appendix C

BIGLOBAL ORR-SOMMERFELD-SQUIRE EQUATIONS

This discussion begins with Equation 2.33, with $\widehat{\mathbf{uu}}$ replaced with $\widehat{\mathbf{f}}$, a general forcing input. For this discussion, $\widehat{\mathbf{f}}$ will be expressed as

$$\widehat{\mathbf{f}} = \widehat{\mathbf{f}}_s + \boldsymbol{\nabla}\widehat{F}, \tag{C.1}$$

where $\boldsymbol{\nabla} \cdot \widehat{\mathbf{f}}_s = 0$ and $\widehat{F}$ is a scalar potential. By taking the divergence of the momentum equation, an equation for the pressure can be found as

$$\nabla^2\left(\widehat{p} - \widehat{F}\right) = \nabla^2\widetilde{p} = -2\boldsymbol{\nabla}\overline{\mathbf{U}} : \boldsymbol{\nabla}\widehat{\mathbf{u}}, \tag{C.2}$$

where $\widetilde{p}$ is the pressure, augmented by the scalar potential. The goal of the OSS formulation is to reduce Equation 2.33 into an equation for the wall-normal vorticity, $\widehat{\omega}_2 = ik_z\widehat{u} - \partial\widehat{w}/\partial x$, and the wall-normal velovity, $\widehat{v}$. By using the divergence-free constraint,

$$\frac{\partial\widehat{u}}{\partial x} + ik_z\widehat{w} = -\frac{\partial\widehat{v}}{\partial y} \tag{C.3}$$

and $\widehat{\omega}_2$, the wall-parallel velocities can be expressed as

$$\widehat{u} = \left(\partial_{xx} - k_z^2\right)^{-1}\left(ik_z\widehat{\omega}_2 - \frac{\partial^2\widehat{v}}{\partial x\partial y}\right) \tag{C.4}$$

$$\widehat{w} = \left(\partial_{xx} - k_z^2\right)^{-1}\left(-\frac{\partial\widehat{\omega}_2}{\partial x} - ik_z\frac{\partial\widehat{v}}{\partial y}\right). \tag{C.5}$$

By taking the wall-normal component of the curl of the momentum equation, the following equation can be found

$$\begin{aligned} -i\omega\widehat{\omega}_2 + \overline{\mathbf{U}}\cdot\nabla\widehat{\omega}_2 + \frac{\partial\overline{U}}{\partial x}\widehat{\omega}_2 - \frac{1}{Re}\nabla^2\widehat{\omega}_2 + \frac{\partial\overline{V}}{\partial x}\left(\partial_{xx} - k_z^2\right)^{-1}\frac{\partial^2\widehat{\omega}_2}{\partial x\partial y} \\ + ik_z\left(\frac{\partial\overline{U}}{\partial y}\widehat{v} + \frac{\partial\overline{V}}{\partial x}\left(\partial_{xx} - k_z^2\right)^{-1}\frac{\partial^2\widehat{v}}{\partial y^2}\right) = \widehat{f}_2, \end{aligned} \tag{C.6}$$

where $\widehat{f}_2 = ik_z\widehat{f}_u - \partial\widehat{f}_w\Big/\partial x$. Equation C.6 can be written as

$$\begin{aligned} \left(\mathcal{L}_{SQ} + \frac{\partial\overline{V}}{\partial x}\left(\partial_{xx} - k_z^2\right)^{-1}\frac{\partial^2}{\partial x\partial y}\right)\widehat{\omega}_2 + \left(ik_z\frac{\partial\overline{U}}{\partial y} + ik_z\frac{\partial\overline{V}}{\partial x}\left(\partial_{xx} - k_z^2\right)^{-1}\frac{\partial^2}{\partial y^2}\right)\widehat{v} \\ = \widehat{f}_2. \end{aligned} \tag{C.7}$$

The wall-normal vorticity component of Equation 3.10 is the same as Equation C.7, except with the terms involving $\partial\overline{V}\big/\partial x$ neglected.

Now, by taking the Laplacian of the wall-normal component of the momentum equation, the following equation can be found

$$-i\omega\nabla^2\widehat{v} + \nabla^2\left(\boldsymbol{\nabla}\widehat{v}\cdot\overline{\mathbf{U}} + \boldsymbol{\nabla}\overline{V}\cdot\widehat{\mathbf{u}}\right) - \frac{1}{Re}\nabla^4\widehat{v} + \frac{\partial\left(\nabla^2\widetilde{p}\right)}{\partial y} = \nabla^2\widehat{f}_{s,v}. \tag{C.8}$$

The dilatational piece of $\widehat{\mathbf{f}}$ is absorbed into $\widetilde{p}$. By using Equation C.2 and expanding some of the terms in Equation C.8, the equation becomes

$$\begin{aligned} -i\omega\nabla^2\widehat{v} + \nabla^2\left(\boldsymbol{\nabla}\widehat{v}\cdot\overline{\mathbf{U}} + \frac{\partial\overline{V}}{\partial y}\widehat{v}\right) - 2\frac{\partial}{\partial y}\left(\frac{\partial\overline{U}}{\partial y}\frac{\partial\widehat{v}}{\partial x} + \frac{\partial\overline{V}}{\partial y}\frac{\partial\widehat{v}}{\partial y}\right) - \frac{1}{Re}\nabla^4\widehat{v} \\ + \nabla^2\left(\frac{\partial\overline{V}}{\partial x}\widehat{u}\right) - 2\frac{\partial}{\partial y}\left(\frac{\partial\overline{U}}{\partial x}\frac{\partial\widehat{u}}{\partial x} + \frac{\partial\overline{V}}{\partial x}\frac{\partial\widehat{u}}{\partial y}\right) = \nabla^2\widehat{f}_{s,v}. \end{aligned} \tag{C.9}$$

By using Equation C.4, Equation C.9 can be expressed in terms of only $\widehat{v}$ and $\widehat{\omega}_2$, but the full expression is omitted for brevity. Since Equations C.6 and C.9 fully represent Equation 2.33 and eliminate $\widetilde{p}$, the $\widehat{p}$ and F do not affect the linear amplification. This observation was made in Rosenberg (2018). Due to this, the optimal forcing can be treated as solely solenoidal such that $\widehat{\mathbf{f}} = \widehat{\mathbf{f}}_s$.

These terms can be expanded such that

$$\begin{aligned} -i\omega\nabla^2\widehat{v} + \overline{\mathbf{U}}\cdot\left(\boldsymbol{\nabla}\left(\nabla^2\widehat{v}\right)\right) - \frac{\partial^2\overline{U}}{\partial y^2}\frac{\partial\widehat{v}}{\partial x} - \frac{1}{Re}\nabla^4\widehat{v} \\ + 2\left(\frac{\partial\overline{U}}{\partial x}\frac{\partial^2\widehat{v}}{\partial x^2} + \frac{\partial\overline{V}}{\partial x}\frac{\partial^2\widehat{v}}{\partial x\partial y}\right) + \frac{\partial}{\partial y}\left(\nabla^2\overline{V}\right)\widehat{v} + \left(\nabla^2\overline{V}\right)\frac{\partial\widehat{v}}{\partial y} \\ + 2\frac{\partial^2\overline{V}}{\partial x\partial y}\frac{\partial\widehat{v}}{\partial x} + \frac{\partial\overline{V}}{\partial y}\nabla^2\widehat{v} + \frac{\partial^2\overline{U}}{\partial x^2}\frac{\partial\widehat{v}}{\partial x} + \nabla^2\left(\frac{\partial\overline{V}}{\partial x}\widehat{u}\right) - 2\frac{\partial}{\partial y}\left(\frac{\partial\overline{V}}{\partial x}\frac{\partial\widehat{u}}{\partial y}\right) \\ + 2\left(\frac{\partial^2\overline{U}}{\partial x\partial y}\frac{\partial}{\partial x} + \frac{\partial\overline{U}}{\partial x}\frac{\partial^2}{\partial x\partial y}\right)\left(\partial_{xx} - k_z^2\right)^{-1}\left(\frac{\partial^2\widehat{v}}{\partial x\partial y} - ik_z\widehat{\omega}_2\right) = \nabla^2\widehat{f}_v. \end{aligned} \tag{C.10}$$

Note that the $\widehat{u}$ terms can still be expanded. This form agrees with the terms in Ran et al. (2019), if the terms involving $\partial\overline{V}\big/\partial x$ and $\partial\overline{U}\big/\partial xx$ are neglected. The first 4 terms can be expressed as $\nabla^2\mathcal{L}_{OS}$. Finally, the inverse Laplacian can be applied to both sides to complete the OSS formulation of the biglobal analysis. This formulation involves $\left(\partial_{xx} - k_z^2\right)^{-1}$, ∇^{-2}, and second and third order derivatives of $\overline{\mathbf{U}}$.

Appendix D

DOMAIN LENGTH EFFECTS ON SWEEPS

D.1 Domain Length Effect on Small Scales

By increasing Re_τ and holding L_x^+ constant, L_x/δ_{99} decreases. As a result, large scale modes, which scale with outer units, are suppressed since they are not supported in these smaller domains. To show that the domain length suppresses large scale modes, the inner sweep for b1nI in Section 4.3 will be recomputed by restricting the domain from $L_x^+ = 9000$ to $L_x^+ = 2150$. The parameters of the sweep will be kept the same, except for a smaller domain and $N_x = 150$.

In Figure D.1, the results of the sweep using $L_x^+ = 2150$ are compared to the original sweep using $L_x^+ = 9000$. The near-wall peak moves from $\lambda_z^+ = 116$ when using $L_x^+ = 9000$ to $\lambda_z^+ = 63$ when using $L_x^+ = 2150$. The location of the near-wall peak also moves closer to the wall, in accordance with the smaller energetic structures in the smaller domain. There is a decrease in amplification of $\lambda_z^+ = 100$ when the domain size is decreased. Furthermore, the $L_x^+ = 2150$ sweep has a decrease in amplification of the large scales because the domain size is decreased in both inner and outer units. The decrease in the amplification of the large scales is similar to what was observed in Figure 3.11 where increasing Re_τ and fixed L_x^+ decreased the outer scaled domain length and the amplification of the large scales. The observations

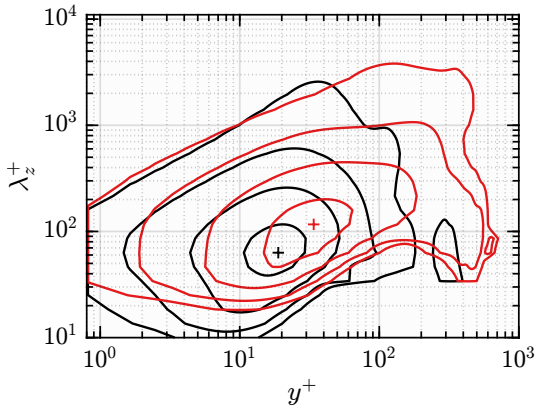

Figure D.1: Comparison of inner scaled sweep for b1nI from Table 4.1 where the black corresponds to $L_x^+ = 2150$ and red to $L_x = 9000$. The contour levels are .1%, 1%, 10%, 60%, and 90% of the maximum value of each sweep. The crosses denote the maximum value of each sweep.

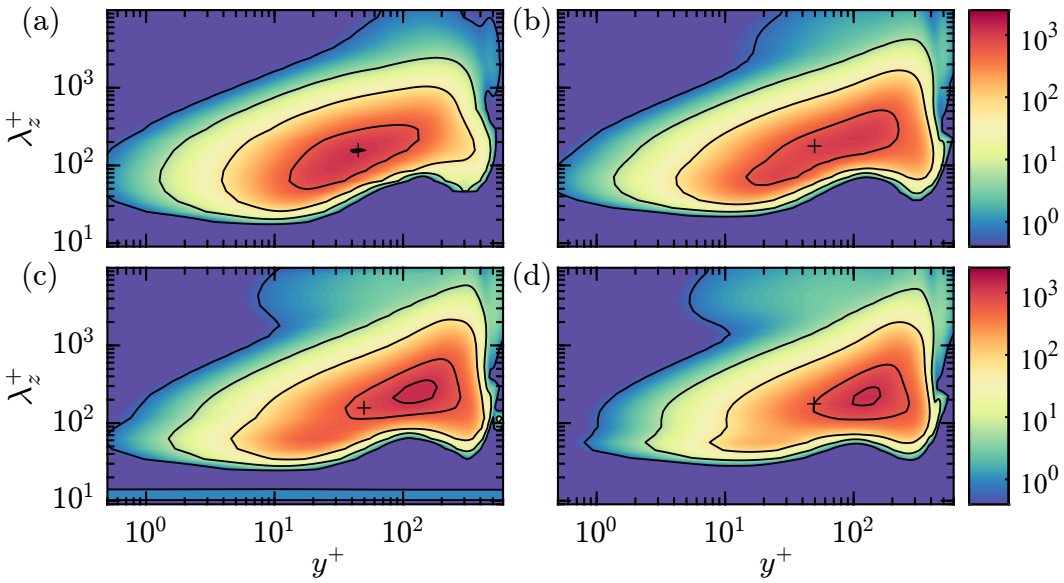

Figure D.2: Figure 4.14 replotted using a longer domain for Ω_r in Equation 4.9.

made here extend to those made with the high *Re* ZPG TBL since the APG affects $\overline{U}$ mostly in $y^+ \geq 100$ where E_{uu}^+ is suppressed.

D.2 Domain Length Effect on Large Scale Amplification

The inner product for the response modes in Section 4.4 only considered the energy of the response modes within Ω_r which had a streamwise length of $4\delta_{99}(x_c)$ to ensure that the small scales were centered at x_c. Here, the calculations are recomputed with $\Omega_r = [x_c - 6.5\delta_{99}, x_c + 6.5\delta_{99}] \times [0, y_{max}]$ for a streamwise length of $13\delta_{99}$. In Figure 4.14, $E_{uu}^+(x_c, y, k_z)$ is plotted for the same datasets as Section 4.4 and the updated $\langle \cdot, \cdot \rangle_r$. Once again, there is no secondary peak in S0 and there are large secondary peaks in the outer region. The outer region amplification increases with $\overline{\beta}$, though m18n has less amplification in the outer region than b2n. There is a peak near the wall, though this peak is not as amplified as the one seen in Section 4.4. This is likely because the large domain in Ω_r keeps the small scale modes from being centered at x_c.

In Figure D.3, K_{uu}^+ is replotted with the new inner product for the response modes. The inner peak in K_{uu}^+ is weakened in b2n and m18n because the small scales are outside of the interrogation window. The outer scaled peak is prominent in the APG TBL and absent in the ZPG TBL. The outer peak in m18n is smaller than the outer peak in b2n, which was not observed in Figure 4.16. The difference is likely due to the smaller domain length in m18n than b2n. The modes for b2n have a larger

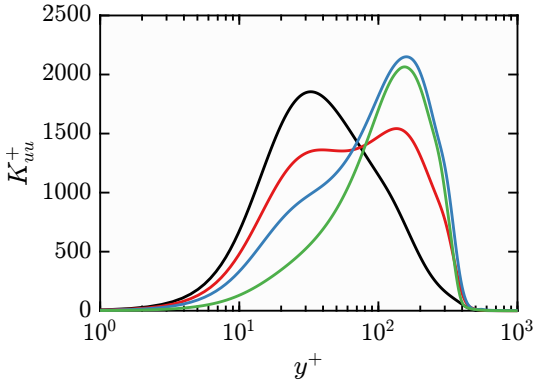

Figure D.3: Figure 4.16 replotted using a longer domain for Ω_r in Equation 4.9.

domain upstream of Ω_r to allow $\boldsymbol{\phi}_1$ to develop and force $\boldsymbol{\psi}_1$ within Ω_r. This effect is less prominent when Ω_r is smaller because Ω_r is far upstream from the inlet allowing $\boldsymbol{\phi}_1$ to sufficiently develop downstream.

Appendix E

LINEAR TERMS OF THE NAVIER STOKES EQUATIONS FOR A HYPERSONIC TURBULENT BOUNDARY LAYER

E.1 Preliminaries

The following relation will be used to linearize the left hand side of the equations, which are of the form $\breve{f}D\breve{g}/Dt$ for quantities $\breve{f}$ and $\breve{g}$. Assuming that $\breve{f} = \overline{f}(y) + f(x,y,z,t)$, $\breve{g} = \overline{g}(y) + g(x,y,z,t)$, and $\breve{\mathbf{u}} = \overline{U}(y)\mathbf{e}_x + \mathbf{u}(x,y,z,t)$ then

$$\breve{f}\frac{D\breve{g}}{Dt} = \overline{f}\left(\frac{\partial g}{\partial t} + \overline{u}\frac{\partial g}{\partial x} + \frac{\partial \overline{g}}{\partial y}v\right) + f\left(\frac{\partial \overline{g}}{\partial t} + \overline{g}\boldsymbol{\nabla}\cdot\overline{\mathbf{u}} + \overline{\mathbf{u}}\cdot\boldsymbol{\nabla}\overline{g}\right) + n.l. \tag{E.1}$$

$$= \overline{f}\left(\frac{\partial g}{\partial t} + \overline{u}\frac{\partial g}{\partial x} + \frac{\partial \overline{g}}{\partial y}v\right) + n.l., \tag{E.2}$$

where $n.l.$ denotes nonlinear terms. The linear terms of $\breve{f}D\breve{g}/Dt$ do not include any variation in $\breve{\mathbf{f}}$, and only have the variation of $\breve{\mathbf{g}}$ and the shear-driven term $\overline{f}\frac{\partial \overline{g}}{\partial y}v$. For shorthand,

$$\frac{\partial \overline{f}}{\partial q_j} = \left.\frac{\partial \breve{f}}{\partial q_j}\right|_{\overline{\mathbf{q}}} \tag{E.3}$$

will also be used interchangeably. Finally, as a reminder,

$$\overline{f} = \breve{f}(\overline{\mathbf{q}}) \tag{E.4}$$

which ensures that if $\breve{f} = 0$, then $\overline{f} = 0$.

E.2 Linearization of the Single Species CIG Equations

Assuming that $\breve{\mathbf{q}} = \overline{\mathbf{q}}(y) + \mathbf{q}(x,y,z,t)$ with $\mathbf{q} = [u, v, w, T, \rho]$, Equation 5.1, can be rewritten as

$$\begin{aligned}\overline{\rho}\left(\frac{\partial u_i}{\partial t} + \frac{\partial \overline{U}}{\partial y}v\delta_{i1} + \overline{U}\frac{\partial u_i}{\partial x}\right) = &-\frac{1}{\gamma_e Ma^2}\left\{\frac{\partial}{\partial y}\left(\left.\frac{\partial p}{\partial \theta_j}\right|_{\overline{\theta}}\right)\theta_j\delta_{i,2} + \left.\frac{\partial p}{\partial \theta_j}\right|_{\overline{\theta}}\nabla\theta_j\right\}\\ &+\frac{1}{Re}\left\{\frac{\partial \overline{\mu}}{\partial y}\left(\frac{\partial u_i}{\partial y} + \frac{\partial v}{\partial x_i} - \frac{2}{3}\frac{\partial u_j}{\partial x_j}\delta_{i2}\right) + \delta_{i,1}\frac{\partial \overline{U}}{\partial y}\frac{\partial \mu}{\partial y}\right.\\ &\left.+\overline{\mu}\left(\frac{\partial^2 u_i}{\partial x_j^2} + \frac{1}{3}\frac{\partial^2 u_i}{\partial x_i \partial x_j}\right) + \delta_{i,1}\frac{\partial^2 \overline{U}}{\partial y^2}\mu + \delta_{i,2}\frac{\partial \overline{U}}{\partial y}\frac{\partial \mu}{\partial x}\right\}\\ &+n.l.,\end{aligned} \tag{E.5}$$

where $\partial_{x_1} = ik_x$, $\partial_{x_2} = \partial_y$, and $\partial_{x_3} = ik_z$ and $n.l.$ denotes the nonlinear terms. Note that ∂_x denotes ik_x. Note that index notation is assumed and that $\breve{\theta} = [\breve{T}, \breve{\rho}]$. Equation 5.3 is then

$$\frac{\partial \rho}{\partial t} + \overline{U}\frac{\partial \rho}{\partial x} + \frac{\partial \overline{\rho}}{\partial y}v = \overline{\rho}\boldsymbol{\nabla}\cdot\mathbf{u} + n.l. \tag{E.6}$$

Finally, Equation 5.2 becomes

$$\overline{c}_v\overline{\rho}\left(\frac{\partial T}{\partial t} + \overline{U}\frac{\partial T}{\partial x} + \frac{\partial \overline{T}}{\partial y}v\right) = -(\gamma_e - 1)\overline{p}\nabla\cdot\mathbf{u} + (\gamma_e - 1)\gamma_e\frac{Ma^2}{Re}\left\{\left(\frac{\partial \overline{U}}{\partial y}\right)^2\mu + 2\overline{\mu}\left(\frac{\partial \overline{U}}{\partial y}\frac{\partial u}{\partial y} + ik_x\frac{\partial \overline{U}}{\partial y}v\right)\right\} + \frac{\gamma_e}{PrRe}\left(\frac{\partial \overline{k}}{\partial y}\frac{\partial T}{\partial y} + \overline{k}\nabla^2 T + \frac{\partial \overline{T}}{\partial y}\frac{\partial k}{\partial y} + \frac{\partial^2 \overline{T}}{\partial y^2}k\right). \tag{E.7}$$

Once it is assumed that $\mathbf{q} = \widehat{\mathbf{q}}(y)\exp(-i\omega t + ik_x x + ik_z z)$, then $\widehat{\mathcal{L}}$ can be defined.

Explicitly, the $L_{i,j}$ terms in Equation 5.9 are

$$L_{1,1} = ik_x\overline{U} - \frac{1}{\overline{\rho}Re}\left[\frac{\partial \overline{\mu}}{\partial y}\frac{\partial}{\partial y} + \overline{\mu}\left(-\frac{4}{3}k_x^2 - k_z^2 + \frac{\partial^2}{\partial y^2}\right)\right] \tag{E.8}$$

$$L_{1,2} = \frac{\partial \overline{U}}{\partial y} - \frac{1}{\overline{\rho}Re}\left[ik_x\frac{\partial \overline{\mu}}{\partial y} + \frac{1}{3}ik_x\overline{\mu}\frac{\partial}{\partial y}\right] \tag{E.9}$$

$$L_{1,3} = \frac{1}{3}\frac{1}{\overline{\rho}Re}k_x k_z\overline{\mu} \tag{E.10}$$

$$L_{1,4} = \frac{ik_x}{\gamma_e Ma^2}\frac{1}{\overline{\rho}}\frac{\partial \overline{p}}{\partial T} - \frac{1}{\overline{\rho}Re}\frac{\partial \overline{U}}{\partial y}\left[\frac{\partial}{\partial y}\left(\frac{\partial \overline{\mu}}{\partial T}\right) + \frac{\partial \overline{\mu}}{\partial T}\frac{\partial}{\partial y}\right] - \frac{1}{\overline{\rho}Re}\frac{\partial^2 \overline{U}}{\partial y^2}\frac{\partial \overline{\mu}}{\partial T} \tag{E.11}$$

$$L_{1,5} = \frac{ik_x}{\gamma_e Ma^2}\frac{1}{\overline{\rho}}\frac{\partial \overline{p}}{\partial \rho} \tag{E.12}$$

$$L_{2,1} = -\frac{1}{\overline{\rho}Re}\left[-\frac{2}{3}ik_x\frac{\partial \overline{\mu}}{\partial y} + \frac{1}{3}ik_x\overline{\mu}\frac{\partial}{\partial y}\right] \tag{E.13}$$

$$L_{2,2} = ik_x\overline{U} - \frac{1}{\overline{\rho}Re}\left[\frac{4}{3}\frac{\partial \overline{\mu}}{\partial y}\frac{\partial}{\partial y} + \overline{\mu}\left(-k_x^2 - k_z^2 + \frac{4}{3}\frac{\partial^2}{\partial y^2}\right)\right] \tag{E.14}$$

$$L_{2,3} = -ik_z\frac{1}{\overline{\rho}Re}\left[-\frac{2}{3}\frac{\partial \overline{\mu}}{\partial y} + \frac{1}{3}\overline{\mu}\frac{\partial}{\partial y}\right] \tag{E.15}$$

$$L_{2,4} = \frac{1}{\gamma_e Ma^2\overline{\rho}}\left[\frac{\partial}{\partial y}\left(\frac{\partial \overline{p}}{\partial T}\right) + \frac{\partial \overline{p}}{\partial T}\frac{\partial}{\partial y}\right] - ik_x\frac{1}{\overline{\rho}Re}\frac{\partial \overline{U}}{\partial y}\frac{\partial \overline{\mu}}{\partial T} \tag{E.16}$$

$$L_{2,5} = \frac{1}{\gamma_e Ma^2\overline{\rho}}\left[\frac{\partial}{\partial y}\left(\frac{\partial \overline{p}}{\partial \rho}\right) + \frac{\partial \overline{p}}{\partial \rho}\frac{\partial}{\partial y}\right] \tag{E.17}$$

$$L_{3,1} = \frac{1}{3}\frac{1}{\overline{\rho}Re}\overline{\mu}k_z k_x \tag{E.18}$$

$$L_{3,2} = -\frac{1}{\overline{\rho}Re}ik_z\left[\frac{\partial\overline{\mu}}{\partial y} + \frac{1}{3}\overline{\mu}\frac{\partial}{\partial y}\right] \tag{E.19}$$

$$L_{3,3} = ik_x\overline{U} - \frac{1}{\overline{\rho}Re}\left[\frac{\partial\overline{\mu}}{\partial y}\frac{\partial}{\partial y} + \overline{\mu}\left(-\frac{4}{3}k_x^2 - k_z^2 + \frac{\partial^2}{\partial y^2}\right)\right] \tag{E.20}$$

$$L_{3,4} = \frac{ik_z}{\gamma_e Ma^2}\frac{1}{\overline{\rho}}\frac{\partial\overline{p}}{\partial T} \tag{E.21}$$

$$L_{3,5} = \frac{ik_z}{\gamma_e Ma^2}\frac{1}{\overline{\rho}}\frac{\partial\overline{p}}{\partial \rho} \tag{E.22}$$

$$L_{4,1} = \frac{ik_x}{\overline{c}_v\overline{\rho}}(\gamma_e - 1)\overline{p} - 2\frac{(\gamma_e - 1)\gamma_e Ma^2}{\overline{c}_v\overline{\rho}Re}\overline{\mu}\frac{\partial\overline{U}}{\partial y}\frac{\partial}{\partial y} \tag{E.23}$$

$$L_{4,2} = \frac{\partial\overline{T}}{\partial y} + \frac{(\gamma_e - 1)}{\overline{c}_v\overline{\rho}}\overline{p}\frac{\partial}{\partial y} - 2ik_x\frac{(\gamma_e - 1)\gamma_e Ma^2}{\overline{c}_v\overline{\rho}Re}\overline{\mu}\frac{\partial\overline{U}}{\partial y} \tag{E.24}$$

$$L_{4,3} = ik_z\frac{(\gamma_e - 1)}{\overline{c}_v\overline{\rho}}\overline{p} \tag{E.25}$$

$$\begin{aligned} L_{4,4} = \left(ik_x\overline{U}\right) - \frac{\gamma_e}{\overline{c}_v\overline{\rho}PrRe}\Bigg[&\frac{\partial\overline{k}}{\partial y}\frac{\partial}{\partial y} + \overline{k}\left(-k_x^2 - k_z^2 + \frac{\partial^2}{\partial y^2}\right) + \frac{\partial^2\overline{T}}{\partial y^2}\frac{\partial\overline{k}}{\partial T} \\ &+\frac{\partial\overline{T}}{\partial y}\frac{\partial}{\partial y}\left(\frac{\partial\overline{k}}{\partial T}\right) + \frac{\partial\overline{T}}{\partial y}\frac{\partial\overline{k}}{\partial T}\frac{\partial}{\partial y}\Bigg] - \frac{(\gamma_e - 1)\gamma_e Ma^2}{\overline{c}_v\overline{\rho}Re}\left(\frac{\partial\overline{U}}{\partial y}\right)^2\frac{\partial\overline{\mu}}{\partial T} \end{aligned} \tag{E.26}$$

$$L_{4,5} = 0 \tag{E.27}$$

$$L_{5,1} = ik_x\overline{\rho} \tag{E.28}$$

$$L_{5,2} = \frac{\partial\overline{\rho}}{\partial y} + \overline{\rho}\frac{\partial}{\partial y} \tag{E.29}$$

$$L_{5,3} = ik_z\overline{\rho} \tag{E.30}$$

$$L_{5,4} = 0 \tag{E.31}$$

$$L_{5,5} = ik_x\overline{U} \tag{E.32}$$

Since the temperature equation related terms, ($L_{4,i}$) are the only terms with $\overline{c}_v$ and $\overline{k}$, these are the only terms in the LNSE that are explicitly affected by the CIG assumption.

E.3 Linearization of the Governing Equations for a Mixture of Ideal Gases in Chemical Nonequilibrium

Just as in the previous section, $\breve{\mathbf{q}} = \overline{\mathbf{q}}(y) + \mathbf{q}(x, y, z, t)$ will be used to separate the linear and nonlinear equations. Before advancing, the diffusive flux will be defined

as

$$\breve{\mathbf{d}}_{i_s} = \breve{\rho}_{i_s} \breve{\mathbf{V}}_{i_s} \tag{E.33}$$

to simplify some terms. The linearization of Equation 5.15 is the same as Equation E.5, except that the fluctuation $\mu = \sum_i \frac{\partial \mu}{\partial \theta_i}\Big|_{\overline{\theta}} \theta_i$ where $\breve{\theta} = \left[\breve{T}, \breve{\rho}_{N_2}, \breve{\rho}_{O_2}, \breve{\rho}_{NO}, \breve{\rho}_N, \breve{\rho}_O\right]$. Equation 5.17 becomes

$$\left(\frac{\partial \rho_{i_s}}{\partial t} + \overline{u}\frac{\partial \rho_{i_s}}{\partial x} + \frac{\partial \overline{\rho}_{i_s}}{\partial y} v\right) = -\overline{\rho}_{i_s} \nabla \cdot \mathbf{u} - \nabla \cdot \mathbf{d}_{i_s} + \dot{\omega}_{i_s} + n.l. \tag{E.34}$$

Before continuing, it is worth making some notes on the diffusive fluxes and the chemical rates of mass production. In order to conserve mass, the diffusive velocities and chemical rates of mass production are defined such that

$$\sum_i^{N_s} \breve{\mathbf{d}}_i = \sum_i^{N_s} \breve{\rho}_i \breve{\mathbf{V}}_i = \mathbf{0} \tag{E.35}$$

$$\sum_i^{N_s} \breve{\dot{\omega}}_i = 0. \tag{E.36}$$

This ensures that

$$\sum_i^{N_s} \overline{\mathbf{d}}_i = \sum_i^{N_s} \overline{\rho}_i \overline{\mathbf{V}}_i = \mathbf{0}, \tag{E.37}$$

$$\sum_i^{N_s} \overline{\dot{\omega}}_i = 0. \tag{E.38}$$

It follows then that for the fluctuations,

$$\sum_i^{N_s} \mathbf{d}_i = \sum_i^{N_s} (\rho_i \bar{\mathbf{V}}_i + \bar{\rho}_i \mathbf{V}_i) = \mathbf{0}, \tag{E.39}$$

$$\sum_i^{N_s} \dot{\omega}_i = \sum_i^{N_s} \frac{\partial \overline{\dot{\omega}}_i}{\partial \theta_j} \theta_j = 0, \tag{E.40}$$

where summation over j is implied. Hence, if Equation E.34 is summed over i_s, then

$$\frac{\partial \rho}{\partial t} + \overline{U}\frac{\partial \rho}{\partial x} + \frac{\partial \overline{\rho}}{\partial y} v = \overline{\rho} \boldsymbol{\nabla} \cdot \mathbf{u} + n.l. \tag{E.41}$$

is recovered. So using the linear individual species continuity equations enforces the linear mixture continuity equation.

Equation 5.16 becomes

$$\begin{aligned}\overline{c}_v\overline{\rho}\left(\frac{\partial T}{\partial t}+\overline{u}\frac{\partial T}{\partial x}+\frac{\partial \overline{T}}{\partial y}v\right)=&-(\gamma_e-1)\overline{p}\nabla\cdot\mathbf{u}+\frac{(\gamma_e-1)\gamma_e Ma^2}{Re}\left\{\left(\frac{\partial\overline{u}}{\partial y}\right)^2\mu+\right.\\&\left.2\overline{\mu}\left(\frac{\partial\overline{u}}{\partial y}\frac{\partial u}{\partial y}+ik_x\frac{\partial\overline{u}}{\partial y}v\right)\right\}+\frac{\gamma_e}{PrRe}\left(\frac{\partial\overline{k}}{\partial y}\frac{\partial T}{\partial y}+\overline{k}\nabla^2T+\frac{\partial\overline{T}}{\partial y}\frac{\partial k}{\partial y}+\frac{\partial^2\overline{T}}{\partial y^2}k\right)+\\&\sum_{i_s}^{N_s}\left[-\overline{\dot{\omega}}_{i_s}e_{i_s}-\frac{\gamma_e}{Re}\left\{\frac{\partial\overline{T}}{\partial y}\overline{\rho}_{i_s}\overline{V}_{i_s}c_{p,i_s}+\overline{c}_{p,i_s}\left(\frac{\partial\overline{T}}{\partial y}d_{2,i_s}+\overline{\rho}_{i_s}\overline{V}_{i_s}\frac{\partial T}{\partial y}\right)\right\}\right.\\&\left.+\frac{\overline{M}_e}{M_{i_s}}\frac{\gamma_e-1}{Re}\left(\overline{T}\nabla\cdot\mathbf{d}_{i_s}+\frac{\partial(\overline{\rho}_{i_s}\overline{V}_{i_s})}{\partial y}T\right)-\overline{e}_{i_s}\dot{\omega}_{i_s}-\overline{\dot{\omega}}_{i_s}e_{i_s}\right],\end{aligned}\tag{E.42}$$

where d_{2,i_s} denotes the wall-normal component of $\mathbf{d}_{i_s}$.

Equations E.34 and E.42 make use of $\breve{\mathbf{d}}_{i_s}$. Here, this term will be expanded explicitly. To do so, Equation 5.20 will set $W_{i_s}=M_{i_s}^{-1}$. As such, Equation 5.20 will be written as

$$\breve{\mathbf{d}}_i=\breve{\rho}_i\breve{\mathbf{V}}_i=-\frac{\breve{D}_i}{Sc_i}\frac{\breve{\rho}_kW_k}{W_i}\nabla\breve{X}_i+\breve{Y}_i\sum_{j=1}^{N_s}\frac{\breve{D}_j}{Sc_j}\frac{\breve{\rho}_kW_k}{W_j}\nabla\breve{X}_j,\tag{E.43}$$

where the summation over k is implied through indicial notation. The mean $\overline{\mathbf{d}}_i$ is

$$\overline{\mathbf{d}}_i=\overline{\rho}_i\overline{V}_i\mathbf{e}_y=\left(-\frac{\overline{D}_i}{Sc_i}\frac{\overline{\rho}_kW_k}{W_i}\frac{\mathrm{d}\overline{X}_i}{\mathrm{d}y}+\overline{Y}_i\sum_{j=1}^{N_s}\frac{\overline{D}_j}{Sc_j}\frac{\overline{\rho}_kW_k}{W_j}\frac{\mathrm{d}\overline{X}_j}{\mathrm{d}y}\right)\mathbf{e}_y.\tag{E.44}$$

Now for the fluctuation $\mathbf{d}_i$,

$$\begin{aligned}\mathbf{d}_i=&-\frac{\overline{D}_i}{Sc_i}\frac{\overline{\rho}_lW_l}{W_i}\left[\frac{\partial}{\partial y}\left(\frac{\partial\overline{X}_i}{\partial\rho_j}\rho_j\right)\mathbf{e}_y+\frac{\partial\overline{X}_i}{\partial\rho_j}\nabla\rho_j\right]\\&-\frac{\partial\overline{X}_i}{\partial y}\left[\frac{\overline{\rho}_lW_l}{W_i}\frac{\partial D_i}{\partial\theta_j}\frac{\theta_j}{Sc_i}+\frac{\overline{D}_i}{Sc_i}\frac{W_j}{W_i}\rho_j\right]\mathbf{e}_y\\&+\overline{Y}_i\sum_{k=1}^{N_s}\left\{\frac{\overline{D}_k}{Sc_k}\frac{\overline{\rho}_lW_l}{W_k}\left[\frac{\partial}{\partial y}\left(\frac{\partial\overline{X}_k}{\partial\rho_j}\right)\rho_j\mathbf{e}_y+\frac{\partial\overline{X}_k}{\partial\rho_j}\nabla\rho_j\right]+\frac{\partial\overline{X}_k}{\partial y}\left[\frac{\overline{\rho}_lW_l}{W_k}\frac{\partial D_k}{\partial\theta_j}\frac{\theta_j}{Sc_k}\right.\right.\\&\left.\left.+\frac{\overline{D}_k}{Sc_k}\frac{W_j}{W_k}\rho_j\right]\mathbf{e}_y\right\}+\left(\sum_{k=1}^{N_s}\frac{\overline{D}_k}{Sc_k}\frac{\overline{\rho}_lW_l}{W_k}\frac{\partial\overline{X}_k}{\partial y}\right)\frac{\partial\overline{Y}_i}{\partial\rho_j}\rho_j\mathbf{e}_y\\=&A_{i,j}(y)\theta_j\mathbf{e}_y+B_{i,j}(y)\nabla\theta_j,\end{aligned}\tag{E.45}$$

where $A_{i,j}$ and $B_{i,j}$ are defined to shorten the equations and summation over j and l is implied. The expressions for $A_{i,j}$ and $B_{i,j}$ are

$$\begin{aligned} A_{i,j} = &- \frac{\overline{D}_i}{Sc_i}\frac{\overline{\rho}_l W_l}{W_i}\frac{\partial}{\partial y}\left(\frac{\partial \overline{X}_i}{\partial \theta_j}\right) - \frac{1}{Sc_i}\frac{\partial \overline{X}_i}{\partial y}\left[\frac{\overline{\rho}_l W_l}{W_i}\frac{\partial D_i}{\partial \theta_j} + \overline{D}_i\frac{W_j}{W_i}\right] \\ &+ \left(\sum_{k=1}^{N_s}\frac{\overline{D}_k}{Sc_k}\frac{\overline{\rho}_l W_l}{W_k}\frac{\partial \overline{X}_k}{\partial y}\right)\frac{\partial \overline{Y}_i}{\partial \rho_j} \\ &+ \overline{Y}_i\sum_{k=1}^{N_s}\left\{\frac{\overline{D}_k}{Sc_k}\frac{\overline{\rho}_l W_l}{W_k}\frac{\partial}{\partial y}\left(\frac{\partial \overline{X}_k}{\partial \theta_j}\right) - \frac{1}{Sc_k}\frac{\partial \overline{X}_k}{\partial y}\left[\frac{\overline{\rho}_l W_l}{W_k}\frac{\partial D_k}{\partial \theta_j} + \overline{D}_k\frac{W_j}{W_k}\right]\right\} \end{aligned} \tag{E.46}$$

$$B_{i,j} = -\frac{\overline{D}_i}{Sc_i}\frac{\overline{\rho}_l W_l}{W_i}\frac{\partial \overline{X}_i}{\partial \rho_j} + \overline{Y}_i\sum_{k=1}^{N_s}\frac{\overline{D}_k}{Sc_k}\frac{\overline{\rho}_l W_l}{W_k}\frac{\partial \overline{X}_k}{\partial \rho_j}. \tag{E.47}$$

As Anderson Jr. (2006) notes:

> Clearly, you can see that a major aspect of such a nonequlibrium analysis is simply bookkeeping, making certain to keep track of all of the terms in the equations.

This becomes apparent for the block entries in Equation 5.24 listed below.

$$L_{1,1} = ik_x\overline{u} - \frac{1}{\overline{\rho}Re}\left[\frac{\partial \overline{\mu}}{\partial y}\frac{\partial}{\partial y} + \overline{\mu}\left(-\frac{4}{3}k_x^2 - k_z^2 + \frac{\partial^2}{\partial y^2}\right)\right] \tag{E.48}$$

$$L_{1,2} = \frac{\partial \overline{u}}{\partial y} - \frac{1}{\overline{\rho}Re}\left[ik_x\frac{\partial \overline{\mu}}{\partial y} + \frac{1}{3}ik_x\overline{\mu}\frac{\partial}{\partial y}\right] \tag{E.49}$$

$$L_{1,3} = \frac{1}{3}\frac{1}{\overline{\rho}Re}k_x k_z\overline{\mu} \tag{E.50}$$

$$L_{1,4} = \frac{ik_x}{\gamma_e Ma^2}\frac{1}{\overline{\rho}}\frac{\partial \overline{p}}{\partial T} - \frac{1}{\overline{\rho}Re}\frac{\partial \overline{u}}{\partial y}\left[\frac{\partial}{\partial y}\left(\frac{\partial \overline{\mu}}{\partial T}\right) + \frac{\partial \overline{\mu}}{\partial T}\frac{\partial}{\partial y}\right] - \frac{1}{\overline{\rho}Re}\frac{\partial^2 \overline{u}}{\partial y^2}\frac{\partial \overline{\mu}}{\partial T} \tag{E.51}$$

$$L_{1,4+i} = \frac{ik_x}{\gamma_e Ma^2}\frac{1}{\overline{\rho}}\frac{\overline{M}_e\overline{T}}{M_i} - \frac{1}{\overline{\rho}Re}\frac{\partial \overline{u}}{\partial y}\left[\frac{\partial}{\partial y}\left(\frac{\partial \overline{\mu}}{\partial \rho_i}\right) + \frac{\partial \overline{\mu}}{\partial \rho_i}\frac{\partial}{\partial y}\right] - \frac{1}{\overline{\rho}Re}\frac{\partial^2 \overline{u}}{\partial y^2}\frac{\partial \overline{\mu}}{\partial \rho_i} \tag{E.52}$$

$$L_{2,1} = -\frac{1}{\overline{\rho}Re}\left[-\frac{2}{3}ik_x\frac{\partial \overline{\mu}}{\partial y} + \frac{1}{3}ik_x\overline{\mu}\frac{\partial}{\partial y}\right] \tag{E.53}$$

$$L_{2,2} = ik_x\overline{u} - \frac{1}{\overline{\rho}Re}\left[\frac{4}{3}\frac{\partial \overline{\mu}}{\partial y}\frac{\partial}{\partial y} + \overline{\mu}\left(-k_x^2 - k_z^2 + \frac{4}{3}\frac{\partial^2}{\partial y^2}\right)\right] \tag{E.54}$$

$$L_{2,3} = -ik_z\frac{1}{\overline{\rho}Re}\left[-\frac{2}{3}\frac{\partial \overline{\mu}}{\partial y} + \frac{1}{3}\overline{\mu}\frac{\partial}{\partial y}\right] \tag{E.55}$$

$$L_{2,4} = \frac{1}{\gamma_e Ma^2 \overline{\rho}} \left[\frac{\partial}{\partial y} \left(\frac{\partial \overline{p}}{\partial T} \right) + \frac{\partial p}{\partial T} \frac{\partial}{\partial y} \right] - ik_x \frac{1}{\overline{\rho} Re} \frac{\partial \overline{u}}{\partial y} \frac{\partial \overline{\mu}}{\partial T} \tag{E.56}$$

$$L_{2,4+i} = \frac{1}{\gamma_e Ma^2 \overline{\rho}} \frac{\overline{M}_e}{M_i} \left[\frac{\partial \overline{T}}{\partial y} + \overline{T} \frac{\partial}{\partial y} \right] - ik_x \frac{1}{\overline{\rho} Re} \frac{\partial \overline{u}}{\partial y} \frac{\partial \overline{\mu}}{\partial \rho_i} \tag{E.57}$$

$$L_{3,1} = \frac{1}{3} \frac{1}{\overline{\rho} Re} \overline{\mu} k_z k_x \tag{E.58}$$

$$L_{3,2} = -\frac{1}{\overline{\rho} Re} ik_z \left[\frac{\partial \overline{\mu}}{\partial y} + \frac{1}{3} \overline{\mu} \frac{\partial}{\partial y} \right] \tag{E.59}$$

$$L_{3,3} = ik_x \overline{u} - \frac{1}{\overline{\rho} Re} \left[\frac{\partial \overline{\mu}}{\partial y} \frac{\partial}{\partial y} + \overline{\mu} \left(-\frac{4}{3} k_x^2 - k_z^2 + \frac{\partial^2}{\partial y^2} \right) \right] \tag{E.60}$$

$$L_{3,4} = \frac{ik_z}{\gamma_e Ma^2} \frac{1}{\overline{\rho}} \frac{\partial \overline{p}}{\partial T} \tag{E.61}$$

$$L_{3,4+i} = \frac{ik_z}{\gamma_e Ma^2} \frac{1}{\overline{\rho}} \frac{\overline{M}_e \overline{T}}{M_i} \tag{E.62}$$

$$L_{4,1} = \frac{ik_x}{\overline{c}_v \overline{\rho}} (\gamma_e - 1) \overline{p} - 2 \frac{(\gamma_e - 1) \gamma_e Ma^2}{\overline{c}_v \overline{\rho} Re} \overline{\mu} \frac{\partial \overline{u}}{\partial y} \frac{\partial}{\partial y} \tag{E.63}$$

$$L_{4,2} = \frac{\partial \overline{T}}{\partial y} + \frac{(\gamma_e - 1)}{\overline{c}_v \overline{\rho}} \overline{p} \frac{\partial}{\partial y} - 2ik_x \frac{(\gamma_e - 1) \gamma_e Ma^2}{\overline{c}_v \overline{\rho} Re} \overline{\mu} \frac{\partial \overline{u}}{\partial y} \tag{E.64}$$

$$L_{4,3} = ik_z \frac{(\gamma_e - 1)}{\overline{c}_v \overline{\rho}} \overline{p} \tag{E.65}$$

$$\begin{aligned} L^e_{4,4} = (ik_x \overline{u}) - \frac{\gamma_e}{\overline{c}_v \overline{\rho} PrRe} \Bigg[& \frac{\partial \overline{k}}{\partial y} \frac{\partial}{\partial y} + \overline{k} \left(-k_x^2 - k_z^2 + \frac{\partial^2}{\partial y^2} \right) + \frac{\partial^2 \overline{T}}{\partial y^2} \frac{\partial \overline{k}}{\partial T} \\ & + \frac{\partial \overline{T}}{\partial y} \frac{\partial}{\partial y} \left(\frac{\partial \overline{k}}{\partial T} \right) + \frac{\partial \overline{T}}{\partial y} \frac{\partial \overline{k}}{\partial T} \frac{\partial}{\partial y} \Bigg] - \frac{(\gamma_e - 1) \gamma_e Ma^2}{\overline{c}_v \overline{\rho} Re} \left(\frac{\partial \overline{u}}{\partial y} \right)^2 \frac{\partial \overline{\mu}}{\partial T} \end{aligned} \tag{E.66}$$

$$\begin{aligned} L^n_{4,4} = & \frac{1}{\overline{c}_v \overline{\rho}} \sum_{j=1}^{N_s} \left(\overline{\dot{\omega}}_j \frac{\partial \overline{e}_j}{\partial T} + \overline{e}_j \frac{\partial \overline{\dot{\omega}}_j}{\partial T} \right) + \frac{\gamma_e}{\overline{c}_v \overline{\rho} Re} \sum_{j=1}^{N_s} \Bigg[\frac{\partial \overline{T}}{\partial y} \frac{\overline{\rho}_j \overline{V}_j}{Sc_j} \frac{\partial \overline{c}_{p,j}}{\partial T} \\ & + \overline{c}_{pj} \left\{ \frac{\partial \overline{T}}{\partial y} \left(A_{jT} + B_{jT} \frac{\partial}{\partial y} \right) + \frac{\overline{\rho}_i \overline{V}_i}{Sc_i} \frac{\partial}{\partial y} \right\} \Bigg] \\ & - \frac{(\gamma_e - 1)}{\overline{c}_v \overline{\rho} Re} \sum_{i=1}^{N_s} \frac{\overline{M}_e}{M_i} \Bigg[\frac{\partial}{\partial y} \left(\frac{\overline{\rho}_i \overline{V}_i}{Sc_i} \right) \\ & + \overline{T} \left\{ B_{iT} \left(-k_x^2 - k_z^2 + \frac{\partial^2}{\partial y^2} \right) + \left(A_{iT} + \frac{\partial B_{iT}}{\partial y} \right) \frac{\partial}{\partial y} + \frac{\partial A_{iT}}{\partial y} \right\} \Bigg] \end{aligned} \tag{E.67}$$

$$L_{4,4} = L^e_{4,4} + L^n_{4,4} \tag{E.68}$$

$$
\begin{aligned}
L_{4,i} = &-\frac{\gamma_e}{\overline{c}_v\overline{\rho}PrRe}\left[\frac{\partial^2\overline{T}}{\partial y^2}\frac{\partial\overline{k}}{\partial\rho_i}+\frac{\partial\overline{T}}{\partial y}\frac{\partial}{\partial y}\left(\frac{\partial\overline{k}}{\partial\rho_i}\right)+\frac{\partial\overline{T}}{\partial y}\frac{\partial\overline{k}}{\partial\rho_i}\frac{\partial}{\partial y}\right] \\
&+\frac{1}{\overline{c}_v\overline{\rho}}\sum_{j=1}^{N_s}\overline{e}_j\frac{\partial\overline{\dot{\omega}}_j}{\partial\rho_i}+\frac{\gamma_e}{\overline{c}_v\overline{\rho}Re}\sum_{j=1}^{N_s}\left[\overline{c}_{pj}\frac{\partial\overline{T}}{\partial y}\left(A_{ji}+B_{ji}\frac{\partial}{\partial y}\right)\right] \\
&-\frac{(\gamma_e-1)}{\overline{c}_v\overline{\rho}Re}\sum_{i=1}^{N_s}\frac{\overline{M}_e}{M_i}\left[\overline{T}\left\{\left(A_{iT}+\frac{\partial B_{iT}}{\partial y}\right)\frac{\partial}{\partial y}\right.\right. \\
&+B_{iT}\left(-k_x^2-k_z^2+\frac{\partial^2}{\partial y^2}\right) \\
&\left.\left.+\frac{\partial A_{iT}}{\partial y}\right\}\right]-\frac{(\gamma_e-1)\gamma_e Ma^2}{\overline{c}_v\overline{\rho}Re}\left(\frac{\partial\overline{u}}{\partial y}\right)^2\frac{\partial\overline{\mu}}{\partial\rho_i}
\end{aligned}
\tag{E.69}
$$

$$
L_{i,1} = ik_x\overline{\rho}_i \tag{E.70}
$$

$$
L_{i,2} = \frac{\partial\overline{\rho}_i}{\partial y}+\overline{\rho}_i\frac{\partial}{\partial y} \tag{E.71}
$$

$$
L_{i,3} = ik_z\overline{\rho}_i \tag{E.72}
$$

$$
L_{i,4} = -\frac{\partial\overline{\dot{\omega}}_i}{\partial T}+\frac{1}{Re}\left[\frac{\partial A_{iT}}{\partial y}+\left(A_{iT}+\frac{\partial B_{iT}}{\partial y}\right)\frac{\partial}{\partial y}+B_{iT}\left(\frac{\partial^2}{\partial y^2}-k_x^2-k_z^2\right)\right] \tag{E.73}
$$

$$
\begin{aligned}
L_{i,i} = &\, ik_x\overline{u}-\frac{\partial\overline{\dot{\omega}}_i}{\partial\rho_i} \\
&+\frac{1}{Re}\left[\frac{\partial A_{ii}}{\partial y}+\left(A_{ii}+\frac{\partial B_{ii}}{\partial y}\right)\frac{\partial}{\partial y}+B_{ii}\left(\frac{\partial^2}{\partial y^2}-k_x^2-k_z^2\right)\right]
\end{aligned}
\tag{E.74}
$$

$$
L_{i,j(j\neq i)} = -\frac{\partial\overline{\dot{\omega}}_i}{\partial\rho_j}+\frac{1}{Re}\left[\frac{\partial A_{ij}}{\partial y}+\left(A_{ij}+\frac{\partial B_{ij}}{\partial y}\right)\frac{\partial}{\partial y}+B_{ij}\left(\frac{\partial^2}{\partial y^2}-k_x^2-k_z^2\right)\right] \tag{E.75}
$$

$L^e_{4,4}$ and $L^n_{4,4}$ are defined to explicitly separate the terms related to the chemical nonequilibrium in $L_{4,4}$. $L^e_{4,4}$ is $L_{4,4}$ if chemical equilibrium or a single species CIG is used. The only terms related to the chemical nonequilibrium are $L^n_{4,4}$, $L_{4,i}$, $L_{i,1}$, $L_{i,2}$, $L_{i,3}$, $L_{i,4}$, and $L_{i,j}$.

Appendix F

EFFECT OF THE INNER PRODUCT ON THE RESOLVENT MODES USING CHEMICAL NONEQUILIBRIUM

The resolvent analysis study of a mixture in chemical nonequilibrium in Chapter 5 used an inner product that differed from the inner product used in Franko, MacCormack, and Lele (2010). Namely, the inner product in Equation 5.26 is

$$\mathcal{W}_c = \text{diag}\left(\overline{\rho}, \overline{\rho}, \overline{\rho}, \frac{\overline{\rho c}_v}{\overline{T} Ma^2 \gamma_e (\gamma_e - 1)}, \frac{\overline{M}_e \overline{T}}{M_1 \gamma_e Ma^2 \overline{\rho}_1}, \ldots, \frac{\overline{M}_e \overline{T}}{M_5 \gamma_e Ma^2 \overline{\rho}_5}\right), \tag{F.1}$$

which is constructed to remove the influence of compressive work on the inner product (Chu, 1965; Hanifi, Schmid, and Henningson, 1996; Franko, MacCormack, and Lele, 2010). However, dvision by $\overline{\rho}_{i_s}$ creates issues in the freestream where $\overline{\rho}_{NO} = \overline{\rho}_N = \overline{\rho}_O = 0$ because the freestream temperature is too cold to support dissociation of N_2 and O_2. To deal with this, Chapter 5 regularizes $\mathcal{W}$ by replacing $\overline{\rho}_{i_s}$ with $\overline{\rho}_{i_s} + \epsilon$, where $\epsilon \ll 1$. On the other hand, Franko, MacCormack, and Lele (2010) used $\overline{\rho}$ instead of $\overline{\rho}_{i_s}$ such that

$$\mathcal{W}_c' = \text{diag}\left(\overline{\rho}, \overline{\rho}, \overline{\rho}, \frac{\overline{\rho c}_v}{\overline{T} Ma^2 \gamma_e (\gamma_e - 1)}, \frac{\overline{M}_e \overline{T}}{M_1 \gamma_e Ma^2 \overline{\rho}}, \ldots, \frac{\overline{M}_e \overline{T}}{M_5 \gamma_e Ma^2 \overline{\rho}}\right). \tag{F.2}$$

Although this may be used to regularize the issues at the freestream, it affects the inner product even within the boundary layer. Most importantly, $\mathcal{W}'$ can not be considered a Chu norm because it does not remove the compressive work, even within the boundary layer. As a result, any results using a single species approximation, such as a chemical equilibrium assumption, that uses the single species Chu norm, defined in Equation 5.10, can not compare with the mixture results that use $\mathcal{W}_c'$ because the inner products do not satisfy the same assumptions. Here, the effects of using $\mathcal{W}_c'$ on the resolvent analysis of a mixture in chemical nonequilibrium will be discussed.

In Figure F.1, several components of $\boldsymbol{\psi}_1$ and $\boldsymbol{\phi}_1$ are compared using chemical equilibrium and chemical nonequilibrium using $\mathcal{W}_c$ and $\mathcal{W}_c'$ for the relatively subsonic mode studied in Section 5.6. Although the modes computed using $\mathcal{W}_c$ and the chemical equilibrium assumption do not agree exactly, their response mode shape and amplitude agrees better than for the mode computed with $\mathcal{W}_c'$, even for the

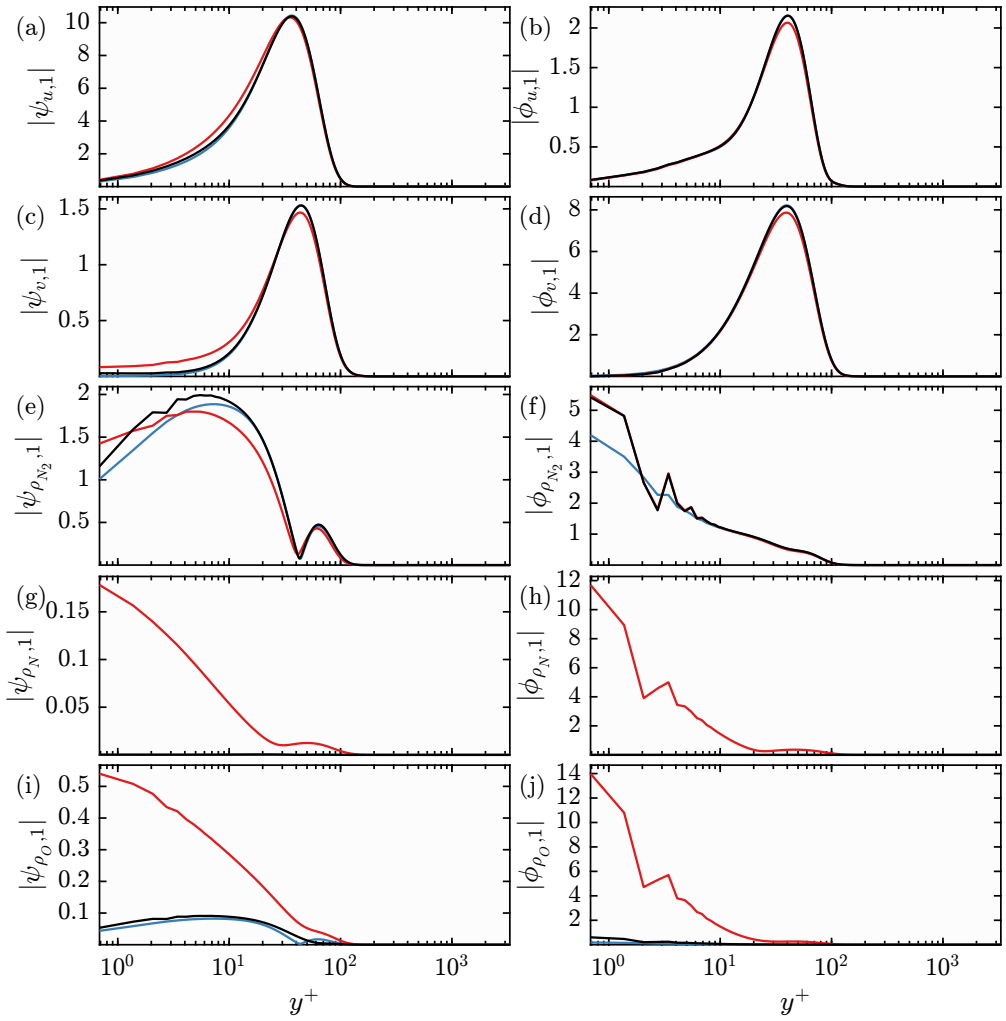

Figure F.1: $|\psi_{u,1}|$ (a), $|\phi_{u,1}|$ (b), $|\psi_{v,1}|$ (c), $|\phi_{v,1}|$ (d), $|\psi_{\rho_{N_2},1}|$ (e), $|\phi_{\rho_{N_2},1}|$ (f), $|\psi_{\rho_N,1}|$ (g), $|\phi_{\rho_N,1}|$ (h), $|\psi_{\rho_O,1}|$ (i), $|\phi_{\rho_O,1}|$ (j) for representative subsonic modes ($k_x = 2\pi/.9$, $k_z = 2\pi/.09$, $c = .48$). Modes computed using chemical equilibrium are in blue. Modes computed using $\mathcal{W}_c$ and $\mathcal{W}_c'$ are in black and red.

$\overline{\rho}_{i_s}$ components. The choice of inner product affects the u and v components of the leading mode. In turn, the chemical equilibrium and chemical nonequilibrium using $\mathcal{W}_c$ velocity components of $\boldsymbol{\psi}_1$ and $\boldsymbol{\phi}_1$ are almost indistinguishable while the streamwise components of the modes computed using $\mathcal{W}_c'$ are visibly affected. The $\phi_{\rho_{N_2},1}$ component is hardly affected by the choice of inner product, likely because $\overline{\rho}_{N_2}$ is a large fraction of $\overline{\rho}$. Perhaps for this reason, $\psi_{\rho_{N_2},1}$ agrees for the three approaches. On the other hand, the agreement in the dissociated components N and O is poor when the inner product is changed. For starters, the ρ_N components of $\boldsymbol{\psi}_1$ and $\boldsymbol{\phi}_1$ become at least three and five orders of magnitude larger when computed using $\mathcal{W}_c'$. Furthermore $\mathcal{W}_c'$ predicts that the ρ_N component is on the same order of

magnitude as the ρ_O component in the response mode. For this temperature, such species densities are not expected. Lastly, comparing the ρ_O components shows that using $\mathcal{W}_c'$ produces modes with larger amplitudes near the wall. Finally, the values of σ_1 are 6.62 using $\mathcal{W}_c$, 6.64 using chemical equilibrium, and 6.84 using $\mathcal{W}_c'$.

Although the choice of inner product affects primarily the ρ_{i_s} components, its effect can be seen on even the velocity components. The modes computed using the chemical equilibrium approach and the chemical nonequilibrium approach using $\mathcal{W}_c$ agree well because their inner products satisfy the same assumption, namely that compressive work is not included in the norm. Changing the inner product causes unphysical behavior in the response mode shape by increasing the production of ρ_N in the response modes on par with the other dissociated components.

Now the effect of the inner product on the relatively supersonic modes studied in Section 5.6 is studied. Figure F.2 plots various components of $\boldsymbol{\psi}_1$ and $\boldsymbol{\phi}_1$, which display support in the freestream characteristic of the relatively supersonic modes even with $\mathcal{W}_c'$. For this mode, the u and v components of the modes computed with $\mathcal{W}_c'$ differ substantially throughout the domain. The effects of using $\mathcal{W}_c'$ become more severe when the dissociated components are compared. The ρ_O components using $\mathcal{W}_c'$ are nonzero in the freestream. These components are driven through forcing from the dissociated ρ_{i_s} components, which act as chemical sources in the freestream. Because of the presence of dissociated components in the freestream, the X_{i_s} components are also nonzero, despite the freestream temperature being too small to support chemical reactions. The nonzero X_{i_s} are driven by the shear terms related to $\frac{\partial\overline{\dot{\omega}}_i}{\partial\rho_j}$, which provide component-wise amplification from ρ_j to ρ_i. Furthermore, the values of the X_N response components are an order of magnitude smaller than the X_{N_2} response components, which is not expected for the mean temperatures used here. Finally, the values of σ_1 are 45.75 using $\mathcal{W}_c$, 45.75 using chemical equilibrium, and 137.48 using $\mathcal{W}_c'$.

The use of $\mathcal{W}_c'$ supports dissociated components in the freestream. This allows for forcing from said dissociated components to act as sources in the freestream which causes changes in the species concentrations in the freestream. Such behavior is not expected at the freestream temperatures used in this analysis. When $\mathcal{W}_c$ is used, the freestream dissociated components are penalized in the inner product. Using the inner product used in Franko, MacCormack, and Lele (2010) causes non-negligible traces of dissociated components throughout the domain to be predicted using a linear approach. The large presence of the dissociated components can affect even

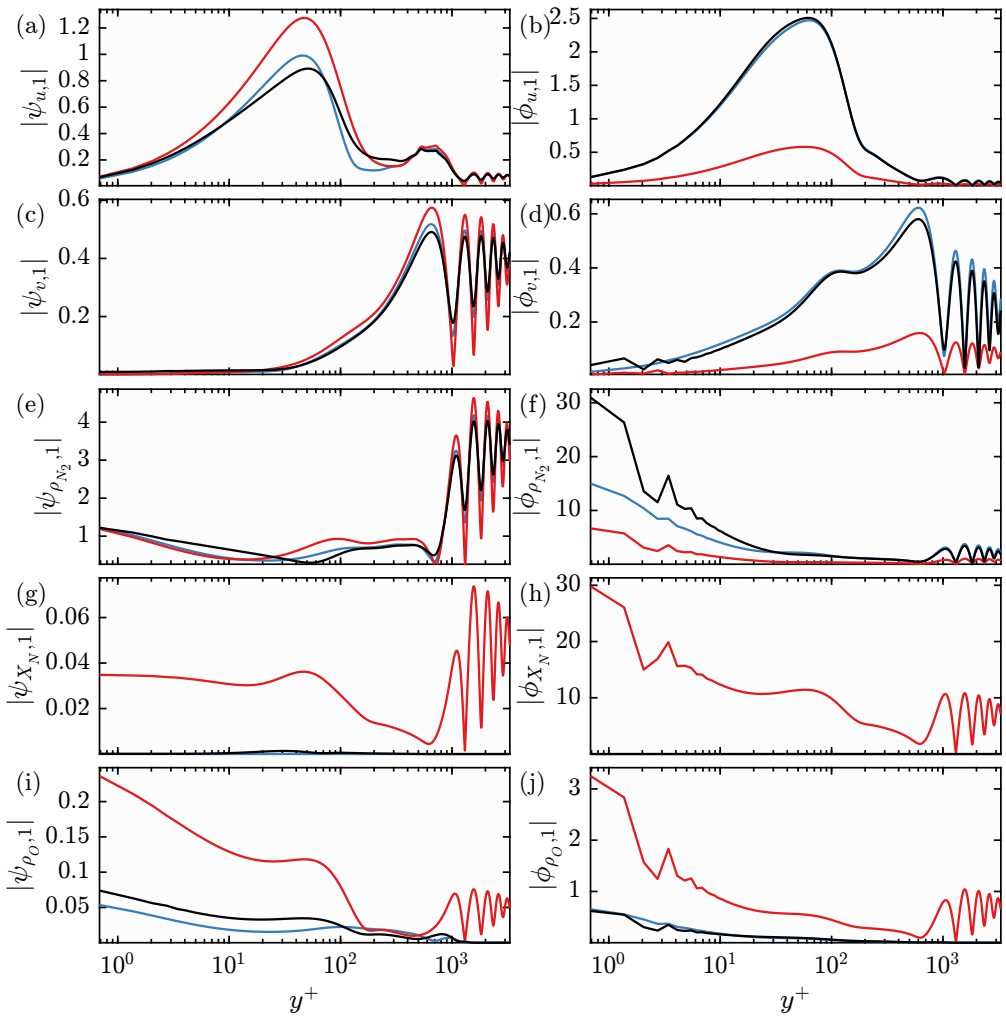

Figure F.2: $|\psi_{u,1}|$ (a), $|\phi_{u,1}|$ (b), $|\psi_{v,1}|$ (c), $|\phi_{v,1}|$ (d), $|\psi_{X_{N_2},1}|$ (e), $|\phi_{X_{N_2},1}|$ (f), $|\psi_{X_N,1}|$ (g), $|\phi_{X_N,1}|$ (h), $|\psi_{\rho_O,1}|$ (i), $|\phi_{\rho_O,1}|$ (j) for representative supersonic modes ($k_x = 2\pi/5$, $k_z = 2\pi/10$, $c = .48$). Modes computed using chemical equilibrium are in blue. Modes computed using $\mathcal{W}_c$ and $\mathcal{W}_c'$ are in black and red.

the u and v components.

The effect of the inner product can be seen by considering how the inner product affects the weighting of $\mathcal{A} = (-i\omega + \widehat{\mathcal{L}})$. Equation 2.15 can be rewritten as

$$\mathcal{A}\boldsymbol{\psi}_1 = \sigma_1 \boldsymbol{\phi}_1. \tag{F.3}$$

Since $\boldsymbol{\psi}_1$ and $\boldsymbol{\phi}_1$ are orthonormal with respect to the inner products $\langle\cdot,\cdot\rangle_r = \langle\cdot,\cdot\rangle_f$ from Equation 2.7 and 2.8, the vectors $\boldsymbol{\psi}_{W,1} = \mathcal{W}_c^{1/2}\boldsymbol{\psi_1}$ and $\boldsymbol{\phi}_{W,1} = \mathcal{W}_c^{1/2}\boldsymbol{\phi_1}$ are orthornomal with respect to the inner product $\langle\cdot,\cdot\rangle$ in Equation 2.9. $\boldsymbol{\psi}_{W,1}$ and $\boldsymbol{\phi}_{W,1}$

can be introduced by manipulating Equation F.3 as

$$\mathcal{W}_c^{1/2}\mathcal{A}\boldsymbol{\psi}_1 = \sigma_1\mathcal{W}_c^{1/2}\boldsymbol{\phi}_1 \tag{F.4}$$

$$\mathcal{W}_c^{1/2}\mathcal{A}\mathcal{W}_c^{-1/2}\mathcal{W}_c^{1/2}\boldsymbol{\psi}_1 = \sigma_1\mathcal{W}_c^{1/2}\boldsymbol{\phi}_1 \mathcal{A}_W\boldsymbol{\psi}_{W,1} \qquad = \sigma_1\boldsymbol{\phi}_{W,1}, \tag{F.5}$$

where $\mathcal{A}_W = \mathcal{W}_c^{1/2}\mathcal{A}\mathcal{W}_c^{-1/2}$. Now the SVD of $\mathcal{A}$ using the inner products $\langle\cdot,\cdot\rangle_r$ and $\langle\cdot,\cdot\rangle_f$ is equivalent to the SVD of $\mathcal{A}_W$ with the 2-norm $\langle\cdot,\cdot\rangle$.

The effect of the choice of norm on $\mathcal{A}_W$ will be presented by considering the scaling of the terms in the operator. This will be done by defining the block diagonal form of $\mathcal{A}$ as

$$\mathcal{A} = \begin{bmatrix} A_{\mathbf{u},\mathbf{u}} & A_{\mathbf{u},T} & A_{\mathbf{u},i} & A_{\mathbf{u},j} \\ A_{T,\mathbf{u}} & A_{T,T} & A_{T,i} & A_{T,j} \\ A_{i,\mathbf{u}} & A_{i,T} & A_{i,i} & A_{i,j} \\ A_{j,\mathbf{u}} & A_{j,T} & A_{j,i} & A_{j,j} \end{bmatrix}. \tag{F.6}$$

The block terms, $A_{l,k}$ denote terms in the LNSE. The subscript k denotes which blocks act on $q_{j=k}$ and the subscript $l = \mathbf{u}$ denotes the momentum equation, $l = T$ the temperature equation, $l = i$ is the ith species continuity equation and $l = j$ is the jth species continuity equation. Here, i will be taken to represent the undissociated species while j represents the dissociated species. From Equations E.70, E.71, and E.72, the blocks $A_{i,\mathbf{u}} \sim \rho_i$ and $A_{j,\mathbf{u}} \sim \rho_j$. $\mathcal{W}_c$ can be scaled as

$$\mathcal{W}_c^{1/2} \sim \text{diag}\left(1, 1, \frac{1}{\sqrt{\overline{\rho}_i}}, \frac{1}{\sqrt{\overline{\rho}_j}}\right). \tag{F.7}$$

As such,

$$\mathcal{A}_W \sim \begin{bmatrix} A_{\mathbf{u},\mathbf{u}} & A_{\mathbf{u},T} & A_{\mathbf{u},i}\sqrt{\overline{\rho}_i} & A_{\mathbf{u},j}\sqrt{\overline{\rho}_j} \\ A_{T,\mathbf{u}} & A_{T,T} & A_{T,i}\sqrt{\overline{\rho}_i} & A_{T,j}\sqrt{\overline{\rho}_j} \\ \sqrt{\overline{\rho}_i} & \frac{1}{\sqrt{\overline{\rho}_i}}A_{i,T} & A_{i,i} & \frac{\sqrt{\overline{\rho}_j}}{\sqrt{\overline{\rho}_i}}A_{i,j} \\ \sqrt{\overline{\rho}_j} & \frac{1}{\sqrt{\overline{\rho}_j}}A_{j,T} & \frac{\sqrt{\overline{\rho}_i}}{\sqrt{\overline{\rho}_j}}A_{j,j} & A_{j,j} \end{bmatrix}. \tag{F.8}$$

Because $\overline{\rho}_j \ll 1$, the $A_{\mathbf{u},j}$, $A_{T,j}$, and $A_{i,j}$ terms are negligible, especially in the freestream. This mitigates the nonnormal component-wise amplification from ρ_j to $\mathbf{u}$, T, and ρ_i. Otherwise the $A_{i,j}$ terms, even in the freestream, are nonzero because of the $\frac{\partial\overline{\dot{\omega}}i}{\partial\rho_j}$ terms. The $\mathcal{W}_c$ inner product provides weighting that removes that source of amplification. The ρ_j is instead acted on by $A_{j,j}$ which provides molecular diffusion, thus damping its contribution. On the other hand, the $A_{j,T}$ and $A_{j,i}$ terms

become weighted by $\left(\overline{\rho}_j\right)^{-1/2}$. This serves to increase the amplification from T and ρ_i to ρ_j. The $\frac{\partial\overline{\omega}j}{\partial\rho_i}$ terms are negligible in the freestream, so any nonnormal amplification of ρ_j is not an issue.

Now, this analysis will be repeated, except using $\mathcal{W}_c'$. Since $\overline{\rho} \sim 1$, $\mathcal{W}_c' \sim \mathcal{I}$. This causes

$$\mathcal{A}_W \sim \begin{bmatrix} A_{\mathbf{u},\mathbf{u}} & A_{\mathbf{u},T} & A_{\mathbf{u},i} & A_{\mathbf{u},j} \\ A_{T,\mathbf{u}} & A_{T,T} & A_{T,i} & A_{T,j} \\ \overline{\rho}_i & A_{i,T} & A_{i,i} & A_{i,j} \\ \overline{\rho}_j & A_{j,T} & A_{j,j} & A_{j,j} \end{bmatrix}. \tag{F.9}$$

Using $\mathcal{W}_c'$ does not bias any of the terms in $\mathcal{A}_W$ with the species densities. This allows component-wise amplification from ρ_j through the $\frac{\partial\overline{\omega}i}{\partial\rho_j}$ terms in $A_{i,j}$. This encourages nonzero ρ_j, even in the freestream. This explains the behavior seen in Figure F.2. In conclusion, using $\mathcal{W}_c'$ leads to unphysical behavior by allowing non-negligible amplification of the dissociated components. This effect can be mitigated by using $\mathcal{W}_c$ instead as it biases nonnormal amplification from the dissociated components.